NASA Conference Publication 3144

Physics of Forced Unsteady Separation

Edited by
L. W. Carr
Ames Research Center
Moffett Field, California

Proceedings of a NASA/AFOSR/ARO workshop held at
NASA Ames Research Center,
Moffett Field, California
April 17-19, 1990

National Aeronautics and
Space Administration

Ames Research Center
Moffett Field, California 94035-1000

1992

FOREWORD

During the past decade, significant effort has been applied to analysis and understanding of various aspects of dynamic flow field behavior. The inability to control the effects of dynamic stall has proven to be the limiting factor that has precluded use of dynamic lift on helicopters or aircraft. Even though significant effort has been expended on attempts to control the dynamic stall vortex that occurs on rapidly pitching aerodynamic surfaces, progress has been slow, and results have been limited. However, control and use of dynamic lift offers much potential for dramatic improvement of aircraft and helicopter performance, and has been identified as a critical research topic by both the Air force Office of Scientific Research (AFOSR) and the Army Research Office (ARO), which have supported major research efforts in this area.

During discussions of this topic with Capt. Hank Helin, USAF, program manager for Unsteady and Separated Flows for AFOSR, and Dr. Tom Doligalski, Chief, Fluid Dynamics Branch, Engineering Sciences Division of the ARO, we came to the conclusion that dynamic stall control was ONLY possible if the physics of the forced unsteady separation event itself was better understood. We felt that it was time that emphasis be shifted from modeling of the dynamic stall vortex movement down the airfoil; it should be placed on the need for better understanding of the forced unsteady separation process itself. The title of the workshop was then chosen to emphasize this area.

It became clear that there was a need for the research community to become more aware of the work being performed by the various scientists supported by the research offices. It was also clear that there was a need for greater interaction between the various researchers in an environment where discussion focused on the subject of unsteady separation could be sustained. This became the theme of the workshop and governed the scheduling of the meetings, as well as the guidance given to the various scientists who were invited to attend.

The workshop was a success, mostly due to the enthusiastic participation of the attendees. The sessions became forums for discussion and analysis of research findings, rather than the usual sequence of presentation without time for discussion prevalent at national meetings in the recent past.

The speakers were asked to submit abstracts for publication, and responded with written versions that range from abstract to full paper; these have all been included. In some cases, selected viewgraphs from the authors' presentations also have been included, where these add to the message of the written text. Unfortunately, publication page-number limits have precluded the inclusion of a full set of viewgraphs, but every effort has been made to include all those viewgraphs that significantly supplement the written text.

Lawrence W. Carr
Editor and Workshop Coordinator

CONTENTS

CONTENTS (cont'd)

UNSTEADY SEPARATION EXPERIMENTS ON 2-D AIRFOILS, 3-D WINGS, AND MODEL HELICOPTER ROTORS

Peter F. Lorber and Franklin O. Carta
United Technologies Research Center
East Hartford, CT 06108

ABSTRACT FOR NASA/AFOSR/ARO WORKSHOP ON
PHYSICS OF FORCED UNSTEADY SEPARATION
APRIL 17-19, 1990

Information on unsteady separation and dynamic stall is being obtained from two experimental programs that have been underway at United Technologies Research Center since 1984. The first program is designed to obtain detailed surface pressure and boundary layer condition information during high amplitude pitching oscillations of a large (17.3 in chord) model wing in a wind tunnel. The second program involves the construction and testing of a pressure-instrumented model helicopter rotor. This presentation describes some of the results of these experiments, and in particular compares the detailed dynamic stall inception information obtained from the oscillating wing with the unsteady separation and reverse flow results measured on the retreating blade side of the model rotor during wind tunnel testing.

An inital, two-dimensional oscillating wing experiment was performed in 1986 under AFOSR sponsorship, and has been documented in Refs. 1 and 2. Surface pressure and hot film data were acquired for constant pitch rate ramps and sinusoidal oscillations in the range of α = 0 to 30 deg, for M = 0.2, 0.3, and 0.4, and Re = 2,000,000 to 4,000,000. Figure 1 shows typical results for an M = 0.2, A = $\dot{\alpha}c/2U_\infty$ = 0.01 ramp. This figure is similar to those in Refs. 1 and 2, and shows time histories of the ensemble-averaged pressures at each of the 18 transducers on the airfoil surface. A negative pressure spike (caused by the dynaic stall vortex) forms near τ = 0.47, and moves back along the airfoil. Figure 2 (not previously published) shows chordwise pressure distributions at several values of τ during this process. The passage of the vortex is shown by the pressure bulge on the upper surface. The references discuss the effects of pitch rate, pitching waveform, and Mach number on the stall process. Compressibility effects were very significant, as a small supersonic bubble forms near the leading edge at M = 0.4, and the peak suction pressures and the unsteady increments to the airlods are much weaker. Reference 3 describes a Navier-Stokes simulation of the 2-D experiments. Good agreement was obtained up through the formation of the dynamic stall vortex, while many of the quantitative aspects of the periodic vortex shedding after stall were missed.

This study is now being extended under ARO and AFOSR sponsorship to include three-dimensional measurements on a finite tip model. In addition to obtaining information on how the presence of the wing tip affects the dynamic stall process, this experiment is intended to study sweep and compressibility effects. The model, shown in Fig. 3, consists of a square wing with the same (17.3 in) chord and airfoil section (SSC-A09) as the 2-D wing. The instrumentation consists of chordwise arrays of pressure transducers at 5 spanwise stations (112

transducers) and arrays of surface hot film gages at 3 spanwise stations (16 total gages) to determine transistion and separation information. The model will be tested at 3 sweep angles: Λ = 0, 15, and 30 deg, and at Mach numbers between 0.2 and (structural loads permitting) 0.6. The experiment is scheduled to be completed in 1990.

In addition to large amplitude ramps and sinusoids, information will be obtained on small amplitude ($\pm$0.5 to 2 deg) oscillations near the static stall angle. This program will be sponsored by NASA Lewis and ARO, and is designed to study the incipient stages of stall flutter, with particular application to aircraft propellors. Results of an earlier, smaller scale experiment were reported in Ref. 4. The aerodynamic damping was found to be substantially more negative for very small amplitude oscillations, allowing a rapid growth to a limit cycle motion.

The helicopter rotor program involves the construction and testing of a heavily instrumented, 9.5 ft diameter scale model of a current-technology main rotor (Fig. 4). The model contains 176 miniature pressure transducers, as well as strain gages, temperature sensors, and surface hot film gages. Hover testing was described in Ref. 5, and aerodynamic results from a 1989 wind tunnel test are given in Ref. 6. A great deal of information has been obtained using this model rotor. Of current interest is the behavior of the inboard portion of the retreating blade at moderately high advance ratios ($\mu = U_\infty/\Omega R \sim 0.28$-$0.36$). This region is subject to rapid increases in angle of attack and rapid reductions in relative velocity. Figure 5 shows chordwise pressure distributions for r/R = 0.4 at four azimuths on the retreating side. The flow appears highly loaded but attached at ψ = 190, shows leading edge separation at at ψ = 220, has a very large aft loading at ψ = 270, and is beginning to reattach at ψ = 320. Time histories of the ensemble averaged pressures at r/R = 0.225 and 0.4 are shown in Fig. 6. Sharp negative pressure spikes are present (on the upper surface only) near ψ = 175 at r/R = 0.225 and near ψ = 210 at r/R = 0.4. The flow appears to separate after the spikes have passed, as shown by flat ensemble averaged pressures between ψ = 180 and 315. This phenomenon is similar to the shedding of the dynamic stall vortex on the oscillating 2-D airfoil (Fig. 1). The non-dimensional convection speed of the spike (0.25 times the local relative velocity) is also similar.

The rotor flow field has many complexities not present with the 2-D airfoil. The sequence observed on the retreating blade side at a particular radial station may include: forming and shedding a leading edge vortex, entering the region of reverse relative velocity, shifting from positive to negative lift, shedding a vortex from the trailing edge that moves towards the leading edge, resuming positive relative velocity and lift, and interacting with the wake of the rotor hub. Additional complications include radial velocity and twist gradients and aeroelastic deflections. With all of these factors present, it is encouraging to see some similarities to the simpler, oscillating 2-D results, but one must not forget how complex the rotor flow field actually is. This observation is lent particular weight by the many references to the helicopter stall problem in the introductory sections of oscillating airfoil papers.

References

1. Lorber, P.F., and Carta, F.O., "Airfoil Dynamic Stall at Constant pitch Rate and High reynolds Number," AIAA J. Aircraft, Vol 25, pp. 548-556, June 1988.

2. Lorber, P.F., and Carta, F.O., "Unsteady Stall Penetration Experiments at High Reynolds Number," AFOSR TR-87-1202, April 1987.

3. Patterson, M.T., and Lorber, P.F., "Computational and Experimental Studies of Compressible Dynamic Stall," 4th Symposium on Numerical and Physical Aspects of Aerodynamic Flows, Long Beach, CA, Jan 1989 (accepted for publication in the J. Fluids & Structures, 1990).

4. Carta, F.O., and Lorber, P.F., "Experimental Study of the Aerodynamics of Incipient Torsional Stall Flutter," AIAA J. Propulsion and Power, Vol. 3, pp.164-170, March-April, 1987.

5. Lorber, P.F., Stauter, R.C., and Landgrebe, A.J., "A Comprehensive Hover Test of the Airloads and Airflow of an Extensively Instrumented Model Helicopter Rotor," 45th Annual Forum of the American Helicopter Society, Boston, MA, May 1989.

6. Lorber, P.F., "Aerodynamic Results of a Pressure-Instrumented Model Rotor Test at the DNW," to be presented at the 46th Annual Forum of the American Helicopter Society, Washington, DC, May 1990.

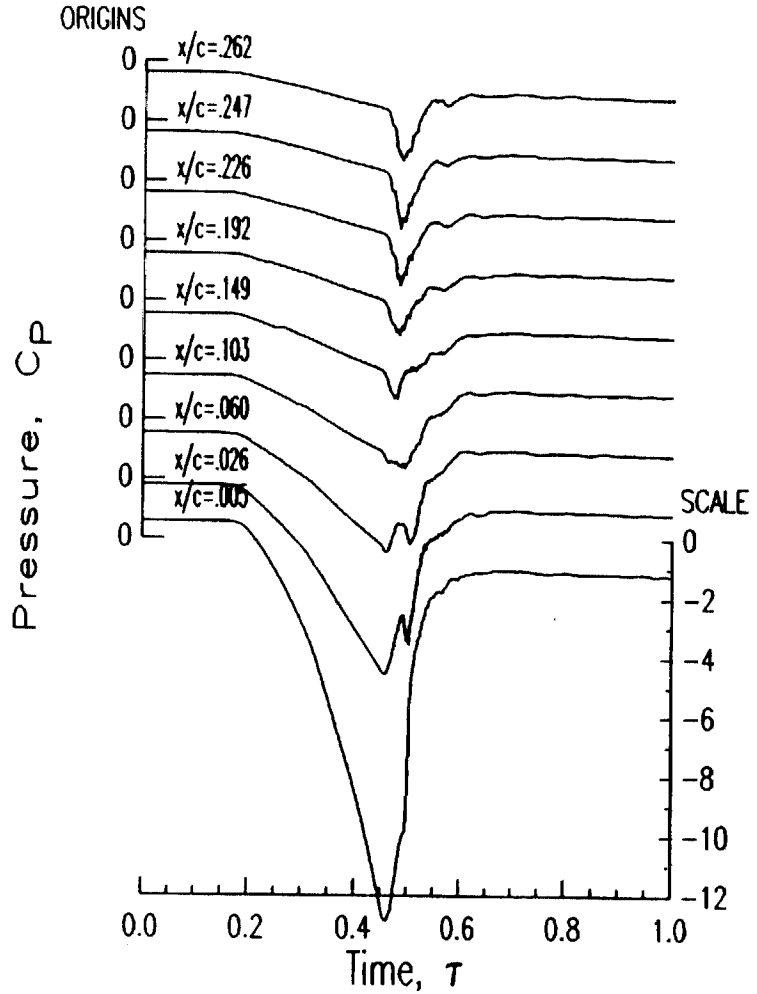

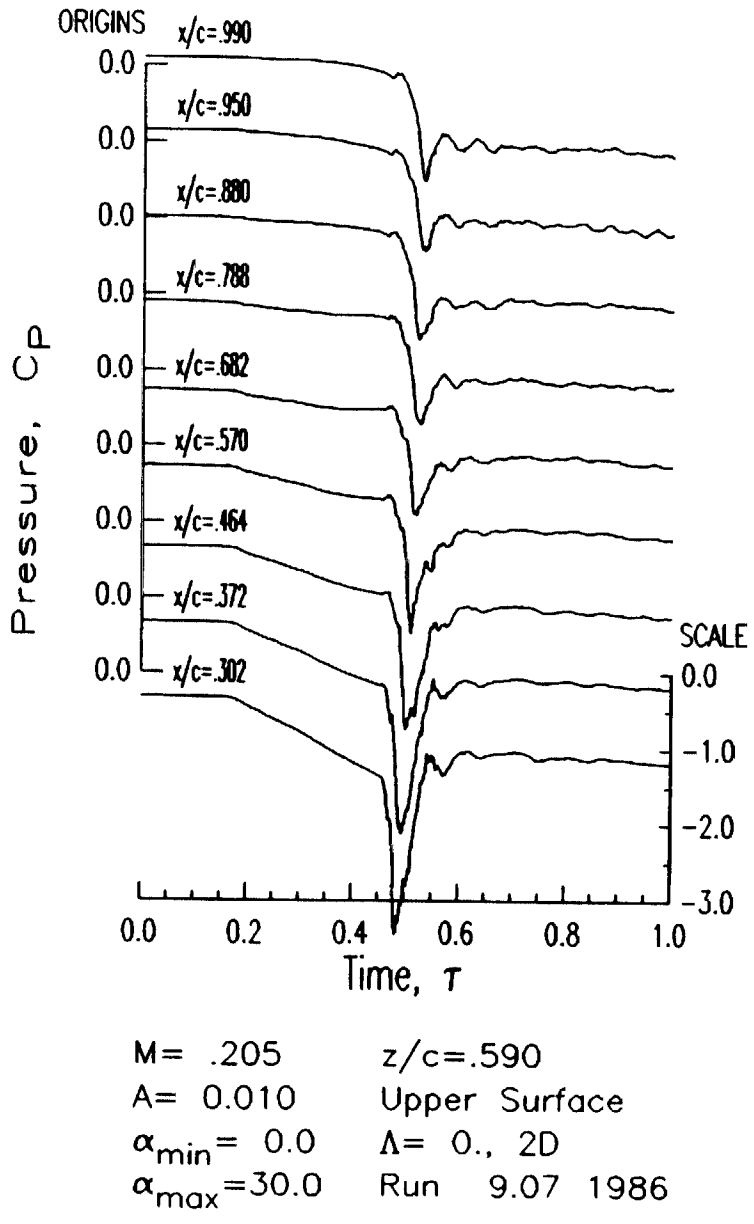

Figure 1. Pressure time histories showing dynamic stall on the 2-D oscillating wing.

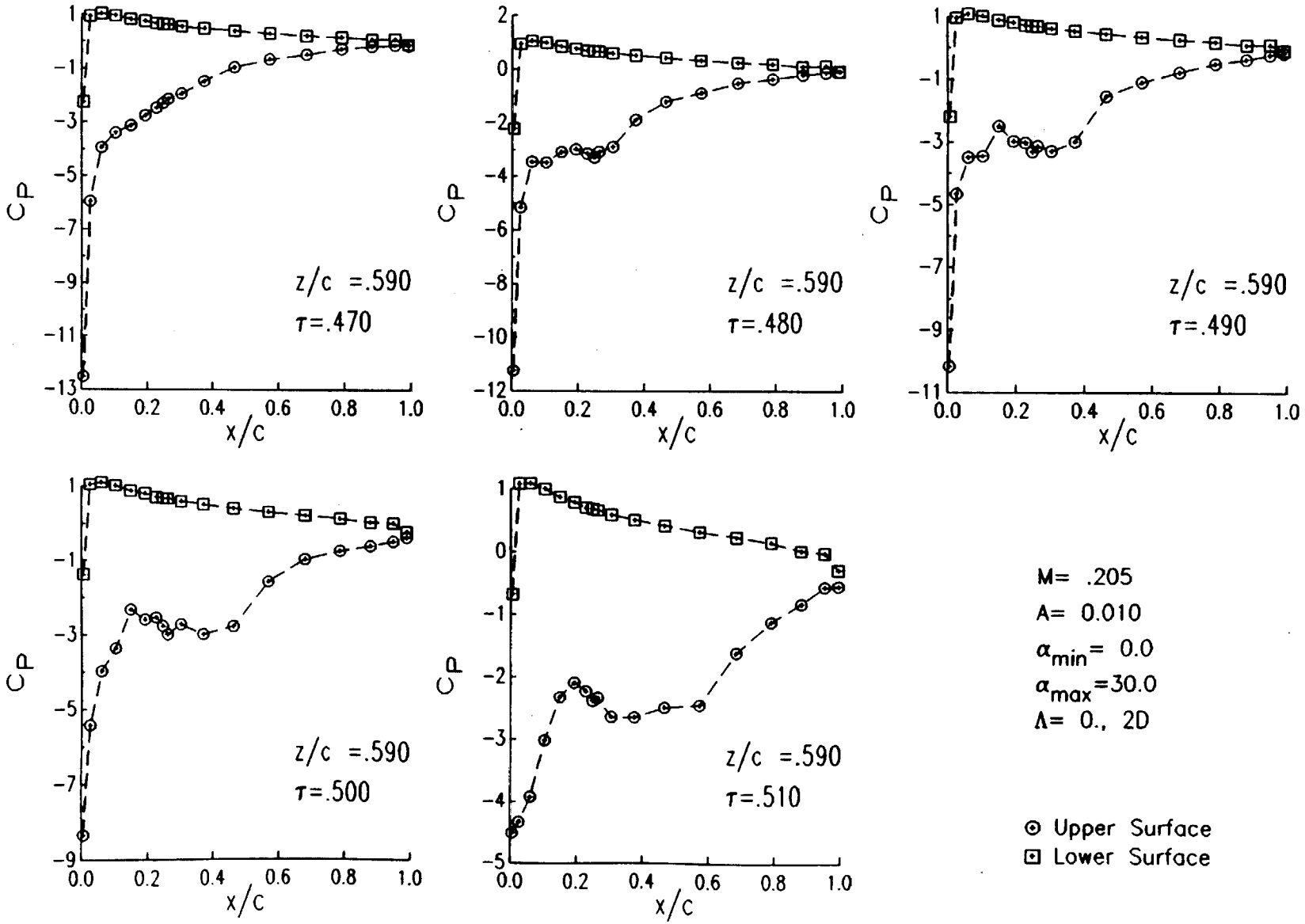

Figure 2. Chordwise pressure distributions showing propagation of the dynamic stall vortex on the 2-D oscillating wing.

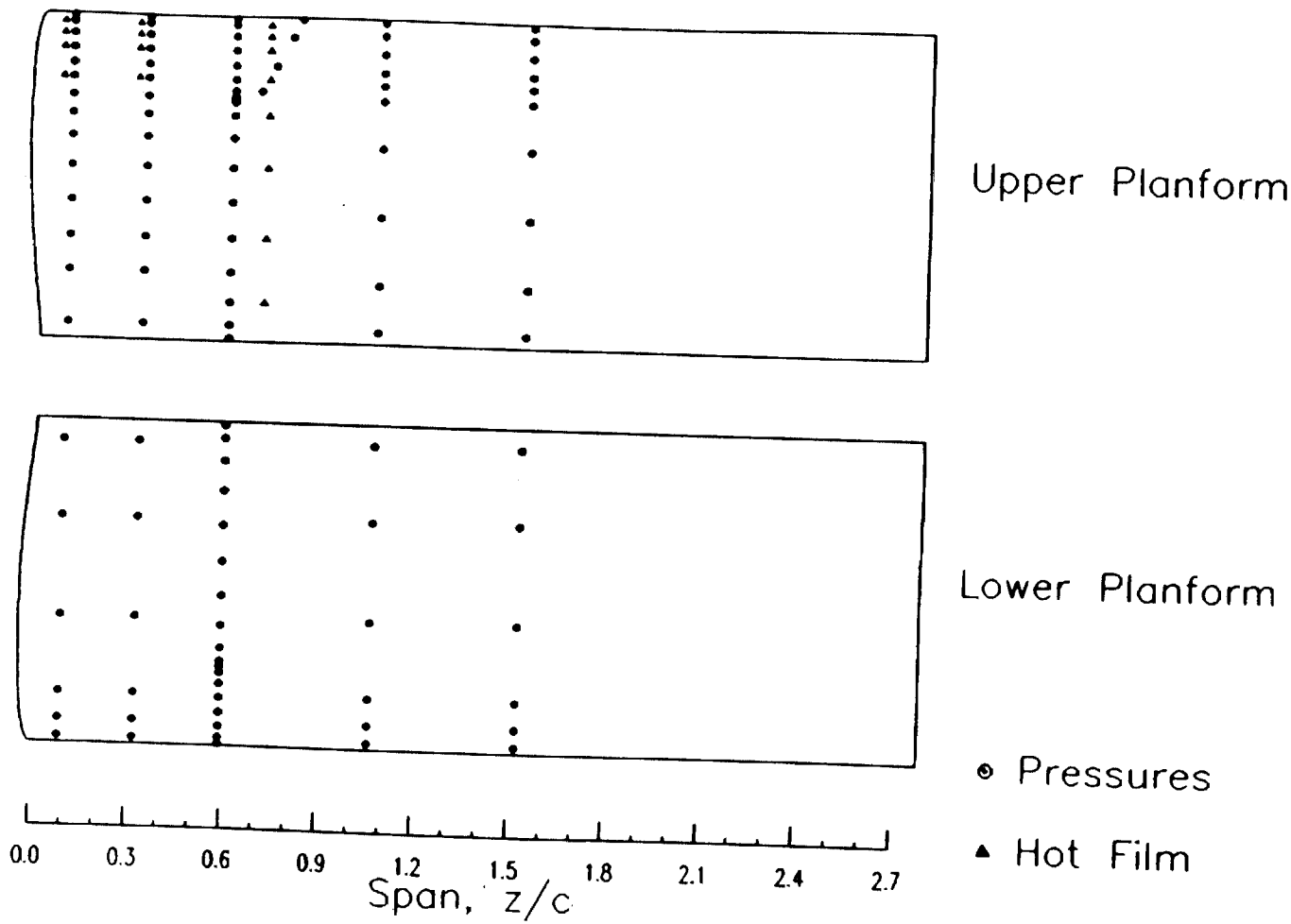

Figure 3. 3-D oscillating wing planform and instrumentation layout.

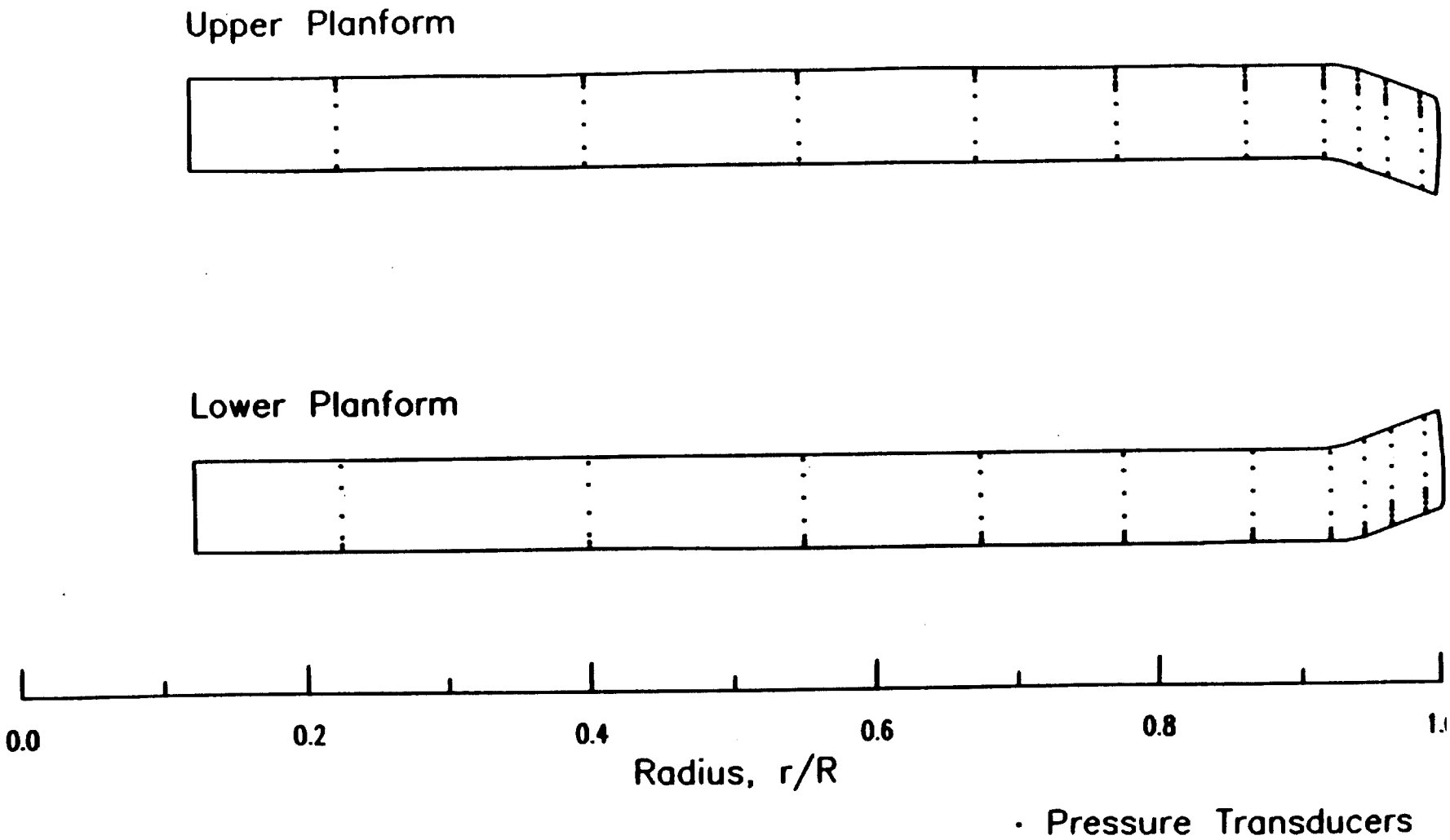

Figure 4. Model helicopter rotor planform and instrumentation layout.

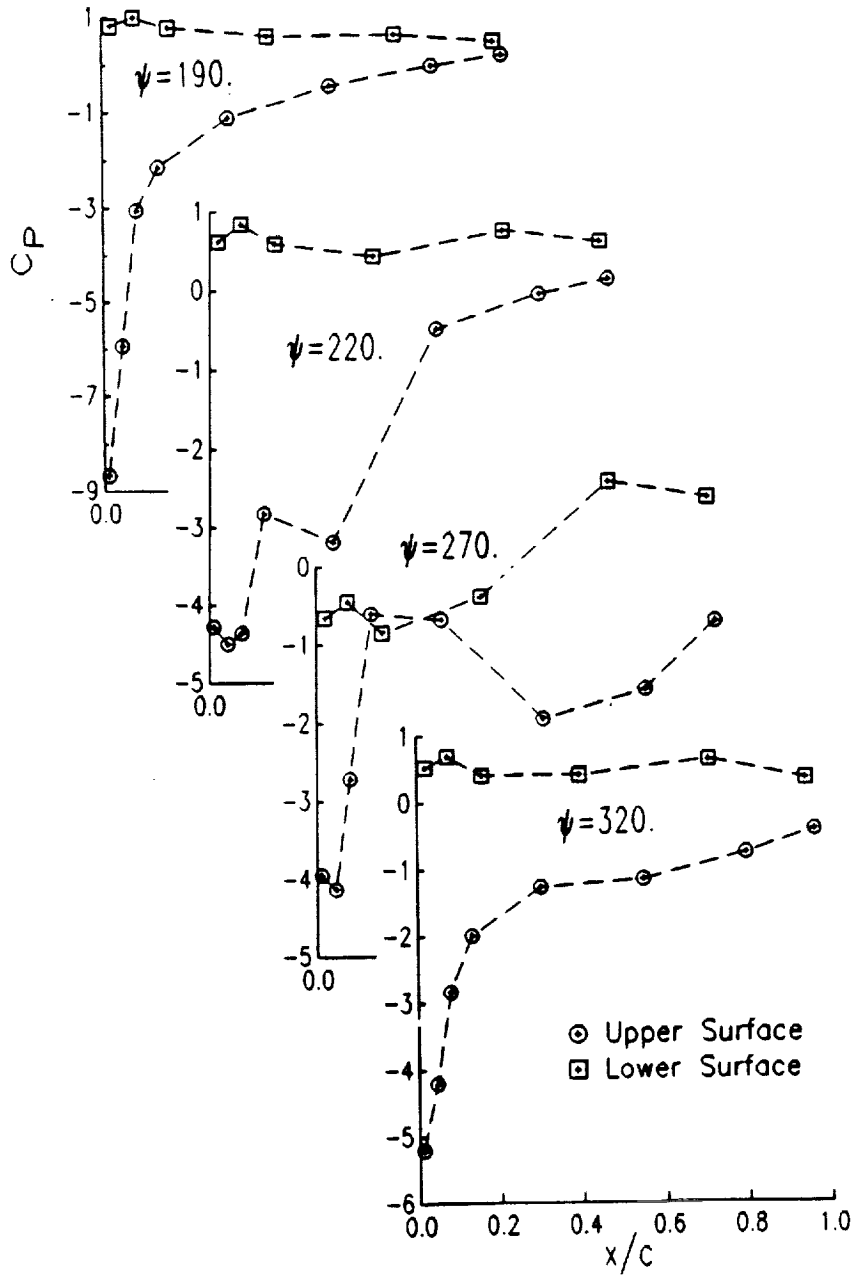

Figure 5. Chordwise pressure distributions on the model helicopter rotor, showing the separation process at r/R = 0.4.

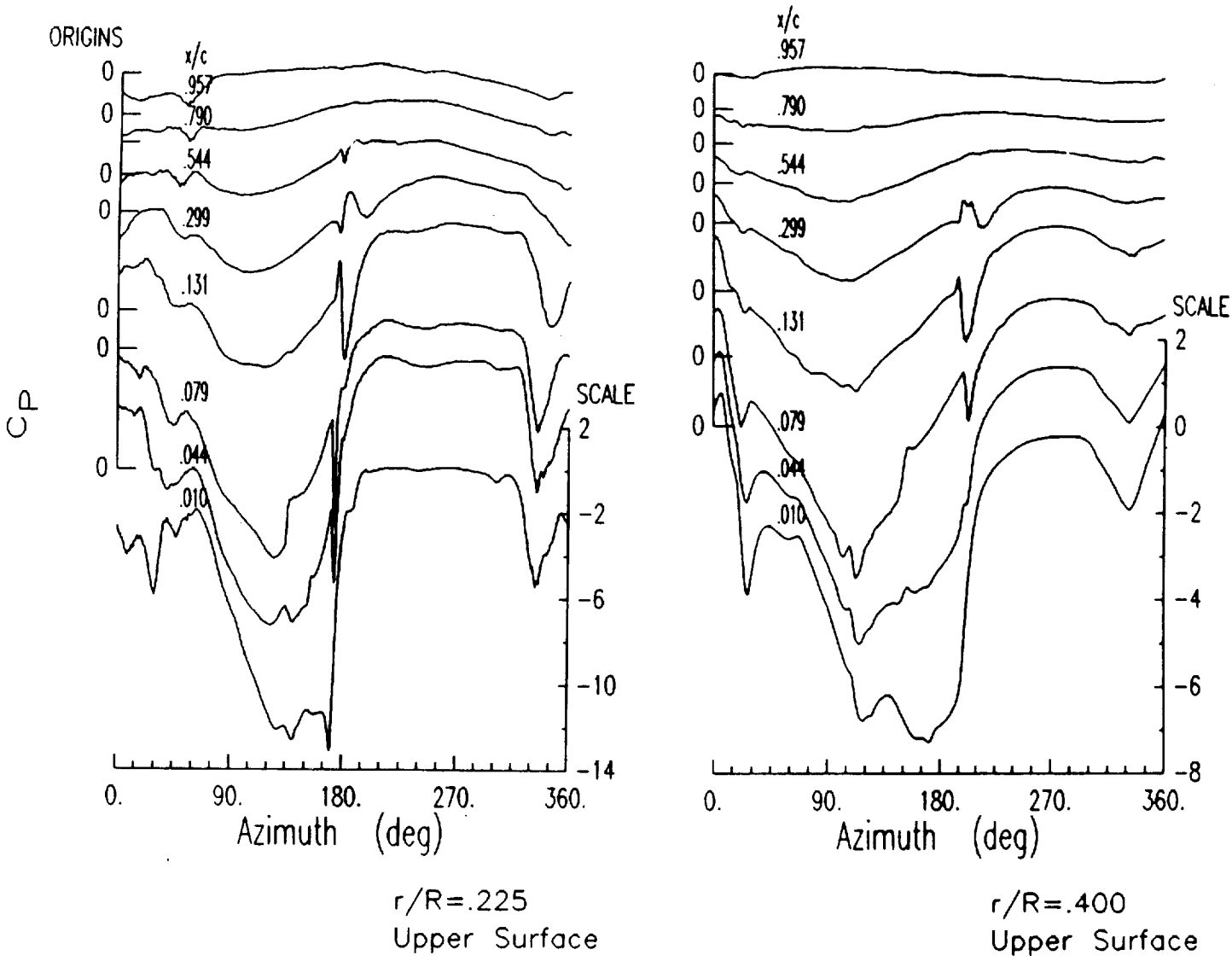

Figure 6. Pressure time histories on the model helicopter rotor, showing vortex formation and flow separation.

2-D AIRFOIL EXPERIMENT

- Pressure and Hot Film Instrumented 8 ft Span Wing
- Sikorsky SSC-A09 9% thick airfoil
- M = 0.2, 0.3, 0.4
- Re = 2 to 4 million (c = 17.3 in)
- $\alpha = 0.0 \Rightarrow 30.0$ deg Ramps and Sinusoids
- $A = \frac{\dot{\alpha} c}{2U} = 0.001$ to 0.02
- 1986 Test under AFOSR Sponsorship

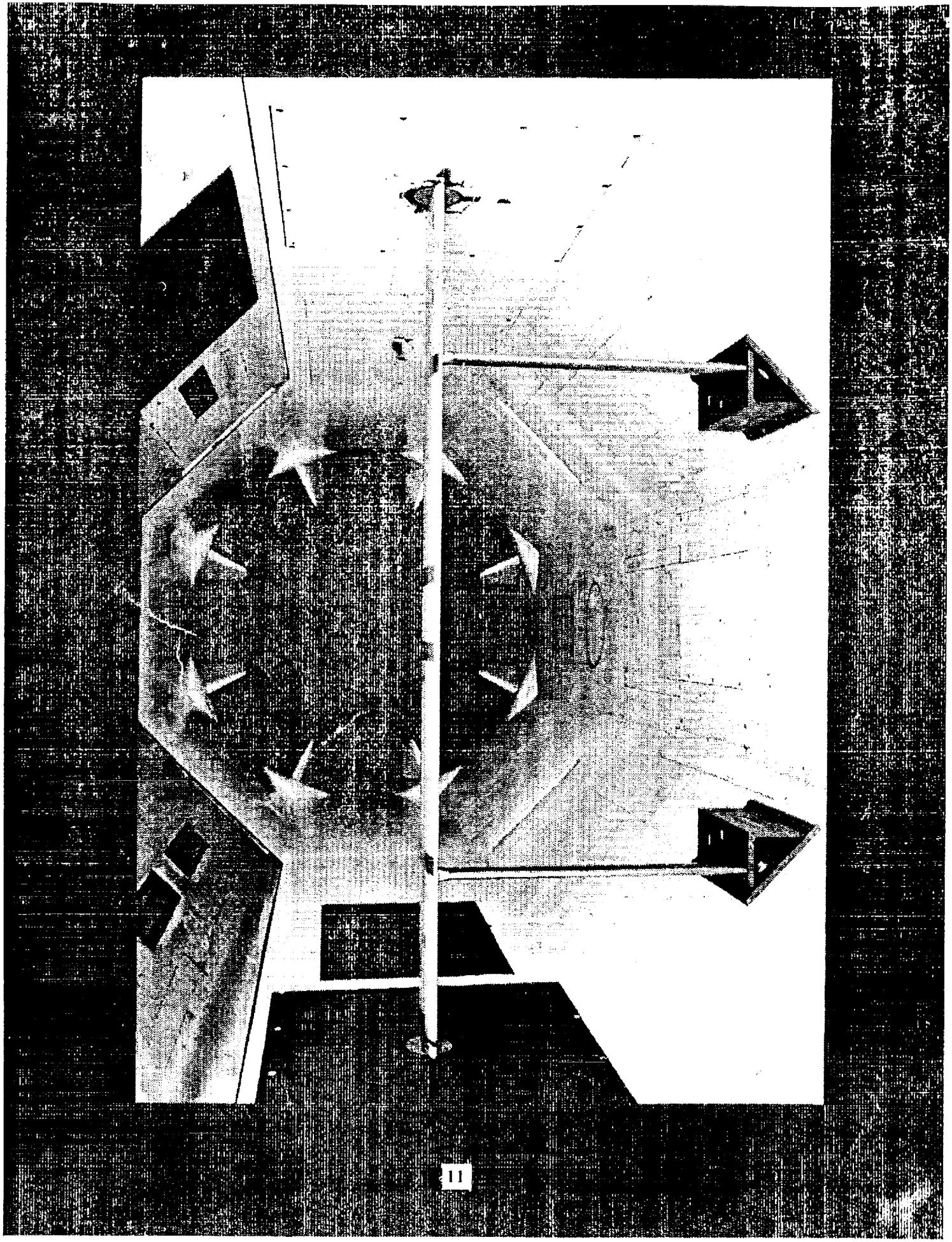

AIRFOIL CONSTANT-PITCH-RATE MOTION

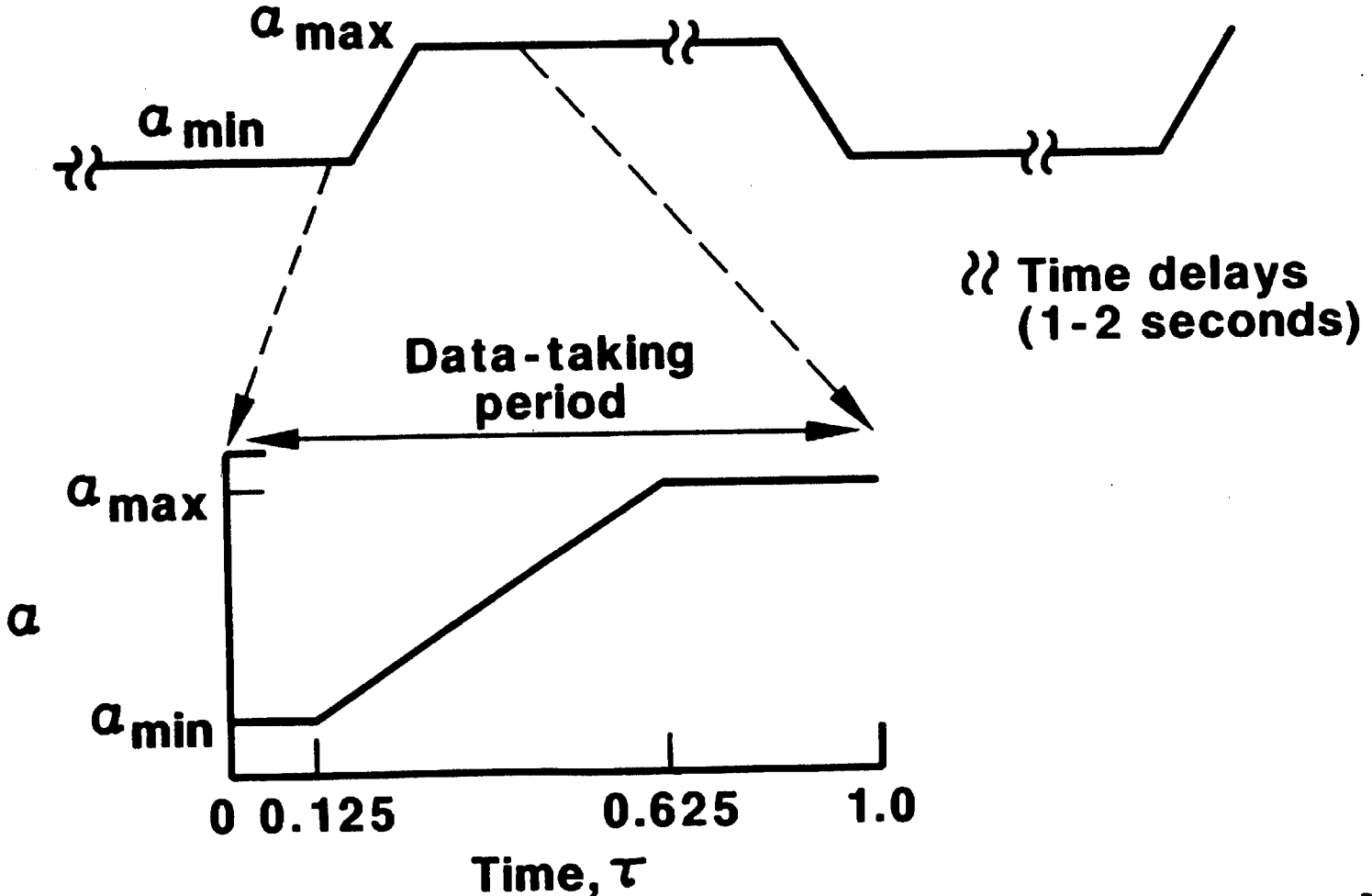

RD1199ETX.001

2-D AIRFOIL COMPUTATIONS

- Compressible Navier-Stokes Method (NS2D by Sankar, et. al)
- Computations Made by Patterson (1988) at M=0.2 and 0.4
- Correctly Predicts Lift Slope, Peak Lift, and Stall Angle
- Correctly Predicts Reduced Lift and Earlier Stall at M=0.2
- Overpredicts Post-stall Vortex Shedding
- Smears Shock near Leading Edge

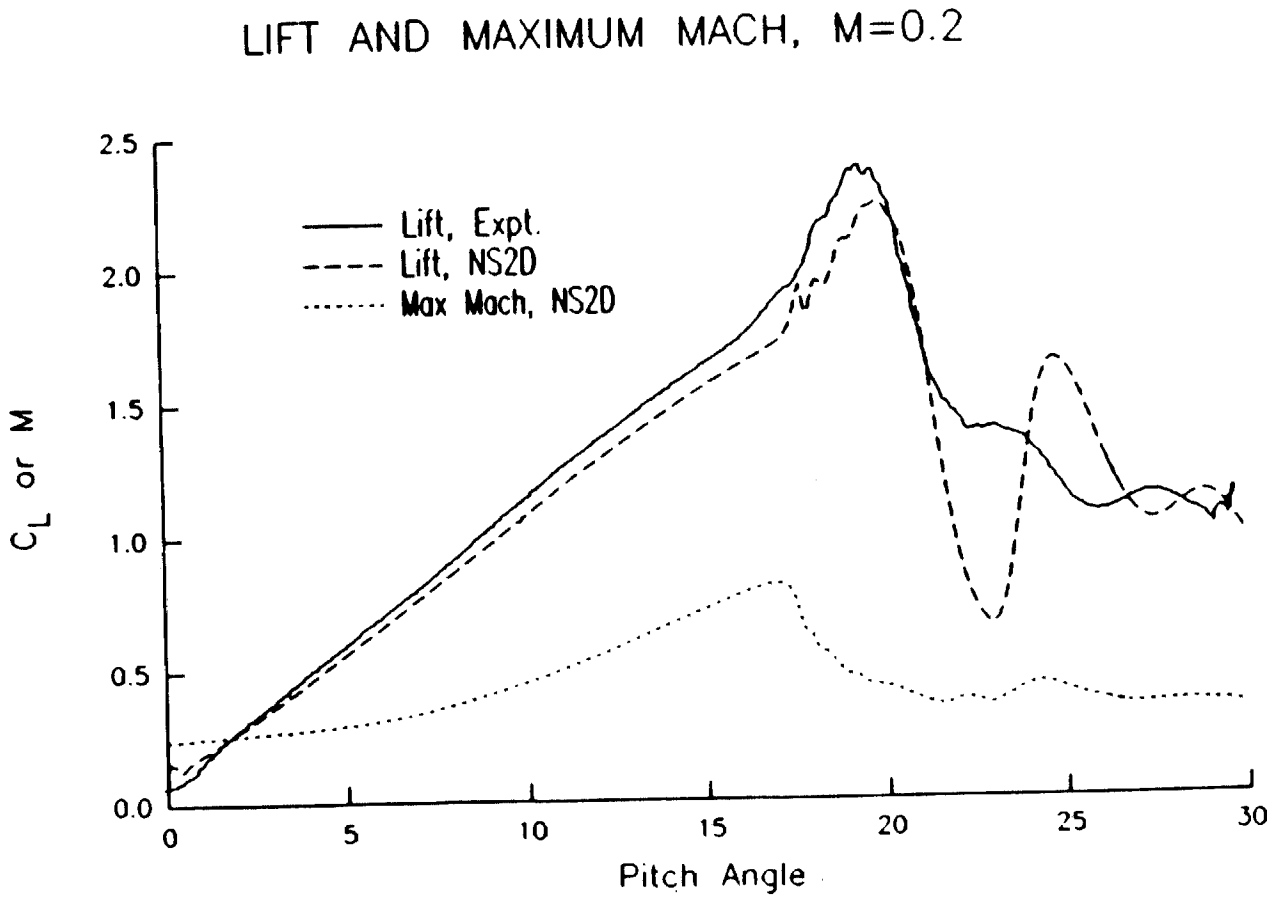
LIFT AND MAXIMUM MACH, M=0.2
Lift, Expt.
Lift, NS2D
Max Mach, NS2D
C_L or M
2.5
2.0
1.5
1.0
0.5
0.0
0
5
10
15
20
25
30
Pitch Angle

3-D OSCILLATING WING EXPERIMENT

- Pressure and Hot Film Instrumented 4 ft Span Wing
- Sikorsky SSC-A09 9% thick airfoil
- M = 0.2, 0.3, 0.4, 0.5, 0.6
- $\Lambda = 0, 15, 30$ deg
- Re = 2 to 6 million (c = 17.3 in)
- $\alpha = 0.0 \Rightarrow 30.0$ deg Ramps and Sinusoids
- $A = \frac{\dot{\alpha} c}{2U} = 0.001$ to 0.02 or 0.04
- 1990 Test under ARO/AFOSR Sponsorship

INCIPIENT STALL EXPERIMENT

- Application to Stall Flutter of Propellers
- Small Amplitude Oscillations near Static Stall
- Preliminary Experiment in Small Wind Tunnel in 1984
- Amplitudes of 0.5, 2.0 and 4.0 deg at M=0.18
- Saw Increased Negative Pitch Damping at Small Amplitude

INCIPIENT STALL EXPERIMENT - FUTURE

- NASA Lewis Sponsored Addition to 3-D Oscillating Wing Test
- Improved Resolution of Pressures
- Improved Flow Quality
- Higher Mach Numbers and Frequencies
- Addition of 3-D Tip and Sweep Effects

MODEL HELICOPTER ROTOR EXPERIMENT

- 1989 Joint UTRC/Army/NASA/Sikorsky Test at DNW, Holland
- Measured Aerodynamics, Acoustics, Performance, & Dynamics
- Pressure-Instrumented 9.4ft Dia. Model of Sikorsky Main Rotor
- Mach and Aeroelastically Scaled
- Data from 109 Level Flight, Descent, and Hover Conditions

ROTOR TEST INSTRUMENTATION

- 176 Blade Pressure Transducers
- 19 In-Flow and Out-of-Flow Microphones
- 16 Blade Bending and Torsion Strain Gages
- 3 Blade Control Angles and 4 Control Loads
- 7 Rotor Balance and Torque Loads
- Shaft Angle, RPM, and Wind Tunnel Conditions

AERODYNAMIC COEFFICIENT DEFINITIONS

- Surface Pressure Coefficient

$$C_P'(x,r,\psi) = \frac{P(x,r,\psi)-P_\infty}{0.5\rho_\infty(\Omega r)^2}$$

$$C_P(x,r,\psi) = \frac{P(x,r,\psi)-P_\infty}{0.5\rho_\infty(\Omega r(1+\frac{\mu R}{r}sin(\psi-\lambda)))^2}$$

- Normal Force Coefficient (Blade Section Axes)

$$C_N(r,\psi) = \frac{\partial N/\partial r}{0.5\rho_\infty(\Omega r(1+\frac{\mu R}{r}sin(\psi-\lambda)))^2 c(r)}$$

- Section Thrust Coefficient (Shaft Axes)

$$C_t(r,\psi) = \frac{\partial t/\partial r}{0.5\rho_\infty(\Omega R)^2 c}$$

MODEL HELICOPTER ROTOR RETREATING SIDE EVENTS

- Inboard Leading Edge Vortex Shedding Similar to 2-D Airfoil
- Aerodynamics Complicated by:
  1. Reverse Flow
  2. Radial Gradients in Velocity and Twist
  3. Streamwise Velocity and Flapping Oscillations
  4. Wake Interactions

RETREATING SIDE EVENTS - $\mu = 0.30$

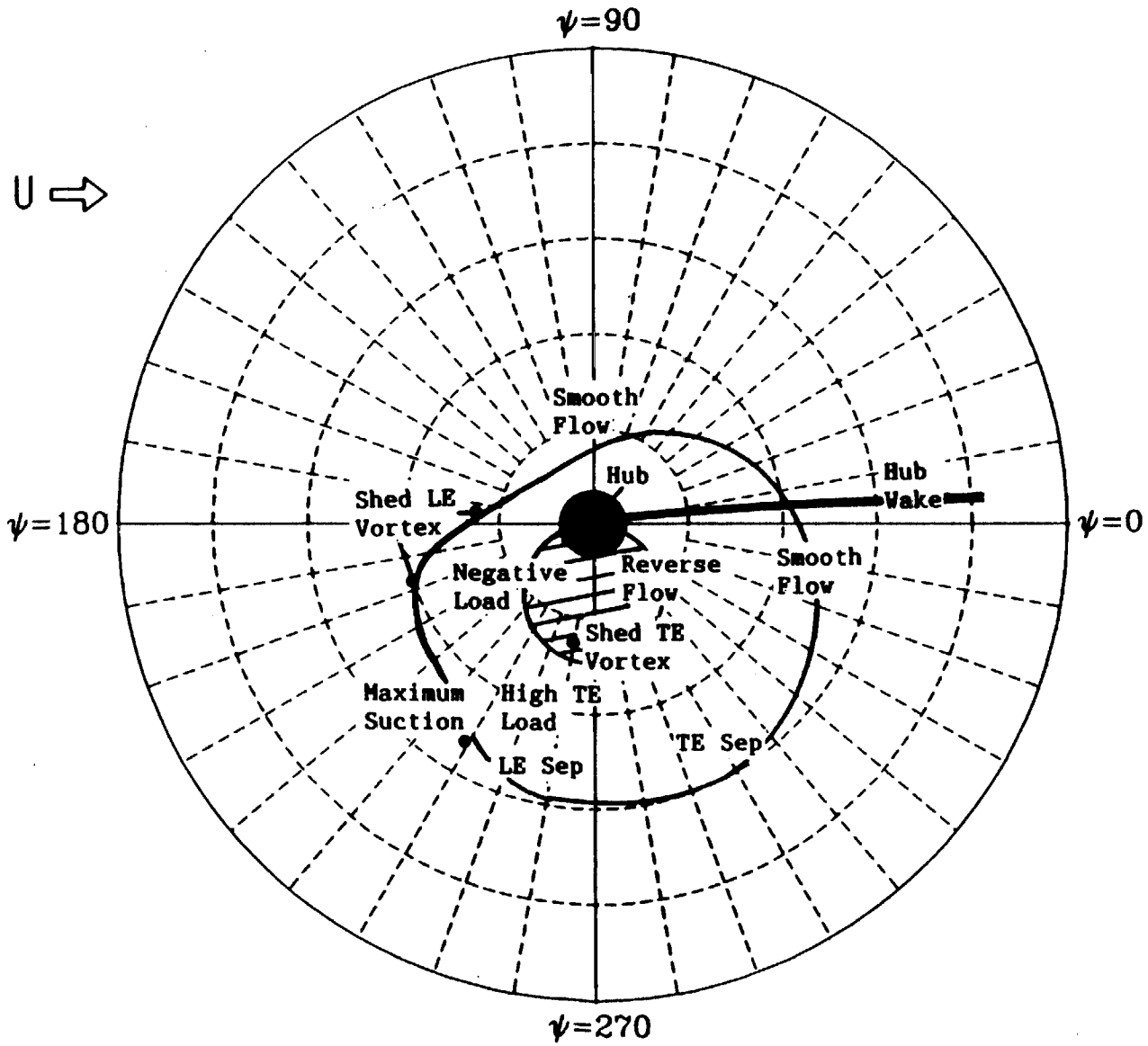

COMPARISON OF PITCH RATE HISTORY EFFECTS ON DYNAMIC STALL

M.S.Chandrasekhara
Navy-NASA Joint Institute of Aeronautics
Department of Aeronautics and Astronautics
Naval Postgraduate School, Monterey, CA

L.W.Carr
Aeroflightdynamics Directorate
U.S.Army ARTA and Fluid Dynamics Research Branch
NASA Ames Research Center, Moffett Field, CA

and
S.Ahmed *
MCAT Institute, San Jose, CA

Presented at the NASA/AFOSR/ARO Workshop on Physics of Forced Unsteady Separation
April 17-19, 1990
NASA Ames Research Center, Moffett Field, CA 94035

1. INTRODUCTION

Dynamic stall of an airfoil is a classic case of forced unsteady separated flow. Flow separation is brought about by large incidences introduced by the large amplitude unsteady pitching motion of an airfoil. One of the parameters that affects the dynamic stall process is the history of the unsteady motion, (McCroskey [1]). In addition, the problem is complicated by the effects of compressibility that rapidly appear over the airfoil even at low Mach numbers at moderately high angles of attack. Consequently, it is of interest to know the effects of pitch rate history on the dynamic stall process. This abstract compares the results of a flow visualization study of the problem with two different pitch rate histories, namely, oscillating airfoil motion and a linear change in the angle of attack due to a transient pitching motion.

2. DESCRIPTION OF THE RESEARCH

Stroboscopic schlieren studies were conducted while a 3 in. chord, NACA 0012 airfoil was executing unsteady motion. Two separate motion histories were considered. The first was a sinusoidal variation of the angle of attack and the second was a rapid ramp motion of the airfoil. Two independent drives were designed to produce the necessary pitch rate histories and are described in Carr and Chandrasekhara[2] and Chandrasekhara and Carr[3] respectively. A large body of data enveloping a Mach number M = 0.2 - 0.45 was collected. Since the pitch rate continuously changes for an oscillating airfoil, the angles of attack at

* *On Leave from National Aeronautical Laboratory, Bangalore, India*

which the pitch rates match were obtained by comparing them with those available for the ramp type motionexperiment. The angle of attack was varied from 0 - 60^0 in the ramp motion. The corresponding variation for the oscillatory motion was

$$\alpha = \alpha_0 + \alpha_m sin(\omega t) = 10^0 + 10^0 sin(\omega t)$$

Data was also obtained at other values of the amplitude of oscillation (2^0 and 5^0). However, to achieve a proper comparison, only the case of 10 degree amplitude that results in a total angle of attack range of 0 - 20^0 will be used.

3. RESULTS AND DISCUSSION

Fig. 1 shows the schlieren pictures at M = 0.2 at an instantaneous angle of attack of approximately 17^0 for the two pitch rate histories at a non-dimensional pitch rate defined as $\alpha^+ = \frac{\dot{\alpha} c}{U_\infty} = 0.025$. As can be seen from the figure, the flow over the airfoil in ramp motion has already reached deep stall conditions, whereas that over the oscillating airfoil shows a clearly defined dynamic stall vortex at 60% chord location, indicating that the airfoil is still producing dynamic lift. At a higher α^+ value of 0.03, the two flows are nearly identical even at an angle of attack of $\approx 15^0$.

Similar results were obtained at M = 0.25, 0.3 and 0.35. In all cases, at low pitch rates, deep stall occured over the airfoil in ramp type motion at the angles of attack for which the flow over the oscillating airfoil was dominated by a strong, tightly wound dynamic stall vortex which was still located over the upper surface. This result was true, despite the fact that at lower angles of attack, the two flows appeared nearly identical. In addition, in instances where the dynamic stall vortex could still be identified for the transient pitching case, it was significantly diffused, indicating that it was in a disorganised state as opposed to the oscillating case, where it was well organised. This trend persisted in the Mach number range that extended into the compressible regime, namely beyond M = 0.3. A table of the results for the different conditions is included to summarise the results discussed.

It is somewhat surprising to note the trends obtained in this comparison. An explanation of this effect could be offered for this as follows: A sinusoidal motion produces pitch rates that increase from 0 to 0.035 during the pitch-up phase for k = 0.1 and an amplitude of 10 degrees. Its maximum occurs at the mean angle of attack. Beyond this, the pitch rate decreases, but at the angle at which the comparions were made (17.07^0) in Fig. 1 , the pitch rate is still significant (0.025). For the ramp motion, the pitch rate reaches a constant value by $\alpha \approx 6^0$. Chandrasekhara and Carr[4] have shown that stall can be delayed to higher angles of attack by increasing the pitch rate. It appears from the pitch rate variation with angle of attack that an oscillating motion can produce higher amounts of vorticity which will cause the dynamic stall vortex to be more organised and coherent. This leads to the conclusion that motion with continuously changing acceleration can support larger flow gradients and thus is more desirable.

4. CONCLUSIONS

The study shows that pitch rate history is a very important parameter in the analysis of dynamic stall. Pitch rate history plays a dominant role by controlling the strength and behavior of the dynamic stall vortex. Vorticity created by repetitive motion appears to have the energy to sustain higher pressure gradients in the flow.

5. REFERENCES

1. McCroskey, W.J., "The Phenomenon of Dynamic Stall", NASA TM 81264, March 1981.

2. Carr, L.W. and Chandrasekhara, M.S., "Design and Development of a Compressible Dynamic Stall Facility", *AIAA Paper No. 89-0647*, Jan. 1989.

3. Chandrasekhara, M.S. and Carr, L.W., "Design and Development of a Facility for Compressible Dynamic Stall Studies of a Rapidly Pitching Airfoil", *Proc. 13th ICIASF*, Goettinegen, W.Germany, September 1989.

4. Chandrasekhara, M.S. and Carr, L.W., "Flow Visualization Studies of the Mach Number Effects on the Dynamic Stall of an Oscillating Airfoil", *AIAA Paper No. 89-0023*, Jan. 1989.

Table 1. Comparison of Pitch Rate History Effects through Flow Visualization

No.	Ramp Type Motion	Oscillatory Motion	α^+
	M = 0.2, k = 0.1		
1.	$\alpha = 17^0$ Nearly deep stall Transverse scales large	$\alpha = 17.07^0$ Tightly wound vortex at ≈60% chord	0.025
2.	$\alpha = 15^0$ Flow nearly identical in both cases	$\alpha = 15.23^0$	0.03
	M = 0.2, k = 0.075		
1.	$\alpha = 13^0$ Very nearly identical flow in both cases	$\alpha = 13.82^0$	0.025

	M = 0.25, k = 0.1		
1.	$\alpha = 18^0$ Deep stall, trailing vortex, large transverse flow scales	$\alpha = 18.1^0$ Vortex at 75% chord and well organised	0.02
2.	$\alpha = 17^0$ Vortex present, but disorganised at 55%chord Indications of flow breakdown	$\alpha = 17.07^0$ Well organised vortex at 50% chord	0.025
3.	$\alpha = 15^0$ Flow very nearly similar in the two cases	$\alpha = 15.23^0$	0.03
	M = 0.25, k = 0.075		
1.	$\alpha = 16.5^0$ Deep stall. Shear layer vortex at mid-chord, large transverse scales	$\alpha = 16.5^0$ Well organised at vortex $\approx 60\%$	0.02
2.	$\alpha = 13^0$ Beginnings of a vortex	$\alpha = 13.5^0$ Imprint of a vortex	0.025

	M = 0.3, k = 0.1		
1.	$\alpha = 18^0$ Vortex well above the surface, near deep stall large transverse disturbance Disorganised flow	$\alpha = 18.1^0$ Vortex near 90% chord transverse disturbance getting larger	0.02
2.	$\alpha = 17^0$ Vortex at 65% chord flow getting disorganised, large vortex	$\alpha = 17.1^0$ Vortex at ≈55-60% chord Well organised flow	0.025
3.	$\alpha = 15^0$ Vortex at 15% chord Other features of flow nearly alike	$\alpha = 15.23^0$ vortex at 15% chord	0.03
	M = 0.3, k = 0.075		
1.	$\alpha = 16.5^0$ Total flow breakdown	$\alpha = 16.5^0$ organised vortex at 55% chord	0.02
2.	$\alpha = 13^0$ Flow nearly identical in the two cases	$\alpha = 13^0$	0.025
	M = 0.35, k = 0.1		
1.	$\alpha = 17^0$ Large vortex, but not organised	$\alpha = 17.07.1^0$ Organised large vortex at the same location	0.025
2.	$\alpha = 15^0$ Vortex at 30% chord Otherwise nearly identical flow	$\alpha = 15^0$ votrex at 25% chord	0.03

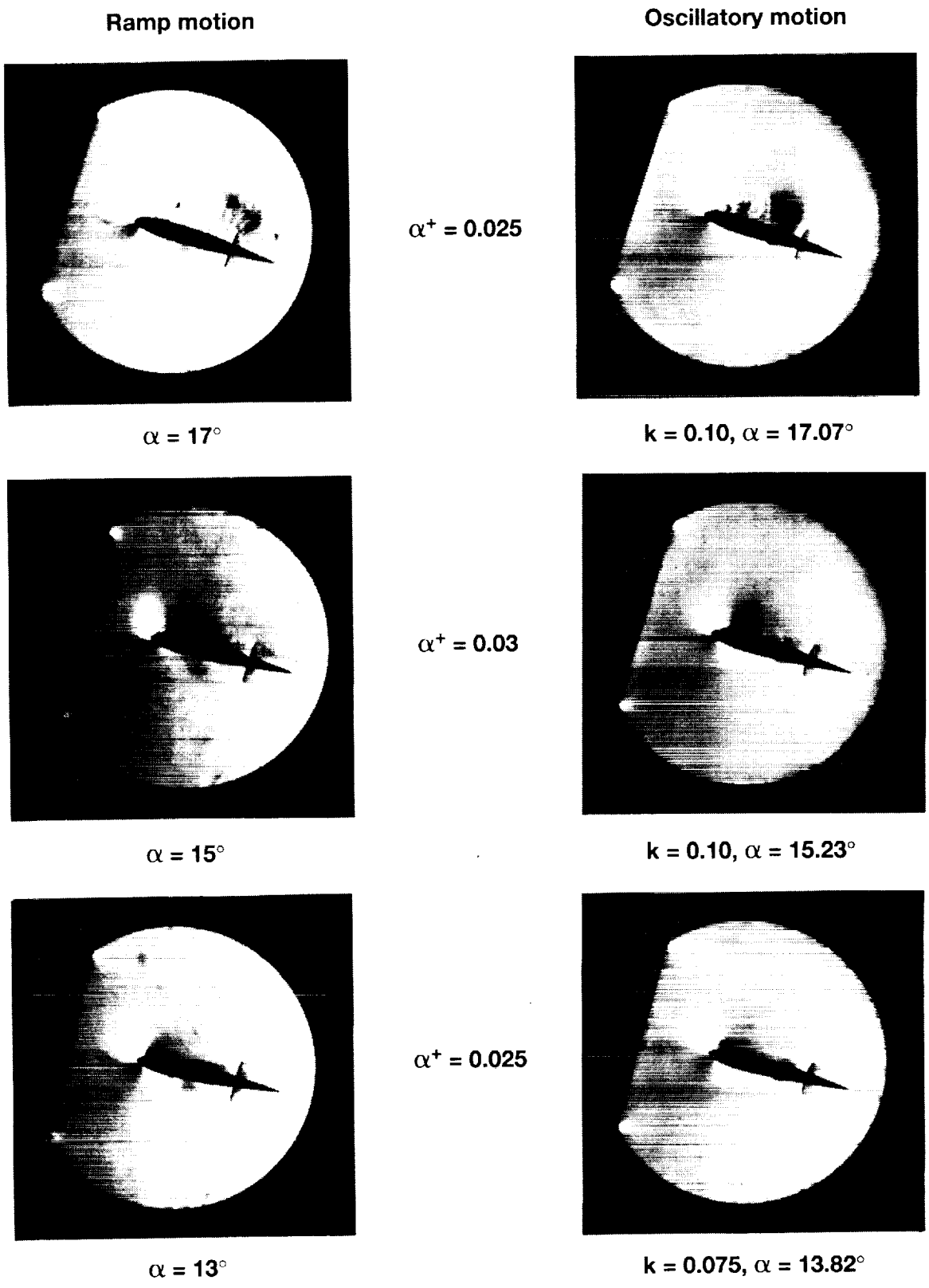

Figure 1. Comparison of Pitch Rate History Effects
(M = 0.20)

METHOD

Produce different unsteady airfoil motions

1. Oscillating airfoil

$$\alpha = 10° + 10° \sin \omega t, \; (0 \leq \alpha \leq 20°)$$

2. Transient pitching airfoil

$$\alpha = c\, t, \; (0 \leq \alpha \leq 60°), \; \dot{\alpha} = \text{constant}$$

Compare flow over airfoil at the same α at which the pitch rates match

Nondimensional pitch rate is defined as

$$\alpha^{+}_{ramp} = \frac{\dot{\alpha} c}{U_\infty} \quad , \quad \alpha^{+}_{osc} = 2k\alpha_m \cos \omega t$$

$$k = \frac{\pi f c}{U_\infty}$$

APPROACH

Conduct stroboscopic schlieren flow visualization for

$$0.2 \leq M \leq 0.45$$

$$0 \leq k \leq 0.1$$

$$0 \leq \alpha^{+} \leq 0.045$$

Compare schlieren pictures at the same α for different M, reduced frequency, and α^{+}

CONCLUDING REMARKS

1. Pitch rate history has significant effect on dynamic stall process and vortex behavior

2. Stall is alleviated when motion history produces changing acceleration

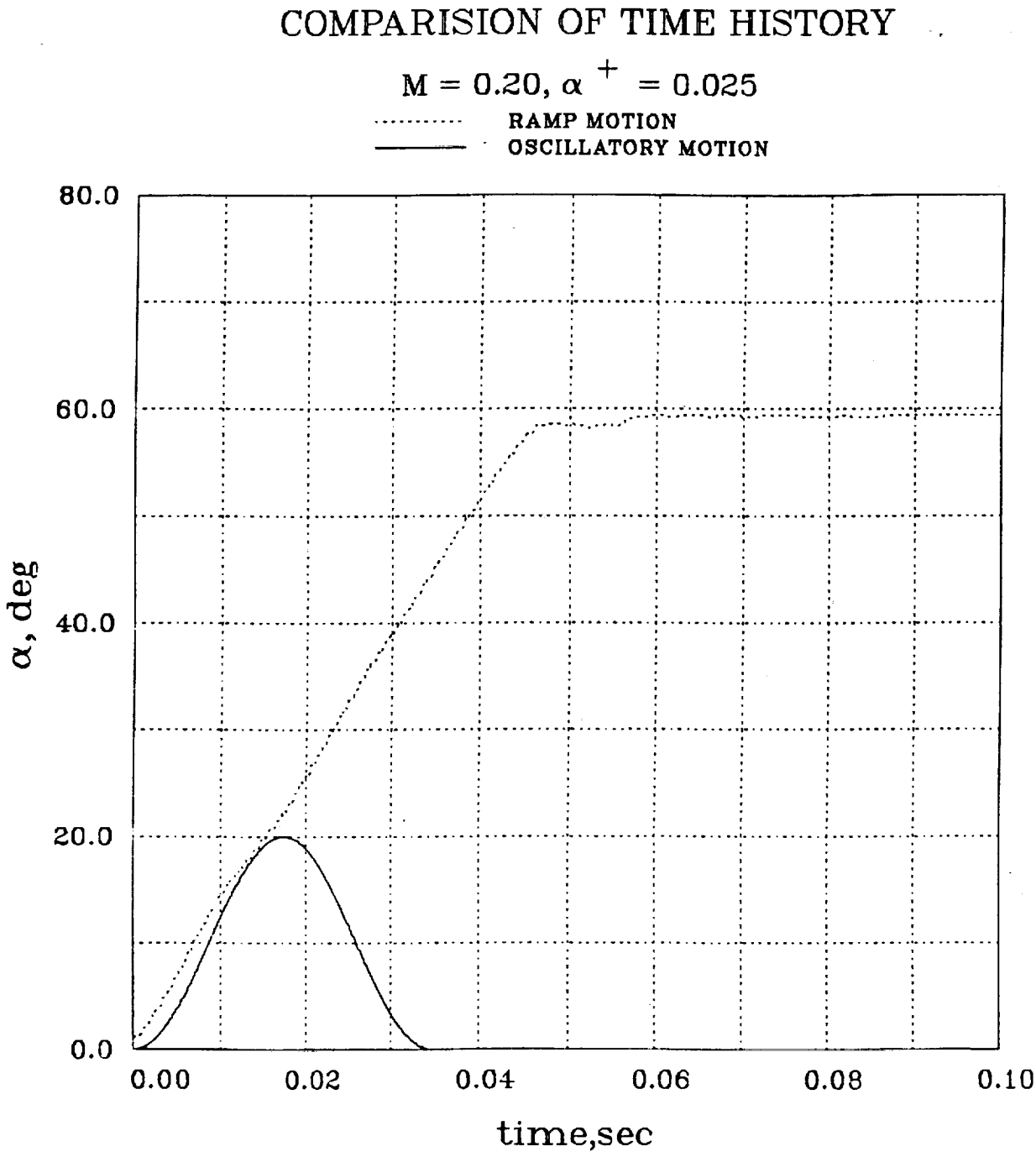

Run No. 00129B

SLOPES	0 – 10 Deg:	1510.68
	0 – 30 Deg:	1309.37
	0 – 57 Deg:	1285.50

VARIATION OF PITCH RATE WITH ANGLE OF ATTACK

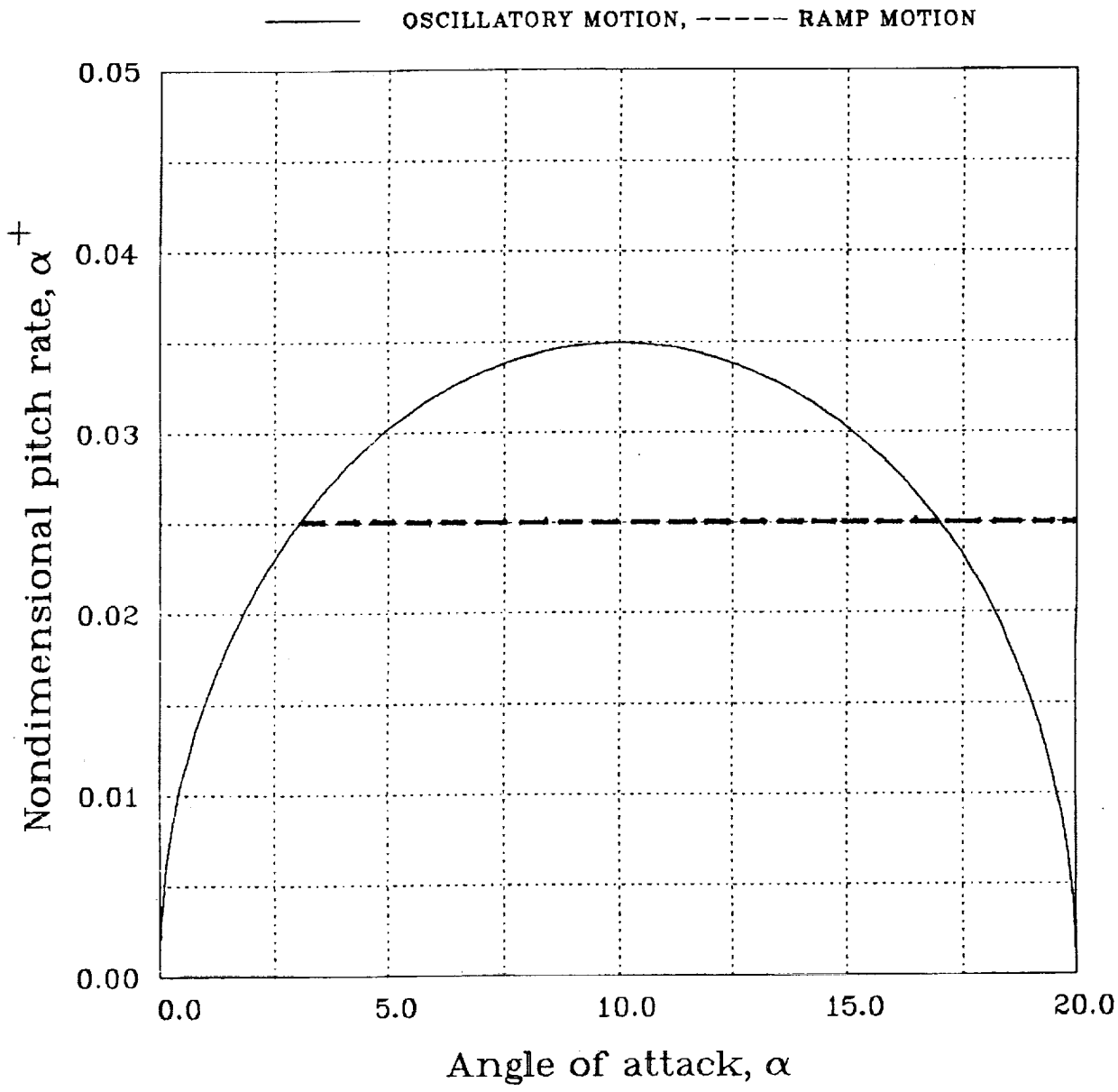

N94-34969

Unsteady Flow Past an Airfoil Pitched at Constant Rate

by L. Lourenco, L. Van Dommelen, C. Shih & A. Krothapalli

Department of Mechanical Engineering
FAMU/FSU College of Engineering
Tallahassee, FL 32316-2175
Florida A & M University and Florida State University

This program is sponsored by AFOSR

Abstract

The unsteady flow past a NACA 0012 airfoil that is undertaking a constant-rate pitching up motion is investigated experimentally by the PIDV technique in a water towing tank. The Reynolds number is 5000, based upon the airfoil's chord and the free-stream velocity. The airfoil is pitching impulsively from 0 to 30° with a dimensionless pitch rate $\dot{\alpha}$ of 0.131. Instantaneous velocity and associated vorticity data have been acquired over the entire flow field. The primary vortex dominates the flow behavior after it separates from the leading edge of the airfoil. Complete stall emerges after this vortex detaches from the airfoil and triggers the shedding of a counter-rotating vortex near the trailing edge. A parallel computational study using the discrete vortex, random walk approximation has also been conducted. In general, the computational results agree very well with the experiment.

1. Introduction

Due to the recent interest in developing a supermaneuverable fighter aircraft, a complete knowledge of the unsteady flow behavior over a wing is necessary in order to improve the post stall aerodynamic performance. Although much progress has been made both experimentally and numerically throughout the years,[1,2] a fundamental understanding of the problem is still lacking. The difficulty mainly arises from the fact that these flows are extremely complex and are not amenable to standard experimental and numerical techniques. For example, one of the most important feature about the flow past an unsteady airfoil is the emergency of one or several large scale vortical eddies after the flow separates from the upper surface. Later evolution of these vortical structures dominate the behavior of the flow past the airfoil's surface. They either induce considerably lift increase as they move along the surface, or trigger a catastrophic flow breakdown when taking off from the airfoil's surface.[3,4] In order to understand the mutual influence between these vortices and their interactions with the lifting surface, it is necessary to study not only their development in time but also their spatial correlation at each instant. In other words, quantitative information about the entire flow field is essential. This immediately excludes the use of traditional single-point measurement techniques, such as hot-wire anemometry or LDA. In view of this, a new experimental technique, Particle Image Displacement Velocimetry, herein abbreviated as PIDV, has been developed in our laboratory, which is capable of providing with great detail and accuracy about the instantaneous two-dimensional velocity and associated vorticity fields.[5]

The second part of this research involves a computational simulation of the Navier-Stokes equations using a discrete vortex, random walk scheme.[6] In general, the global flow features predicted by the computational scheme compare extremely well with the experiment.

2. Particle Image Displacement Velocimetry

PIDV technique can be regarded as a modified flow visualization method that is capable of providing quantitative data of the entire flow field. The operation of this technique involves the illumination of the flow field of interest, seeded with small tracer particles, with a thin laser light sheet as shown in figure 1. The light scattered by the seeding particles, which follow the local fluid motion, provided they are small enough, generates a moving particle-image pattern. This pattern is recorded using a multiple exposure photographic technique. The distance between the corresponding particle images being proportional to the local flow velocity. An optical Fourier transform is used to convert this spatial information into local velocity data. This process uses a focused laser beam to interrogate a small area of the multiple exposed photographic film. The diffraction pattern produced by the coherent illumination of the multiple images in the photographic transparency generates Young's fringes, in the Fourier plane of a lens, provided that the particle image-pairs inside the interrogating volume correlate, see figure 2. These fringes have an orientation that is perpendicular to the direction of the local displacement and a spacing inversely proportional to the displacement. A fully-automated process has been devised to acquire and analyze the fringe images at the Fluid Mechanics Research Laboratory of the Florida State University. The system consists of the following hardware components: a DEC MicroVax workstation II computer, Gould IP-8500 digital image processor, a frame digitizer, and a pipeline processor. For automatically scanning of the film transparency, a two-dimensional Klinger traversing mechanism with controller is used, see figure 3.

One important limitation of this method is that it is not possible to discriminate against the directional ambiguity introduced by the possible reversing motion in the flow field. To resolve this problem, a "velocity bias technique" has been proposed.[7,8] A uniform reference motion is added to the flow, thus superposing a velocity shift to the real flow field. A properly chosen shift can insure that all image displacements occur in the same direction, thereby eliminating the ambiguity. The true flow field can be recovered later by removing this artificial shift from the raw velocity data. The shift effect can be achieved by several methods; it can be done actively by using a rotating mirror, or passively by the use of a Calcite crystal.[9] In this work, a rotating mirror, General Scanning model # 6325D, with a scanner control, model # CX-660, is used to provide the image shift.

A dual pulsed laser system, consisting of two Spectral-Physics DCR-11 Nd-Yag pulsed laser systems, is used to provide the double pulses. As shown in figure 4, the light beams emitted from the two lasers are made collinear using a system of prisms and polarizing cube beam combiners. The second laser is triggered by the first laser via a Systron Donner 100C pulse generator. Separation between the pulses can be varied from a fraction of one μsec. to a few seconds by adjusting the pulse generator. A cylindrical lens is used to project the combined beam into a laser sheet to illuminate the mid-span section of the airfoil. Metallic coated particles (TSI model 10087), with an average diameter of 4 μm, were used as the flow tracers. A 35 mm camera (Nikon F-3) was used to record the flow field.

The pulsed lasers were triggered continuously at a frequency about 10 hertz in order to utilize their full power. That means the scanning motion of the mirror and the camera

shutter release should also be phase-locked to that frequency. Due to this restraint, the time interval between pictures had to be chosen to be a multiple of the laser pulsing period, and it was set at 0.3 second for this experiment. Synchronization between components was accomplished by using the Tektronix modular electronics system as shown in figure 5. On the other hand, this system also provided the phase-reference between the motion of the airfoil and the PIDV photographic timing sequence , see figure 6.

3. Experimental Facility

The experiments were performed in a towing water tank facility, which is 1.8 meter long and 43 by 55 cm in cross-sectional area. The towing carriage was driven by a DC servo motor with a towing speed varying from 0.3 to 30 cm/sec. A NACA 0012 airfoil with a chord length of 6 cm and an aspect ratio of 6.67, is used. This corresponds to a Reynolds number between 200 and 20000, based upon the towing speed and the airfoil's chord. The towing speed was controlled by a motor speed control system, Electro-Craft model # E-652, via digital-to-analog converter. Acceleration and deceleration ramps were included for smooth traverse. The airfoil's pitching motion was provided by a Klinger stepping motor with a programmable controller, Klinger model CC-1.2, which was pre-programmed and activated by the host computer. The airfoil's angle changed linearly from 0 to 30° after the airfoil had been towed for more than one chord length and presumably had established a steady-state travel. All motions were monitored by a DEC Vaxstation II computer, see figure 6.

4. Numerical Simulation Scheme

Random-walk vortex simulations of the full Navier-Stokes equations were performed for a comparison with the PIDV data. In the computations, the flow field was represented by discrete vortex blobs. The diffusion processes were simulated by adding a random component of magnitude $\sqrt{2\nu\Delta t}$ to the vortex motion.

In the method, no accuracy is lost in describing the strong convection process typical of unsteady separated flows. Additionally, the computational domain is truly infinite; there are no artificial boundary conditions. But most importantly, since computational elements are only used in the limited regions containing appreciable vorticity, the resolution, (the smallest scales the computation can distinguish), is very high.

The fast solution-adaptive Laurent series technique[10] was used to allow a large number of vortex blobs to be included without using a mesh-based fast solver to find the velocity.

The normal wall boundary condition was satisfied by mirror vortices, after a mapping of the airfoil onto a circle. The mapping used was a generalized Von Mises transform which exactly reproduces the slightly blunted trailing edge of the NACA 0012.

The no-slip boundary condition was satisfied by the addition of vortices at the wall dur-

ing each time-step. First all vortices within a distance of $1.27\sqrt{2\nu\Delta t}$ were removed. Then a ring of new vortices was added at a distance $0.675\sqrt{2\nu\Delta t}$ to correct the wall slip to zero. (The distance for adding vortices equals the diffusion distance of the vorticity generated by the wall during the time-step for the true Navier-Stokes equations; the removal distance was chosen based on a statistical study requiring that the scheme handles locally uniform vorticity distributions accurately, not unlike discretization techniques in finite difference procedures). The vortex diameter was rather arbitrarily chosen to be $0.675\sqrt{2\nu\Delta t}$; testing showed that results depended little on the actual value used.

In order to allow pitching motion, the equations of vortex motion were developed in an inertial reference frame and subsequently converted to an airfoil based system. This is required since Kelvin's theorem cannot be used in a rotating coordinate system. The force on the airfoil is found from differentiating integrals of the vorticity distribution, rather than directly from the wall shear and pressure.

The CYBER 205 results were post-processed on a MicroVax II computer, using a fast Fourier transform to find the streamlines. The vorticity was represented in bit-mapped graphics as half-tones. The dimensionless pitch rate and the Reynolds number are chosen to be exactly the same as those in the experiments for readily comparison.

5. Results and Discussion

5.1 PIDV Data

Reynolds number calculated with the chord length and the free-stream velocity is 5000 for all the results presented. The airfoil is pitching up from an angle of attack of 0 to 30 degrees with a dimensionless pitch rate $\dot{\alpha}$, normalized by the airfoil's chord and free-stream velocity, of 0.131. The unsteady flow development over the airfoil after the pitch-up is presented sequentially from figures 7-(a) to 7-(d). The velocity field data in these figures is acquired in a Cartesian mesh by digitally processing the fringes, produced by point-by-point scanning of the film transparency. The length of each vector is proportional to the local velocity at that point. Also shown is the vorticity level superimposed on the velocity field by using the color code.† The magnitude of the vorticity is given by the color bar at the left lower corner of the figures. The red and purple colors represent the peak levels of the positive (clockwise) and negative (counterclockwise) vorticity.

In figure 7-(a), the airfoil has travelled about 1.27 chord length after the initial pitch up and reaches an angle of attack of 7°, which is below the 12° static stall angle for the NACA 0012 airfoil within this Reynolds number range. There is no noticeable flow development on both the upper and lower surfaces of the airfoil. On the upper surface, boundary layer is slightly thickening with no distinguishable separation. Near the trailing edge, strong negative vorticity has been shed from the lower surface as a result of the airfoil's pitching up motion.

As the airfoil continues to move to about 2.98 chords downstream and at an angle of 20°, which is well beyond the static stall angle, separation start to develop on the upper surface, as shown in figure 7-(b). Near the leading edge, flow separates and reattaches downstream forming a recirculating eddy, which occupies approximately a quarter of the chord. Near the mid-chord of the airfoil, the reattached boundary layer separates again, forming another recirculation eddy that almost covers the entire downstream section. Strong flow reversal can be seen from the trailing edge all the way to about the mid-chord region. On the other side of the airfoil, flow appears to behave smoothly. There is no significant flow breakdown at this stage although the airfoil has already gone beyond the static stall condition.

Not until further downstream, after the airfoil has moved 5.13 chords and reaches its maximum angle of 30°, massive flow separation starts to develop, see figure 7-(c). The leading edge separation bubble grows into a large scale vortex and moves downstream. It induces very strong reverse flows along the airfoil's surface, which can be of the same order of magnitude compared to the free-stream. Interestingly, the reversing flows carry very low level of vorticity as shown by the color code for the vorticity level.

The vortical structure simply rides on this upstream-moving stream. An important consequence is the slowdown of the convection process of the vortex. Following the primary vortex is a series of smaller vortices, which form as a result of the vorticity accumulation of the shear layer that is separating from the leading edge. Under the shear layer vortices and very close to the surface of the airfoil, there are two secondary vortices which have

† Vorticity contour plot will be used for the final mat

the opposite sign of rotation as the vortices right above them. Downstream of the primary vortex, local flows have been propelled to attach onto the airfoil's surface immediately before the trailing edge. This suggests the existence of a stagnation point immediate before the trailing edge. Away from the airfoil, outer flow stream still shows an overall convex curvature, suggesting that the global circulation is preserved and the lift of the airfoil can be maintained or increased even after massive flow separation.

In figure 7-(d), the primary vortex eventually takes off from the trailing edge, at a location of 7.27 chord length after the initial pitch-up, triggering the entire flow into complete breakdown. The primary vortex can be barely observed at the right upper corner in figure 7-(d) as it is gradually leaving the scene. A strong counter-rotating vortex is shed from the lower surface and starts to roll up near the trailing edge and penetrates into the upper surface. Flows separate from the leading edge forming a shear layer without reattaching downstream. An open wake is formed, accompanied by the plunge of the circulation around the airfoil, which characterizes the final stage of the stall of the airfoil. A concave overal curvature suggests a loss of the airfoil's lift.

5.2 Computational Results

Typical two-dimensional computational results from random-walk vortex simulations of the full Navier-Stokes equations are shown in figures 8-(a) to (i). The Reynlods number, the dimensionless pitch rate and the maximum angle of attack are the same as those in the experiment. The only difference is the way the airfoil is pitched. Since a linear pitch-up profile, as adopted in the experiment, will lead to an infinite loading on the airfoil in the computational scheme, consequently, a smooth profile with continuous curvature, which is fitted by a fifth-order polynomial, is chosen instead. Therefore, comparison between the experiment and computational simulation can be considered only qualitatively rather than quantitatively. The instantaneous streamline pattern, along with vorticity field that is represented in bit-mapped graphics as half tones, are shown. In general, the simulated patterns agree well with the experimental data.

In figures 8-(c) and 8-(d), corresponding to $\alpha = 21.7°$ and $26.9°$, respectively, the existence of two vortical eddies agrees with the experiment, see figure 7-(b). The leading edge eddy ends as the separating leading edge shear layer reattaches downstream and re-separates again at mid-chord to form a larger size bubble occupying the downstream half of the airfoil. As this vortex approaches the trailing edge, a counter-rotating vortex is shed from the lower surface. This exactly matches the experimental observation as shown in figure 7-(b).

The leading edge vortex grows and moves downstream in exactly the same manner as revealed from the experiment, compare figures 8-(e) and (f) to figure 7-(c). The size of the primary vortex also compares favorably to the experiment. Other distinct features, such as the formation of the shear layer vortices following the primary vortex and the development of a counter-rotating vortex near the surface, have also been faithfully simulated. As demonstrated in figures 8-(e) and (f), Vortex dynamics appears to play an important role as the primary vortex interacts strongly with the shear layer vortex that immediately follows it as they begine to evolve downstream. By associating the discrete vortex simulation with

the whole-field PIDV measurement, for the first time, this very complex process can be carefully analyzed.

The breakdown process appears to begin with the shedding of a counter-rotating vortex near the trailing edge as the primary vortex is moving away from the airfoil, see figure 8-(g). The situation aggravates as the flow completely separates from the airfoil as shown in figures 8-(h) and 8-(i). The emergence of a concave curvature can be seen as a sign that indicates a total loss of circulation and, consequently, the lift.

Summary

PIDV is capable of providing the velocity and associated vorticity fields with good spatial resolution and accuracy of a very complex unsteady flow field, that is the unsteady flow past an impulsively pitching-up airfoil. Noticeable flow separation develops when $\alpha > 20°$, which is well beyond the static stall angle, with one separation bubble near the leading edge and another eddy presides over the trailing edge region. The development of the leading edge vortex dominates the later flow behaviors. This vortex grows, to a size that is comparable to the airfoil's chord, and moves downstream. Outer flow maintains its convex curvature while the vortex is accumulating its strength; the lift is still increasing. A counter-rotating vortex is released from the trailing edge as soon as the primary vortex detaches from the surface, triggering the airfoil into stall. Strong flow separation prevails and flow separates from the leading edge without downstream reattachment. Surrounding flow has a concave curvature and the airfoil's circulation, along with its lift, drop.

A discrete vortex, random walk computation was undertaken to augment the experimental studies. In general, the simulation results agree extremely well with the experiment.

Acknowledgments

This program is supported by the Air Force Office of Scientific Research.

Final Remarks

As you may have already known, data analysis for the PIDV is quite different from the traditional experimental technique: data collection is undertaken after the completion of the experiment. For now, we have already finished our experiment but our analysis system has been occupied by other project, therefore, we can only provide a small portion of the data we collected. The complete data, which should include data sets with much finer time sequence for a Reynolds number of 1400 and 5000.

References

1. W.J. McCroskey, "Unsteady Airfoils", Ann. Rev. Fluid Mech. Vol. 11, 1982, pp 285-311.

2. W.C. Reynolds and L.W. Carr, "Review of Unsteady, Driven, Separated Flows" AIAA paper no. 85-0527, 1987.

3. C. Shih, M. Lee, and C.M. Ho, "Unsteady Separation over Two- and Three-Dimensional Airfoils", Proceeding of Workshop on Unsteady Separated Flow, July 1987, Colorado Springs, Colorado, pp 38-41.

4. K.W. McAlister and L.W. Carr, "Water-Tunnel Experiments on an Oscillating Airfoil at Re = 21,000", NASA TM 78446, March 1978.

5. A. Krothapalli and L. Lourenco, "Unsteady Separated Flows: A Novel Experimental Approach", AIAA paper 87-0459, 1987.

6. L.L. Van Dommelen, "Lagrangian Techniques for Unsteady Flow Separation", Forum on Unsteady Flow Separation, 1987 ASME Applied Mechanics, Bioengineering and Fluids Engineering Conference, June 14-17, 1987, Cincinatti, OH., pp. 81-84.

7. L. Lourenco, "Application of Laser Speckle and Particle Image Velocimetry in Flows with Velocity Reversal", Bull. Amer. Phys. Soc., Vol. 31, no. 10, 1986, pp. 1723.

8. R.J. Adrian, "Image Shifting to Determine the Polarity of Velocity Vectors Measured by Pulsed Laser Anemometry", Bull. Amer. Phys. Soc., Vol. 31, no. 10, 1986, pp. 1722.

9. L. Lourenco, "A Passive Velocity Bias Technique for PIDV", Bull. Amer. Phys. Soc., Vol. 34, no. 10, 1989, pp. 2267.

10. L.L. Van Dommelen and E.A.Rundensteiner, "Fast Solution of the Two-Dimensional Poisson Equation with Point-Wise Forcing", to appear in the Journal of Computational Physics.

æ

p

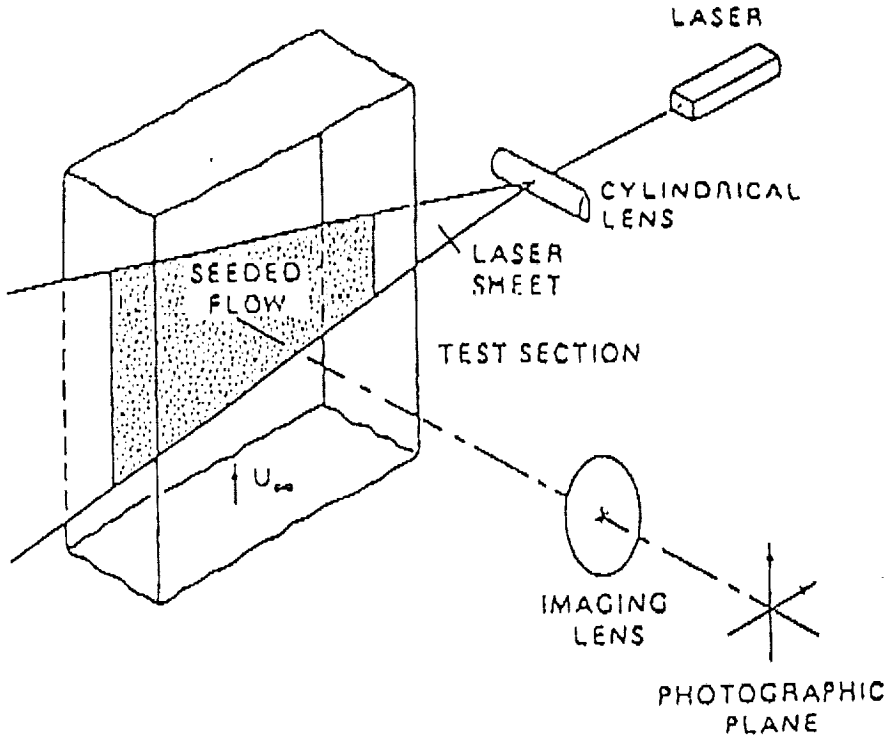

Figure 1. Schematic arrangement for the photographic recording.

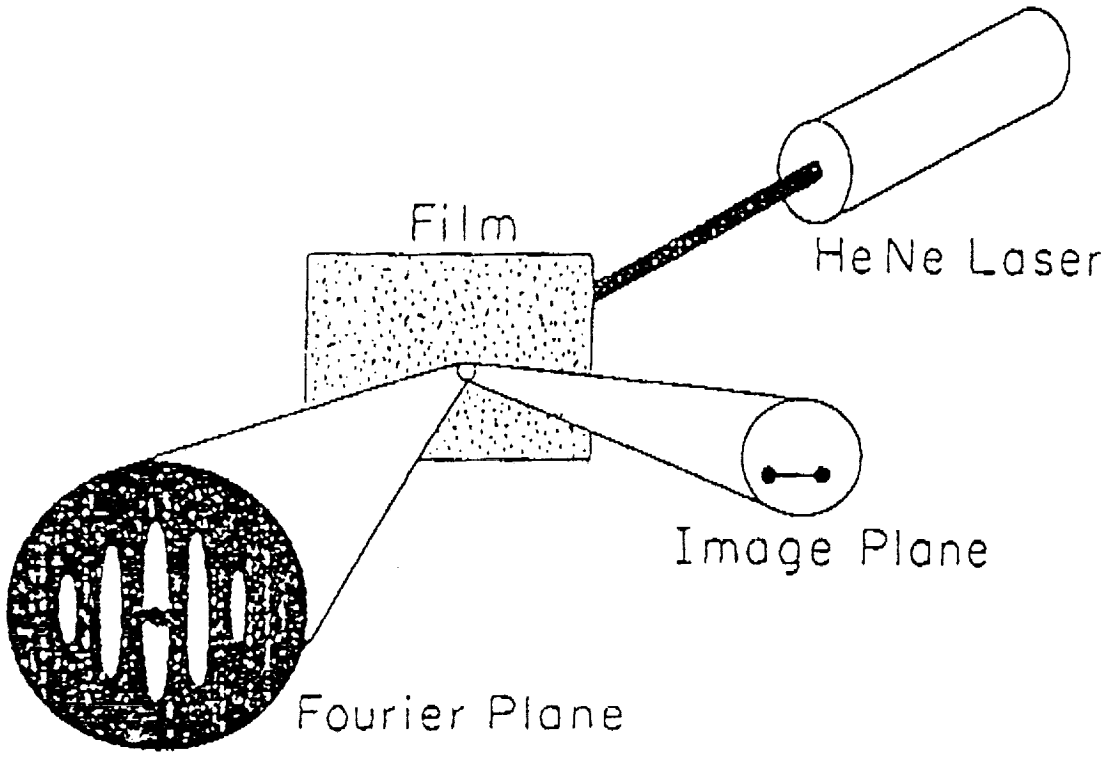

Figure 2. Schematic arrangement for obtaining Young's fringes.

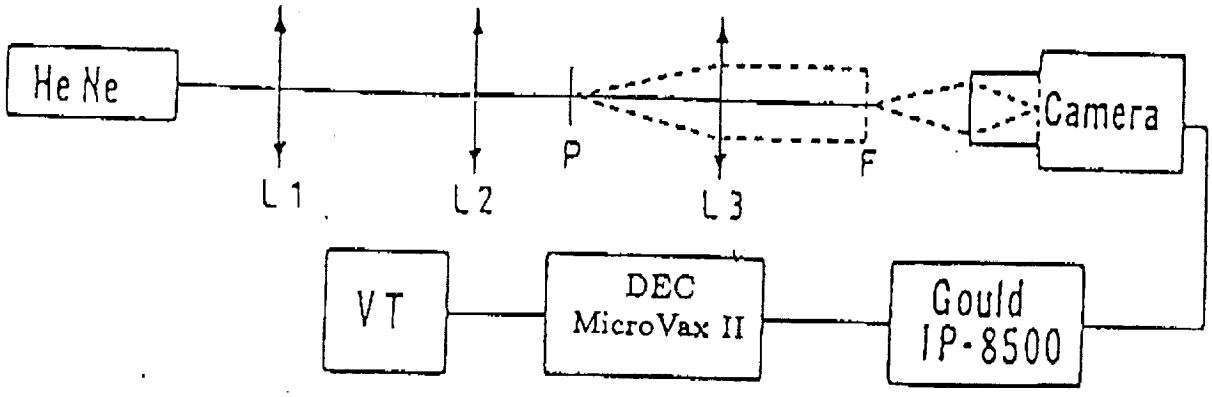

Figure 3. Schematic of the data analysis system

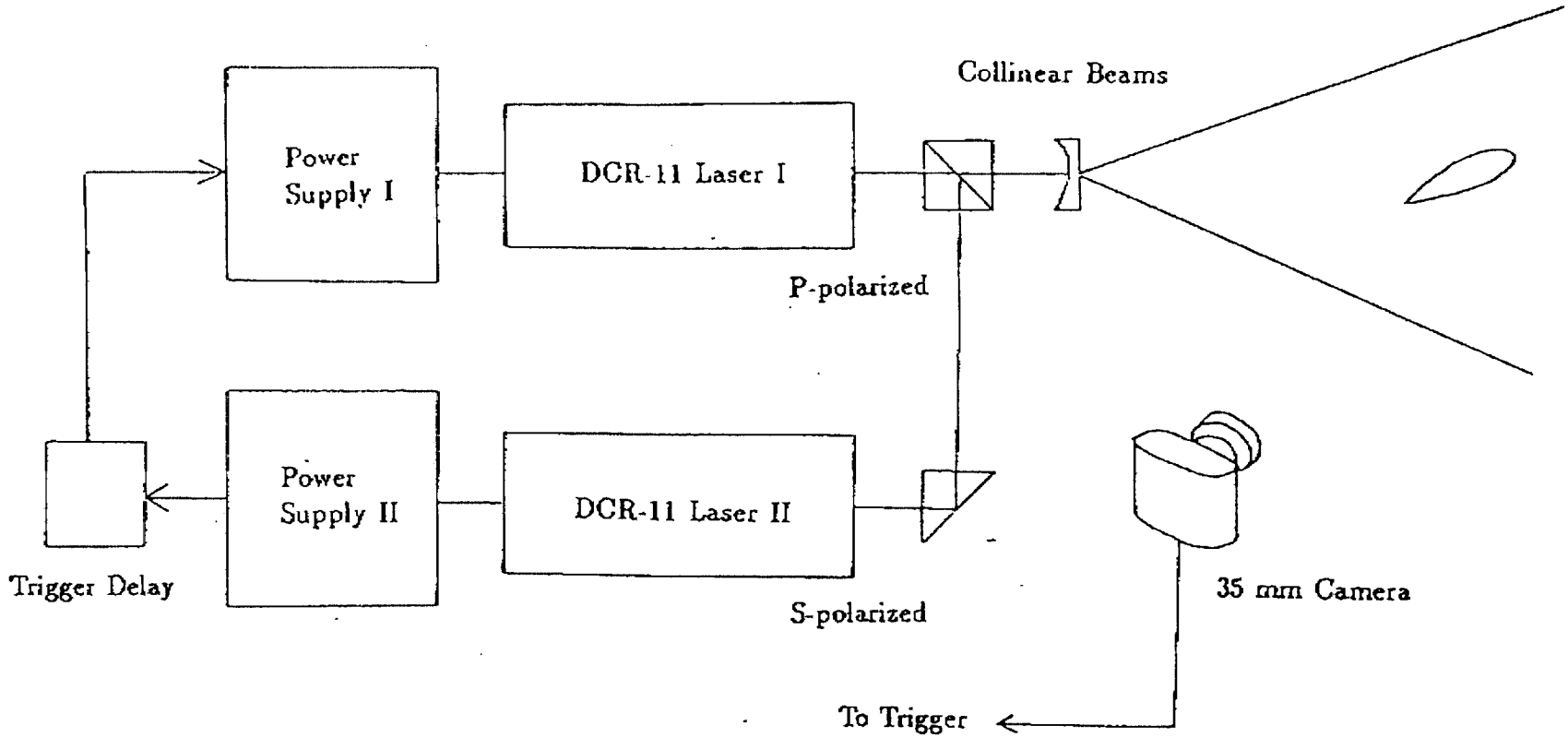

Figure 4. Schematic arrangement for the dual pulsed-laser system

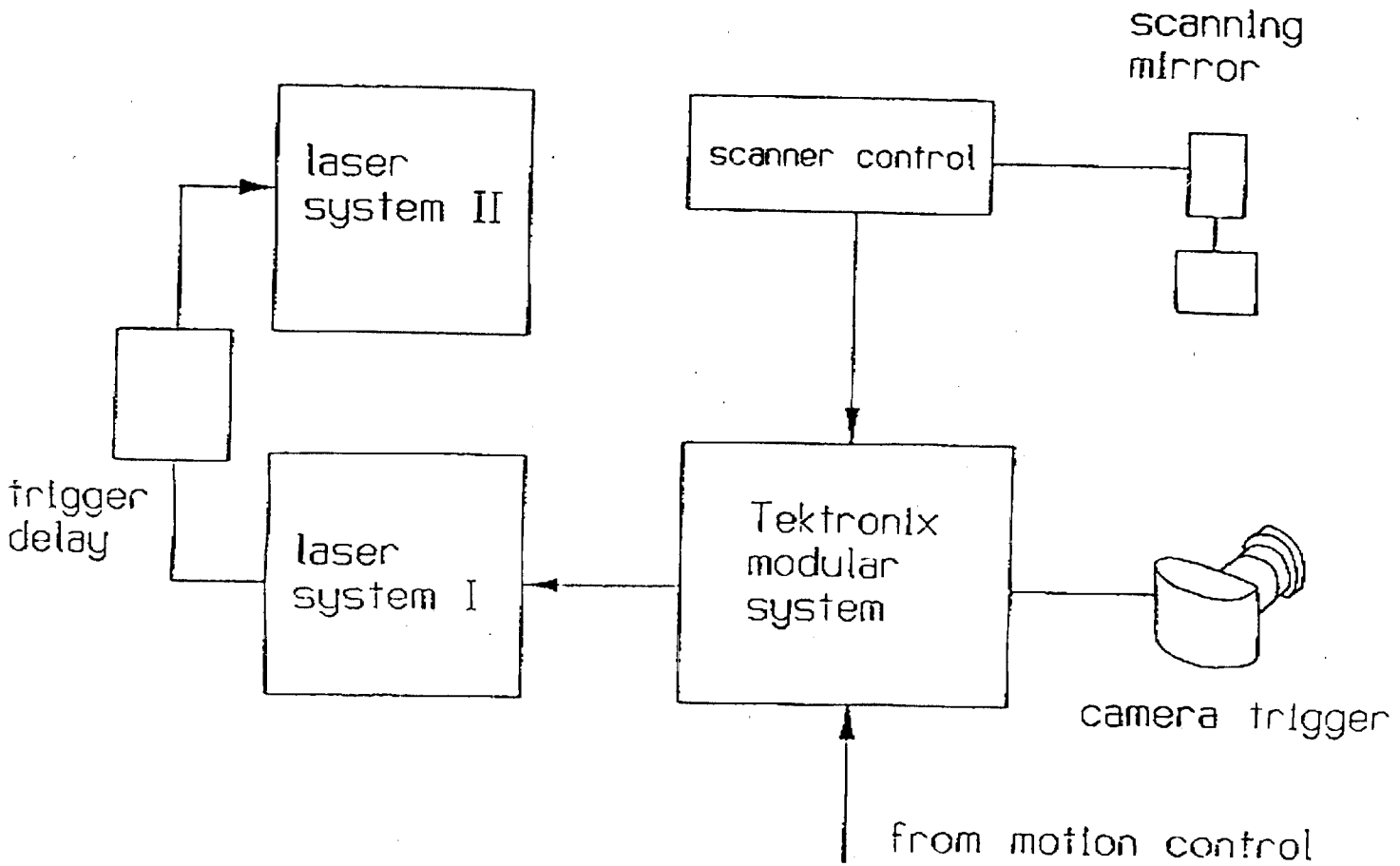

Figure 5. Synchronization arrangement for PIDV

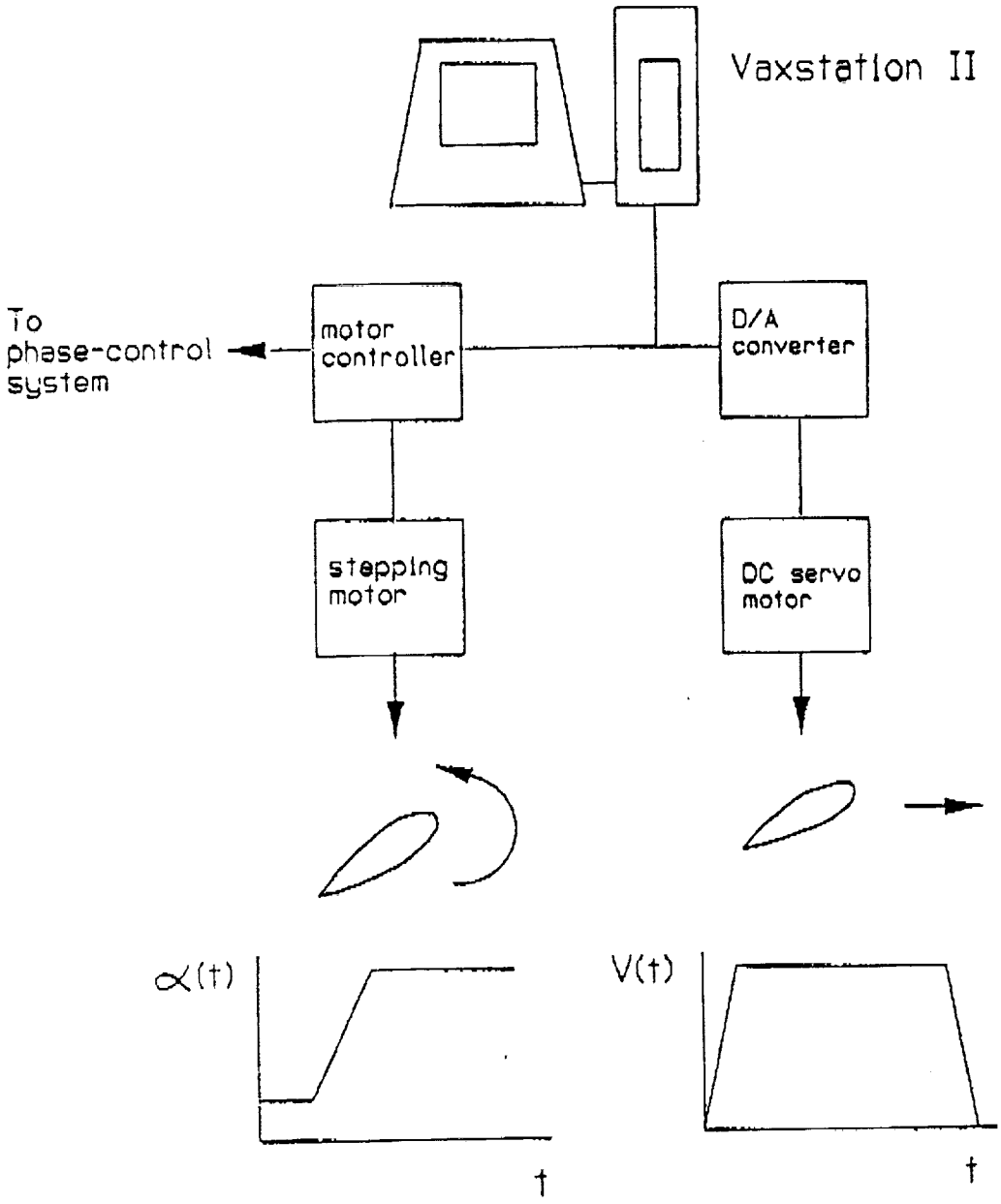

Figure 6. Schematic of the airfoil's motion control system

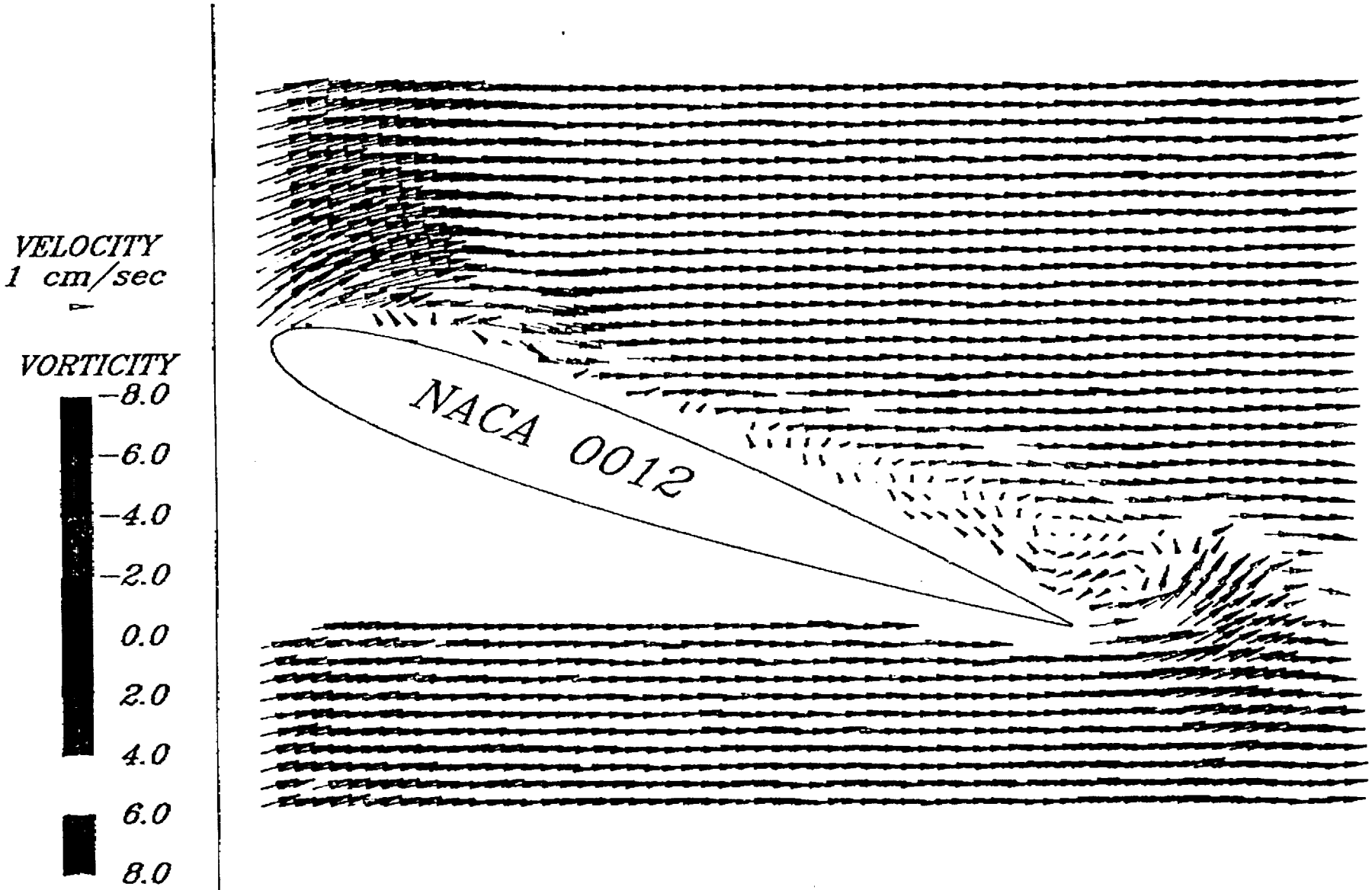

(b) $t^* = 2.98$, $\alpha = 22.4°$;

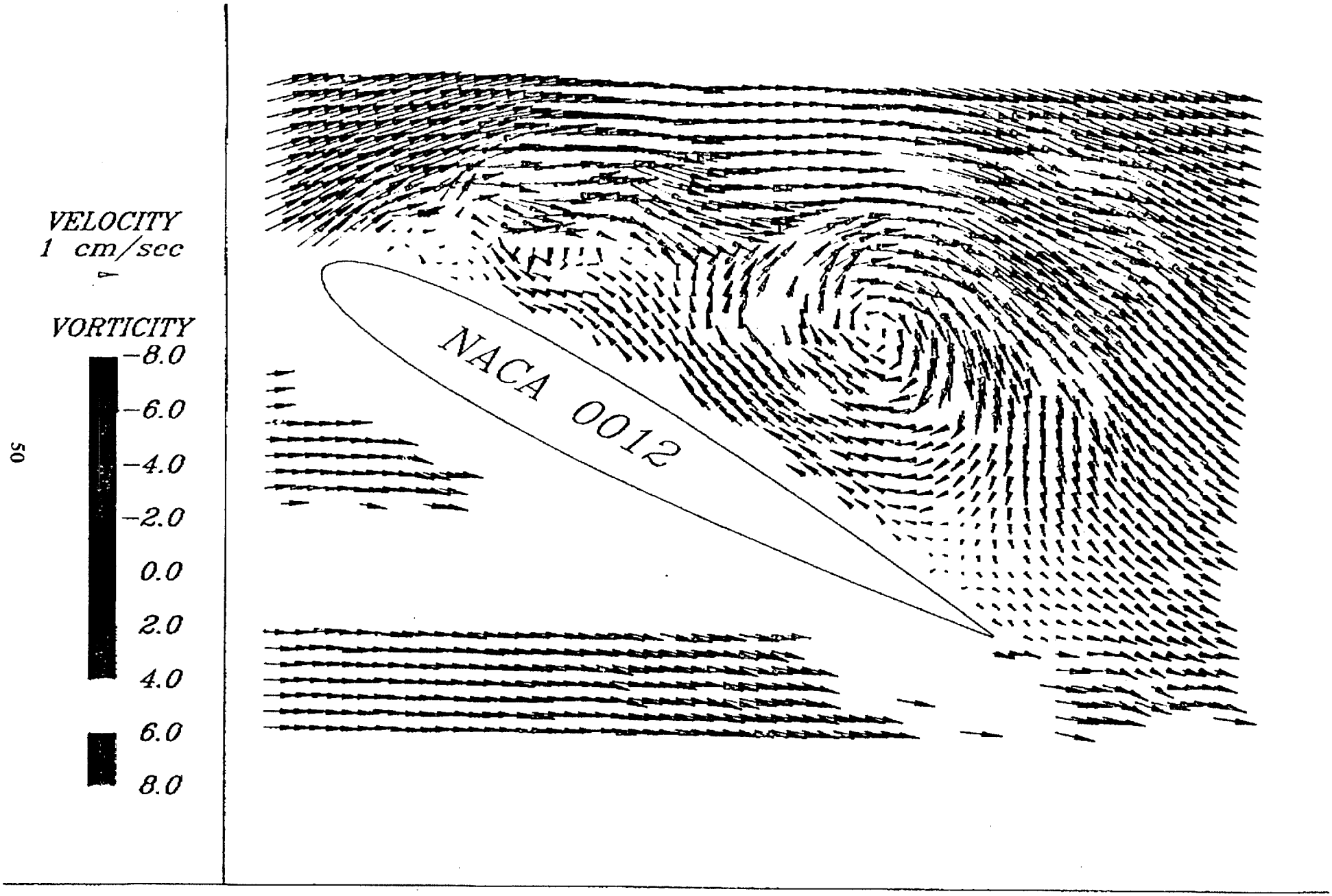

(c) $t^* = 5.13$, $\alpha = 30.0°$;

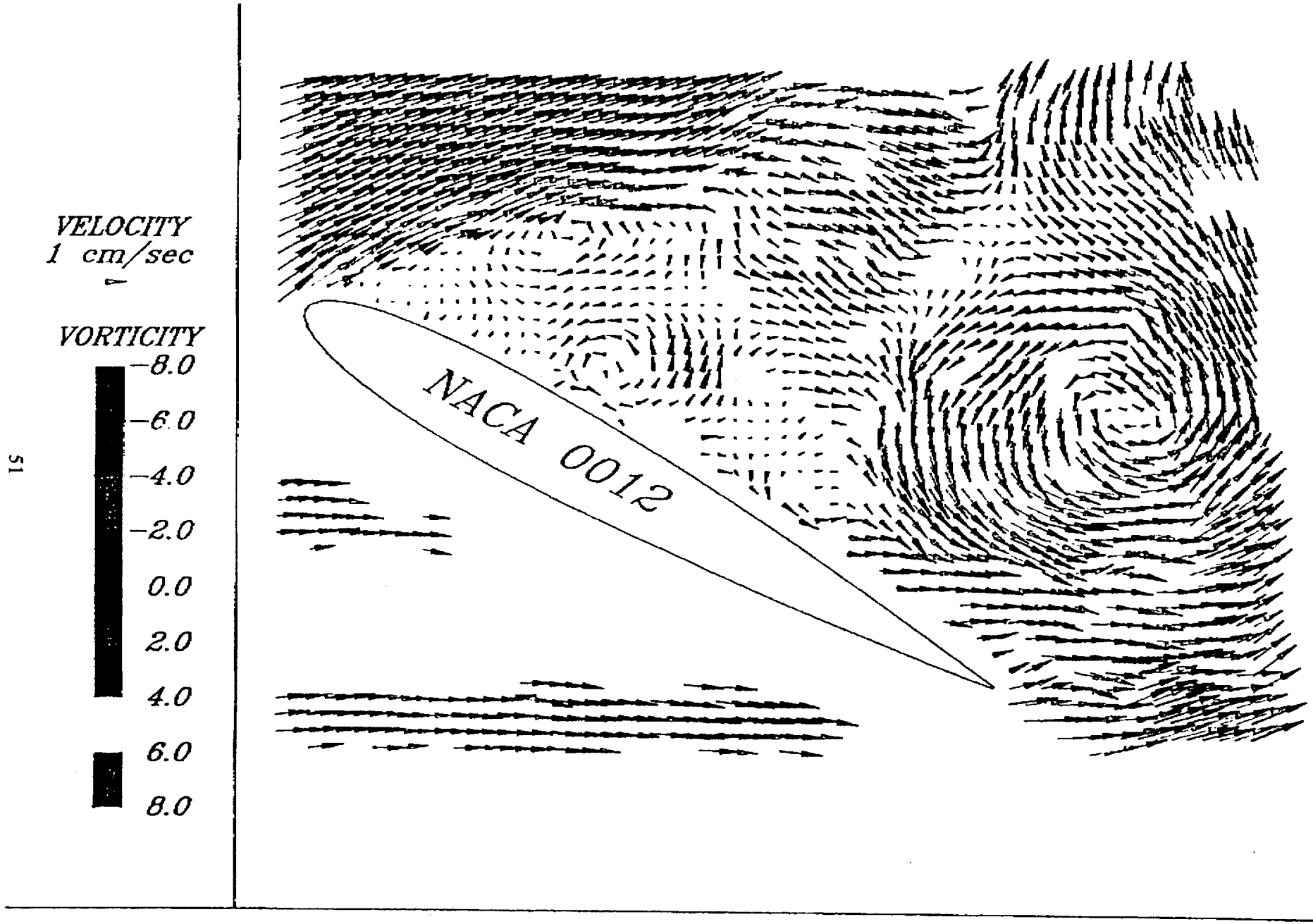

(d) $t^* = 7.27$, $\alpha = 30.0°$.

Figure 7 Time evolution of the instantaneous velocity and associated vorticity fields measured by the PIDV. Re = 5000. $\dot{\alpha} = 0.131$, $t^* = \frac{tU_\infty}{c}$

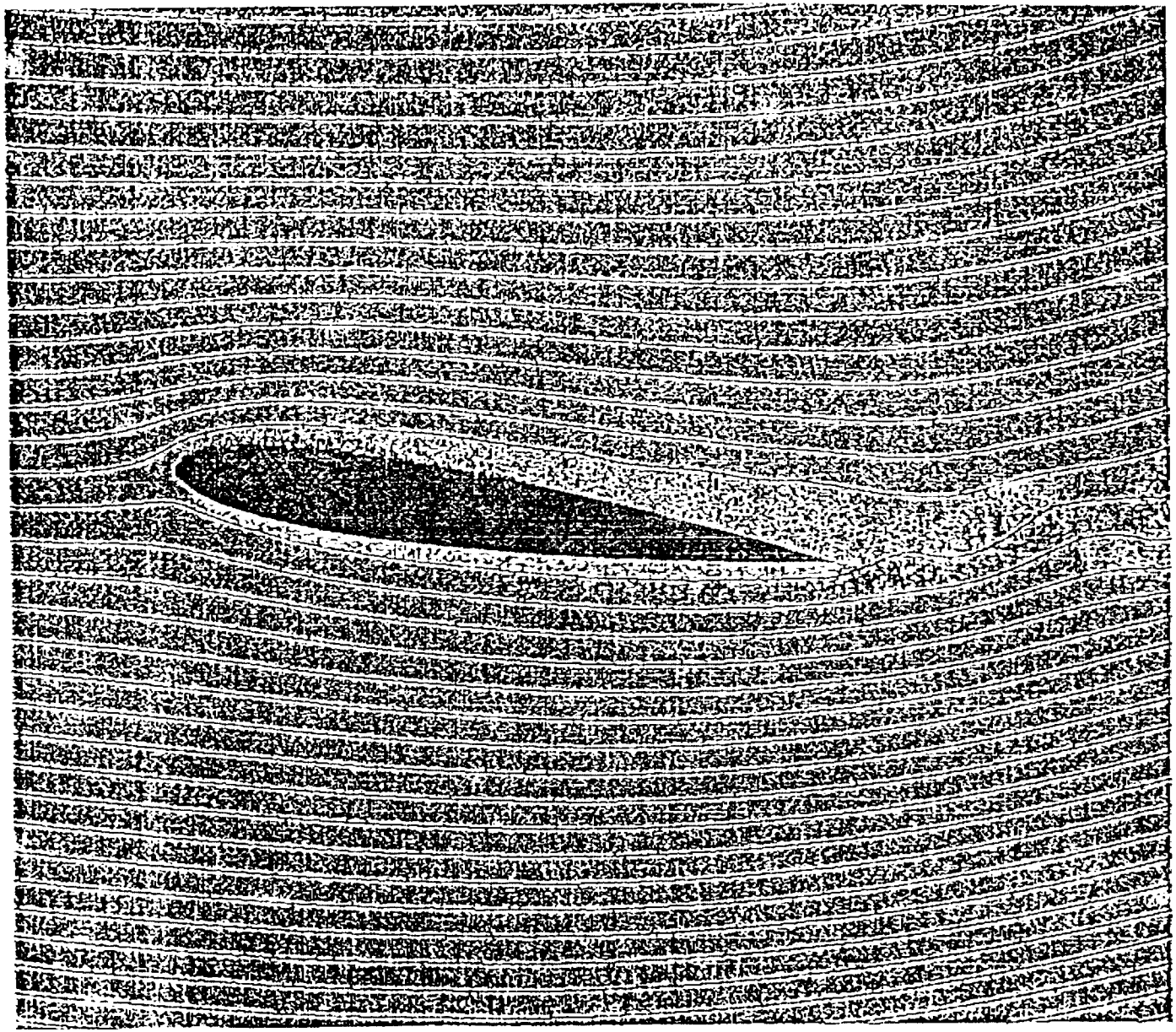

(a) $t^* = 1.5$, $\alpha = 8.3°$;

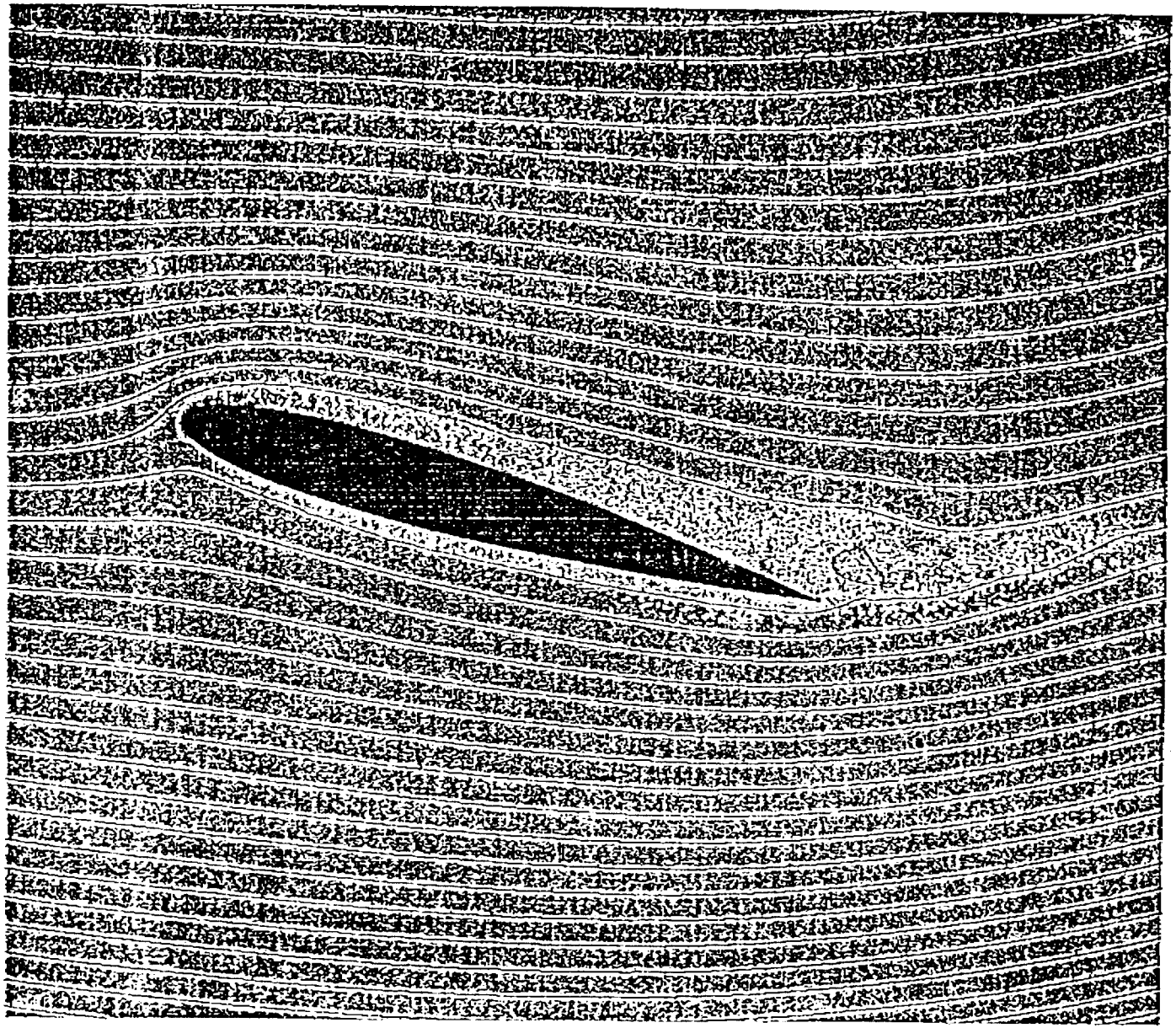

(b) $t^* = 2.0$, $\alpha = 15.0°$;

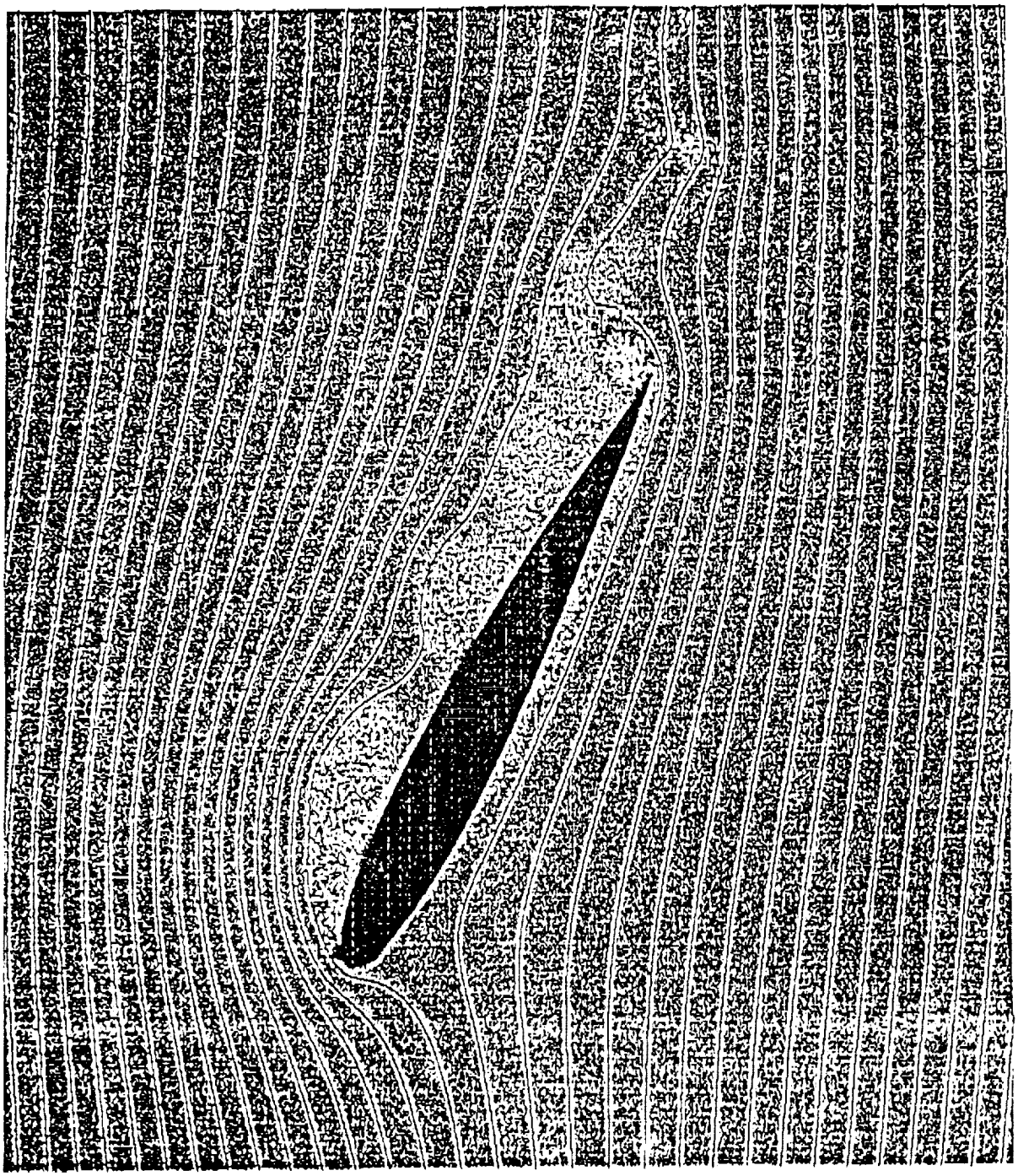

(d) $t^* = 3.0$, $\alpha = 26.9°$;

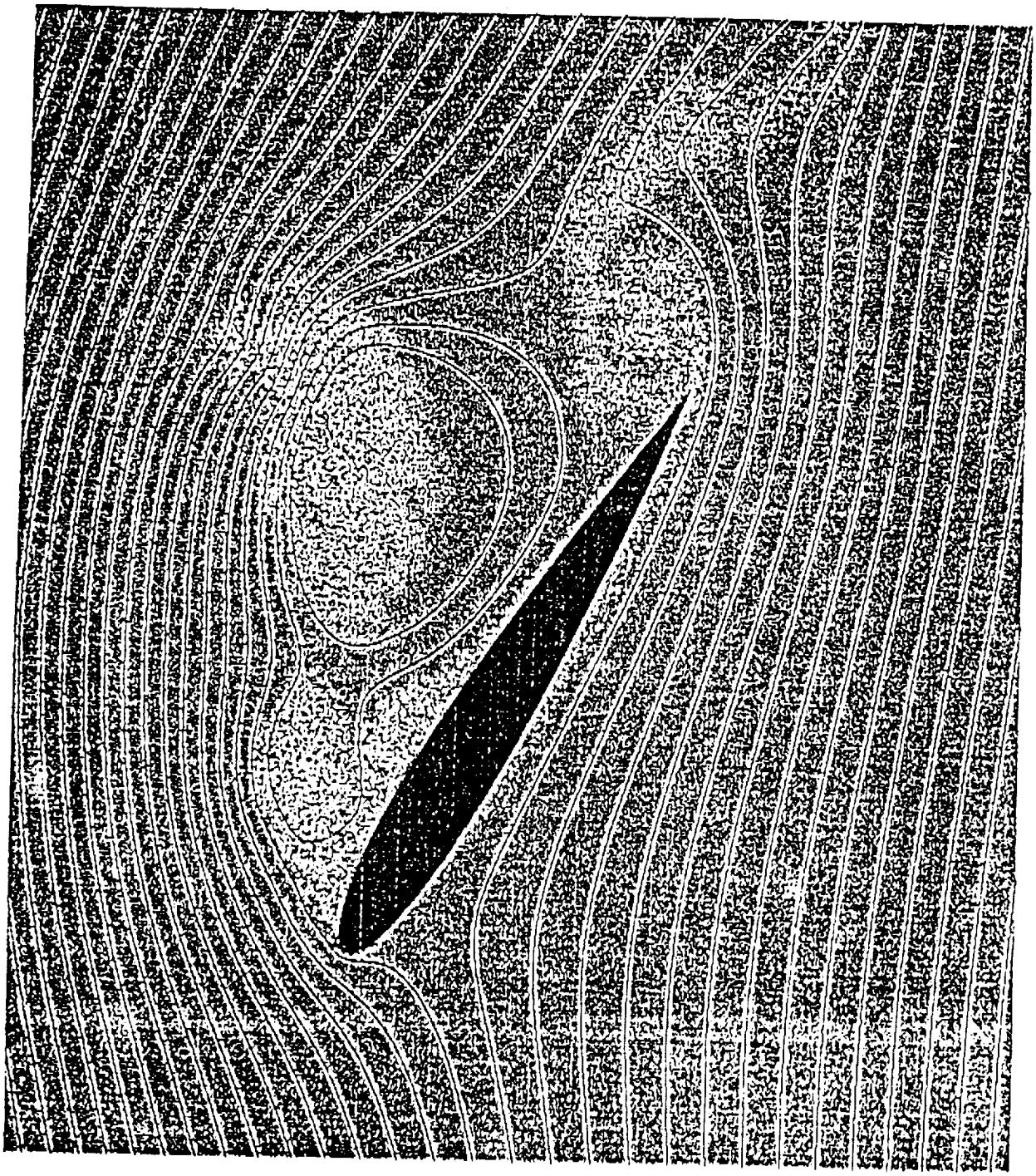

(c) $t^* = 4.5$, $\alpha = 30.0°$;

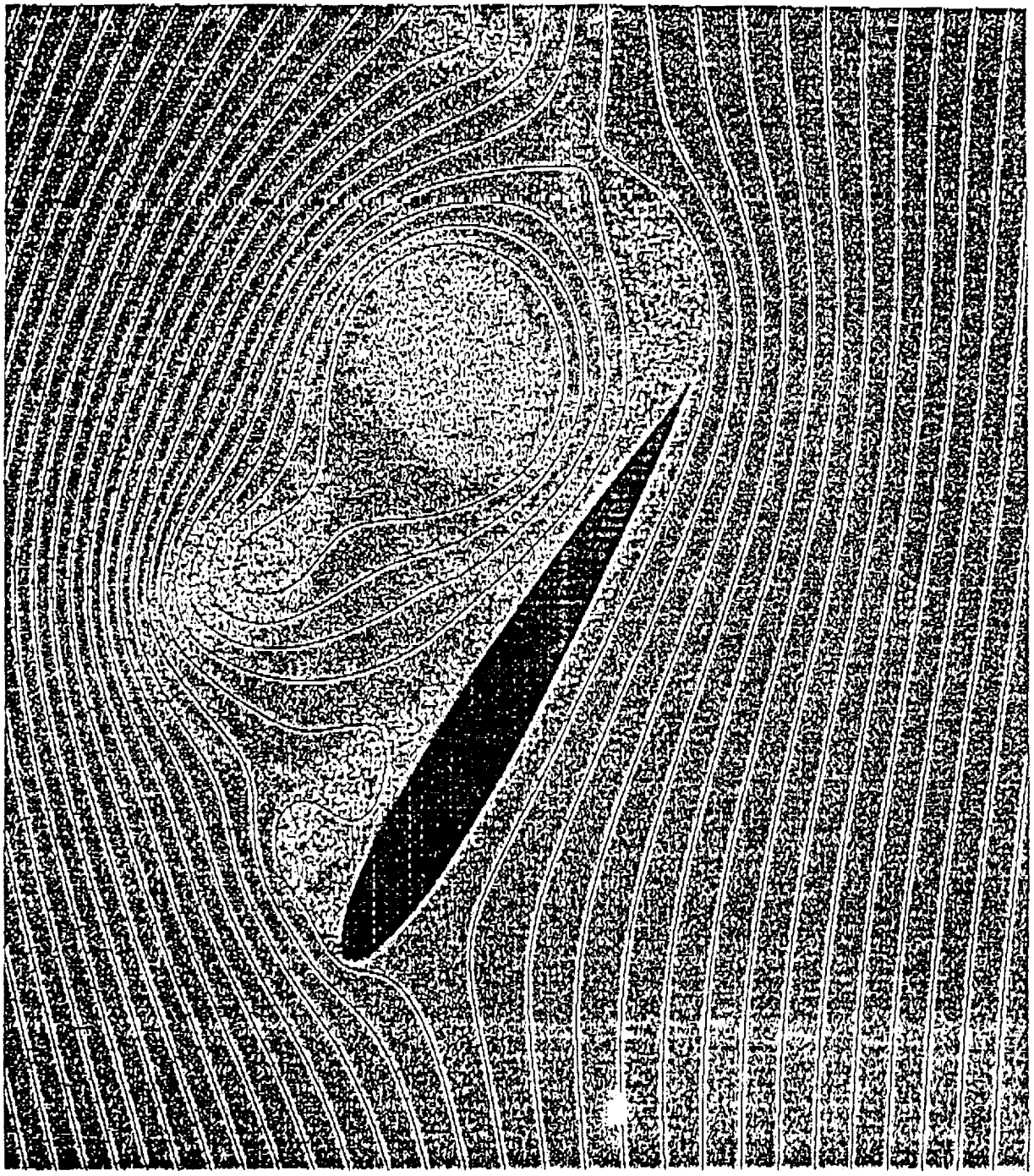

(Γ) $t^* = 5.0$, $\alpha = 30.0°$;

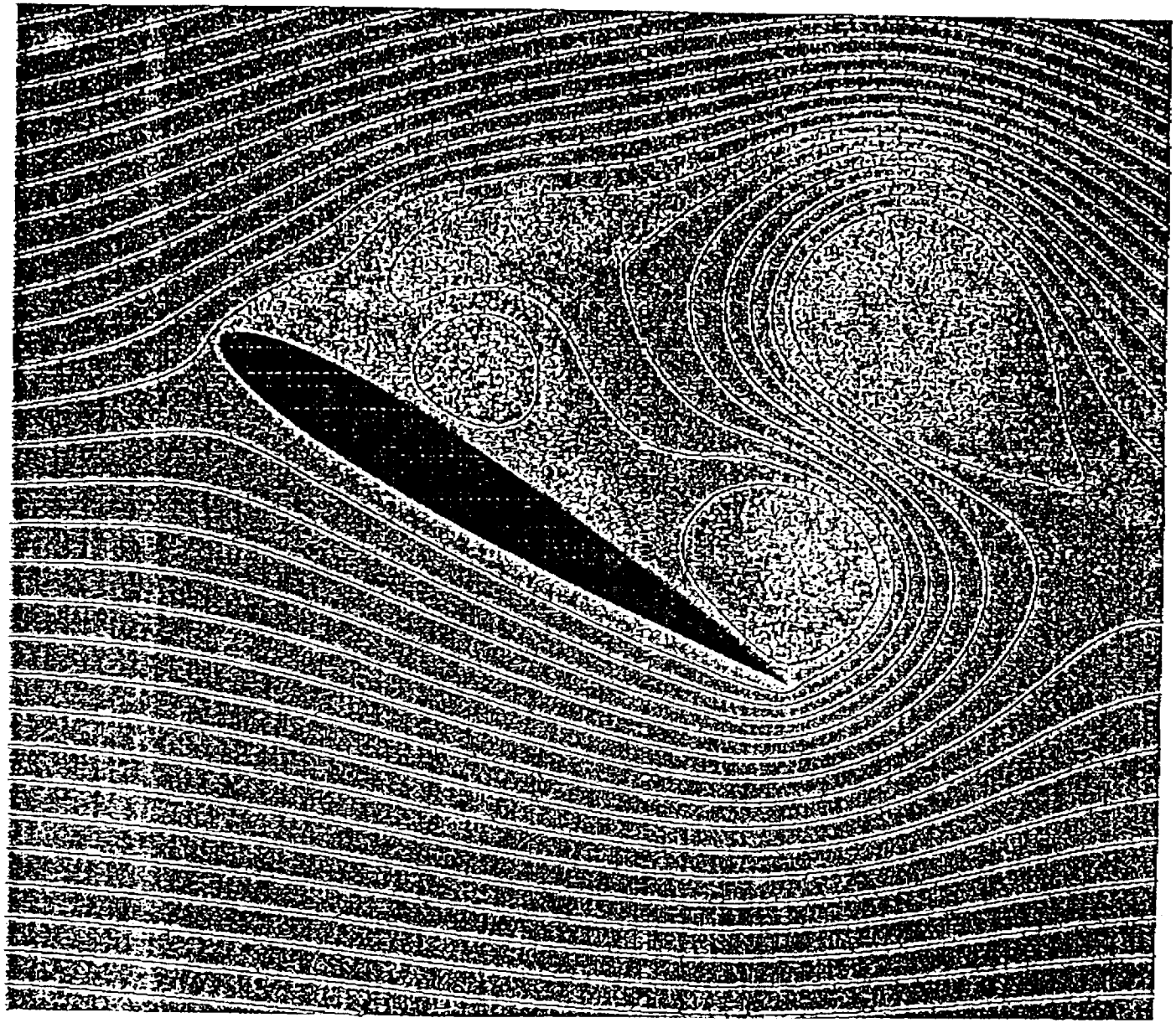

(g) $t^* = 6.0$, $\alpha = 30.0°$;

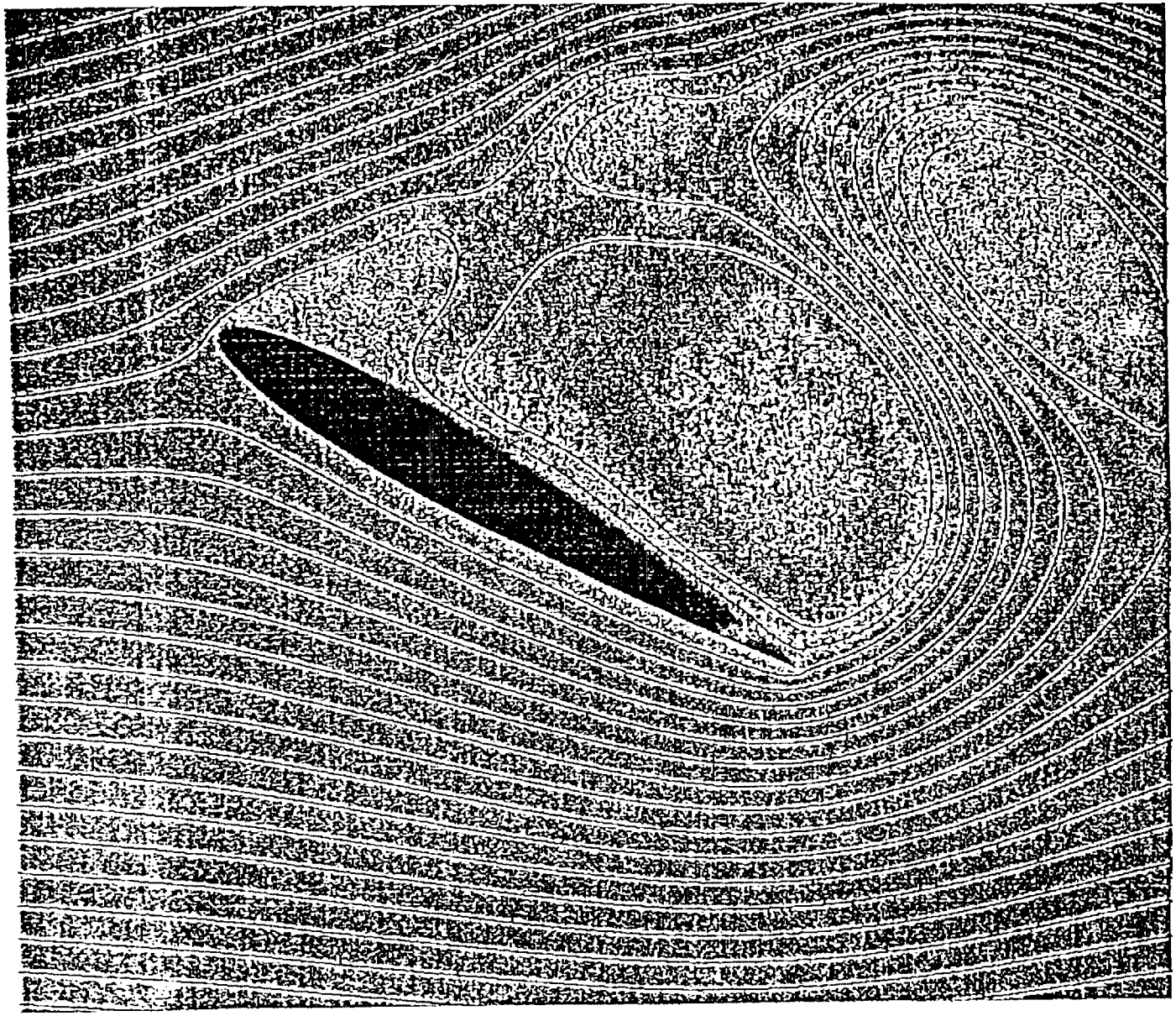

(h) $t^* = 6.5$, $\alpha = 30.0°$;

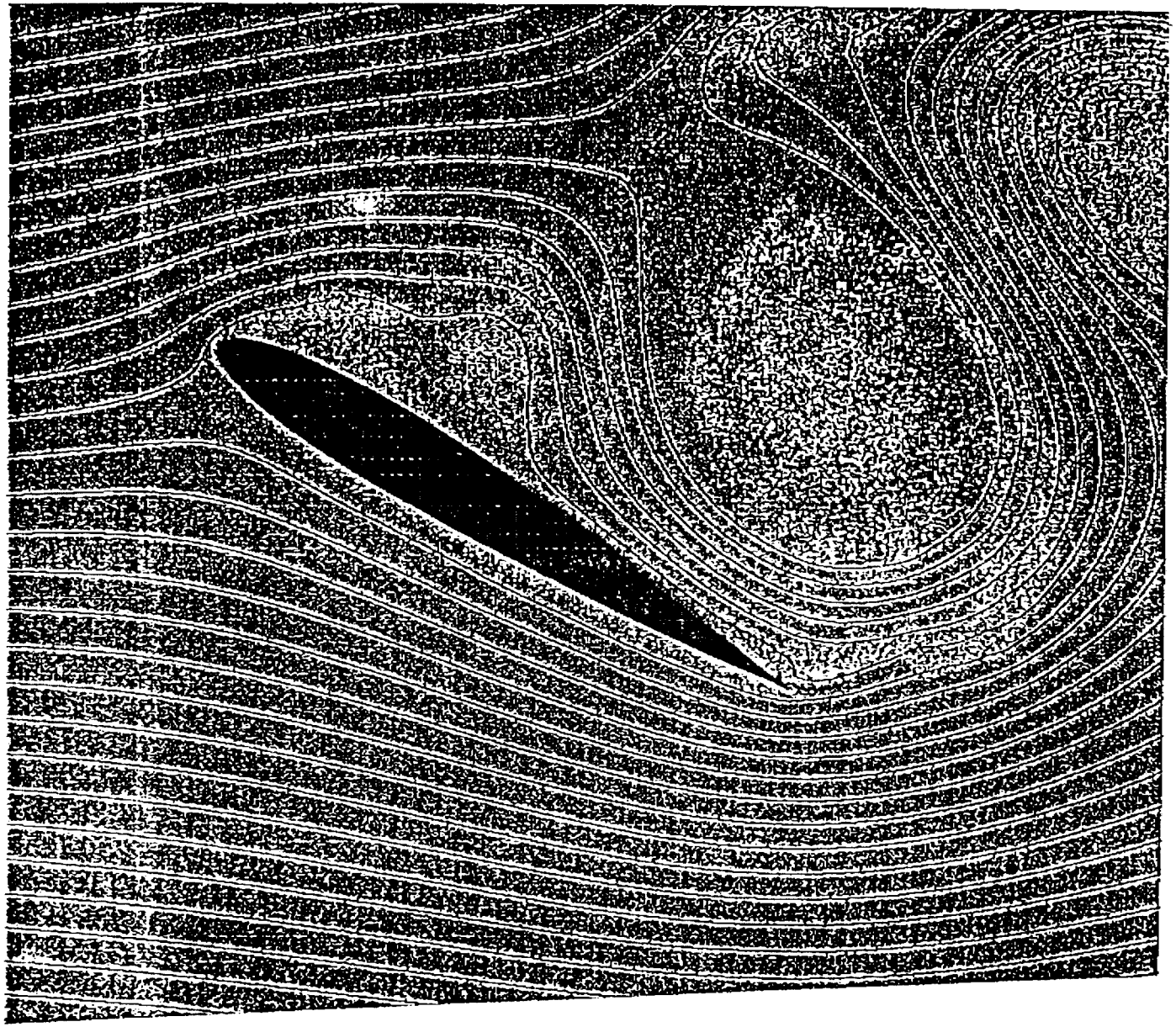

(i) $t^* = 7.0$, $\alpha = 30.0°$.

Figure 8. Computational results of the instantaneous streamline pattern and associated vorticity distribution. Re = 5000. $\dot{\alpha} = 0.131$.

UNSTEADY SEPARATION PROCESS AND VORTICITY BALANCE ON UNSTEADY AIRFOILS

Chih-Ming Ho, Ismet Gursul, Chiang Shih*and Hank Lin

Department of Aerospace Engineering
University of Southern California
Los Angeles, California 90089-1191

ABSTRACT

Low momentum fluid erupts at the unsteady separation region and forms a local shear layer at the viscous-inviscid interface. At the shear layer, the vorticity lumps into a vortex and protrudes into the inviscid region. This process initiates the separation process. The response of airfoils in unsteady free stream was investigated based on this vortex generation and convection concept. This approach enabled us to understand the complicated unsteady aerodynamics from a fundamental point of view.

INTRODUCTION

Unsteady separation is an important feature of many flows. For example, when an airfoil undergoes maneuvering, the lift and drag experience very large variations from the steady state values. The unsteady separation from the leading edge produces coherent vortical structures which can greatly alter the surface loading on the wing (McCrosky, 1982). The separation process and the formation of the vortices can be very different for various operating conditions. On a 2D airfoil, there is no effective vorticity convection mechanism. The separating vortices therefore can not hold on to the chord and are convected by the mean flow. Shih (1988) found that the time needed for the vortex moving along the chord is an important time scale in determining the aerodynamic properties. On a small aspect ratio delta wing, vorticity can be transported along the cores of the leading edge separation vortices. The vortices can be stationary on the wing. Therefore, there is no vortex convection time scale. In this paper, the measured lift of airfoils in an unsteady free stream will be presented and will be interpreted by the vorticity balance concept (Reynolds and Carr, 1985).

1. UNSTEADY SEPARATION MECHANISM

It has been experimentally shown that shear stress vanishes at an interior point away from the wall for both upstream moving separation (Shih, 1988) and downstream moving

*Present Address: Department of Mechanical Engineering, Florida State University, Tallahassee, Florida 32306.

separation (Didden and Ho, 1985). These cases were illustrated in figures 1a and 1b. The data validated the MRS criterion and showed many important aspects of unsteady separation pointed out by Van Dommelen and Shen (1982). Erruption of the boundary layer fluid and the formation of a local shear layer with an inflection point (figure 2) was found to be generic to unsteady separation.

When an external disturbance induces an unsteady adverse pressure gradient (figure 3), the fluid particles near the wall decelerates. Low momentum fluid errupts from the wall region. A local shear layer forms at the boundary of the inviscid and viscous zones. Velocity profile of the local shear layer has an inflectional point between the point $\partial u/\partial y = 0$ near the wall and $\partial u/\partial y = 0$ at free stream. This shear layer is inviscidly unstable and extracts energy from the mean flow.

2. UNSTEADY WATER CHANNEL

Experiments on unsteady airfoils were performed in an unsteady water tunnel (figure 4). The tunnel was operated under constant head. Therefore, the free stream speed was determined by the resistance provided by the exit gate. This arrangement made the tunnel extremely versatile and simple to operate. The opening area of the exit gate was controlled by a computer-driven stepping motor. The free stream velocity was varied as a function of time in many different types of waveforms. The lift was measured by load cells while the velocity field was measured by laser Doppler velocimetry.

3. ATTACHED UNSTEADY FLOW AROUND 2D AIRFOIL

When the flow on the 2D airfoil was attached, the vorticity convection was balanced by a part of the vorticity diffusion. Hence, the convected vorticity did not play a role in the dynamics. The lift was determined by the rest of the vorticity diffused from the surface. Since there was no intrinsic time scale of the vorticity balance, the lift curves of the attached flow was only scaled by the free stream velocity time scale. Based upon the vorticity balance we can show that the local circulation is scaled with the velocity at the edge of the boundary layer.

4. SEPARATED UNSTEADY FLOW AROUND 2D AIRFOIL

During the separated phase, the vorticity measurement indicated that the vorticity diffused from the surface is negligible compared with that shed from the leading edge. In other words, the flow was controlled by the vorticity convection instead of the vorticity diffusion. The vorticity originating from the leading edge rolled up into a vortex which produced high suction on the wing. When this lift generating vortex moved from leading edge to trailing edge, the lift of the unsteady airfoil was much higher than that of the steady one. The lift dropped significantly after the lift generating vortex left the chord. Therefore, the ratio between the vortex convection time scale and external perturbation time scale dictates the lift curve of the airfoil.

5. AN AIRFOIL WITH $C_L > 10$

How to obtain high lift coefficient in the post stall region is the goal of supermaneuverability research. The fundamental understanding of the time scale and the vorticity balance on the separated airfoil mentioned in the above section enabled us to achieve this purpose. We placed a NACA 0012 airfoil at an angle of attack of 20° which is in the static stall region. The reduced frequency was chosen such that a large coherent vortex can be trapped on the chord for an appreciable portion, say 40%, of the cycle. We then obtained a lift coefficient larger than ten. This is shown in figure 5.

ACKNOWLEDGMENT

This work is supported by AFOSR Contract No. F49620-88-C-0061.

REFERENCES

Didden, N. and Ho, C.-M., 1985, "Unsteady separation in a boundary layer produced by an impinging jet", *J. Fluid Mechanics*, Vol. 160, pp. 235–256.

McCrosky, W. J., 1982, "Unsteady Airfoils", *Annual Rev. Fluid Mech.*, Vol. 14, p. 285.

Reynolds, W. C. and Carr, L. W., 1985, "Review of Unsteady, Driven, Separated Flows", AIAA Paper No. 850527.

Shih, C., 1988, "Unsteady Aerodynamics of a Stationary Airfoil in a Periodically Varying Free Steam", USC Ph.D. Thesis.

Van Dommelen, L. L. and Shen, S. F., 1982, The genesis of separation. In *Numerical and Physical Aspects of Aerodynamic Flows* (ed. T. Cebeci), pp. 293–311, Springer.

Upstream moving separation

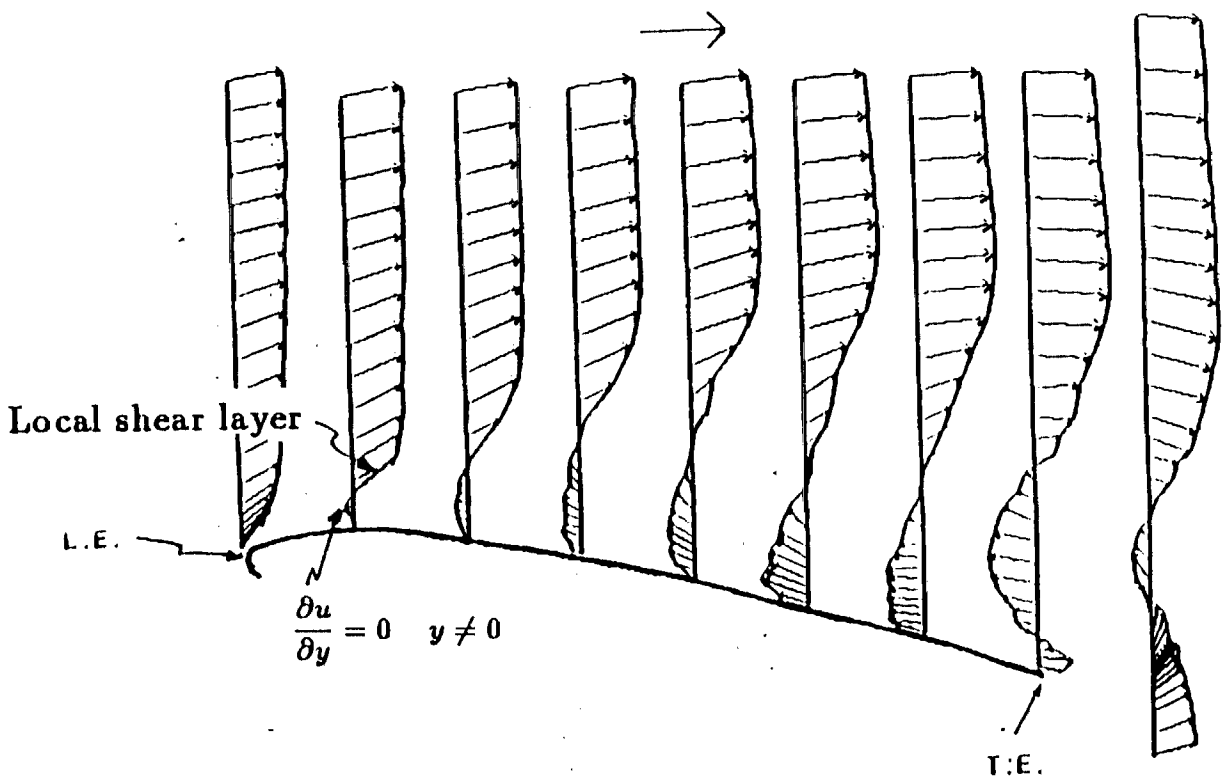

Figure 1a: Upstream moving separation (Shih, 1988).

Downstream moving separation

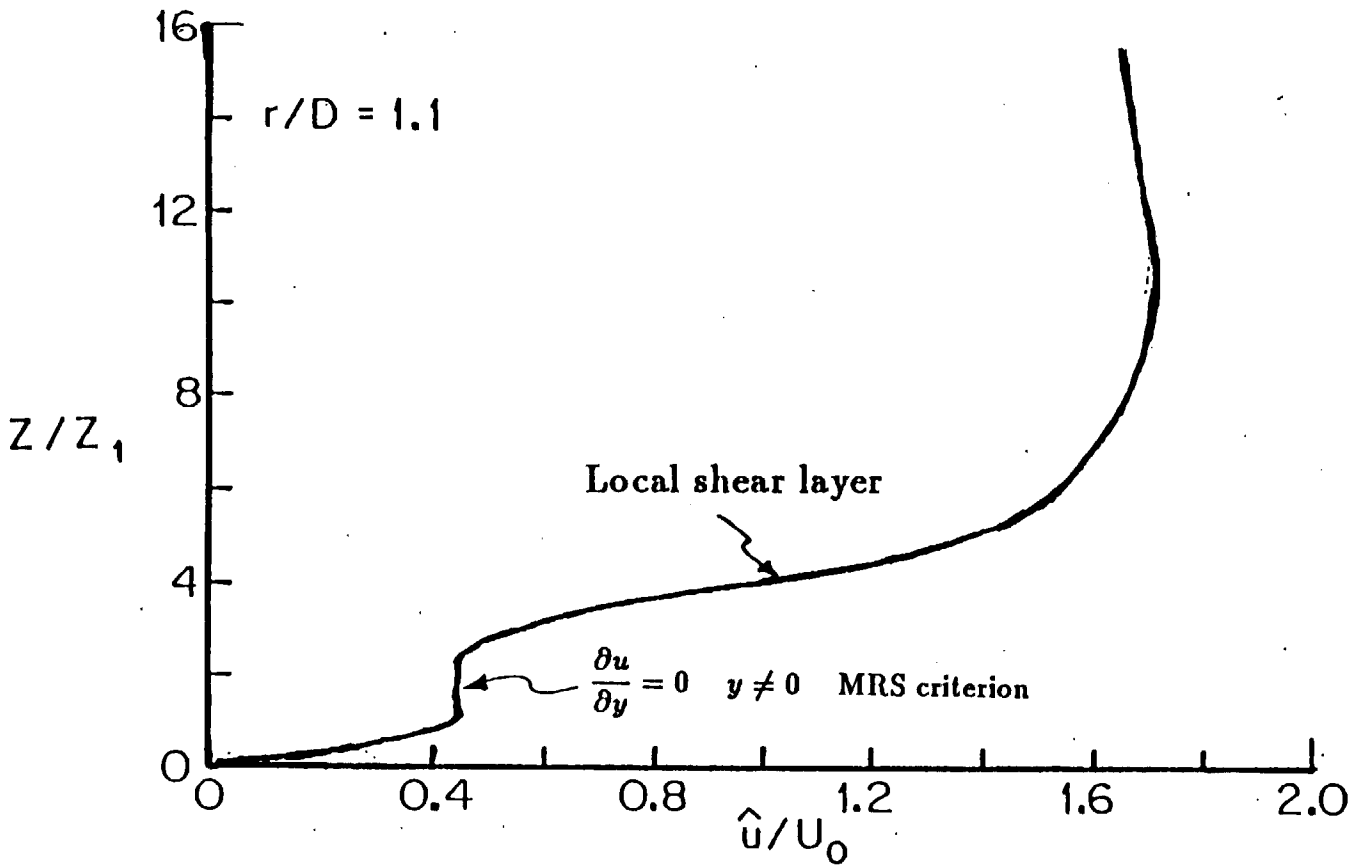

Figure 1b: Downstream moving separation (Didden and Ho, 1985).

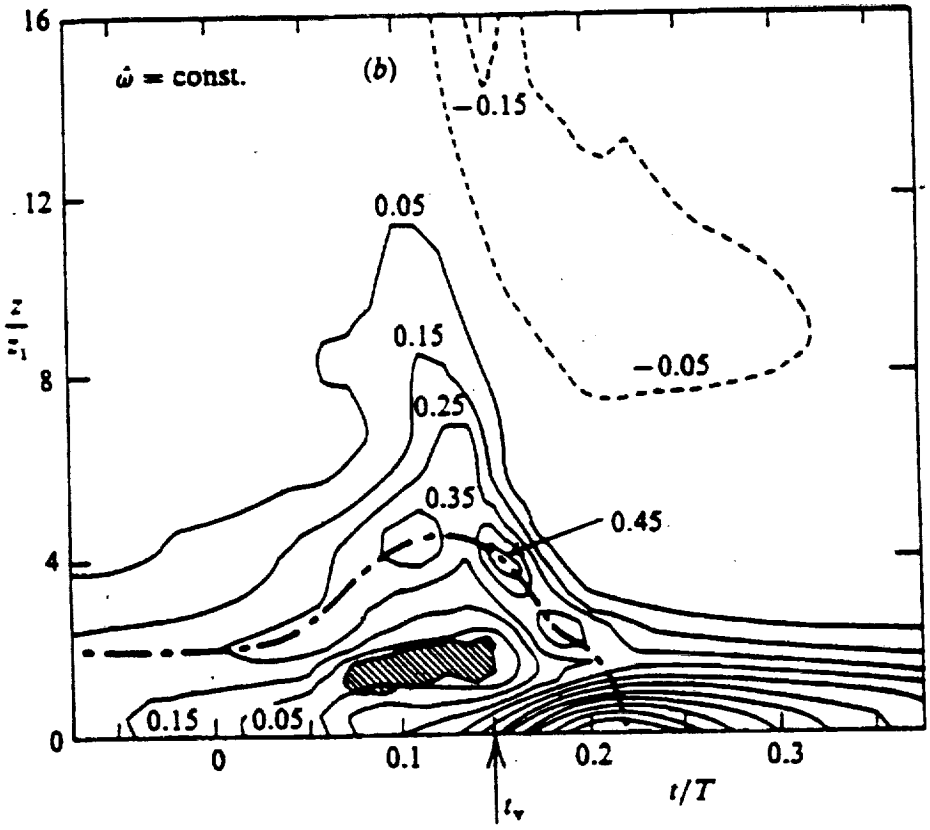

Figure 2: Secondary vortex ejection in vortex induced separation (Didden and Ho, 1985).

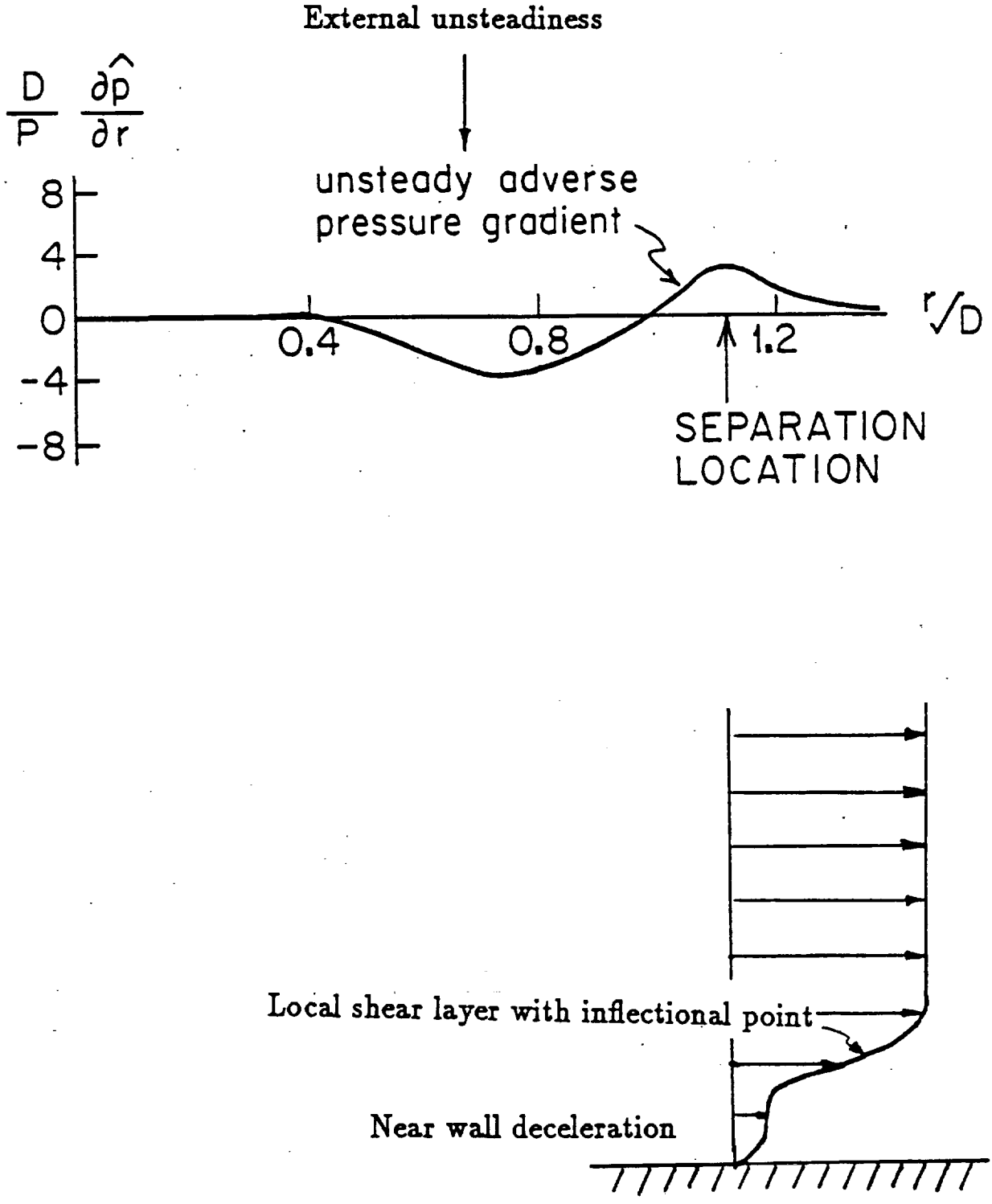

Figure 3: Unsteady separation mechanism.

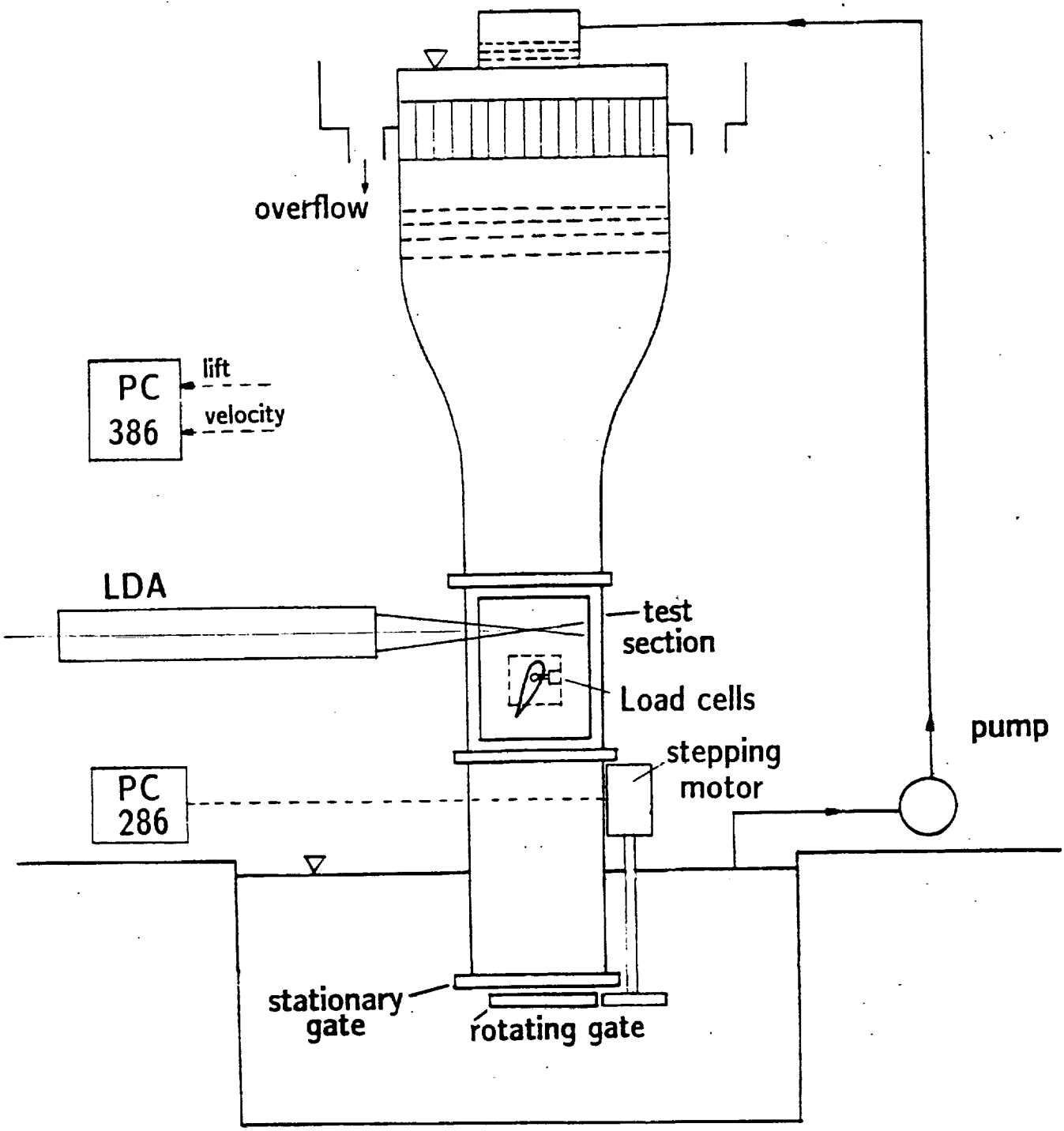

Figure 4: Unsteady water channel.

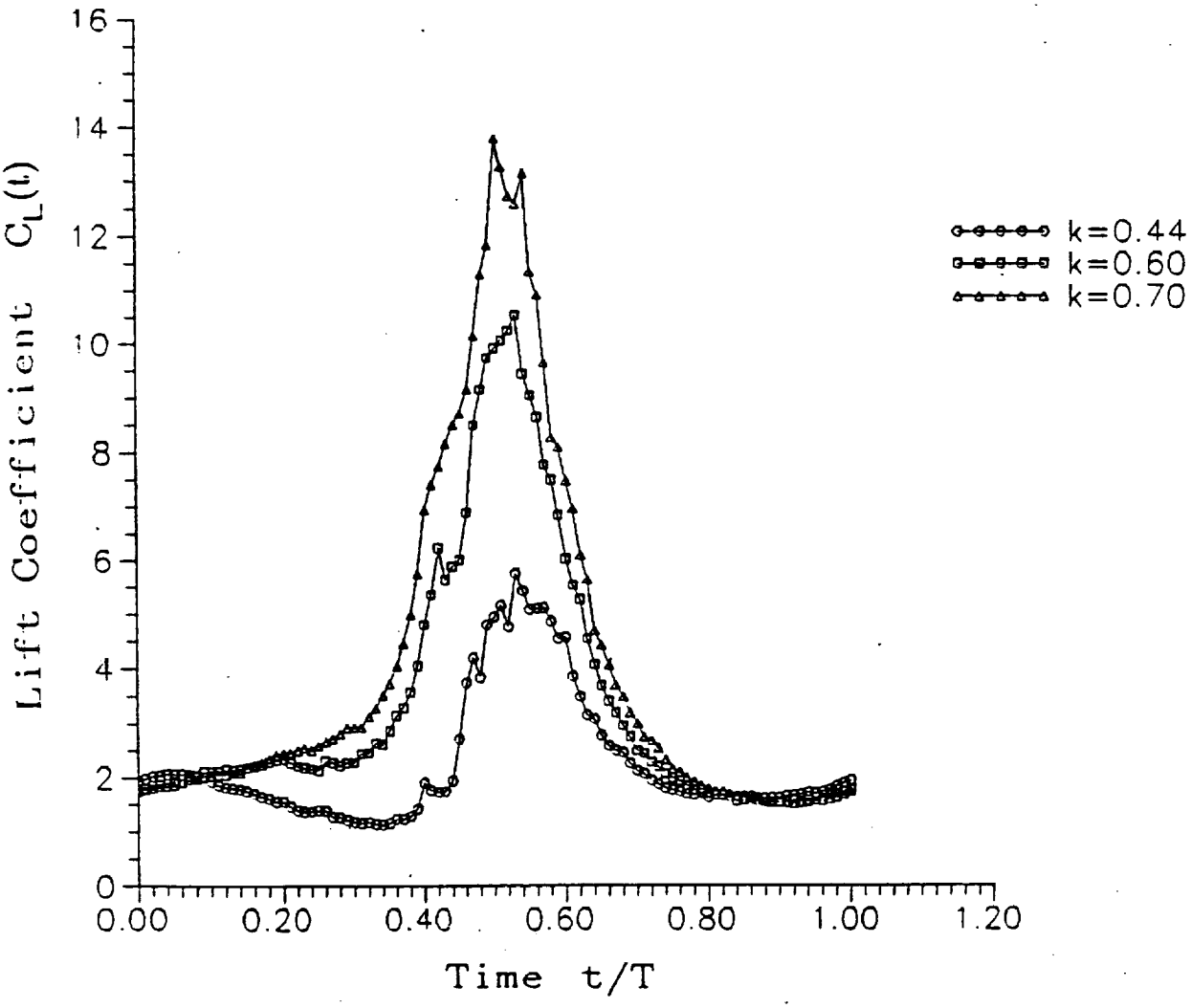

Figure 5: Variation of phase-averaged lift coefficient over a cycle for NACA 0012 at α=20°.

OUTLINE

- Vorticity Balance of Attached flow

- Unsteady Separation Mechanism
  - Downstream moving separation
  - Upstream moving separation
  - 2-D separation ?

- Vorticity Balance of Separated flow

- Unsteady Lift of Post-Stall 2-D Wing
  - Optimum frequency
  - $C_L > 10$

- Unsteady Lift of 3-D Wing
  - Small aspect ratio delta wing
  - Large aspect ratio delta wing

ATTACHED FLOW

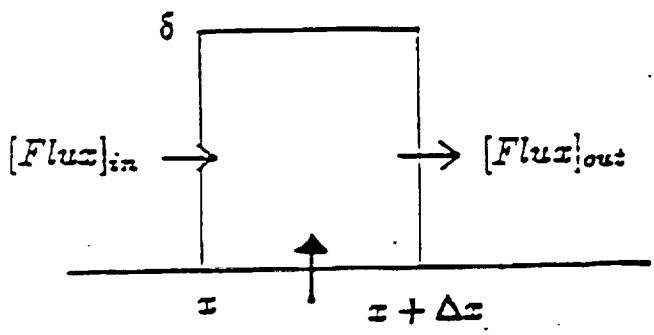

Surface Flux

- Increasing Convection

$$\left[\int_0^\delta U\Omega dy\right]_{in} - \left[\int_0^\delta U\Omega dy\right]_{out} = \left[\int_0^\delta U\frac{\partial U}{\partial y}dy\right]_{in} - \left[\int_0^\delta U\frac{\partial U}{\partial y}dy\right]_{out}$$
$$= \left[\frac{1}{2}U_e^2(x) - \frac{1}{2}U_e^2(x+\Delta x)\right]$$

- Vorticity Flux from the Surface

$$-\int_x^{x+\Delta x}\nu\frac{d\omega}{dy}dx = -\int_x^{x+\Delta x}\frac{1}{\rho}\frac{\partial P}{\partial x}dx$$
$$= \int_x^{x+\Delta x}\frac{\partial U_e}{\partial t}dx + \int_x^{x+\Delta x}U_e\frac{\partial U_e}{\partial x}dx$$
$$= \int_x^{x+\Delta x}\frac{\partial U_e}{\partial t}dx + \left[\frac{1}{2}U_e^2(x+\Delta x) - \frac{1}{2}U_e^2(x)\right]$$

- Surface Flux Dominates the Flow

ATTACHED FLOW

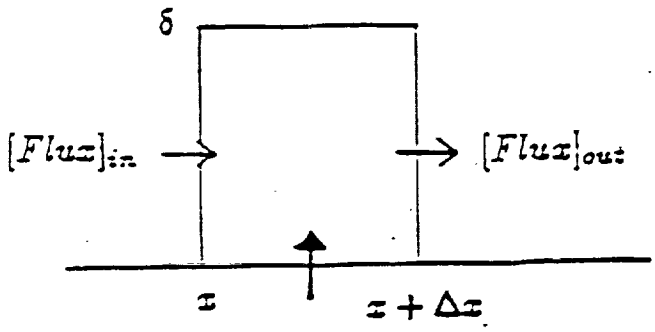

Surface Flux

⊙ Net Vorticity (Circulation) Accumulation

$$\frac{\partial \Gamma}{\partial t} = \int_x^{x+\Delta x} \frac{\partial U_e}{\partial t} dx$$

⊙ Circulation Scale

$$\Gamma = \int \int \Omega dx dy = \int_x^{x+\Delta x} \int_0^{\delta} \frac{\partial U}{\partial y} dy dx$$
$$= \int_x^{x+\Delta x} U_e dx$$

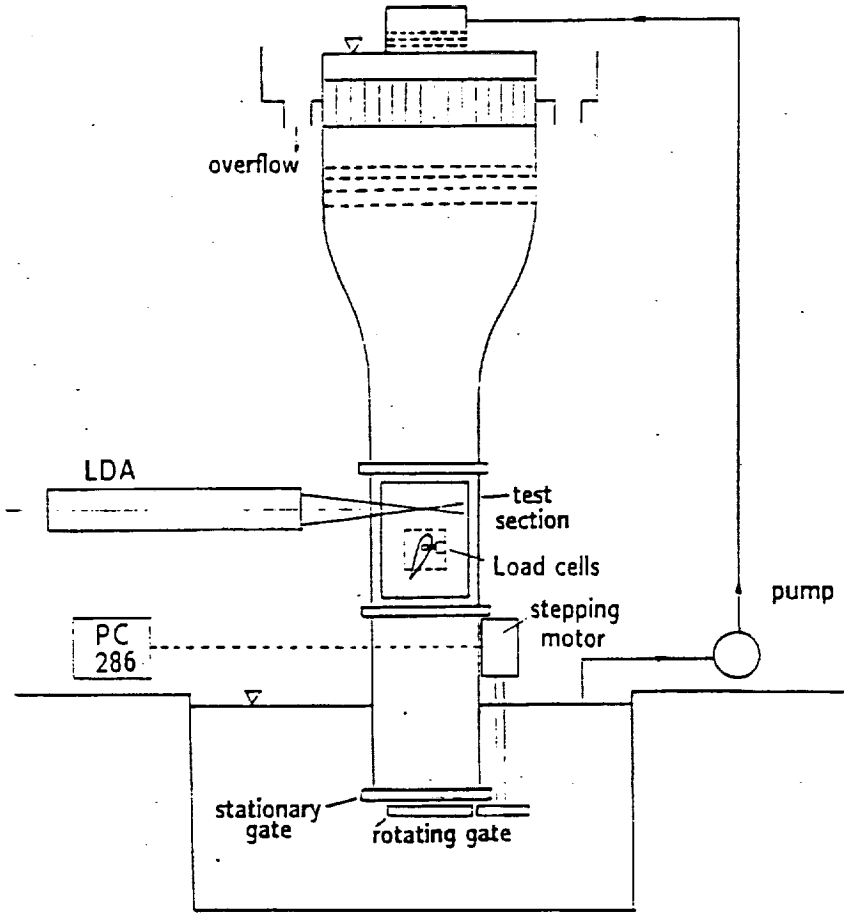
overflow
LDA
test section
Load cells
pump
stepping motor
PC 286
stationary gate
rotating gate

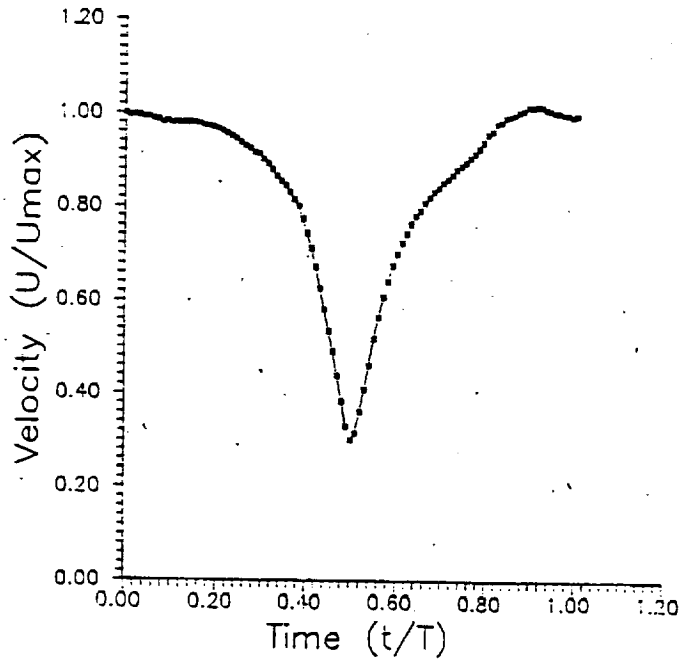
Velocity (U/Umax)
1.20
1.00
0.80
0.60
0.40
0.20
0.00
0.00
0.20
0.40
0.60
0.80
1.00
1.20
Time (t/T)

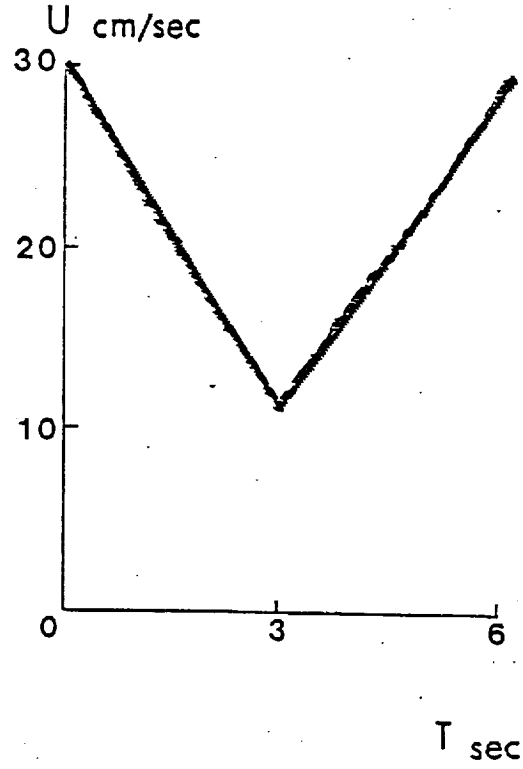
U cm/sec
30
20
10
0
3
6
T sec

- Curves Collapse for Attached Flow
- Single Time Scale

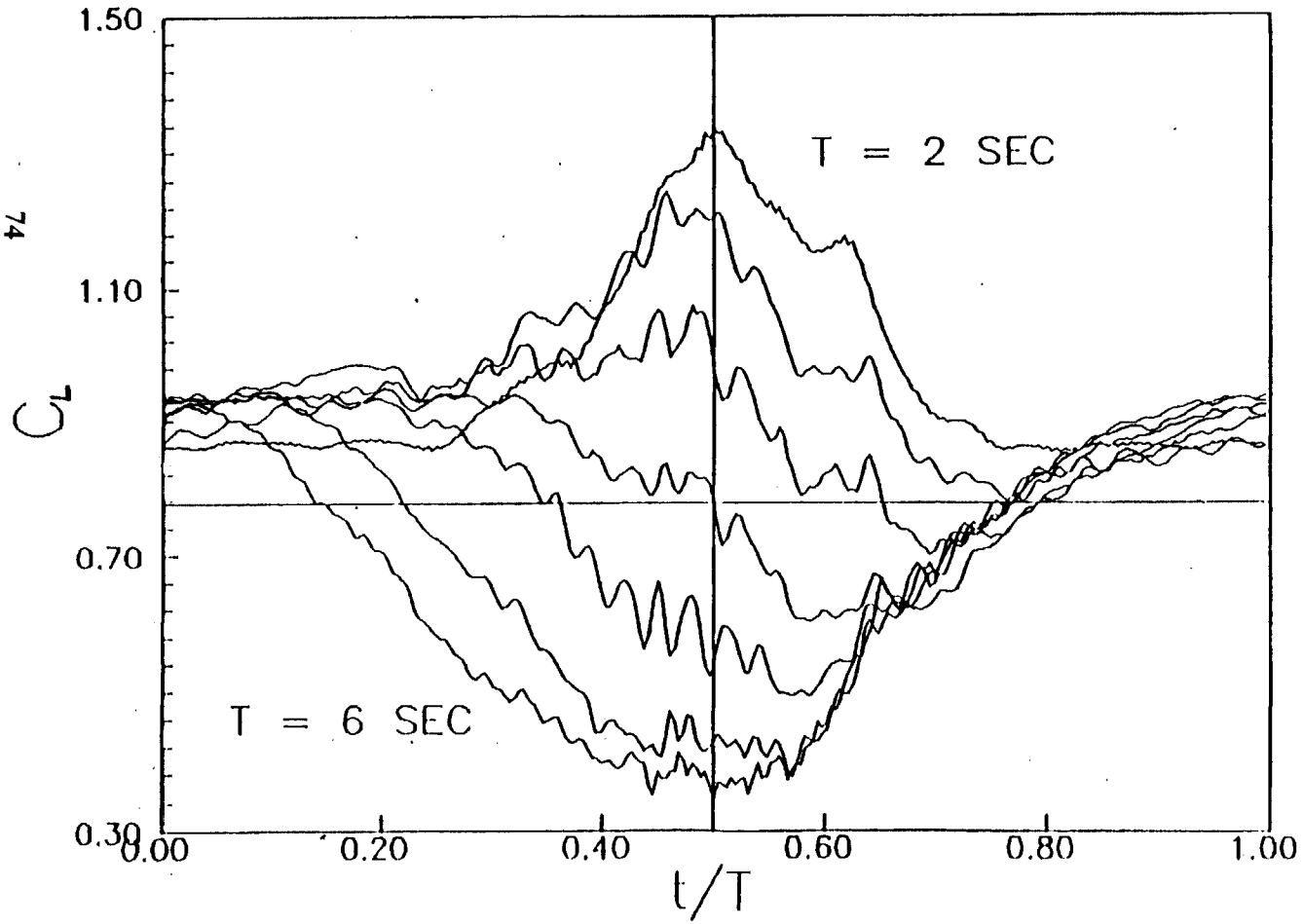

Regional Balance of Phase-Averaged Vorticity

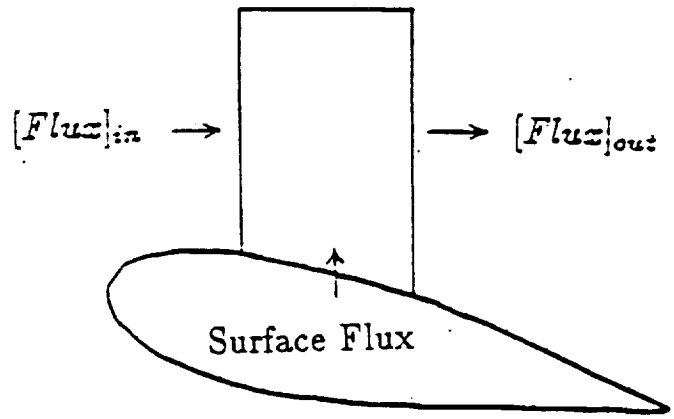

$$\frac{\partial <\Gamma>}{\partial t} = \left[\int <u\omega> dy\right]_{in} - \left[\int <u\omega> dy\right]_{out} - \left[\int \nu \frac{d<\omega>}{dy} dx\right]_s$$

$$<u\omega> \;=\; U\Omega + \frac{\partial}{\partial x} <u'v'> - \frac{1}{2}\frac{\partial}{\partial y} <u'^2 - v'^2>$$

$$<u\omega> \;\approx\; U\Omega$$

$$\frac{\partial <\Gamma>}{\partial t} \;\approx\; \left[\; U\Omega \;\right]_{in} - \left[\; U\Omega \;\right]_{out} - \left[\int \nu \frac{d<\omega>}{dy} dx\right]_s$$

$$\approx \left[\; U\Omega \;\right]_{in} - \left[\; U\Omega \;\right]_{out}$$

— for separated flow except at L.E.

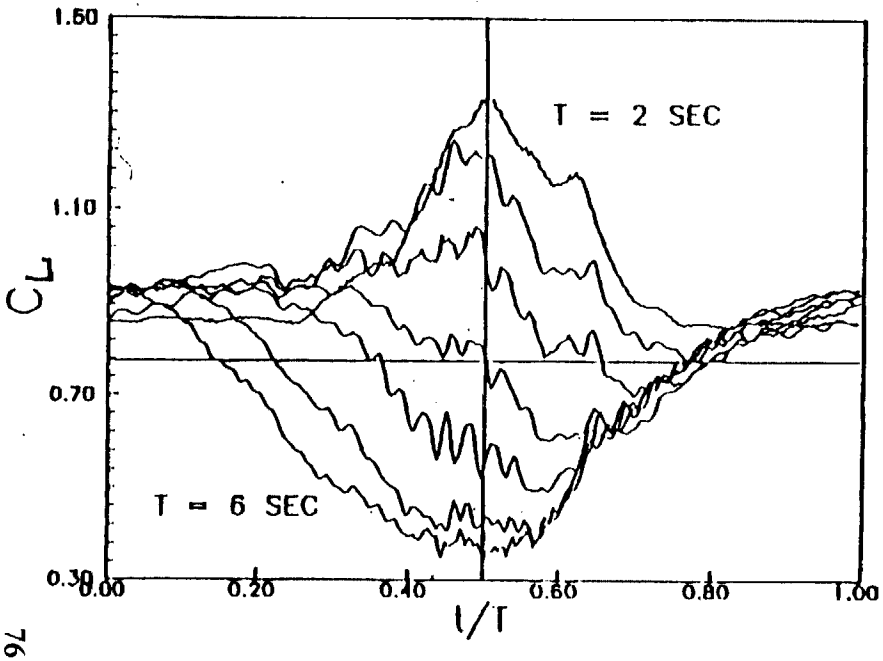

Two Time scales

- $[t_r]_{T=3} \sim [t_r]_{T=2}$
- $[U(t)]_{T=3} > [U(t)]_{T=2}$

$[t_c]_{T=3} < [t_c]_{T=2}$

$[\frac{t_c}{T}]_{T=3} << [\frac{t_c}{T}]_{T=2}$

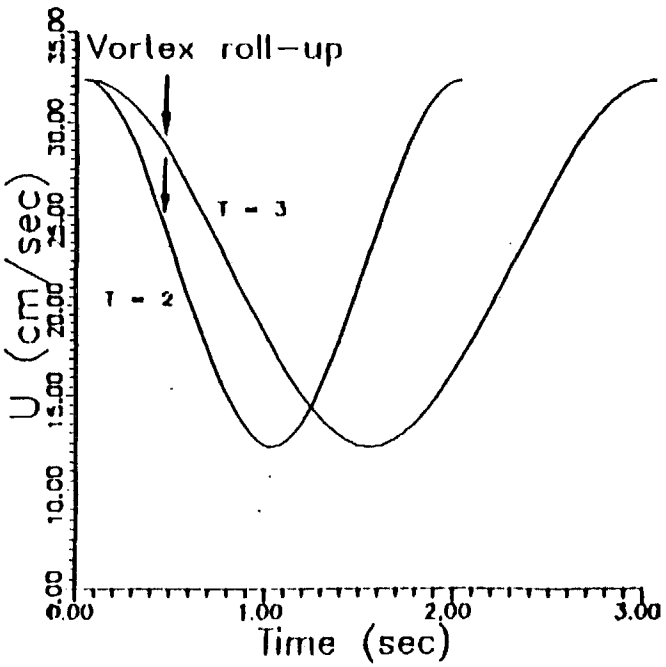

$$C_L = \frac{Lift}{\frac{1}{2}\rho U^2}$$

$U \downarrow$

$C_L \uparrow$

CONCLUSIONS

- Unsteady Separation
  - $\frac{\partial u}{\partial y} = 0 \quad y = \infty$

    Local shear layer $\longrightarrow$ separation vortex

    $\frac{\partial u}{\partial y} = 0$ Near wall $\longleftarrow$ MRS criterion
  - Separation pattern $\longrightarrow$ 3-D
- Vorticity Balance of 2-D Wing
  - Attached flow

    vorticity diffusion

    single time scale
  - Separated flow

    vorticity convection

    multiple time scales
- Unsteady C_L of Post-Stall 2-D Wing
  - $K_{\text{optimum}} \approx 1$
  - $C_L > 10$
- Unsteady C_L of 3-D Wing
  - Attached L.E. Vortices

    single time scale
  - Convected L. E. vortices

    separated 2-D wing

CONTROL OF LEADING-EDGE VORTICES ON A DELTA WING[1]

by

C. Magness, O. Robinson, and D. Rockwell

I. INTRODUCTION

The unsteady flow structure of leading-edge vortices on a delta wing has been investigated using new types of experimental techniques, in order to provide insight into the consequences of various forms of active control. These investigations involve global control of the entire wing and local control applied at crucial locations on or adjacent to the wing. Transient control having long and short time-scales, relative to the convective time-scale C/U_∞, allows substantial modification of the unsteady and time-mean flow structure.

Global control at long time-scale involves pitching the wing at rates an order of magnitude lower than the convective time-scale C/U_∞, but at large amplitudes. The functional form of the pitching maneuver exerts a predominant influence on the trajectory of the feeding sheet, the instantaneous vorticity distribution, and the instantaneous location of vortex breakdown.

Global control at short time-scales of the order of the inherent frequency of the shear layer separating from the leading-edge and the natural frequency of vortex breakdown shows that "resonant" response of the excited shear layer-vortex breakdown system is attainable. The spectral content of the induced disturbance is preserved not only across the entire core of the vortex, but also along the axis of the vortex into the region of vortex breakdown. This unsteady modification results in time-mean alteration of the axial and swirl velocity fields and the location of vortex breakdown.

Localized control at long and short time-scales involves application of various transient forms of suction and blowing using small probes upstream and downstream of the location of vortex breakdown, as well as distributed suction and blowing along the leading-edge of the wing applied in a direction tangential to the feeding sheet. These local control techniques can result in substantial alteration of the location of vortex breakdown; in some cases, it is possible to accomplish this without net mass addition to the flow field.

II. EXPERIMENTAL TECHNIQUES

The unsteady flow structure from the leading-edge of a delta wing subjected to various forms of active control has been characterized using new types of laser-diagnostic systems and image-processing techniques. These methods are integrated with active control systems, driven by central microcomputers. Using these approaches, it is possible to impose active control of arbitrary functional form and examine the response of the instantaneous flow structure. The two- and three-dimensional flow structure is interpreted with the aid of newly-released graphics supercomputers.

III. GLOBAL CONTROL AT LONG TIME SCALES

The concept of a phase shift between the unsteady motion of the wing and the development of the leading-edge vortex is well known. In qualitative visualization studies, Lambourne et al. (1969), Gad-el-Hak and Ho (1985a,b, 1986), and Atta and Rockwell (1989) reveal various features of the visualized cross-section of the vortex during its unsteady

[1]Submitted for presentation at the NASA/AFOSR/ARO Workshop on Physics of Forced Separation, April 17-19, 1990.

development. There also occurs a phase shift of the location of vortex breakdown relative to the wing motion; it has been characterized from various perspectives by Woffelt (1986), Rockwell et al. (1987), Atta and Rockwell (1987), Reynolds and Abtahi (1987), Gilliam, Robinson, Walker, Wisser (1987), and Lemay, Batill, and Nelson (1988).

The following unresolved issues are the focus of this investigation: the effect of arbitrary forms of pitching maneuver on the instantaneous structure of the leading-edge vortex including trajectories of feeding sheets and distributions of vorticity; the influence of vortex breakdown over a portion of the cross-section of the vortex; and the response of the axial location of vortex breakdown in relation to all of these features.

Concerning the nature of the instantaneous structure of the leading-edge vortices, obtained from particle tracking techniques, the following represent the major findings:

(i) For locations upsteam of vortex breakdown, the shape, degree of concentration, and the location of the maxima of the instantaneous vorticity distribution across the vortex core are quite different for the up- and downstrokes of the continuous pitch-up-down maneuvers of the wing. This finding emphasizes the importance of accounting for the instantaneous cross-sectional structure of the vortex, and not simply the instantaneous location of vortex breakdown, in determining the overall loading on the wing.

(ii) Comparison of the vorticity distribution of the leading-edge vortex with the trajectory of the feeding sheet from the edge of the wing shows the relationship between the possible trajectories of the feeding sheet and the corresponding vorticity field. A major factor is the occurrence or non-occurrence of vortex breakdown within the core of the vortex.

Figure 1 shows an excerpt from the current investigation. Contours of constant vorticity were obtained by direct particle tracking and image processing techniques. The experimental parameters correspond to a pitching motion of $15^\circ \leq \alpha \leq 40^\circ$ for a continuous pitch-up-down motion at a pitching rate $\dot{\alpha}C/2U_\infty = 0.15$. The surface of the wing is indicated by the bold horizontal line. The contours of constant vorticity on the left side correspond to the pitch-up portion of the maneuver, and those on the right side to the pitch-down portion. The differences in elevation, orientation, and scale of the vorticity distributions are evident. They are dependent upon the history of the wing motion and appear to be most pronounced at the smallest angle of attack $\alpha = 20^\circ$.

The importance of accounting for vortex breakdown within the core of the vortex is illustrated in Figure 2. Instantaneous positions of the feeding sheets and contours of constant vorticity are shown for the same parameters as in Figure 2, but at $\alpha = 40^\circ$ for two different types of maneuvers. The shaded black region represents the extent of breakdown within the vortex. For the simple pitch-down motion, $\alpha = 40^\circ$ represents the static condition immediately preceding the onset of the maneuver, while the pitch-up-down case at $\alpha = 40^\circ$ includes the integrated history of the upstroke portion of the maneuver. It is evident that the positions of the feeding sheet and the contours of vorticity are substantially different for these two cases.

The structure of the leading-edge vortex at a given cross-section must, of course, be considered in conjunction with the axial movements of the location of vortex breakdown. Magness, Robinson, and Rockwell (1989) preliminarily addressed the effect of the type of pitching maneuver on the general response of the vortex breakdown location as a function of angle of attack. Recent studies have focussed on the vortex response to different classes of maneuver, and the detailed structure of the leading-edge vortices. Regarding the response of the location of the vortex breakdown, the major findings are:

(i) Continuous pitch up-down motions of the wing can preclude occurrence of vortex breakdown on the upstream portion of the wing, relative to that occurring for simple pitch-up and pitch-down motion where relaxation processes having long time scales are allowed to occur.

(ii) For the continuous pitch-up-down maneuver of the wing, the consequence of not allowing the vortex breakdown to relax to its equilibrium state is to produce upstream movements of the vortex breakdown location towards the apex for initial decreases in angle of attack α.

(iii) Combinations of simple ramp-type motions to form a hybrid pitching motion produce overshoots of the static characteristic of vortex breakdown location versus angle of attack, beyond that attainable with any of the simple ramp motions alone.

Figure 3 shows plots characterizing the first two of these three principal findings at two extreme values of reduced frequency. This sort of characterization of the breakdown location serves as a basis for detailed investigations of the flow structure of the leading-edge vortices.

IV. GLOBAL CONTROL AT SHORT TIME SCALES

Perturbation of a delta wing in the pitching mode at sufficiently high frequency and very low amplitude allows control of the detailed flow structure of the leading-edge vortex. In essence, the vortex development and breakdown on a delta wing involves two classes of characteristic frequencies: the inherent instability frequency of the shear layer from the leading-edge; and the frequency at which vortex breakdown occurs. The major issues here are: the structure of the perturbed feeding sheet; the nature of the perturbed onset of vortex breakdown; and the corresponding alteration of the time-mean vortex flow.

Simple considerations of hydrodynamic instability show that the processes of disturbance amplification in the shear layer and in the vortex core during the breakdown process are receptive to a wide range of excitation frequencies. As a consequence, it is possible to attain "resonant" excitation, leading to large alteration of the separating shear layer from the edge of the wing and the breakdown of the vortex core. The preliminary phase of this investigation was reported by Rockwell et al. (1987). This work is described in its completed form by Kuo, Magness, and Rockwell (1989).

The principal findings of this investigation are, in short:

(i) Small amplitude perturbations of the leading-edge lead to substantial alteration of the structure of the shear layer separating from it without occurrence of the classical mechanism of small-scale vortex coalescence.

(ii) The spectral content of the disturbance induced in the shear layer separating from the leading-edge is preserved not only across the core of the vortex, but also along the streamwise extent of the core into the region of vortex breakdown.

(iii) Substantial alteration of the time-mean characteristics of the leading-edge vortex include changes in the axial and swirl velocity fields and modification of the location of vortex breakdown.

Selected excerpts describing certain of the foregoing phenomena are given in Figures 4 through 6. Figure 4 shows the visualization obtained by locating a vertical hydrogen bubble wire along the leading-edge of the wing. The laser sheet that illuminated the marker bubbles was translated to the downstream locations x/C indicated in the photos. Excitation frequency

f_e is normalized with respect to the inherent instability frequency f_i of the shear layer separating from the leading-edge. Large-scale vortical structures are induced over the cross-section of the vortex in the presence of excitation at the inherent instability frequency of the feeding sheet. No small-scale vortex coalescence occurs.

Figure 5 shows spectra of the streamwise component $\tilde{u}$, i.e. $S_{\tilde{u}}$, taken at various locations upstream and downstream of the onset of vortex breakdown. The edge excitation frequency f_e is normalized by the inherent vortex breakdown frequency f_b. For excitation at the first harmonic of the vortex breakdown frequency, i.e. at $f_e/f_b = 2$, the spectral content shows predominance of the excitation frequency and its associated higher harmonics in regions before and after occurrence of vortex breakdown. In this case, the higher harmonic content persists well downstream of the onset of breakdown. For excitation at $f_e/f_b = 1$, there also occur a large number of higher harmonics due to the strong nonlinearity of the shear layer response. This spectral content is maintained over the entire cross-section of the vortex core prior to the occurence of breakdown, emphasizing the nonoccurence of vortex-vortex interactions (i.e. coalescence) in the shear layer as it is wrapped inwards toward the center of the core. Downstream of vortex breakdown, the predominant excitation peak at $f_e/f_b = 1$ persists, but the coherent higher harmonic components are attenuated.

Figure 6 shows contours of constant mean axial velocity $\bar{u}$ and constant fluctuating velocity $\tilde{u}$ over the entire cross-section of the leading-edge vortex at values of excitation frequency f_e, relative to the inherent vortex breakdown frequency f_b, i.e. $f_e/f_b = 1$ (left column) and 2 (right column). The effect of the matched excitation at $f_e/f_b = 1$ is to induce large amplitude fluctuations in the separating shear layer surrounding the core of the vortex, located at the peak of the contours of constant $\bar{u}$ and designated by the symbol +. At $f_e/f_b = 2$, the location of the core of the vortex moves downward towards the surface of the wing and outward towards the leading-edge. The maximum amplitude of the fluctuation $\tilde{u}$ is coincident with the location of the core of the vortex. This coincidence of the maxima of $\bar{u}$ and $\tilde{u}$ corresponds to the early onset of vortex breakdown at the higher excitation frequency $f_e/f_b = 2$.

V. LOCAL CONTROL AT MODERATE AND LONG TIME SCALES

Local control involves localized injection or suction of the flow at defined locations in the flow field and/or the surface of the wing. In a practical sense, this can be achieved by use of small probes, whose tips are located at crucial locations in the vortex core, or slits along the leading-edge of the wing. In essence, these techniques simulate localized point sources/sinks or distributions of them. The major issues here are: determination of the most sensitive location of the applied control; and optimization of the functional form of the unsteady control in the form of blowing/suction.

For the case of localized blowing along the leading-edge of the wing, Wisser, Iwanski, Nielson, and Ng (1988) most recently have revealed an increase in length of the vortex core prior to breakdown and an increase in lift acting on the wing. Not until this past year has the case of localized suction been explored; such simulations of a localized sink are described by Parmenter and Rockwell (1989). Location of a probe in the region downstream of vortex breakdown allows efficient restabilization of the vortex core. Among the principal findings are:

(i) Locations of the simulated point sink downstream of the occurrence of vortex breakdown produces stabilization of the core; such stabilization is attainable at relatively low values of dimensionless suction coefficient C_μ. The transient response time of the stabilization process due to an imposed transient (unsteady sink flow) scales as the magnitude of the imposed transient suction.

(ii) Hysteresis effects occur due to relaxation of the vortex breakdown (on a stationary wing) after abrupt onset or cessation of suction. These hysteresis effects simulate those on a pitching delta wing.

Localized control involving simulations of distributed sources/sinks in the form of a blowing/suction slit along the leading-edge have received little attention except for the steady blowing experiments of Wood and Roberts (1987), Wood, Roberts and Lee (1987) and Roberts, Hesselink, Kroo, and Woods (1987), and the (high frequency) sinusoidal perturbations employed in the investigation of Gad-el-Hak and Blackwelder (1987). The consequences of this type of control on the structure of the large-scale vortex have remained unexplored. Moreover, the possible modification of the nature and location of onset of vortex breakdown has not been pursued. Important considerations in our recent investigations include not only the case of steady blowing, but also the corresponding case of steady suction and, most significantly, the case of cyclic blowing and suction. The major findings of this investigation are:

(i) Both steady suction and steady blowing are effective at low values of C_μ, i.e. both result in lengthening of the vortex core prior to the onset of breakdown.

(ii) The most effective and robust control involves cyclic suction and blowing at an appropriate frequency. This approach involves no net mass addition to or from the flow.

The use of cyclic blowing and suction applied tangentially in the form of a jet $V_j(t)$ at the rounded leading-edge is represented in Figure 7; it is compared with the case of no blowing/suction, i.e. $V_j(t) = 0$. (These data were acquired by Professor W. Gu, a member of our research group.) Comparison of these velocity fields of Figure 7 suggests that application of the control results in restabilization of the vortex from a stalled condition to a well-defined, large-scale vortical structure and downward deflection of the separation streamline from its approximately horizontal position. These trends are associated with downstream movement of the location of vortex breakdown.

VI. ACKNOWLEDGEMENTS

The authors gratefully acknowledge support of the Air Force Office of Scientific Research, as part of a program monitored by Captain H. Helin.

VII. LIST OF REFERENCES

Atta, R. and Rockwell, D. 1987 "Hysteresis of Vortex Development and Breakdown on an Oscillating Delta Wing", *AIAA Journal*, Vol. 25, No. 11, pp. 1512-1513.

Atta, R. and Rockwell, D. 1989 "Leading-Edge Vortices Due to Low Reynolds Number Flow Past a Pitching Delta Wing", *AIAA Journal* (in press).

Gad-el-Hak, M. and Blackwelder, R. F. 1987 "Control of the Discrete Vortices from a Delta Wing", *AIAA Journal*, Vol. 25, No. 8, pp. 1042-1049.

Gad-el-Hak, M. and Ho, C.-M. 1985a "The Pitching Delta Wing", *AIAA Journal*, Vol. 23, No. 11, pp. 1660-1665.

Gad-el-Hak, M. and Ho, C.-M. 1985b "Three-Dimensional Effects on a Pitching Lifting Surface", AIAA Paper No. 85-0041, presented at the AIAA 23rd Aerospace Sciences Meeting, January 14-17, Reno, Nevada.

Gad-el-Hak, M. and Ho, C.-M. 1986 "Unsteady Vortical Flow Around Three-Dimensional Lifting Surfaces", *AIAA Journal*, Vol. 24, No. 5, May, pp. 713-721.

Gilliam, F., Robinson, N., Walker, J., and Wissler, J. 1987 "Visualization of Unsteady Separated Flow About a Pitching Delta Wing", AIAA 25th Aerospace Sciences Meeting, January 12-15, Reno, Nevada.

Kuo, C.-H., Magness, C., and Rockwell, D. 1989 "Control of Vortex Structure on a Delta Wing by Small-Amplitude Perturbations of Angle-of-Attack", submitted for publication.

Lambourne, N. C., Bryer, D. W., and Maybrey, J. F. N. 1969 "The Behavior of Leading-Edge Vortices Over a Delta Wing Following Sudden Change of Incidence", The Aeronautical Research Council Technical Report, Report and Memorandum 3645.

LeMay, S. P., Batill, S. M., and Nelson, R. C. 1988 "Leading-Edge Vortex Dynamics on a Pitching Delta Wing", AIAA Paper No. AIAA-88-2559-CP, AIAA Sixth Applied Aerodynamics Conference, June 6-8, Williamsburg, Virginia.

Magness, C., Robinson, O., and Rockwell, D. 1989 "Control of Leading-Edge Vortices on a Delta Wing", AIAA Paper No. 89-0999, presented at AIAA 2nd Shear Flow Conference, March 13-16, Tempe, Arizona.

Parmenter, K. and Rockwell, D. 1989 "Response of Leading-Edge Vortices to Localized Suction", *AIAA Journal* (in press).

Reynolds, G. A. and Abtahi, A. A. 1987 "Instabilities in Leading-Edge Vortex Development", AIAA Paper No. 87-2424, AIAA Applied Aerodynamics and Atmospheric Flight Dynamics Conference, August 17-19, Monterey, California.

Roberts, L., Hesselink, L., Kroo, I., and Wood, N. 1987 "The Control of Vortical Flows Over a Delta Wing", Proceedings of Workshop on Unsteady Separated Flows at U. S. Air Force Academy. Also see Frank J. Seiler Research Laboratory Report FJSRL-TR-88-0004, September 1988, Air Force Systems Command, United States Air Force.

Rockwell, D., Atta, R., Kuo, C.-H., Hefele, C., Magness, C., and Utsch, T. 1987 "On Unsteady Flow Structure from Swept Edges Subjected to Controlled Motion", Proceedings of Workshop on Unsteady Separated Flows at U. S. Air Force Academy. Also see Frank J. Seiler Research Laboratory Report FJSRL-TR-88-0004, September 1988, Air Force Systems Command, United States Air Force.

Wisser, K., Iwanski, K. T., Nelson, R. C. and Ng, T. T. 1988 "Control of Leading-Edge Vortex Breakdown by Blowing", AIAA Paper No. 88-0504, AIAA 26th Aerospace Sciences Meeting, January, Reno, Nevada.

Wolffelt, K. W. 1986 "Investigation on the Movement of Vortex Burst Position with Dynamically Changing Angle of Attack for a Schematic Delta Wing in a Water Tunnel with Correlation to Similar Studies in Wind Tunnel", AGARD Conference Proceedings #413, Aerodynamic and Related Hydrodynamic Studies Using Water Facilities, Symposium of the Fluid Dynamics Panel, Monterey, California, 20-23 October, 1986.

Wood, N. J. and Roberts, L. 1987 "The Control of Vortical Lift on Delta Wings by Tangential Leading-Edge Blowing", AIAA Paper 87-0158, January.

Wood, N. J., Roberts, L., and Lee, K. T. 1987 "The Control of Vortical Flow on a Delta Wing at High Angles of Attack", AIAA Paper 87-2278, August.

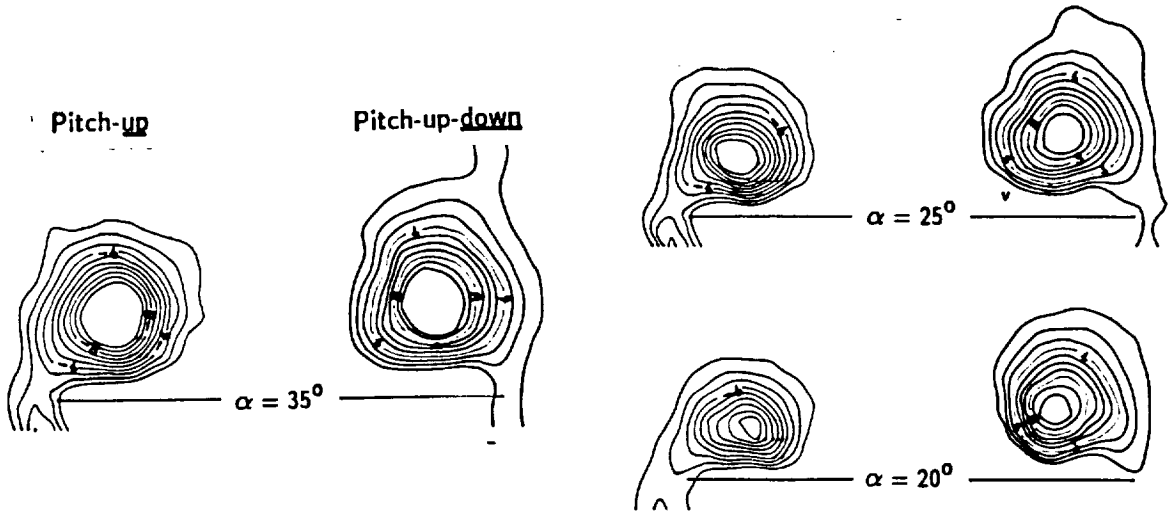

Figure 1: Instantaneous contours of constant vorticity at midchord for continuous pitch-up-down maneuver of delta wing. Sweep angle = 75°; pitch rate $\dot{\alpha}C/2U = 0.15$; pitching axis at midchord.

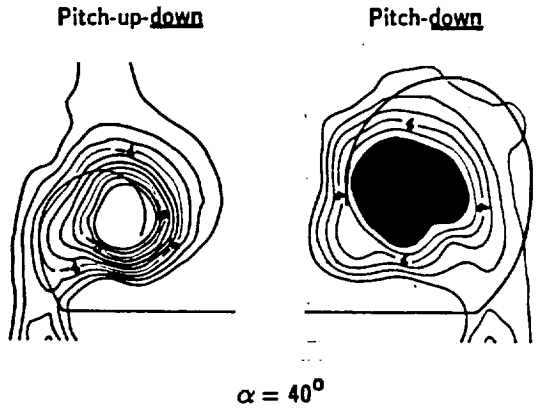

Figure 2: Instantaneous contours of constant vorticity and positions of feeding sheet at $\alpha = 40°$ for continuous pitch-up-down and pitch-down maneuvers. Sweep angle = 75°; pitch rate $\dot{\alpha}C/2U = 0.5$; pitching axis at midchord.

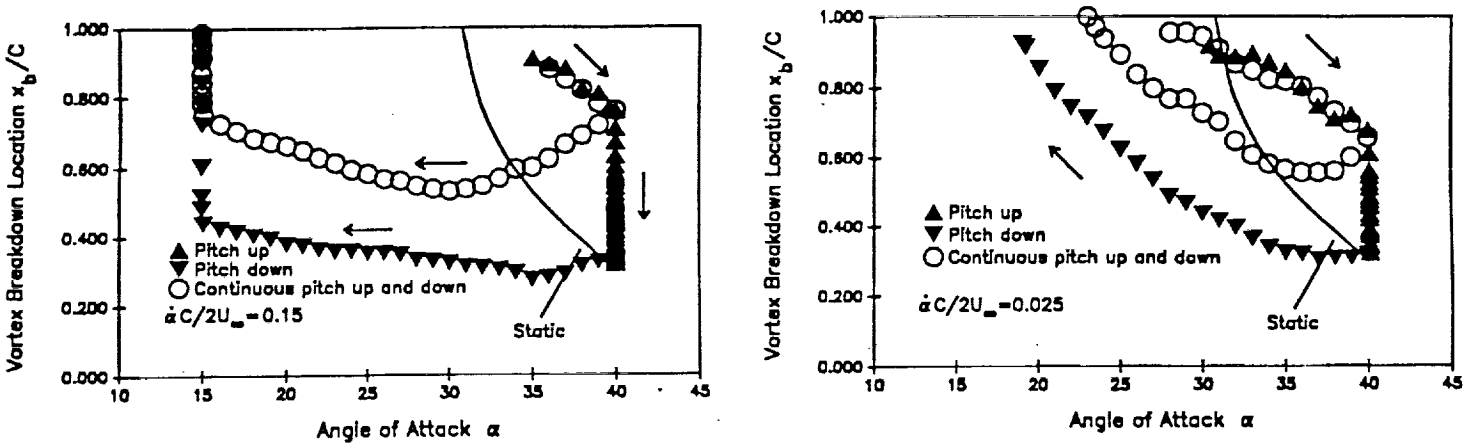

Figure 3: Instantaneous location of vortex breakdown as function of angle of attack for three basic types of delta wing maneuvers and two extreme values of dimensionless pitching rate. Sweep angle of delta wing = 75°.

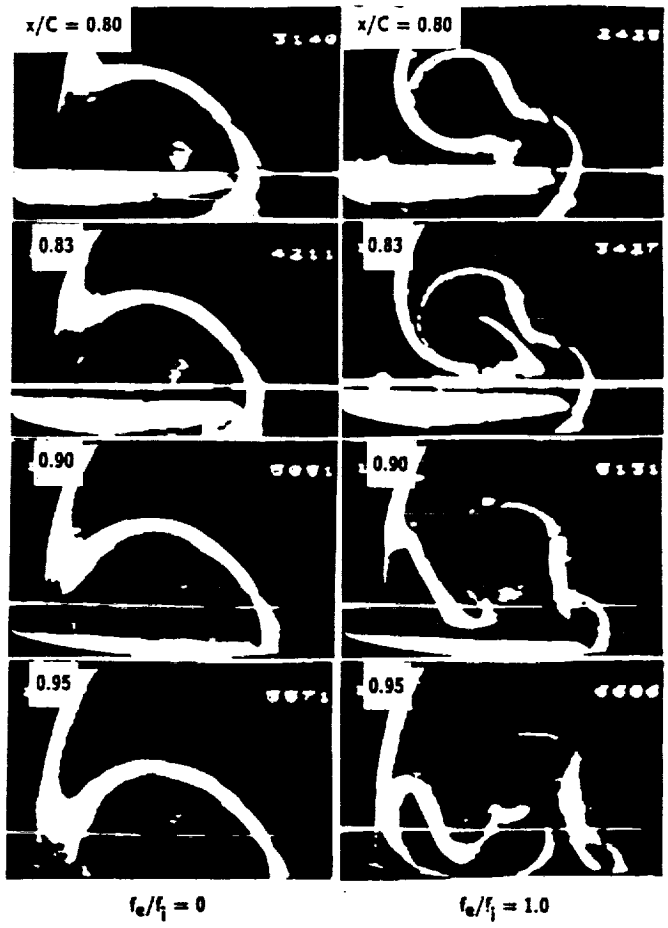

Figure 4: Visualization of flow structure of separating shear layer at several cross-sections along leading-edge of delta wing. Ratio of excitation frequency f_e to inherent instability frequency f_i of separating shear layer is: 0 (left column); 0.5 (middle column); and 1.0 (right column). Angle of attack $\alpha = \bar{\alpha} + \alpha_0 \sin 2\pi f_e t$; $\bar{\alpha} = 20°$, $\alpha_0 = 1°$.

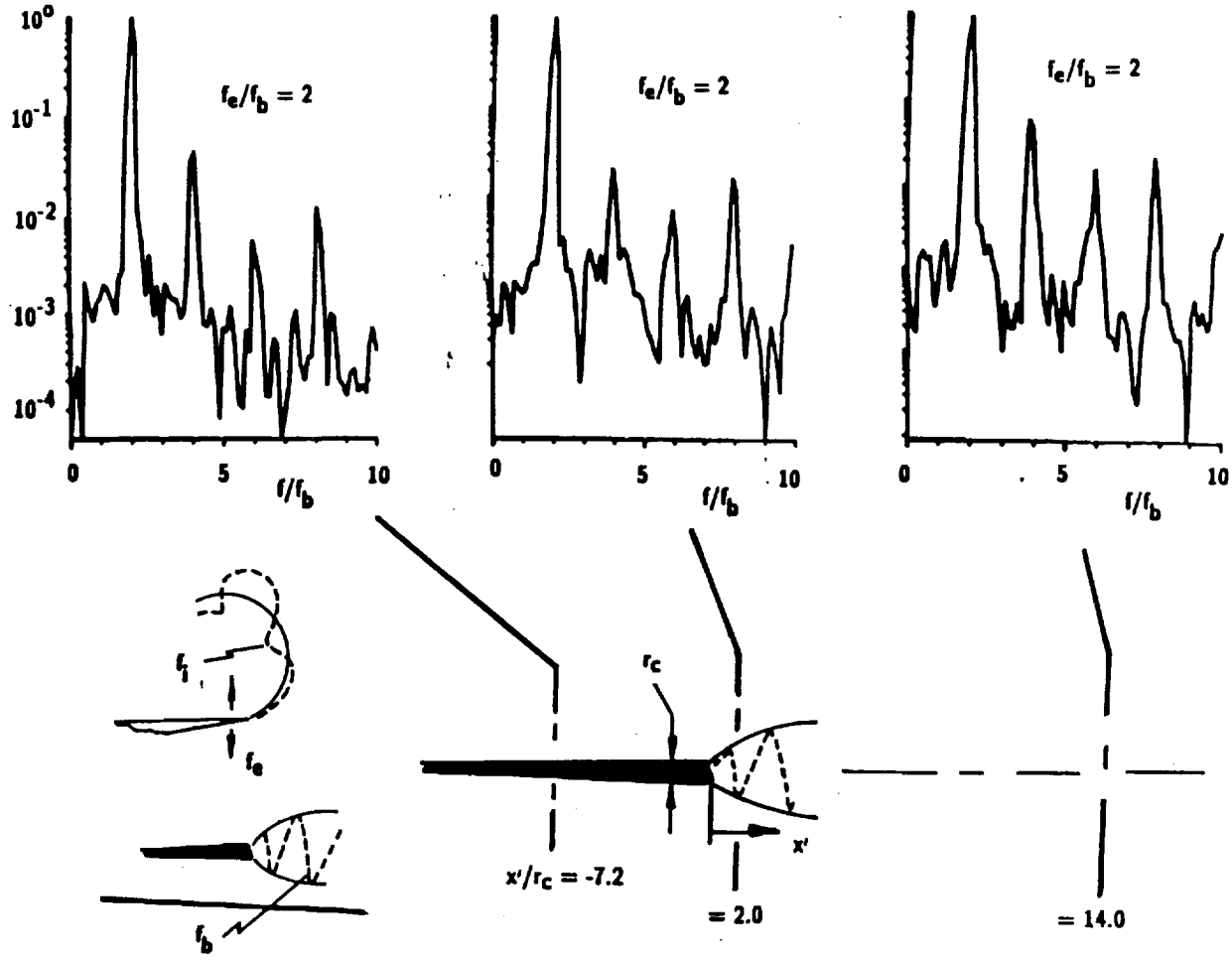

Figure 5: Overview of evolution of spectral content of vortex core upstream and downstream of vortex breakdown. Ratio of excitation frequency f_e to vortex breakdown frequency f_b has values indicated. $f_i/f_b = 2$.

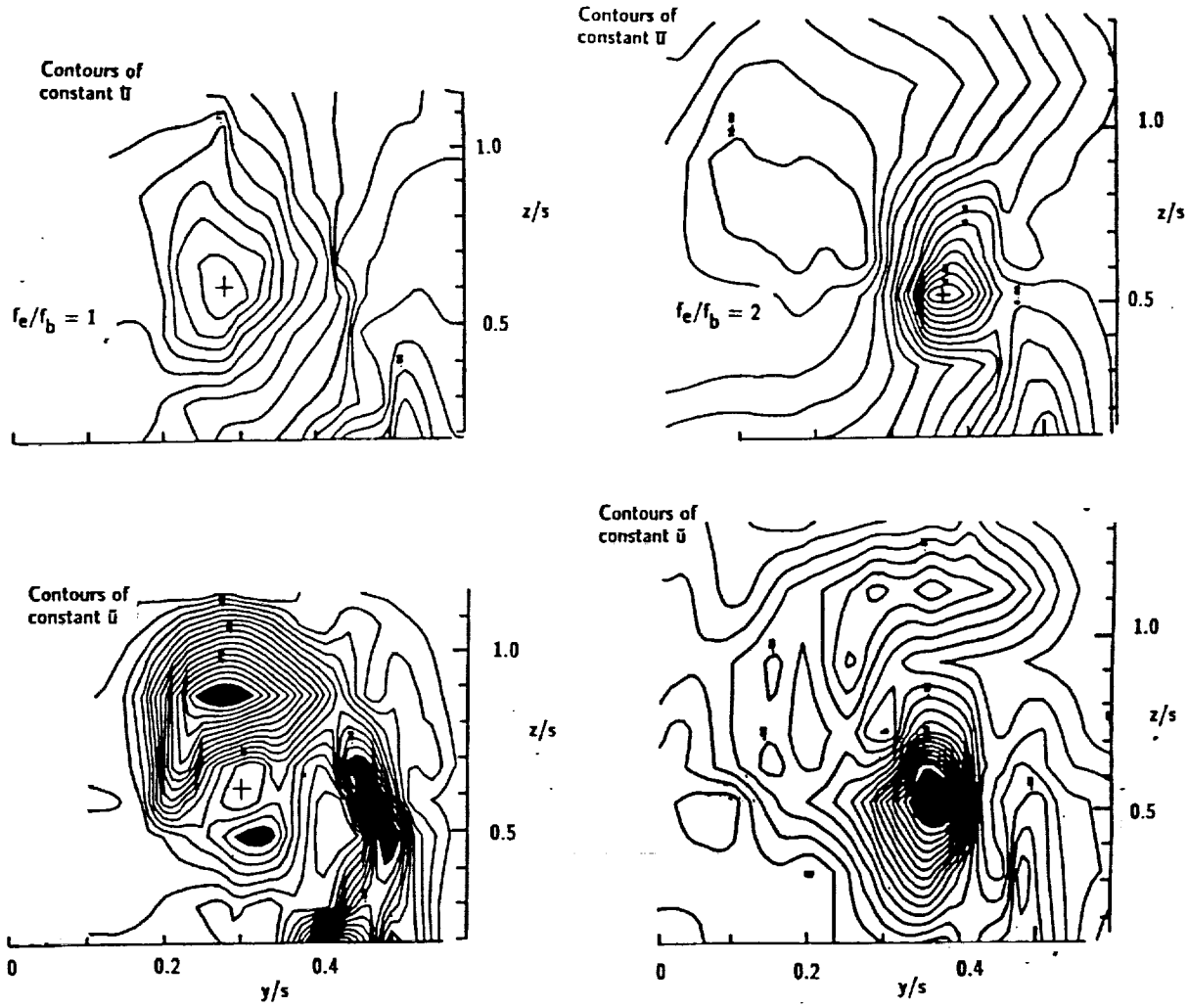

Figure 6: Distribution of mean $\bar{u}$ component of axial velocity over cross-section of vortex upstream of occurrence of vortex breakdown. Data acquired at reference station x/C = 0.38 upstream of vortex breakdown. Ratio of excitation frequency f_e to frequency f_b of inherent vortex breakdown is $f_e/f_b = 1$ (left column) and $f_e/f_b = 2$ (right column). Ratio of inherent instability frequency f_i of separating shear layer to frequency f_b is $f_i/f_b = 2$.

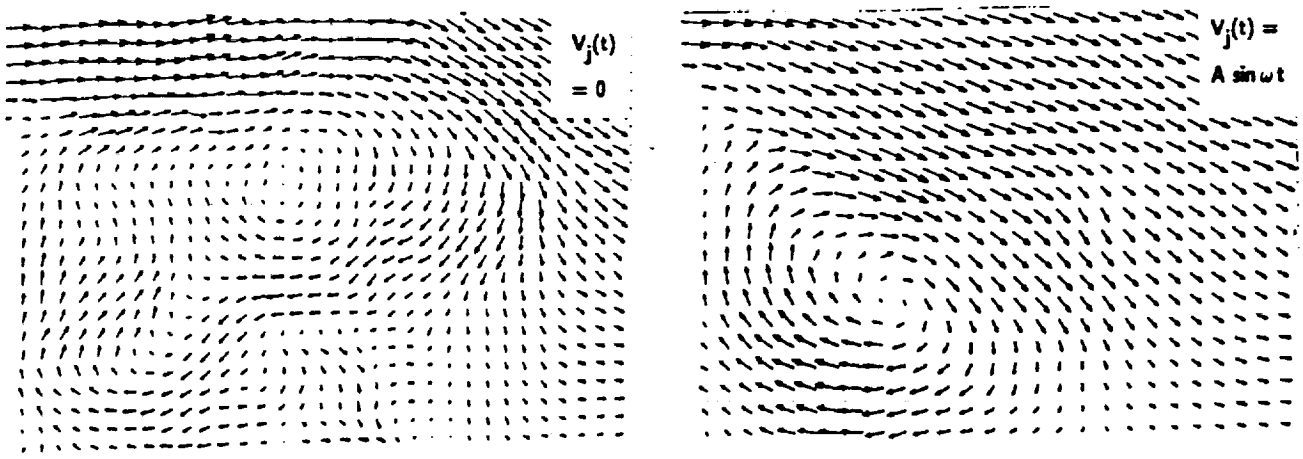

Figure 7: Comparison of velocity fields over cross-section of half delta wing at $\alpha = 45^\circ$ for cases with and without sinusoidal suction/blowing applied tangentially at rounded leading-edge. Laser sheet defining cross-section of visualized vortex located at approximately one-third chord.

OVERVIEW

- Concepts of Control: Time-Scales and Vorticity Budgets
- Experimental Approaches
- Global Control at Small Time-Scales
  $tU/C << 1$
- Global Control at Large Time-Scales
  $tU/C >> 1$
- Local Control at Moderate Time-Scales
  $tU/C \sim 1$

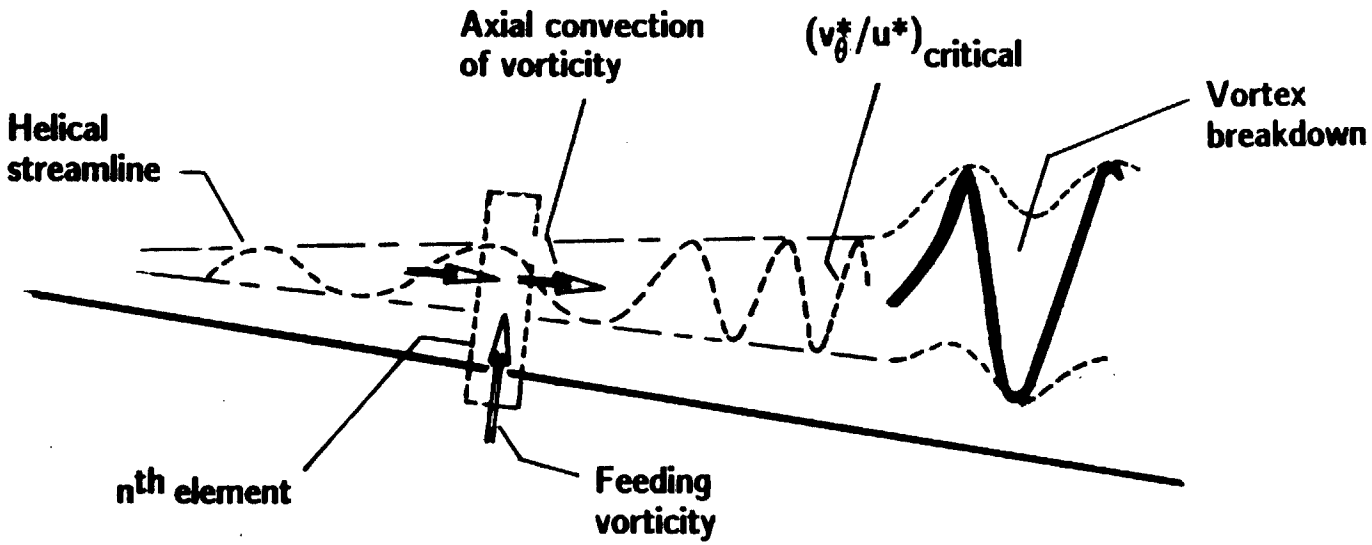
Axial convection
of vorticity
$(v_\theta^*/u^*)_{critical}$
Vortex
breakdown
Helical
streamline
n^{th} element
Feeding
vorticity

SEPARATION/SEPARATED PHENOMENA	PRINCIPAL MECHANISMS
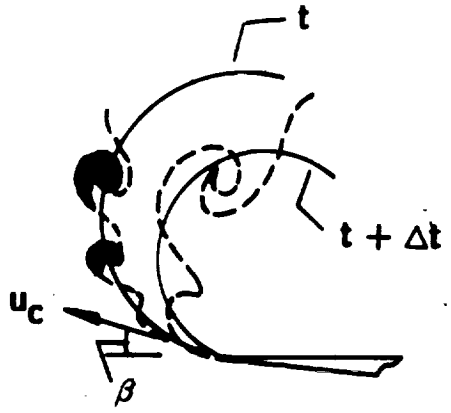	Alteration of unsteady concentrations of vorticity of feeding sheet 10^{-2} C/U and C/U
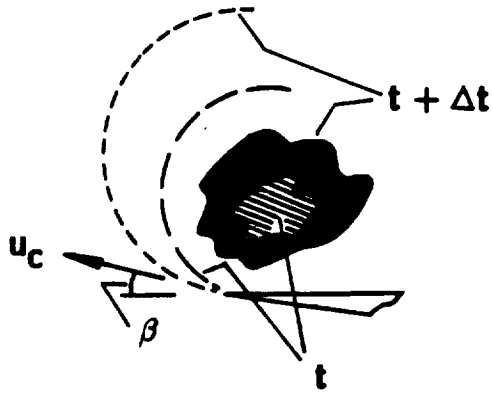	Alteration of axial convection of vorticity due to vortex breakdown 10 to 10^2 C/U

SEPARATION/SEPARATED PHENOMENA	PRINCIPAL MECHANISMS
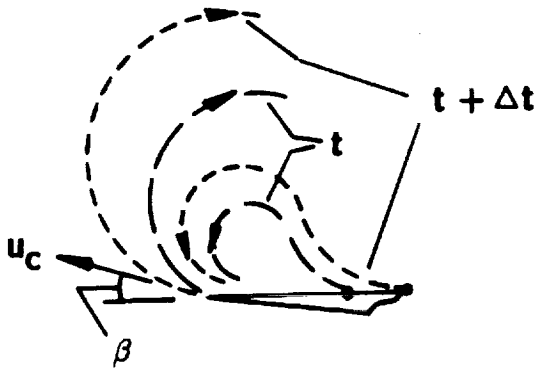	Formation of vortex fed by vorticity from leeward surface C/U
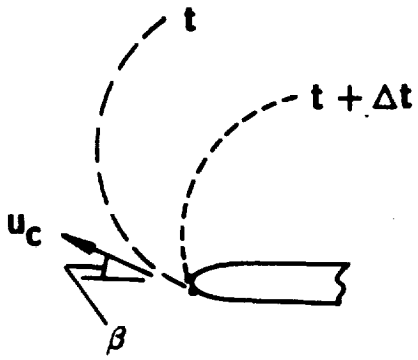	Movement of separation point of vorticity feeding sheet C/U

EXPERIMENTAL APPROACHES

- Quantitative Flow Visualization: Global Velocity Measurements
  - ✓ Bubble Marker Tracking
  - ✓ Particle Tracking
  - ✓ Particle Imaging
- Quantitative Flow Visualization: Construction of Two- and Three-Dimensional Images
- Local Velocity Measurement: Laser-Doppler Anemometry
- Force and Pressure Measurements

EXPERIMENTAL APPROACHES

- Integrated Active Control
  - ✓ Centralized Computer Control of
    - ▫ Wing Motion (Global); Blowing/Suction (Local)
    - ▫ Laser Firing
    - ▫ Image Shifting System
    - ▫ Camera(s)
    - ▫ Data Acquisition Systems
  - ✓ Arbitrary Functional Forms of Global and Active Control

GLOBAL CONTROL AT SMALL TIME SCALES
$tU/C << 1$

- Forced Instability and Concentration of Vorticity in Feeding Sheet
- Resonant Interaction of Instabilities of Feeding Sheet and Vortex Breakdown
- Preservation of Spectral Content Throughout Leading-Edge Vortex
- Modification of Time-Mean Axial and Swirl Velocity Components

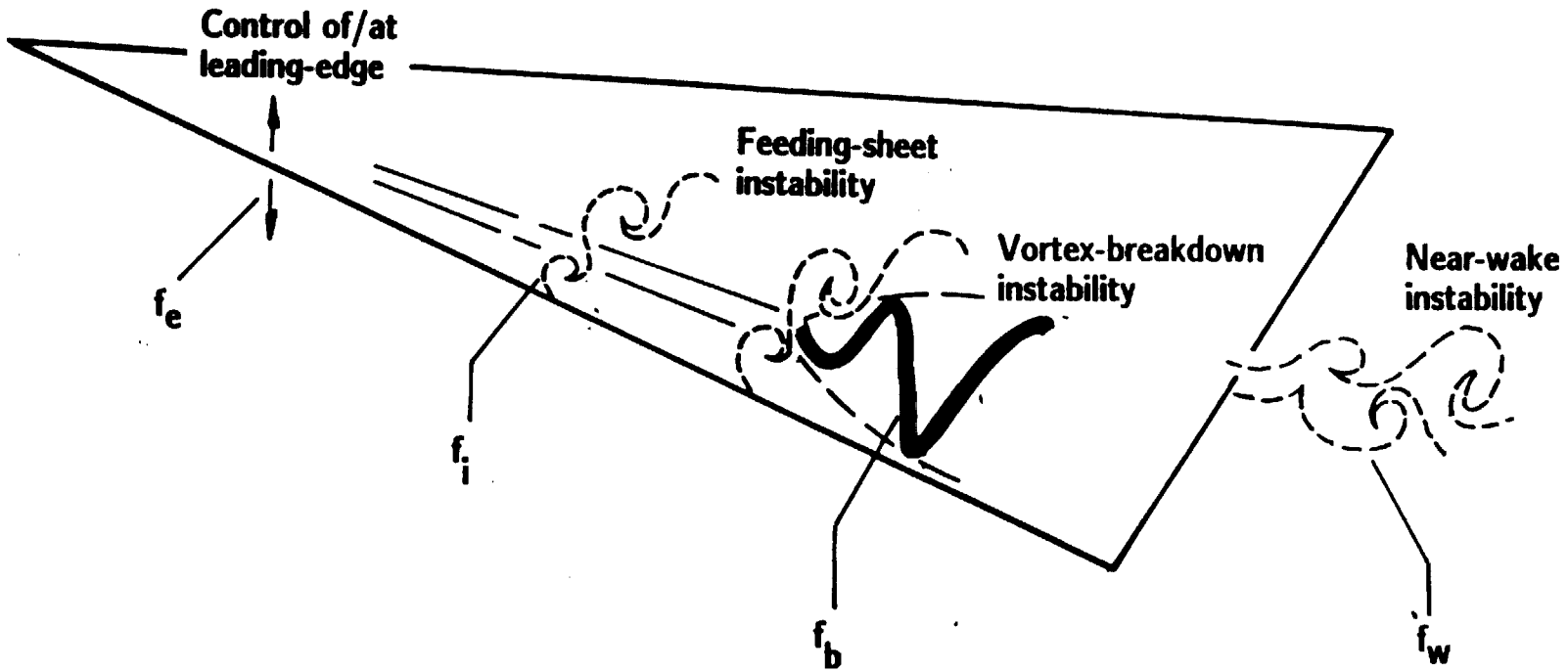
Control of/at
leading-edge
Feeding-sheet
instability
Vortex-breakdown
instability
Near-wake
instability
f_e
f_i
f_b
f_w

GLOBAL CONTROL AT MODERATE AND LARGE TIME SCALES
$tU/C \sim 1$ or $>> 1$

- Response of Leading-Edge Vortex in Absence of Vortex Breakdown: Sensitivity to Integrated History of Motion
- Response of Leading-Edge Vortex in Presence of Vortex Breakdown: Nonlinear Coupling of Feeding Sheet-Vortex Breakdown-Stall Zone
- Response of Vortex Breakdown: Sensitivity to Class of Forcing
- Response of Feeding Sheets and Vorticity Distributions with and without Vortex Breakdown: Sensitivity to Class of Forcing

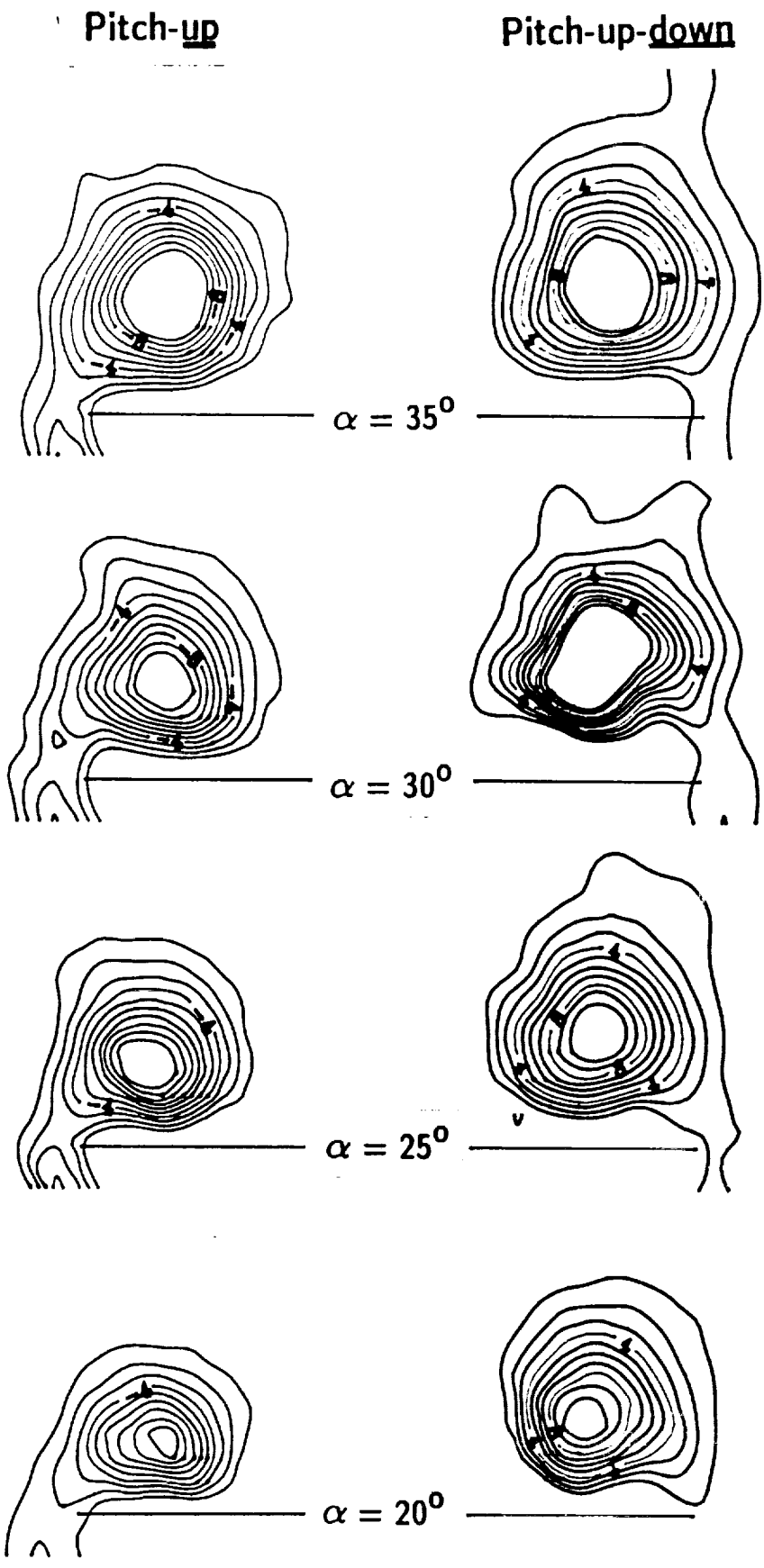
Pitch-up
Pitch-up-down
α = 35°
α = 30°
α = 25°
α = 20°

LOCAL CONTROL AT MODERATE TIME SCALES
$tU/C \sim 1$

- Response of Leading-Edge Vortex to Time-Dependent Variations of Leading-Edge Separation: Restabilization of Vortex Core
- Response of Leading-Edge Vortex: Structure in Cross-Flow Plane During Restabilization in Relation to Separation Conditions
- Response of Leading-Edge Vortex: Variations of Feeding Sheet and Vorticity Distributions of Restabilized Vortex

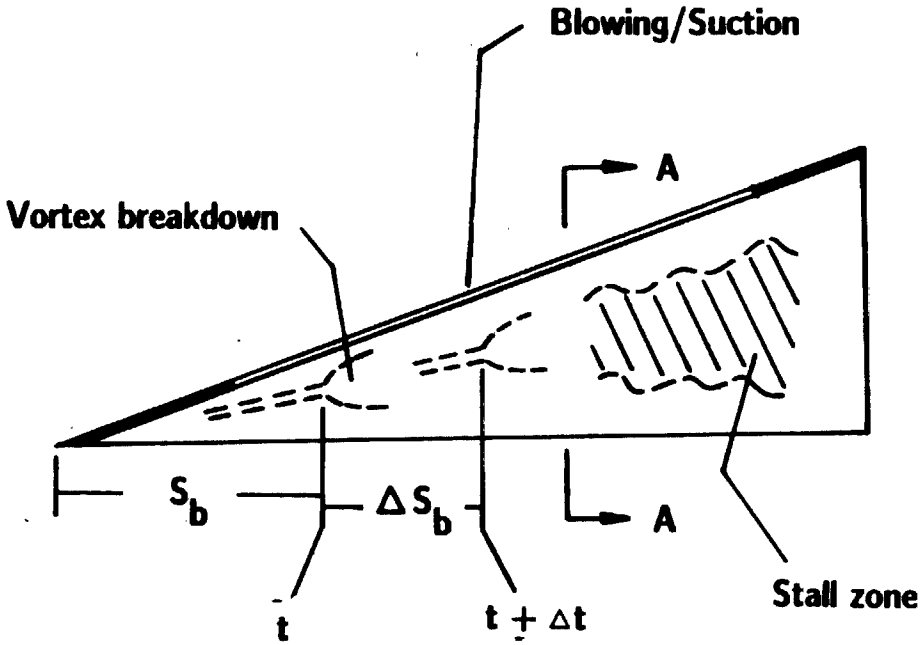
Blowing/Suction
A
Vortex breakdown
S_b
ΔS_b
A
t
t + Δt
Stall zone

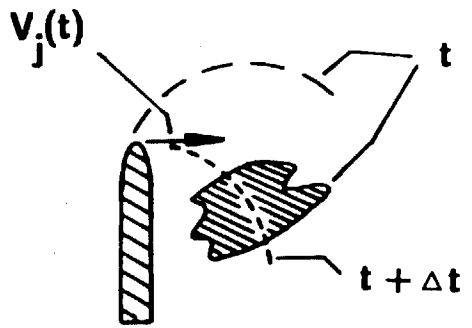
$V_j(t)$
t
t + Δt

The Unsteady Pressure Field and Vorticity Production at the Suction Surface of a Pitching Airfoil

Mukund Acharya* and Metwally H. Metwally**

Fluid Dynamics Research Center
Illinois Institute of Technology
3110 S. State Street, Chicago Il. 60616

Abstract of Paper for presentation at the
NASA/AFOSR/ARO Workshop on Physics of Forced Unsteady Separation
NASA Ames Research Center, April 17-19, 1990

Background The objective of this work is to develop techniques for the control and management of separated flows over airfoils, particularly under unsteady operating conditions. The results are expected to help achieve the ultimate goal, which is flow management for highly maneuverable aircraft.

The key requirements for successful management of unsteady separation over airfoils are: an understanding of the vorticity production and transport over the airfoil surface, the ability to identify the flow state reliably in real time, and the availability of optimal flow controllers that can be activated, when needed, to modify the flow state in the desired manner. In addition, there are issues that need to be resolved in order to achieve the successful integration of these components into an active feedback control system.

In an investigation of a generic, unsteady, separating flow, Ramiz and Acharya (1989a,b) examined the dynamics of formation of a separation zone, and showed that relatively simple techniques involving measurements of the wall static pressure may be used to obtain reliable indicators of flow state. In these experiments, an unsteady separation was introduced in a boundary layer by the motion of a separation generator (a spanwise flap) into the flow. The development of the flow was shown to be governed by a balance between two mechanisms; one responsible for the accumulation of vorticity at the flap, and the other for the detachment and downstream convection of the vorticity. Phase-

*Associate Professor

**Graduate Research Assistant

conditioned measurements of the time-varying flow direction at various locations downstream of the flap, and corresponding wall pressure data were used to track the separation as it developed. A number of possible criteria for flow-state identification, based on the unsteady wall-pressure measurements, were investigated, and two techniques were shown to have good promise. One of these is based on a comparison of the wall pressure signature with a preset threshold, while the other involves an examination of the time derivative of the pressure signal.

Unsteady flow over two-dimensional pitching airfoils The present paper addresses the issue of flow development over a pitching symmetric airfoil. An extensive body of work has been reported in recent years, describing experiments that examine the flow over airfoils undergoing prescribed pitching motions; in most cases these were sinusoidal oscillations about a mean angle of attack. The studies were largely motivated by the need to understand helicopter blade aerodynamics and, more recently, by interest in aircraft supermaneuverability. The bulk of these investigations focused their attention on obtaining an understanding of dynamic stall and the influence of parameters such as airfoil geometry, Reynolds number, oscillation amplitudes and rates. Although knowledge of this phenomenon has improved, (McCroskey (1982), Walker et al. (1985), Reynolds and Carr (1985), Robinson (1988)), some of the underlying mechanisms are not yet understood clearly. In addition, much needs to be done in order to develop effective means to *control* the unsteady separation. Specifically, one needs a clear understanding of the unsteady production of vorticity, its accumulation and detachment from the near-wall region. The establishment of a vorticity balance and a knowledge of the time scales of the evolutionary process are needed for an understanding of the process, and will be a prerequisite for the development of suitable control techniques.

Experiments and results We are carrying out experiments to understand this process in the flow over a NACA 0012 two-dimensional, symmetric airfoil undergoing a controlled pitching motion. The airfoil has a chord of 12 inches and a thickness 12% of chord. Measurements have been made over a Reynolds number range (based on chord) between 28,000 and 120,000. In the unsteady experiments, the airfoil was pitched up from an angle of 0 degrees to 40 degrees at constant velocity; that is, with a ramp-type time motion history. It was then held at this final angle. The non-dimensional pitch rate based on chord length was varied between 0.03 and 0.77.

A flow visualization study was first carried out to map the sequence of events that occur in the region around the leading edge and the suction surface during the pitch-up motion, from the initial fully attached flow condition to the occurrence of dynamic stall. Fig. 1 shows a sample of photographs from a sequence of smoke-wire flow visualization pictures, for a Reynolds number of 28,000 and a pitch rate of 0.154, taken at different instants during the motion of the airfoil. For reference, it is useful to know

that the static stall angle for these conditions is around 13 degrees. It is possible to identify a number of events in the unsteady process that culminates in the shedding of the dynamic stall vortex. During the initial stages of the pitch up, a zone of streakline distortion or reversal is seen close to the surface in the leading edge region. This zone grows along the chord, as seen in the photograph at 11 degrees, and extends all the way to the trailing edge as the airfoil motion progresses (at an angle of around 15 degrees in this instance). Simultaneously, fluid from the trailing edge region flows upstream along the surface of the airfoil, as seen in the photograph at 25 degrees. The behavior of the flow in these zones, the growth and interaction of the two zones, as well as a number of other events (which will be described in the full paper), were systematically examined over the range of parameters to produce maps such as the one shown in Fig. 2. Here, for example, Region I is bounded by two lines. The lower line is the locus of points at which the streakline reversal zone has extended over 12 % of the chord. Along the upper line, this zone has just reached the trailing edge. The upper edge of Region III is the locus of conditions at which the leading edge vortex is shed from the airfoil.

In another phase of the experiments, these events were examined for the signature that they imposed on the wall pressure distribution over the suction surface. The unsteady pressure variation was recorded at 22 locations along the surface during the pitch-up motion, for the same range of parameters. These data were then used to obtain chordwise pressure distributions over the suction surface at different instants during the motion. Fig. 3 shows a sample of these data, for three different pitch rates (0.036, 0.074 and 0.182), at an instant when the airfoil was at an angle of attack of 20 degrees; that is, halfway through its motion. The significantly different states of development of the flow in these cases is reflected in the difference in the pressure distributions. The pressure distribution at static conditions, for which the airfoil is fully stalled, is also shown for reference. The chordwise variation of pressure over the suction surface during the pitch-up motion is shown in Fig. 4 for two sets of conditions. Fig 4(a) shows the evolution of surface pressure for a pitch rate of 0.074 and a Reynolds number of 120,000; the data of Fig. 4(b) are for a pitch rate of 0.49 and a Reynolds number of 88,000. A detailed examination of data such as these yielded several interesting results. The two figures are representative of two classes of behavior, distinguished by low and high pitch rates. In each instance, a suction peak begins to form in a region near the leading edge. As the pitch-up motion continues, the magnitude of the peak increases and it moves much closer to the leading edge. At a later instant, a zone or 'plateau' of constant pressure is seen to develop at a location which is the position along the suction surface where the leading edge vortex ultimately forms and develops. Beynond this stage, the sequence of events is different for the two cases. At low pitch rates, the leading edge vortex remains bound to the surface only until such time as the pressure levels of the suction peak and the constant pressure 'plateau' are the same. It then grows in size and moves down the surface. At higher pitch rates, the vorticity is bound to the airfoil for a longer period. The constant pressure 'plateau' deforms

into a suction peak that characterizes the low pressure core of the leading edge vortex. Vorticity accumulates in this region for a longer period before the vortex grows and moves over the suction surface. The imprint of these events on the pressure evolution is seen clearly in the two figures.

The motion of the surface and the flow events within the viscous region over the suction surface are strongly coupled. The unsteady separation process and the related sequence of events discussed earlier are affected by the vorticity generated at the wall. The accompanying acceleration effects and change in the convective scales result in what Ericsson (1989) refers to as the moving-wall effect. It can be shown that for both steady and unsteady flows, the flux of vorticity *from the surface* is proportional to the instantaneous free-stream pressure gradient. Figs. 5(a) and 5(b) show the variation of wall vorticity flux from the suction surface during the pitch-up motion for the conditions of Figs 4(a) and 4(b) respectively. It is seen that the vorticity flux is confined primarily to the forward portions of the suction surface, and that during the initial phase of the motion this flux is negative in a region very close to the leading edge. The progression of certain significant events such as these, seen in the evolution of both the pressure and the wall vorticiy flux, were tracked for a range of pitch rates and summarized in composite plots such as those shown in Figs. 6(a) and 6(b). A detailed description of these plots and their significance will be described in the presentation, and the correlation between this information and the sequence of events that make up the dynamic stall phenomenon will be discussed. Finally, the implications of these results on the requirements for successful control of the unsteady separation will be examined.

References

Ericsson, L. E. (1989) "Moving-Wall-Induced Shear Flow Control" Symposium on Prediction and Exploitation of Separated Flow", Royal Aeronautical Society, London.

McCroskey, W.J. (1982) "Unsteady Airfoils" *Ann. Rev. Fluid Mech.* **14**, p 281-311.

Ramiz, M. A. and Acharya M., (1989a) "The Dynamical Scaling of a Model Unsteady Separating Flow" submitted to the Physics of Fluids A.

Ramiz, M. A. and Acharya M., (1989b) "The Detection of Flow State in an Unsteady Separating Flow" submitted to the AIAA Journal. (see also AIAA Paper 89-1017, 2nd Shear Flow Control Conference)

Reynolds W.C. and Carr L.W., (1985) "Review of Unsteady, Driven, Separated Flows" AIAA Paper 85-0527.

Robinson, M. (ed) (1988) *Proceedings of the Second Workshop on Unsteady Separated Flows,* USAF Academy, Colorado Springs.

Walker, J.M., Helin, H.E. and Strickland, J.H. (1985) "An Experimental Investigation of an Airfoil Undergoing Large Amplitude Pitching Motions" AIAA Journal, v 23, no. 8, p1141.

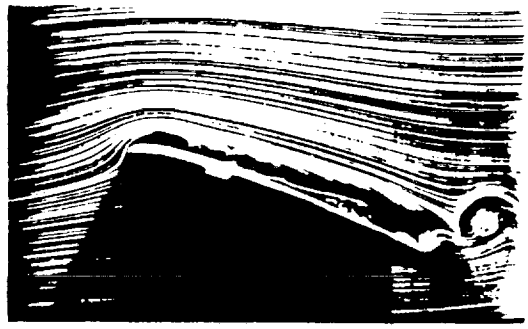

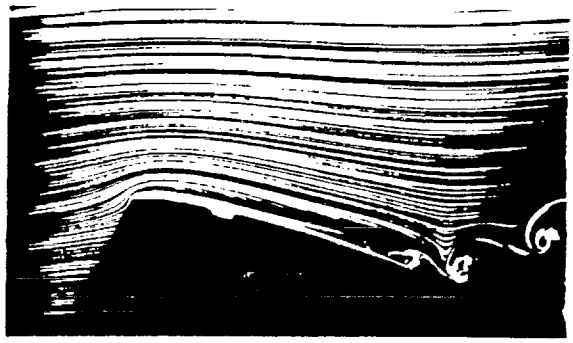

Figure 1

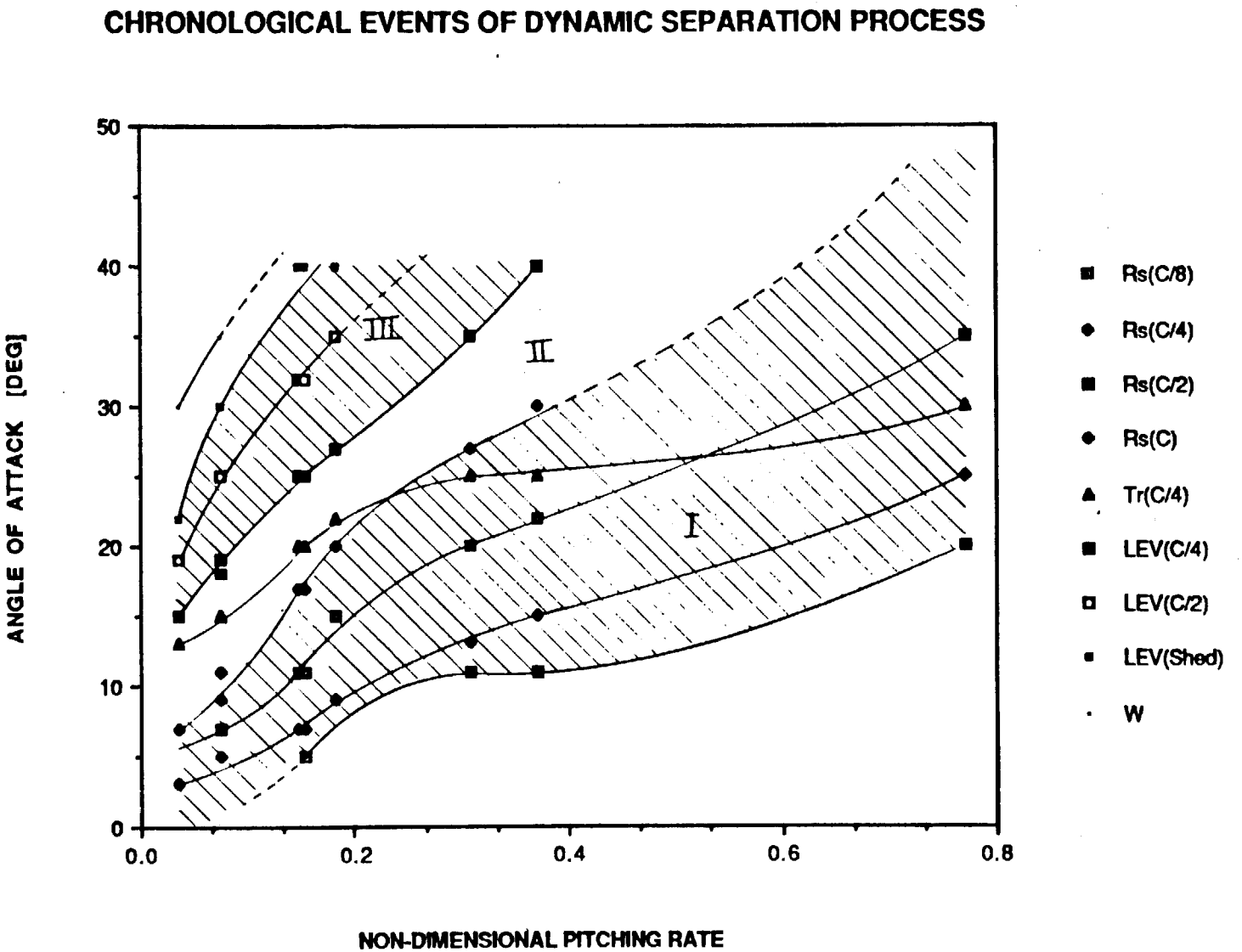
CHRONOLOGICAL EVENTS OF DYNAMIC SEPARATION PROCESS
ANGLE OF ATTACK [DEG]
NON-DIMENSIONAL PITCHING RATE
0
10
20
30
40
50
0.0
0.2
0.4
0.6
0.8
I
II
III
Rs(C/8)
Rs(C/4)
Rs(C/2)
Rs(C)
Tr(C/4)
LEV(C/4)
LEV(C/2)
LEV(Shed)
W

Figure 2

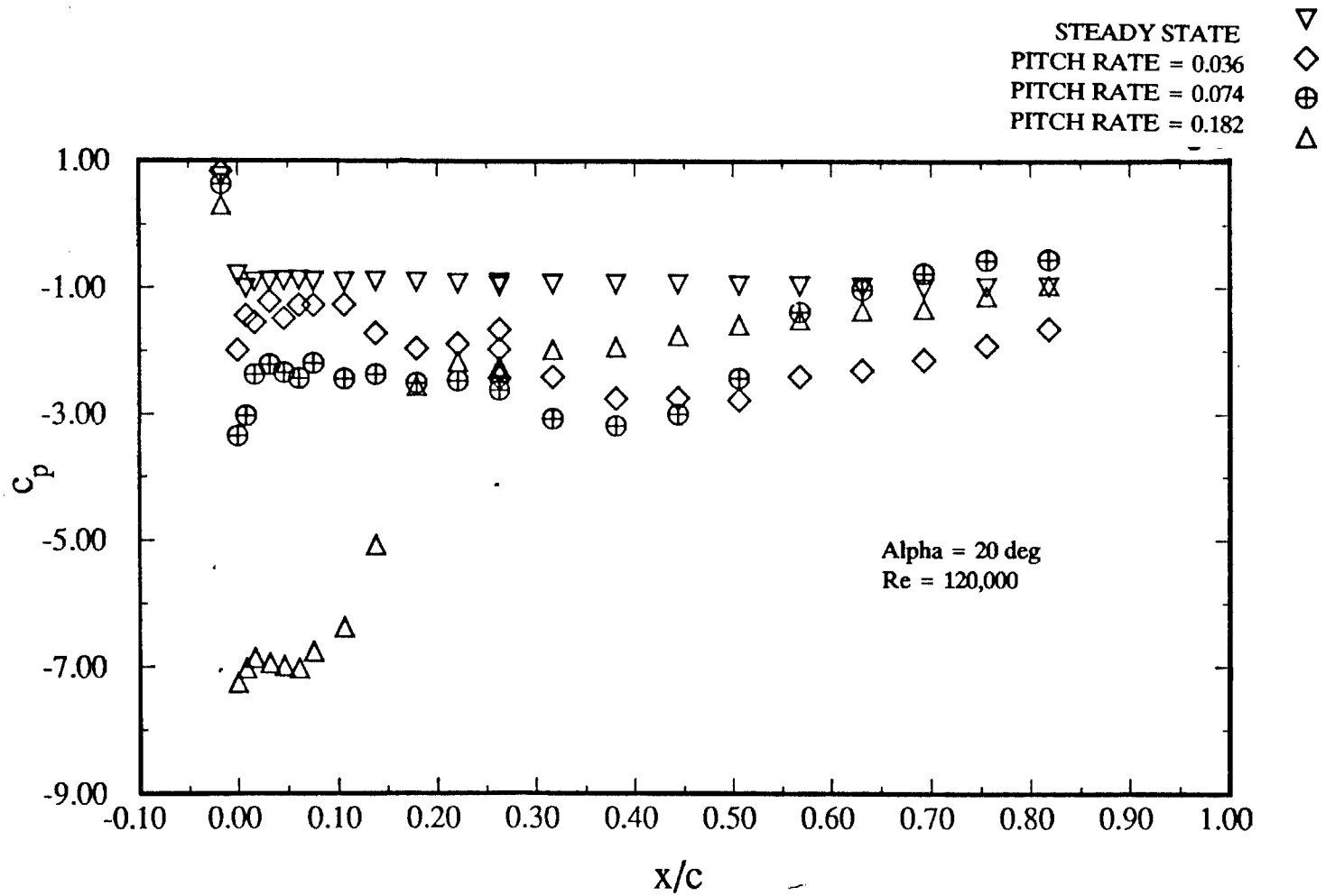
STEADY STATE
PITCH RATE = 0.036
PITCH RATE = 0.074
PITCH RATE = 0.182
1.00
-1.00
-3.00
-5.00
-7.00
-9.00
C_p
-0.10
0.00
0.10
0.20
0.30
0.40
0.50
0.60
0.70
0.80
0.90
1.00
x/c
Alpha = 20 deg
Re = 120,000

Figure 3

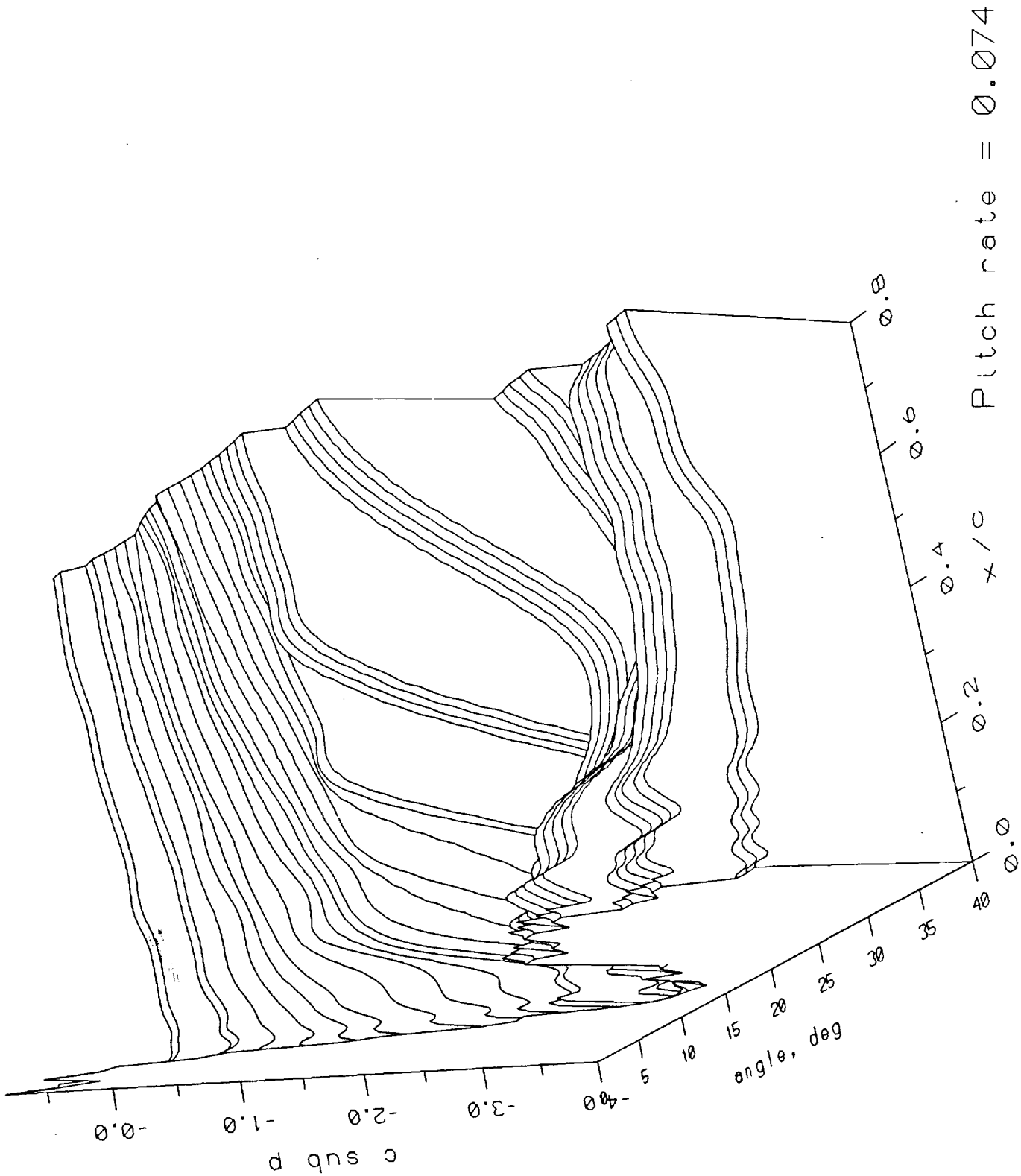
Pitch rate = 0.074
x/c
0.0
0.2
0.4
0.6
0.8
angle, deg
5
10
15
20
25
30
35
40
-4.0
-3.0
-2.0
-1.0
-0.0
c sub p

Figure 4(a)

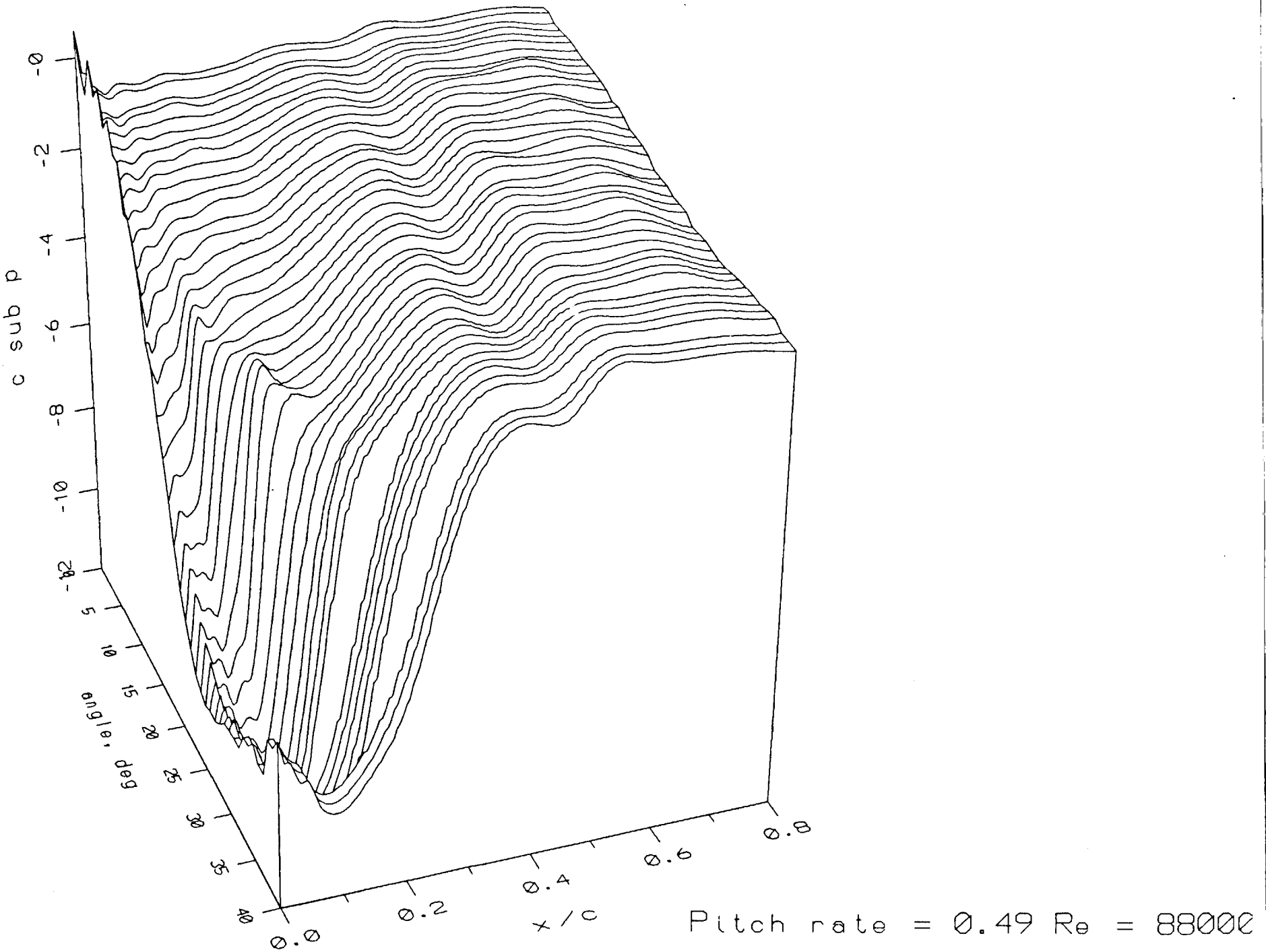
c sub p
-0
-2
-4
-6
-8
-10
-12
angle, deg
5
10
15
20
25
30
35
40
0.0
0.2
0.4
0.6
0.8
x/c
Pitch rate = 0.49 Re = 88000

Figure 4(b)

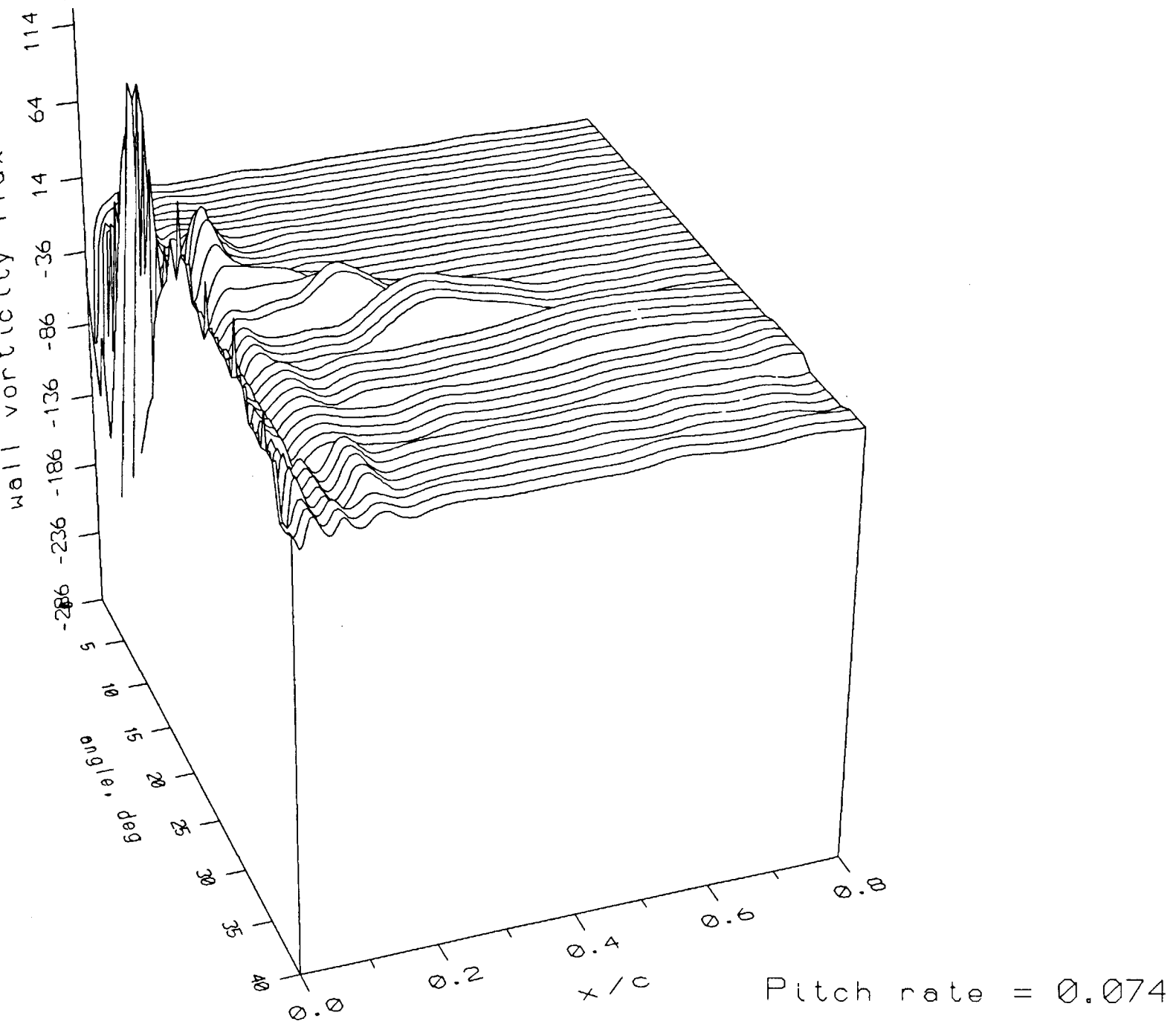
wall vorticity flux
114
64
14
-36
-86
-136
-186
-236
-286
alpha, deg
0
5
10
15
20
25
30
35
40
x/c
0.0
0.2
0.4
0.6
0.8
Pitch rate = 0.074

Figure 5(a)

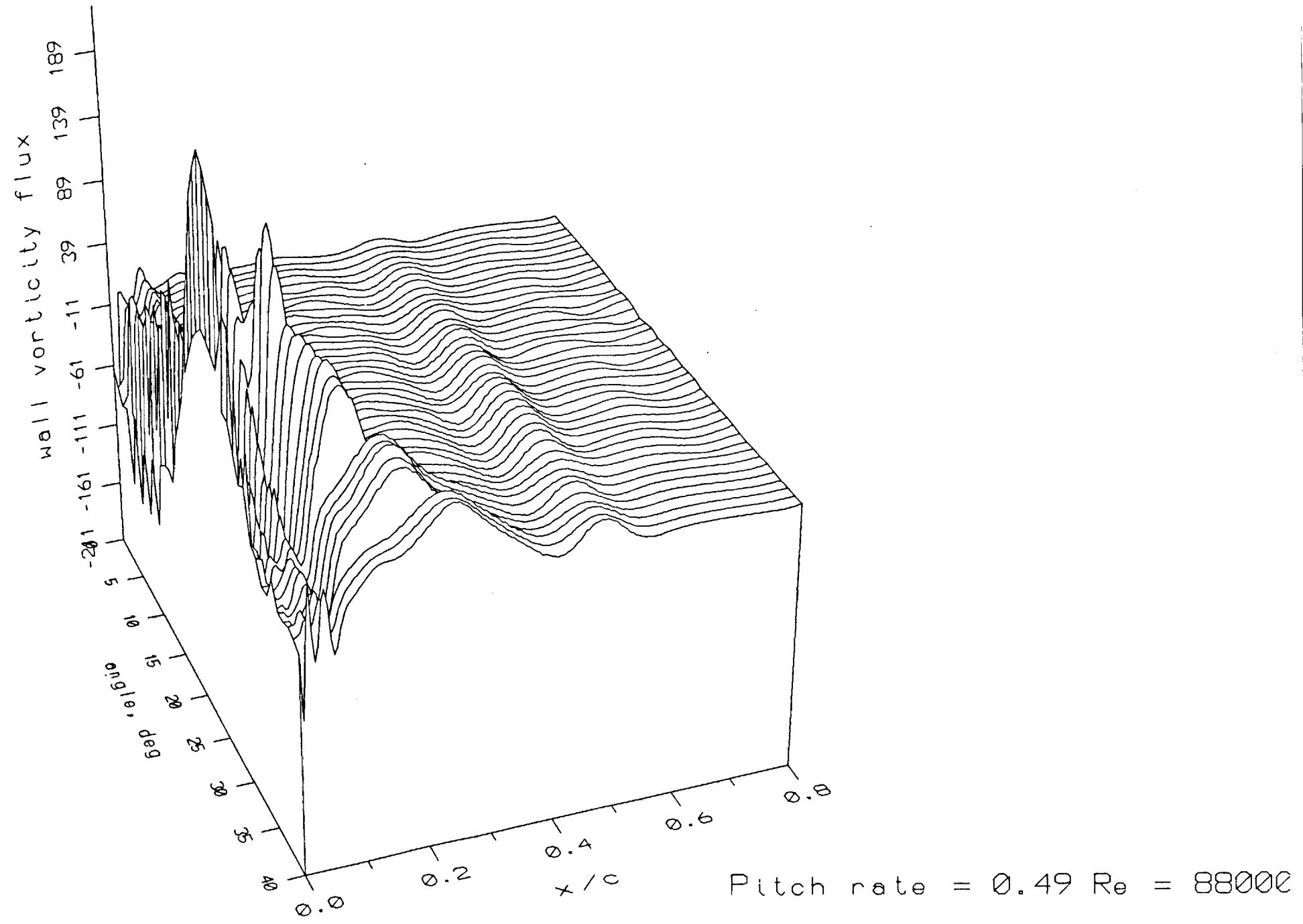
wall vorticity flux
189
139
89
39
-11
-61
-111
-161
-211
gap angle, deg
0
5
10
15
20
25
30
35
40
0.0
0.2
0.4
0.6
0.8
x/c
Pitch rate = 0.49 Re = 88000

Figure 5(b)

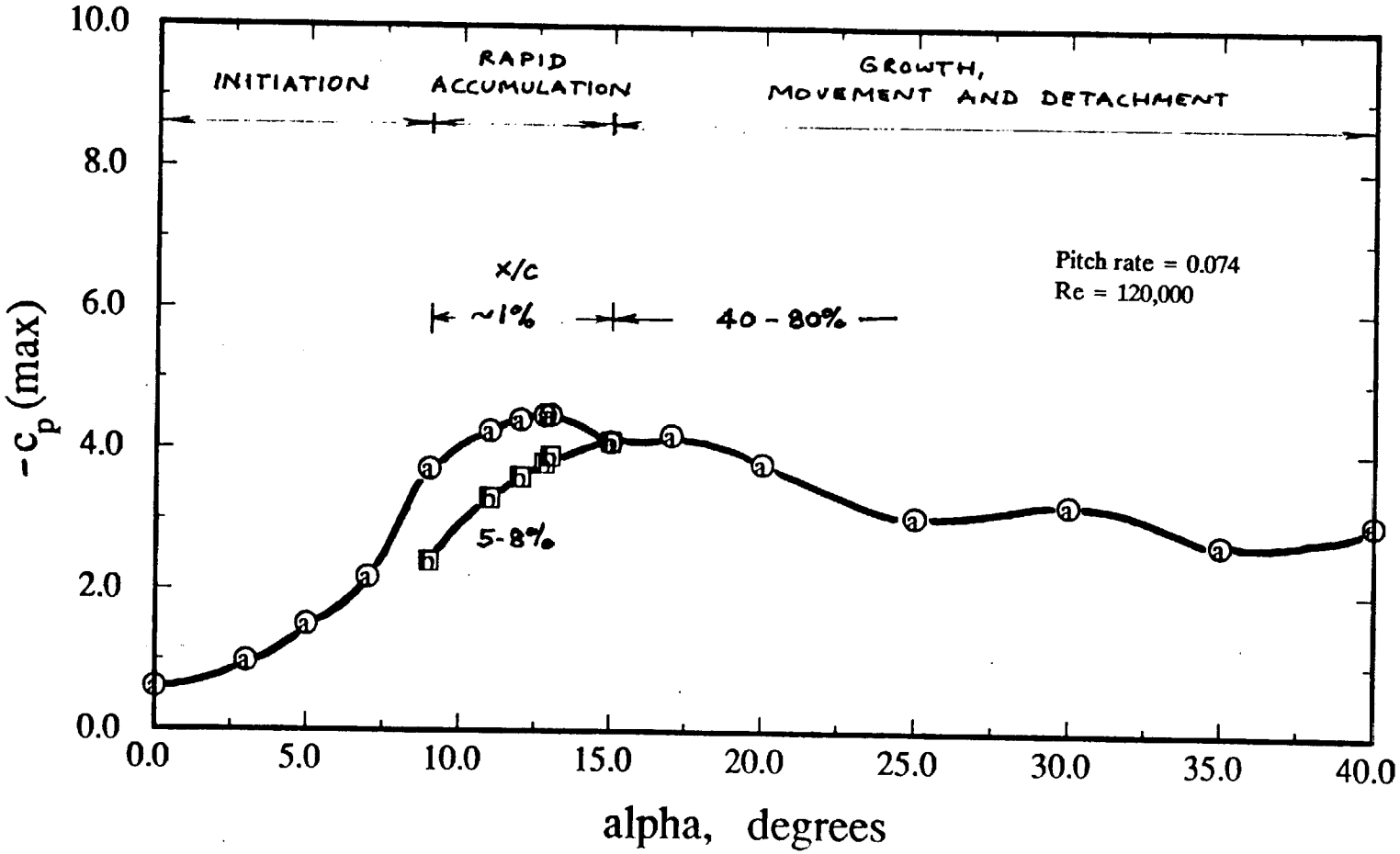
INITIATION
RAPID ACCUMULATION
GROWTH, MOVEMENT AND DETACHMENT
x/c
~1%
40 - 80%
Pitch rate = 0.074
Re = 120,000
5-8%
$-c_p$ (max)
alpha, degrees
10.0
8.0
6.0
4.0
2.0
0.0
0.0
5.0
10.0
15.0
20.0
25.0
30.0
35.0
40.0

Figure 6(a)

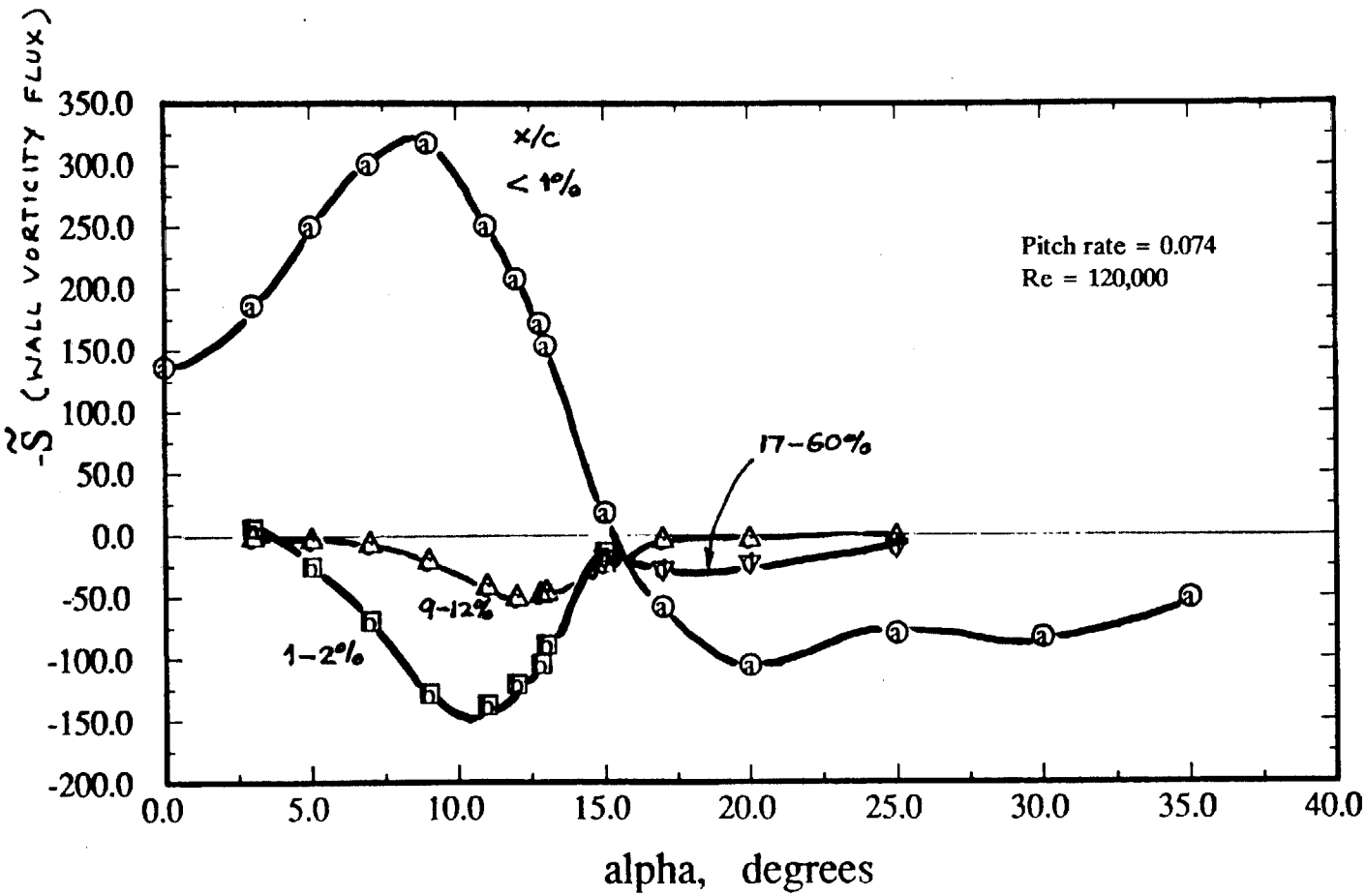
-S̃ (WALL VORTICITY FLUX)
350.0
300.0
250.0
200.0
150.0
100.0
50.0
0.0
-50.0
-100.0
-150.0
-200.0
0.0
5.0
10.0
15.0
20.0
25.0
30.0
35.0
40.0
alpha, degrees
x/c
< 1%
Pitch rate = 0.074
Re = 120,000
17-60%
9-12%
1-2%

Figure 6(b)

EXPERIMENTAL ARRANGEMENT

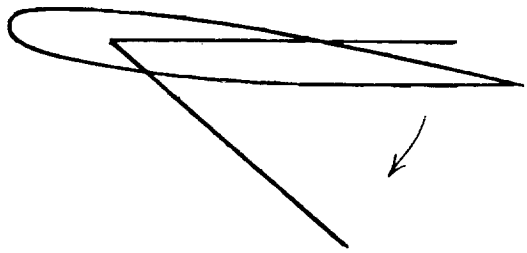

NACA 0012 AIRFOIL, 0.3 m chord

PITCH-UP AT CONSTANT RATE; $0^o \leq \theta \leq 40^o$

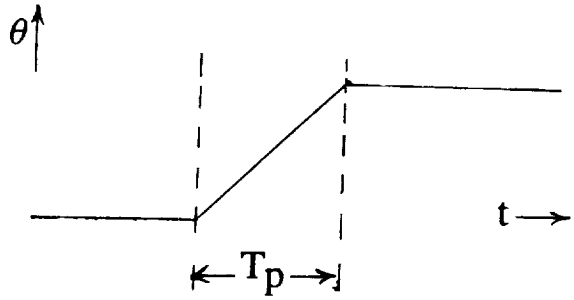

$2.8 \times 10^4 \leq Re_c \leq 1.2 \times 10^5 \quad 0.036 \leq \alpha \leq 0.77$

$$\left[\alpha = \frac{\Delta\theta c}{T_p U_\infty}\right]$$

SEQUENTIAL EVENTS IN UNSTEADY SEPARATION PROCESS

(From flow-visualization records)

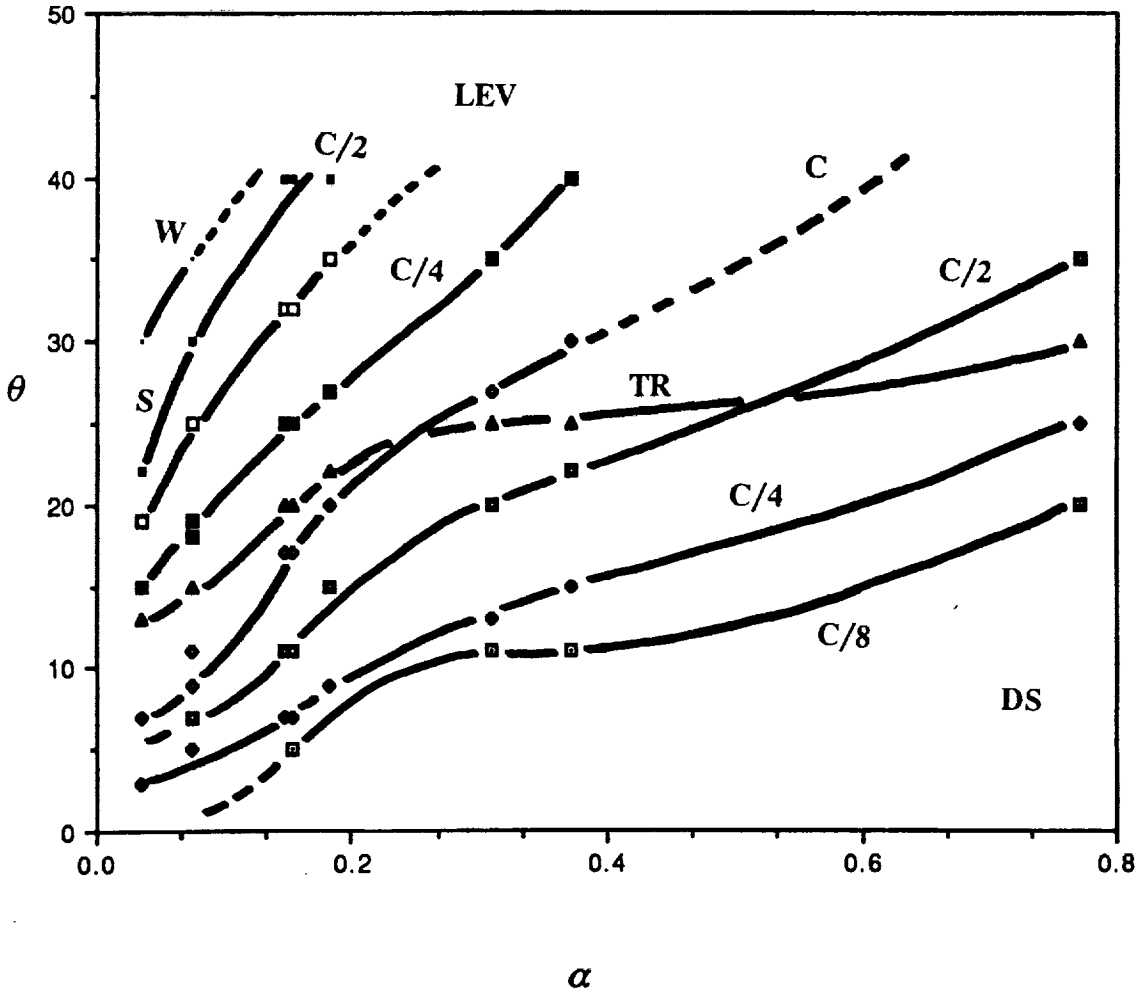

Generalization of Lighthill's discussion
of boundary layers shows that

The flux of vorticity from the wall
is proportional to the instantaneous pressure gradient

$$S = \frac{1}{\rho}\frac{\partial p}{\partial x} \qquad S = S\frac{2c}{U_\infty^2}$$

- Combination of flow visualization, wall pressure and wall vorticity flux provide better understanding of the evolution of unsteady separation over a pitching airfoil

- The flux of vorticity at the wall is confined primarily to a region very close to the leading edge

- Trends in 'significant' events in wall pressure and vorticity flux have been mapped for a range of values of the dimensionless pitch rate

- Results point to alternatives for real-time identification of the state of flow development over the airfoil in unsteady situations

INVESTIGATION OF MECHANISMS FOR VORTICITY GENERATION AND FLOW SEPARATION ON BODIES IN UNSTEADY MOTION

Chuen-Yen Chow and Kai-Hsiung Kao
Department of Aerospace Engineering Sciences
University of Colorado, Boulder, CO 80309-0429

ABSTRACT

Described in this work is an attempt to identify and examine the mechanisms responsible for the generation/shedding of vorticities and the separation of flow from bodies in forced unsteady motions through a viscous fluid. To gain insight into the basic physics of unsteady fluid dynamics, possible mechanisms are isolated and examined separately by assuming different simplified flow arrangements. Even without depending on the availability of the supercomputers, it might be possible to explain or predict some complex unsteady flow phenomena based on the fundamental understanding of the individual mechanisms.

OBSERVED UNSTEADY FLOW PHENOMENA

A numerical study has been made of the flow around an abruptly started elliptic cylinder through an incompressible viscous fluid at a constant angle of attack. The following special features have been observed in the results of that study:

- The zero streamline on the upper surface moves quickly to the trailing edge so that the Kutta condition is automatically satisfied on a body whose trailing edge is not sharp. See Fig. 1. The same phenomenon is also found even on an ellipse of a very small eccentricity as shown in Fig. 2.

- Vorticities are generated from the leading edge and are convected downstream along body surfaces while being diffused sideways. Parts of the vorticities are shed from the trailing edge. See vorticity contour plots in Figs. 1 and 2.

- At a high angle of attack, leading edge separation may occur as

shown in later stages of Fig. 1.

• In contradiction to the inviscid analysis, a body without a sharp trailing edge, such as the elliptic cylinder considered here, can generate a lift in a viscous fluid. Figure 3 reveals that the computed steady-state lift increases with increasing slenderness of the ellipse.

QUESTIONS AND APPROACHES TO FIND ANSWERS

Based on the aforementioned observations, some questions arise concerning the fundamental physics of the unsteady fluid dynamics. In most experimental and numerical studies of unsteady flows, a large number of parameters are involved, such as the body geometry, time dependent body motion, viscous and inertial forces of the fluid, etc. The nonlinear coupling of those parameters makes the flow phenomena too complex to fully comprehend. In searching for answers to those questions, an approach is followed in which the influential parameters are separated and examined individually by choosing various appropriate simplified flow configurations. After the effect of each parameter is throughly understood, even without intensive numerical computations, the overall behavior of a given unsteady flow might become predictable based on a synthesis of the influences from all parameters involved in that particular problem.

Question I. What are the mechanisms that cause the production of vorticity on a body in forced unsteady motion?

To answer this question several classical unsteady flow problems with exact solutions are reviewed. For a flat plate of infinite extension started impulsively into a constant motion U in its own plane, vorticity is generated instantaneously at the surface and diffuses away into the fluid in the normal direction. At a later time the shear stress at the plate is finite, but it cannot generate additional vorticity. The total vorticity contained in the fluid per unit projected area of the plate is a constant, which is proportional to U but independent of the viscosity of the fluid. Examined also are the unsteady plane and cylindrical Couette flows. The conclusion is that vorticity is generated by tangential acceleration of a solid surface, but not by the shear force exerted

by the surface on the fluid.

In the case of the Blasius boundary layer flow, all vorticity is generated at the leading edge. The total amount of vorticity, which is proportional to the relative velocity of the plate through the fluid, is convected downstream without changing its total magnitude despite the presence of wall shear forces along the boundary layer.

The generation of vorticity by tangential pressure gradients along a surface and the consideration for bodies of finite dimensions are omitted in this abstract.

Question II. What are the mechanisms that cause the zero streamline to move toward the rounded trailing edge of a body, and what are those that cause leading edge separation?

The possible influential parameters are many, including for example the body curvature, local vorticity distribution, pressure gradient, and the surface velocity relative to the external flow. The flow structure near the trailing edge of an impulsively started elliptic cylinder was studied previously by us using the method of matched asymptotic expansions. The representative result shown in Fig. 4 describes the process by which a region of concentrated vorticity is lifted off the trailing edge and shed into the wake. The present work examines why such a phenomenon should occur near the trailing edge and how the flow there differs from that near the leading edge.

At an early stage after the impulsive start of the ellipse, as shown in Fig. 1, the flow near the leading edge resembles that around a stagnation point and that near the trailing edge is approximately one with flow directions reversed. Using a simplified model, the leading edge flow is approximated by a stagnation-point flow on an infinite plate facing a stream, whose solution under boundary layer approximations is known. However, by reversing the stream direction to simulate the flow near the trailing edge, the behavior of the boundary layer there is radically changed. Effects of various parameters on the boundary layer structure are then studied by modifying this standard model. For example the orientation of the body surface is simulated by allowing the far flow to incline at an angle, and the unsteady translational and rotational

motions of the surface are approximated by giving the plate certain prescribed normal and tangential velocities. To simulate the effect of body curvature, the flat plate may be replaced by a circular cylinder. In this way a set of geometrically simple yet physically meaningful problems is formulated; most of the problems can be solved using classical boundary layer solution techniques. This study may shed some light on the explanation of many unsteady flow phenomena, such as the differential lift generation abilities of an ellipse with different eccentricities as shown in Fig. 3. The basic solutions may also be used for the prediction of the occurrence of leading edge separation, its suppression and control.

Question III. This question is concerned with the classical Kutta-Joukowski theorem that $L'=\rho U\Gamma$, in which Γ is the circulation computed along a closed path around a lifting body according to the inviscid theory. In a realistic fluid with viscosity, then, how should Γ be computed?

When the no-slip condition is applied on a body without rotation, the circulation around a path coinciding with the body surface is zero. By choosing closed paths further and further away from the body, the computed circulation will first increase but will decrease later, and finally will approach zero again because the total vorticity generated by a translational body vanishes. It appears quite difficult to find an appropriate closed path that contains all the vorticities responsible for the lift, even if the wake vorticities are far from the body. Despite the fact that a satisfactory solution has not yet been found, various attempts to find an answer will be described.

ACKNOWLEDGMENT

This work is sponsored by the Air Force Office of Scientific Research (AFSC) under Contract F49620-88-C-0098.

FIGURE 1: $\eta_1 = 0.1, \alpha = 45^\circ, Re = 200$

Streamlines

Equi-Vorticity Lines

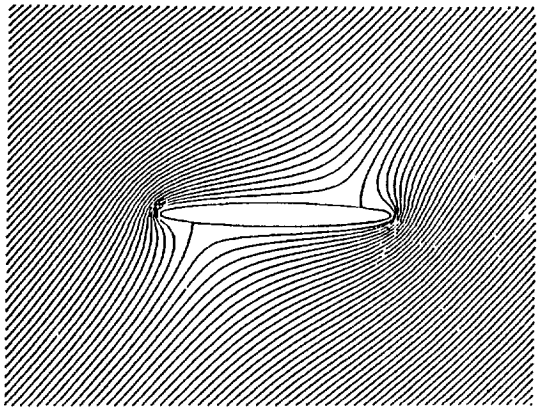

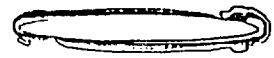

t=0.012

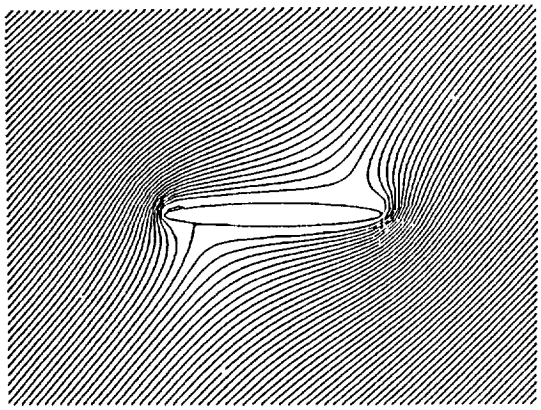

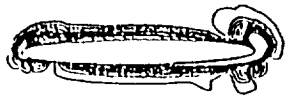

t=0.036

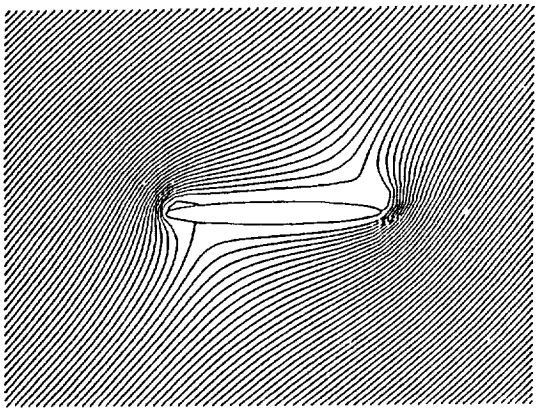

t=0.1

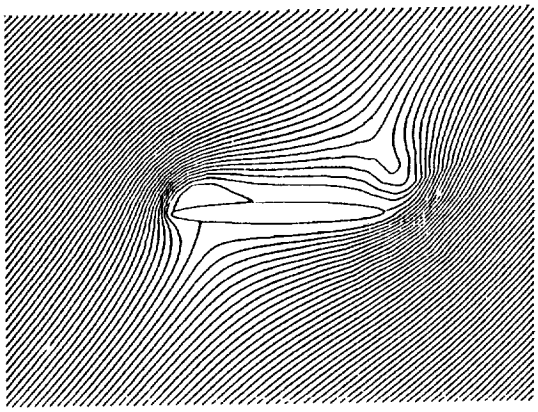

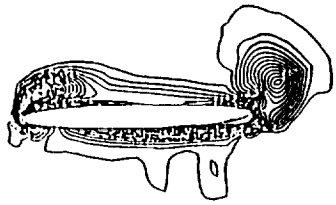

t=0.3

FIGURE 2: $\eta_1 = 1.0, \alpha = 30°, Re = 200$

Streamlines | Equi-Vorticity Lines

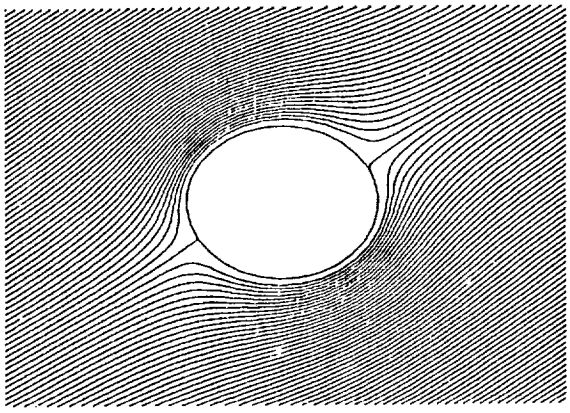

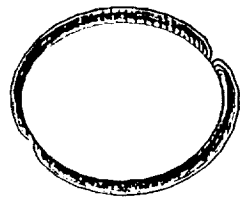

t=0.035

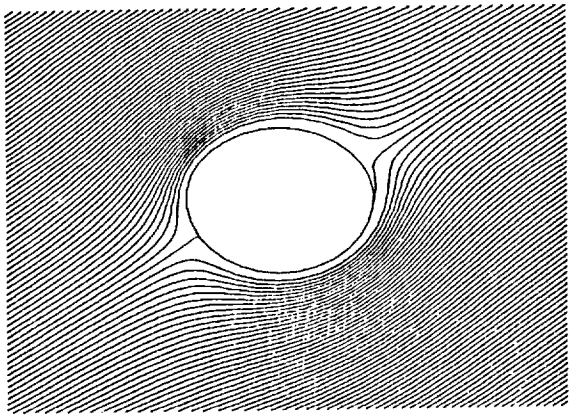

t=0.1

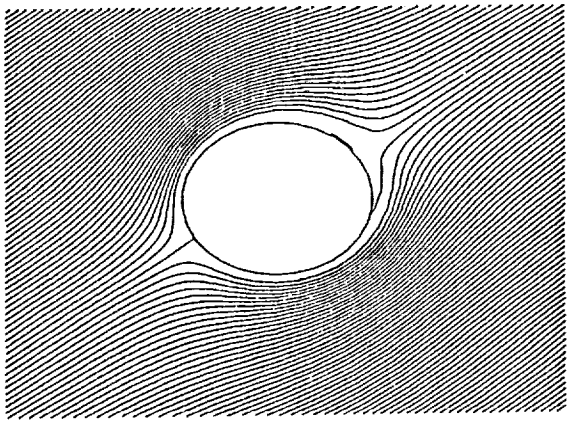

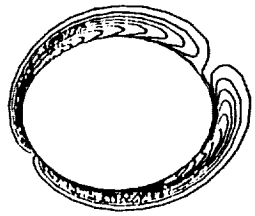

t=0.15

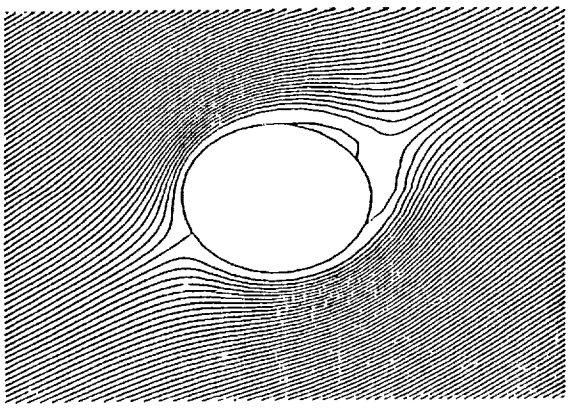

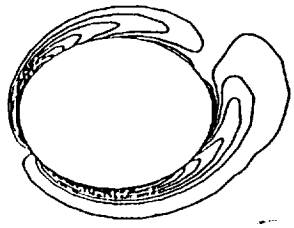

t=0.25

FIGURE 3: C_L vs. time for elliptic cylinders.

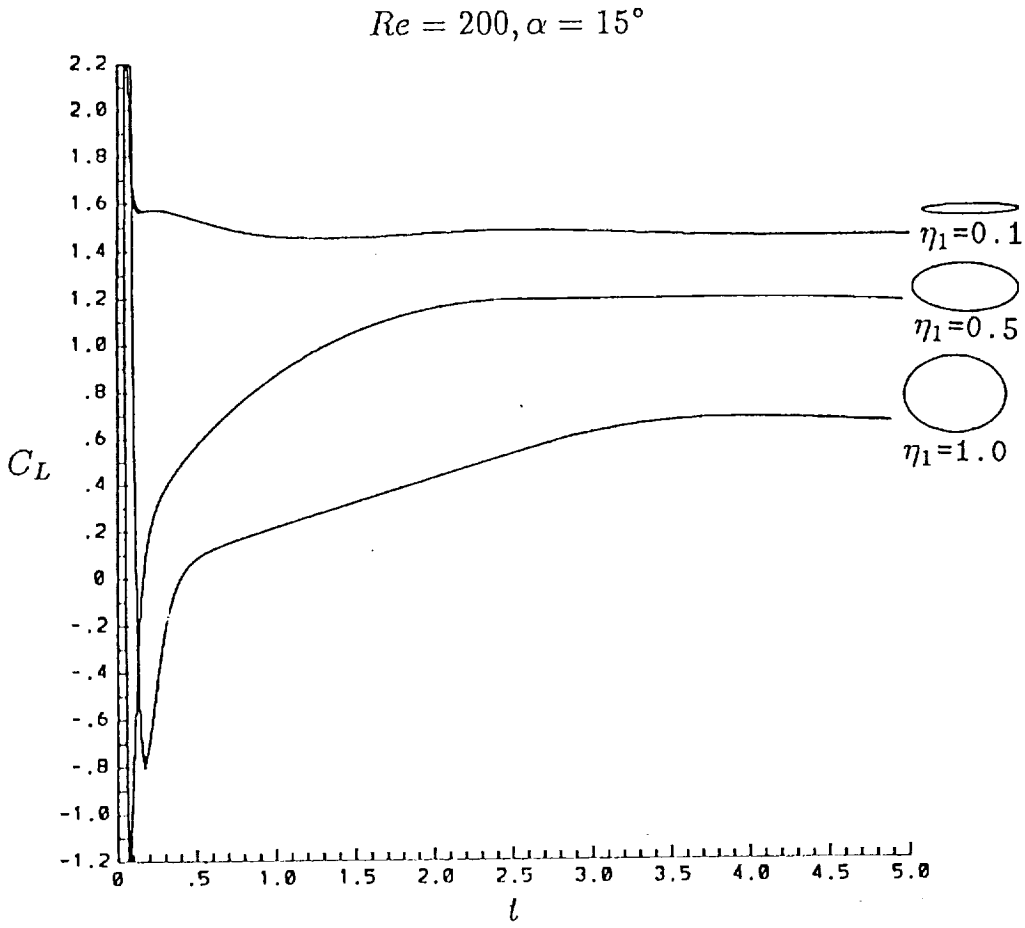

FIGURE 4: Evolution of flow pattern near the trailing edge of an abruptly started elliptic cylinder.

Taken from D. F. Billings' Ph.D. Thesis, University of Colorado at Boulder, 1984.

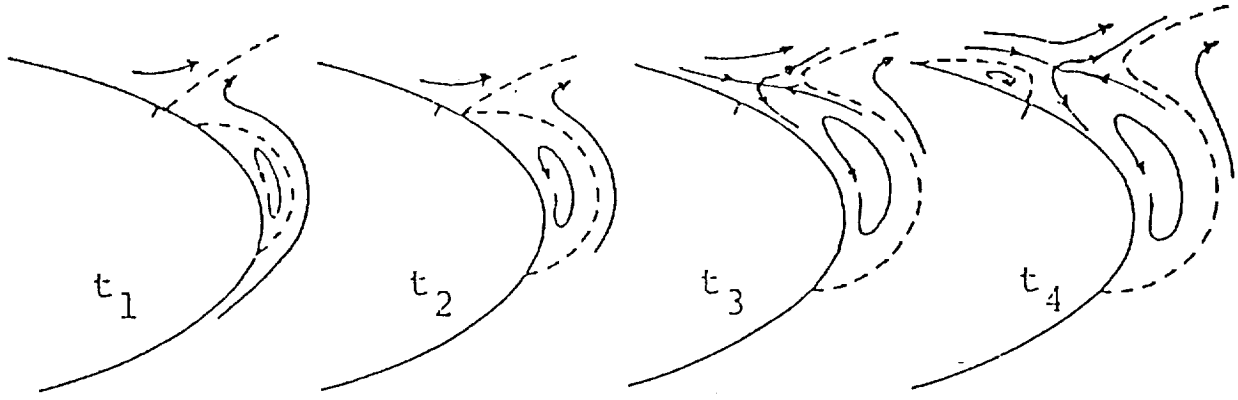

Factors affecting movement of zero streamline in stagnation-point flow:

- Direction of flow
- Unbalanced vorticity
- Orientation of far flow
- Body curvature
- Motion of body surface

Conclusion

Position of the zero streamline changes in an unsteady stagnation-point flow ; it moves from a low into a high vorticity region.

CHARACTERIZATION OF DYNAMIC STALL PHENOMENON USING TWO-DIMENSIONAL UNSTEADY NAVIER-STOKES EQUATIONS†

by

K.N. GHIA, U. GHIA* AND G.A. OSSWALD

Department of Aerospace Engineering and Engineering Mechanics
*Department of Mechanical, Industrial and Nuclear Engineering
University of Cincinnati, Cincinnati, Ohio 45221

Contributions of this Study

Among the new significant aspects of the present work are (i) the treatment of the far-field boundary, (ii) the use of C-grid topology, with the branch-cut singularity treated analytically, (iii) evaluation of the effect of the envelope of prevailing initial states and, finally, (iv) the ability to employ streakline/pathline 'visualization' to probe the unsteady features prevailing in vortex-dominated flows. The far-field boundary is placed at infinity, using appropriate grid stretching. This contributes to the accuracy of the solutions, but raised a number of important issues which needed to be resolved; this includes determining the equivalent time-dependent circulation for the pitching airfoil. A secondary counter-clockwise vortex erupts from within the boundary layer and immediately pinches off the energetic leading-edge shear layer which then, through hydrodynamic instability, rolls up into the dynamic stall vortex. The streakline/pathline visualization serves to provide information for insight into the physics of the unsteady separated flow.

---

† This research is supported, in part, by AFOSR Grants (Nos. 87-0074 and 90-0249), with supercomputer resources being provided by the Ohio Supercomputer Center.

Physical Characteristics and Background

Specifically, the large amptitude rapid pitching motion associated with the initiation of a high angle-of-attack maneuver typically leads to the generation of a dynamic stall vortex whose evolution results in large transient lift, drag and moment that can, for short periods of time, produce loadings significantly larger than those expected during either steady, or quasi-steady flight. Indeed, the successful completion of an abrupt, drastic maneuver can depend upon the ability of holding the dynamic stall vortices in place, at least for the duration of the maneuver, and subsequently bleeding the excess accumulated vorticity in a controlled manner into the wake. Abrupt shedding of large amounts of locally concentrated vorticity can so rapidly alter the lift distribution on a body that a tumbling loss-of-control incident can occur, as the associated rapid changes in moment distribution cannot be tolerated.

Recently, Carr (1988) has comprehensively reviewed the literature on the dynamic stall phenomenon and has also articulated the effect of key parameters on this phenomenon. Helin (1989) has also highlighted recent advances in the field, while stressing the importance of unsteady aerodynamics for highly maneuverable and agile aircraft. In addition, he has raised the important issue of the effect of flow separation on the formation of the energetic dynamic-stall vortex. These two reviews adequately point out some of the unresolved issues associated with the problem of dynamic stall.

On the Analysis of Dynamic Stall

The unsteady Navier-Stokes analysis of K. Ghia, Osswald and Ghia (1985) and Osswald, K. Ghia and U. Ghia (1986) is modified to permit arbitrary three degree-of-freedom maneuvers, using body-fixed coordinates and a C-grid

topology. This formulation not only permits pitching motions, but also plunging and in-plane accelerating or decelerating motions; typically, the airfoil is pitched about the quarter-chord axis. The problem is formulated using vorticity and stream function as dependent variables in a non-using body-fixed reference frame in generalized coordinates. This formulation offers the important advantage over the primitive-variable formulation that the form of the governing equations in inertial and non-inertial reference frames is identical. The far-field boundaries are located at true infinity for this subsonic flow with its fully elliptic nature. The conformal mapping techniques used lead to analytical determination of the corresponding inviscid flow; this inviscid flow constitutes the true far-field boundary condition; by contrast, the studies of Visbal and Shang (1988) and Ekaterinaris (1989) place the far-field boundary at a finite distance from the airfoil, and employ free-stream conditions on the upstream boundary and zero streamwise gradients downstream. The present study uses an analytically determined clustered conformal grid, thereby avoiding numerical error in the computation of the metrics. The C-grid topology employed introduces a singularity at the trailing edge (TE) and all along the branch cut. For the latter, this singularity is treated using the method of analytic continuation, as developed by Osswald, K. Ghia and U. Ghia (1985). The conditions of zero slip and zero normal velocity at the surface of the airfoil are implemented appropriately in terms of the stream function and vorticity. At the TE, the singularity in the grid does play a role in determination of the stream function, which is obtained by satisfying the Kutta condition. The vorticity at the TE is determined using the analysis of Osswald, K. Ghia and U. Ghia (1989). The direct numerical simulation (DNS) methodology developed by the authors is used to solve the

vorticity transport and stream function equations. Central differences are used for all spatial derivatives and no artificial dissipation is added explicitly.

Results and Discussion

In the present study, simulations are carried out for a NACA 0015 airfoil undergoing constant $\dot{\theta}$-pitch-up motion. Two flow configurations are attempted and they are for Re = 10^3 and 10^4. Configuration I, with the lower Re = 10^3, is used in the development phase, since it permits the use of a smaller grid (274, 76) of which 114 grid points are placed on the body. On the other hand, configuration II, with Re = 10^4, is used to compare the results of the experiments of Walker, Helin and Strickland (1985) who considered Re = 45000. This latter configuration was run using a (444,101) grid with 204 grid points on the body; the size of the grid was selected based on the results of Visbal and Shang (1988) who had carried out a grid study and selected this size. In addition, the same constant $\dot{\theta}$-pitch-up motion as used by them is also implemented here and corresponds to nondimensional pitch rate Ω_0= 0.2 with nondimensional acceleration time t_0 = 0.5, and pivot axis location measured from airfoil leading edge x_0= 0.25.

Results of configuration I, in Fig. 1, show that the dynamic stall vortex with its clockwise spinning fluid evolves as the shear layer from the leading edge is pushed away by the counterclockwise spinning vortex close to the body surface and subsequently the shear layer rolls up and forms a dynamic stall vortex. It appears that the eruption of counterclockwise spinning vortex from within the boundary layer is important to formation of the dynamic stall vortex near the leading edge.

Results for configuration II, in Fig. 2, show that $\theta = 0^{o}$ run exhibits unsteady results as opposed to the steady-state results obtained by Visbal and Shang. Their steady-state solutions could strictly be a consequence of the use of both explicit as well as implicit smoothing, i.e., artificial viscosity, to maintain stability in their numerical calculations, which employed the method of Beam and Warming. Present results for configuration II, although not depicted here, show that there are grid related oscillations near the leading edge in the vorticity contours and grid structure and perhaps its density needs to be altered before generating new results and analyzing them. Still, in this case, also the secondary counterclockwise vortex erupts from within the boundary layer on the surface to form the dynamic stall vortex. Unlike wind-tunnel tests, the numerical, experiment in the present study computes the vorticity field directly. By evaluating various individual terms in the vorticity- transport equation, it is possible to examine vorticity accumulation and generation at the body surface as well as in the flux from the boundary to reveal the underlying mechanism and the role of unsteady separation on the evolution of the stall vortex. This is possible once a comprehensive set of results are obtained.

In summarizing, the constant $\dot{\theta}$-pitch-up experiment of Walker et al. (1985) is simulated using direct numerical simulation and an unsteady NS analysis. The preliminary results obtained so far provide the flow structure and the evidence that eruption of secondary counterclockwise vortex near the quarter chord point triggers the formation of the dynamic stall vortex. However, additional results are essential to obtain the budget of vorticity dynamics and to shed further insight into this mechanism underlying the evolution of dynamic stall vortex just stated and its relation to unsteady separation. Based on the existing results of a video presentation of the numerically simulated evolution, convection and shedding

of the dynamic stall vortex is created, but for quantitative information comprehensive data is needed. It should be added that, in the earlier results for flow past a static Joukowski airfoil at 53^0, the authors have seen the formation of a secondary counterclockwise vortex before the leading edge shear layer forms a large clockwise spinning vortex.

REFERENCES

1. Blodgett, G.A. Osswald, K.N. Ghia, U. Ghia, (1990), "Bubbles - An Unsteady Numerical Particle Trace Technique," to be presented at Sixteenth Annual AIAA Mini-Symposium on Aerospace Science and Technology, March, Dayton, Ohio.

2. Carr, L.W., (1988), "Progress in Analysis and Prediction of Dynamic Stall," Journal of Aircraft, Vol. 25, No. 1, pp. 6-17.

3. Ekaterinaris, J.A., (1989), "Compressible Studies on Dynamic Stall," AIAA Paper 89-0024, 27th Aerospace Sciences Meeting, Reno, Nevada, January 9-12.

4. Ghia, K.N., Osswald, G.A., and Ghia, U., (1985), "Analysis of Two-Dimensional Incompressible Flow Past Airfoils Using Unsteady Navier-Stokes Equations," Chapter in Numerical and Physical Aspects of Aerodynamic Flows, Vol. III, Editor: T. Cebeci, Springer-Verlag, New York, January.

5. Helin, H.E., (1989), "The Relevance of Unsteady Aerodynamics for Highly Maneuverable and Agile Aircraft," Proceedings of fourth symposium on Numerical and Physical Aspects of Aerodynamic Flows, Long Beach, California, January.

6. Osswald, G.A., Ghia, K.N. and Ghia, U., (1985), "An Implicit Time-Marching Method for Studying Unsteady Flow with Massive Separation," AIAA CP 854, pp, 25-37.

7. Osswald, G.A., Ghia, K.N., and Ghia, U., (1989), "Analysis of Potential and Viscous Flows Past Arbitrary Two-Dimensional Bodies with Sharp Trailing Edges," AIAA CP 895, pp. 668-677.

8. Visbal, M.R., and Shang, J.S., (1988), "Numerical Investigation of the Flow Structure Around a Rapidly Pitching Airfoil," "Proceedings of AFOSR/FJSRL/DFAM/UC Workshop II on Unsteady Separated Flows, FJSRL-TR-88-0004, pp. 91-108, September.

9. Walker, J.M., Helin, H.E., and Strickland, J.H., (1985), "An Experimental Investigation of an Airfoil Undergoing Large Amplitude Pitching Motions," AIAA Journal, Vol. 23, No. 8, pp. 1141-1142, August.

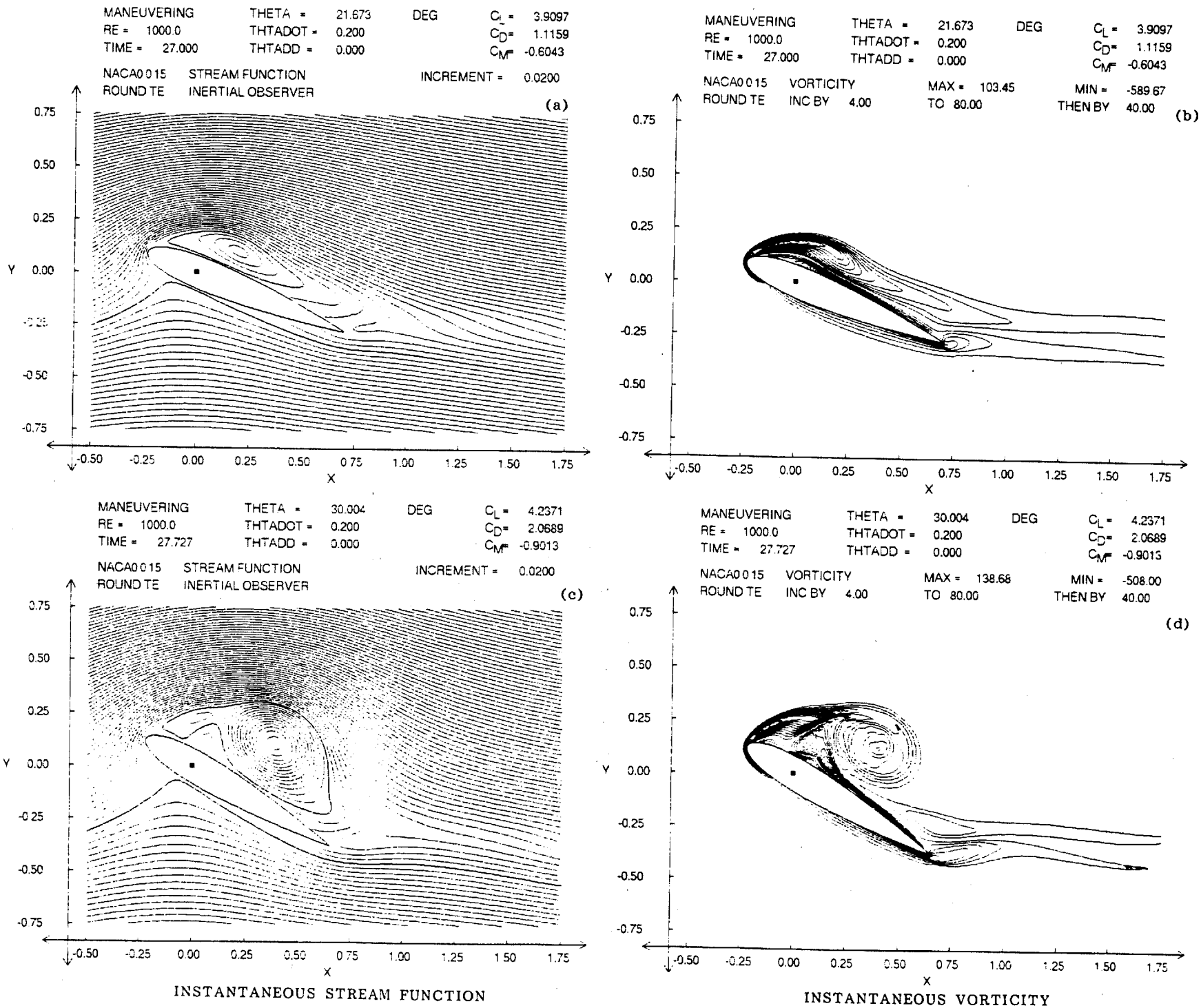

FIG. 1 CONTOURS OF INSTANTANEOUS STREAM FUNCTION AND VORTICITY DEPICTING DYNAMIC STALL, Re = 1,000, (a-b) α = 21.673°, (c-d) α = 30.004°.

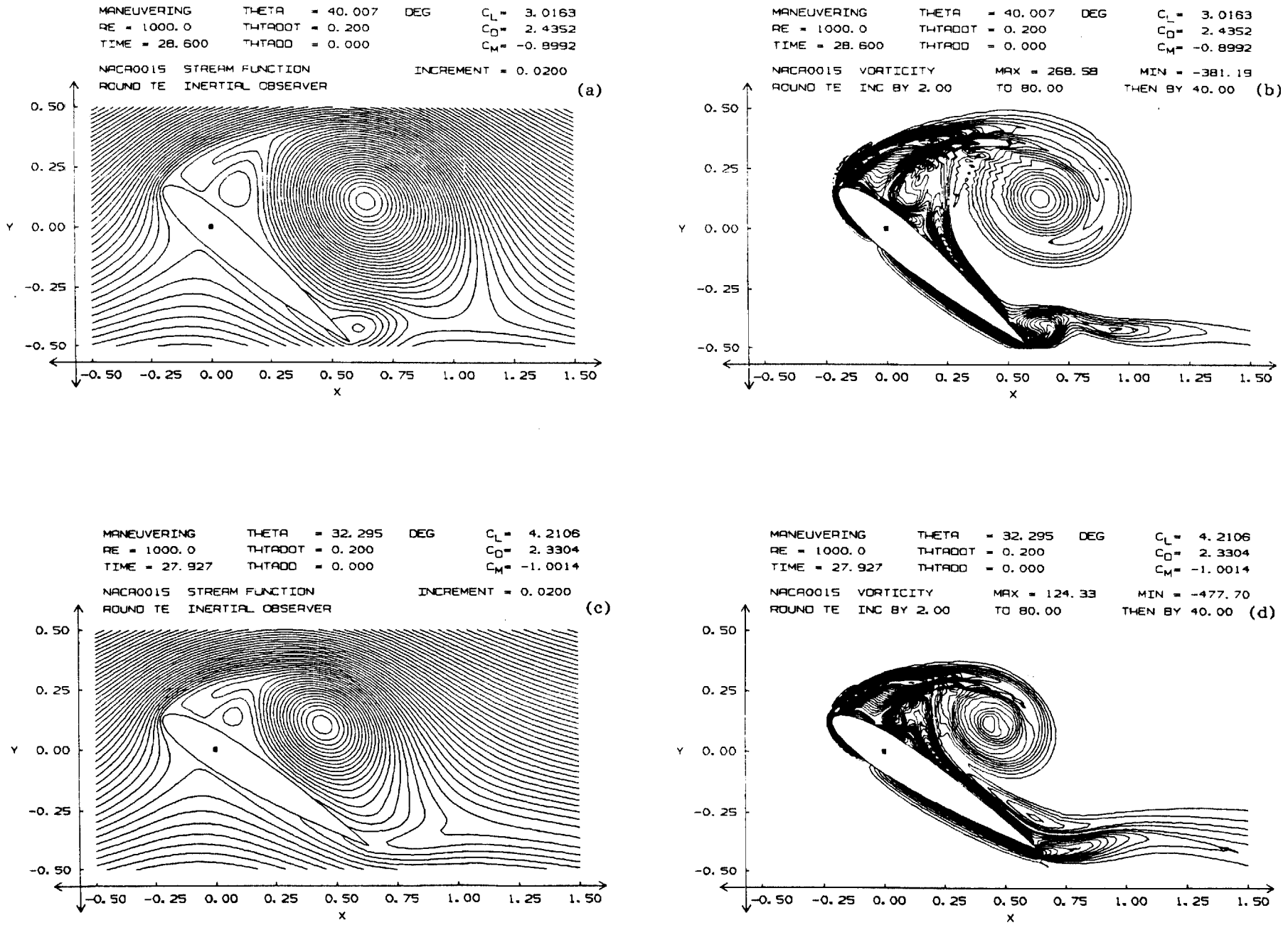

FIG. 1 CONT. CONTOURS OF INSTANTANEOUS STREAM FUNCTION AND VORTICITY DEPICTING DYNAMIC STALL, Re = 1,000, (a-b) α = 40.007°, (c-d) α = 32.295.

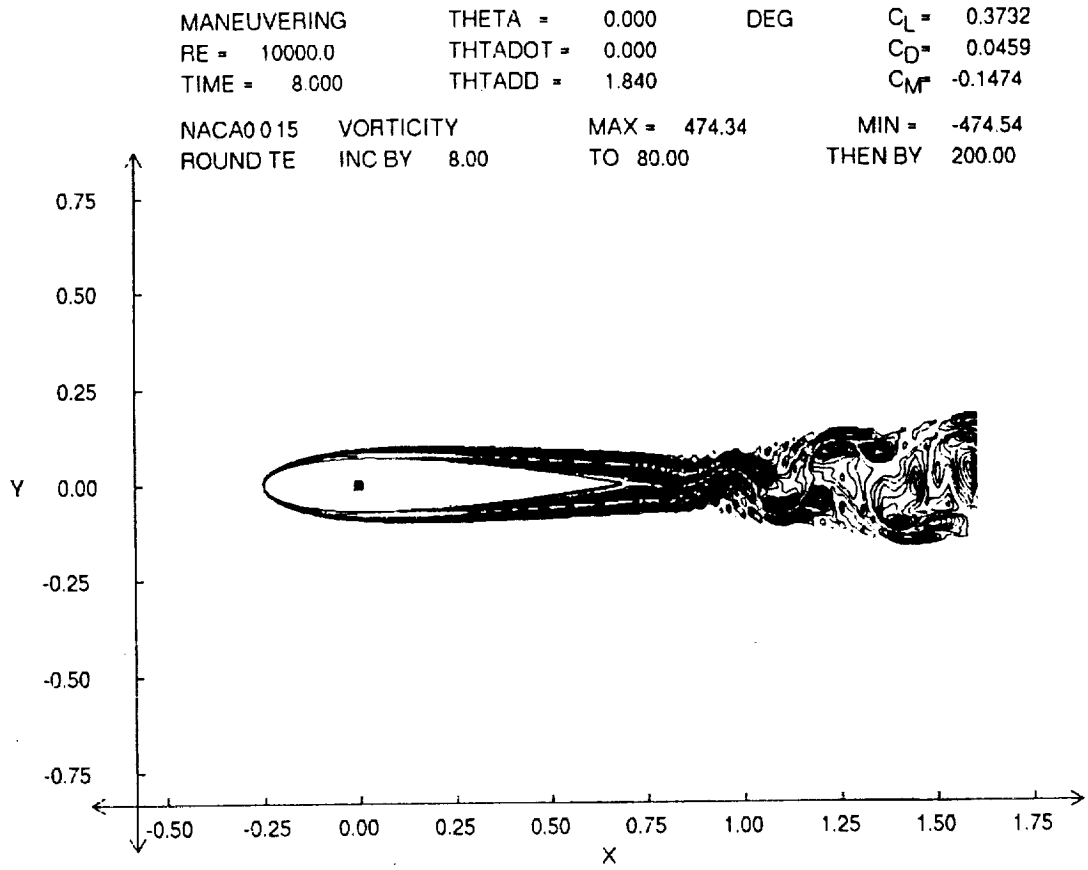

FIG. 2 VORTICITY CONTOURS FOR FLOW PAST A NACA0015 AIRFOIL, Re = 10,000, α = 0°, t = 8.00.

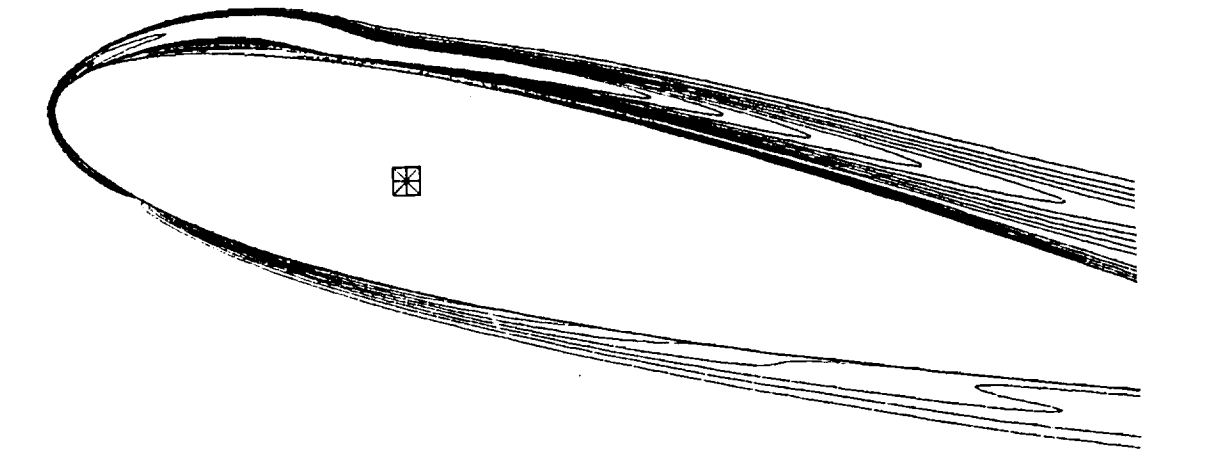

FIG. 2 CONT. ENLARGED VIEW OF LEADING EDGE DEPICTING EVOLUTION OF DYNAMIC STALL, Re = 10,000, α = 13.651°.

INERTIAL VS BODY FIXED OBSERVER

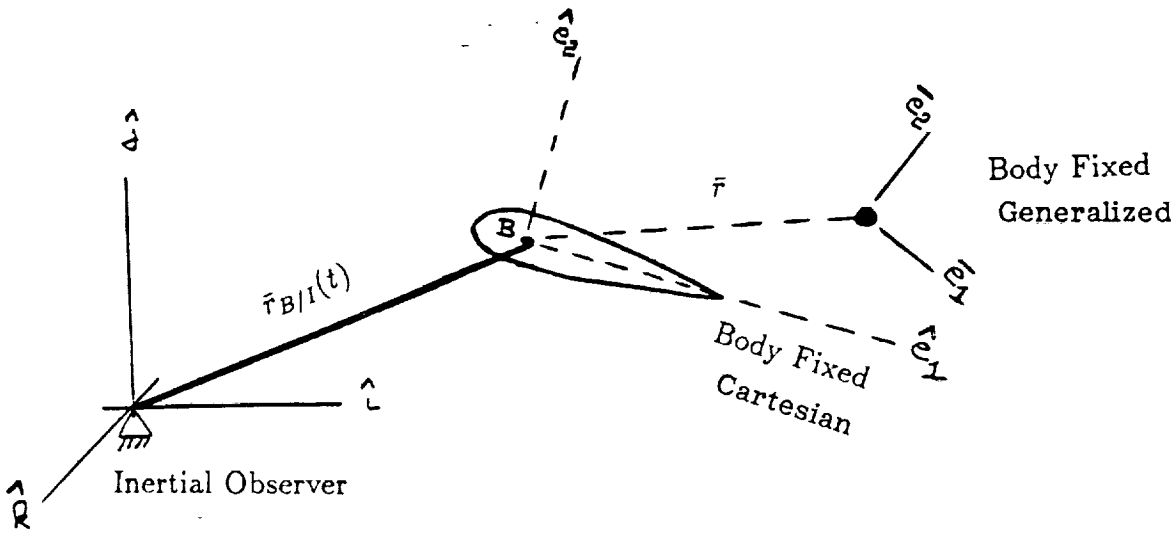

	Inertial Observer	Body Fixed Observer (Apparent)
Position of Fluid Particle:	$\bar{r}_I$	$\bar{r}$
Velocity of Fluid Particle:	$\bar{V}_I$	$\bar{V}$
Acceleration:	$\bar{a}_I$	$\bar{a}$
Vorticity:	$\bar{\omega}_I = \nabla \times \bar{V}_I$	$\bar{\omega} = \nabla \times \bar{V}$

KINEMATICS

$$\bar{r}_I = \bar{r}_{B/I}(t) + \bar{r}$$

$$\bar{V}_I = \bar{V}_{B/I}(t) + \bar{V} + \bar{\Omega}_B(t) \times \bar{r}$$

$$\bar{a}_I = \bar{a}_{B/I}(t) + \bar{a} + 2\bar{\Omega}_B(t) \times \bar{V} + \bar{\alpha}_B(t) \times \bar{r} + \bar{\Omega}_B(t) \times \bar{\Omega}_B(t) \times \bar{r}$$

$$\begin{aligned} \bar{\omega}_I &= \nabla \times \{\bar{V}_{B/I}(t) + \bar{V} + \bar{\Omega}_B(t) \times \bar{r}\} \\ &= 0 + \nabla \times \bar{V} + 2\bar{\Omega}_B(t) \\ &= \bar{\omega} + 2\bar{\Omega}_B(t) \end{aligned}$$

Arbitrary Maneuver Defined by:

$\bar{r}_{B/I}(t)$	
$\bar{V}_{B/I}(t) = \frac{d\bar{r}_{B/I}}{dt}$	$\bar{\Omega}_B(t)$
$\bar{a}_{B/I}(t) = \frac{d^2\bar{r}_{B/I}}{dt^2}$	$\bar{\alpha}_B(t) = \frac{d\bar{\Omega}_B}{dt}$

UNSTEADY INCOMPRESSIBLE NAVIER-STOKES EQUATIONS

INERTIAL OBSERVER

PRIMITIVE VARIABLES

Continuity

$$\nabla \cdot \bar{V}_I = 0$$

Linear Momentum (Bernoulli's Form)

$$\frac{\partial \bar{V}_I}{\partial t} + \left(\nabla \times \bar{V}_I\right) \times \bar{V}_I + \frac{1}{Re}\left(\nabla \times \nabla \times \bar{V}_I\right) = -\nabla\left(p + \frac{|\bar{V}_I|^2}{2}\right)$$

VELOCITY-VORTICITY

Continuity

$$\nabla \cdot \bar{V}_I = 0$$

Kinematic Definition of Vorticity

$$\nabla \times \bar{V}_I = \bar{\omega}_I$$

Vorticity Transport

$$\frac{\partial \bar{\omega}_I}{\partial t} + \nabla \times \left(\bar{\omega}_I \times \bar{V}_I\right) + \frac{1}{Re}\left(\nabla \times \nabla \times \bar{\omega}_I\right) = 0$$

UNSTEADY INCOMPRESSIBLE NAVIER-STOKES EQUATIONS

BODY FIXED (APPARENT) OBSERVER

PRIMITIVE VARIABLES

Continuity

$$\nabla \cdot \bar{V} = 0$$

Linear Momentum (Bernoulli's Form)

$$\underbrace{\frac{\partial \bar{V}}{\partial t} + \bar{\alpha}_B(t) \times \bar{r}} + \underbrace{\left(\nabla \times \bar{V}\right) \times \bar{V} + 2\Omega_B(t) \times \bar{V}} + \frac{1}{Re}\left(\nabla \times \nabla \times \bar{V}\right) =$$

$$\underbrace{-\nabla\left(p + \frac{|\bar{V}|^2}{2} + \bar{a}_{B/I}(t) \cdot \bar{r} - \frac{|\bar{\Omega}_B(t) \times \bar{r}|^2}{2}\right)}$$

VELOCITY-VORTICITY

Continuity

$$\nabla \cdot \bar{V}_I = 0$$

Kinematic Definition of Vorticity

$$\nabla \times \bar{V}_I = \bar{\omega}_I$$

Vorticity Transport

$$\frac{\partial \bar{\omega}_I}{\partial t} + \nabla \times \left(\bar{\omega}_I \times \bar{V}\right) + \frac{1}{Re}\left(\nabla \times \nabla \times \bar{\omega}_I\right) = 0$$

Kinematic Relationship Between Apparent and Inertial Velocity

$$\bar{V} = \bar{V}_I - \bar{V}_{B/I}(t) - \bar{\Omega}_B(t) \times \bar{r}$$

- Solve For Inertial Velocity and Inertial Vorticity Directly in Body Fixed Frame
- Form of Governing Eqs. Unaltered

Inertial Velocity Boundary Conditions Remain Unaltered

Only Differences Are

- Inertial Vorticity Advects with Apparent Velocity

- Additional Vorticity is Created at Body Surface Due to Acceleration of Body

For Two-Dimensional Flow, use

DISTURBANCE STREAM FUNCTION-VORTICITY FORMULATION IN GENERALIZED BODY FIXED COORDINATES

Definition of Disturbance Stream Function (Deviation from Uniform Flow)

$$\psi_{INERTIAL} = [y + \Psi_o] + \psi_I^{DIS}(\xi^1, \xi^2, t)$$

Where Ψ_o is at yet an Unknown Integration Constant Representing a Displacement of the ZERO STREAMLINE at INFINITY

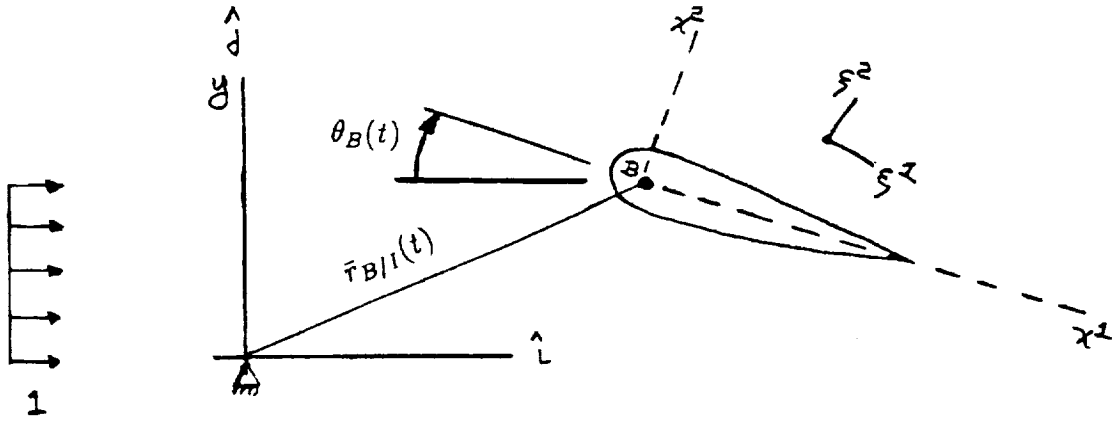

Arbitrarily Maneuvering

$$\psi_{INERTIAL} = [x^2 \cos\theta(t) - x^1 \sin\theta(t) + \Psi_o] + \psi_I^{DIS}(\xi^1, \xi^2, t)$$

ELLIPTIC STREAM FUNCTION PROBLEM

$$\frac{\partial}{\partial \xi^1}\left(\frac{g_{22}}{\sqrt{g}}\frac{\partial \psi_I^{DIS}}{\partial \xi^1}\right)+\frac{\partial}{\partial \xi^2}\left(\frac{g_{11}}{\sqrt{g}}\frac{\partial \psi_I^{DIS}}{\partial \xi^2}\right)=-\sqrt{g}\omega_I^3$$

Subject to the Boundary Conditions

$$\psi_I^{DIS}=0 \text{ at INFINITY}$$

$$\psi_I^{DIS}=\{x^2[V_{B/I}^1(t)-\cos\theta(t)]-x^1[V_{B/I}^2(t)-\sin\theta(t)]-\frac{\Omega_B(t)}{2}[(x^1)^2+(x^2)^2]\}$$

Along Body Surface

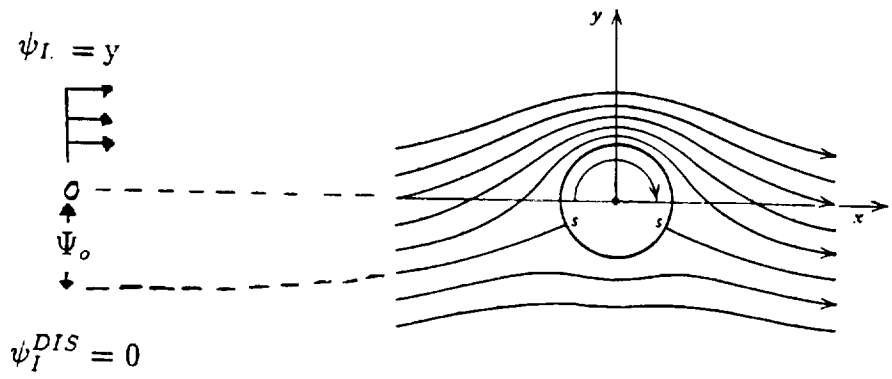

at INFINITY

STRICTLY AN INVISCID EFFECT (ALL VISCOUS DISTURBANCES DISSIPATE WELL BEFORE INFINITY)

DIRECTLY REPRESENTS UNDERLYING INVISCID CIRCULATION SET BY AN INVISCID KUTTA CONDITION AT TRAILING EDGE

KUTTA CONDITION FOR Ψ_o (WEDGE TRAILING EDGE)

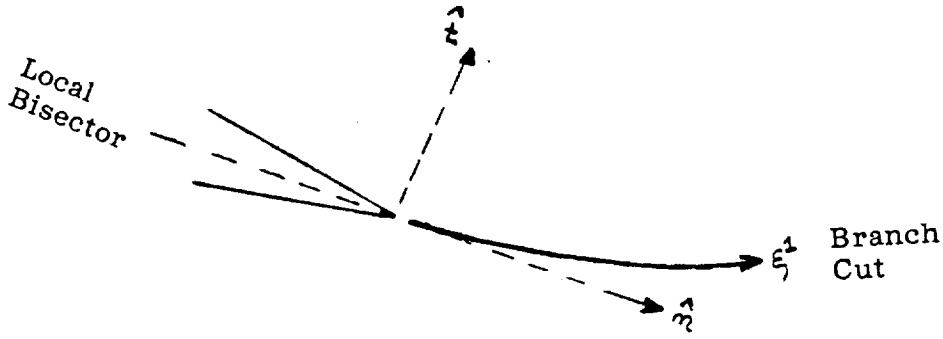

$$\lim_{\substack{\vec{TE} \\ BRANCH\,CUT}} \{\frac{1}{\sqrt{g_{11}}} \frac{\partial \psi^{DIS}_{INVISCID}}{\partial \xi^1}\} =$$
$$\left[\{\cos\theta(t) - V^1_{B/I}(t) + x^2\Omega_B(t)\}\hat{e}_1 + \{\sin\theta(t) - V^2_{B/I}(t) - x^1\Omega_B(t)\}\hat{e}_2\right] \cdot \hat{t}$$

VORTICITY TRANSPORT

$$\sqrt{g}\frac{\partial \omega_I^3}{\partial t} + \frac{\partial}{\partial \xi^1}\left(\omega_I^3[\sqrt{g}V^1]\right) + \frac{\partial}{\partial \xi^2}\left(\omega_I^3[\sqrt{g}V^2]\right) = \frac{1}{Re}\{\frac{\partial}{\partial \xi^1}\left(\frac{g_{22}}{\sqrt{g}}\frac{\partial \omega_I^3}{\partial \xi^1}\right) + \frac{\partial}{\partial \xi^2}\left(\frac{g_{11}}{\sqrt{g}}\frac{\partial \omega_I^3}{\partial \xi^2}\right)$$

where

$$\sqrt{g}V^1 = \frac{[\{\cos\theta(t) - V_{B/I}^1(t) + x^2\Omega_B(t)\}\hat{e}_1 + \{\sin\theta(t) - V_{B/I}^2(t) - x^1\Omega_B(t)\}\hat{e}_2]\cdot\bar{e}_1}{g_{11}/\sqrt{g}} + \frac{\partial \psi_I^{DIS}}{\partial \xi^2}$$

$$\sqrt{g}V^2 = \frac{[\{\cos\theta(t) - V_{B/I}^1(t) + x^2\Omega_B(t)\}\hat{e}_1 + \{\sin\theta(t) - V_{B/I}^2(t) - x^1\Omega_B(t)\}\hat{e}_2]\cdot\bar{e}_2}{g_{22}/\sqrt{g}} + \frac{\partial \psi_I^{DIS}}{\partial \xi^1}$$

Subject to the Boundary Condition

$$\omega_I^3 = 0 \quad \text{at Infinity}$$

and Along the Body

$$-\sqrt{g}\omega_I^3 = \frac{\partial}{\partial \xi^1}\left(\frac{g_{22}}{\sqrt{g}}\frac{\partial \psi_I^{DIS}}{\partial \xi^1}\right) + \frac{\partial}{\partial \xi^2}\left(\frac{g_{11}}{\sqrt{g}}\frac{\partial \psi_I^{DIS}}{\partial \xi^2}\right)$$

Subject to the Constraint

$$\frac{g_{11}}{\sqrt{g}}\frac{\partial \psi_I^{DIS}}{\partial \xi^2} = [\{\cos\theta(t) - V_{B/I}^1(t) + x^2\Omega_B(t)\}\hat{e}_1 + \{\sin\theta(t) - V_{B/I}^2(t) - x^1\Omega_B(t)\}\hat{e}_2]\cdot\bar{e}_2$$

THE PITCH UP MANEUVER OF VISBAL AND SHANG

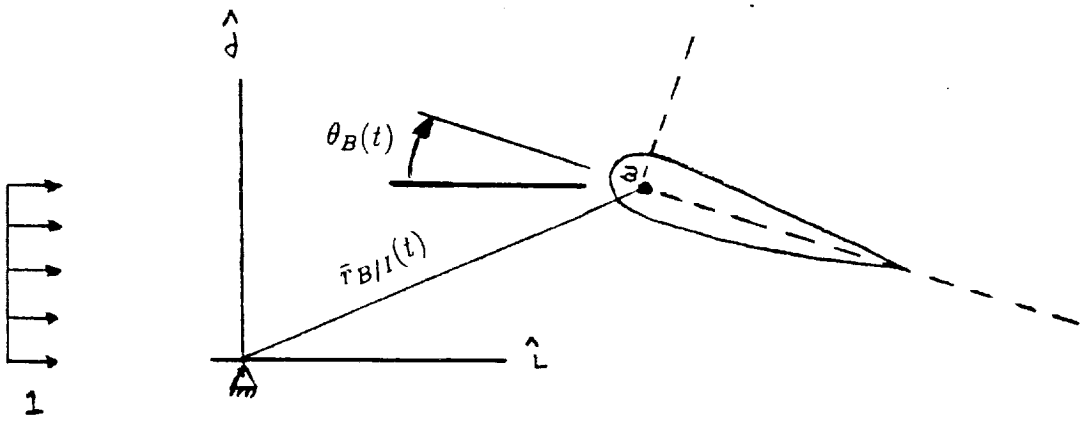

$$\bar{r}_{B/I}(t) = 0$$

$$\bar{V}_{B/I}(t) = 0$$

$$\bar{a}_{B/I}(t) = 0$$

$$\theta_B(t) = \Omega_o \left[t - (\frac{t_o}{4.6})(1 - \exp -(\frac{4.6}{t_o})t) \right]$$

$$\Omega_B(t) = -\Omega_o \left(1 - \exp -(\frac{4.6}{t_o})t \right)$$

$$\alpha_B(t) = -(\frac{4.6}{t_o})\Omega_o \exp -(\frac{4.6}{t_o})t$$

Where

Ω_o - Nondimensional Pitch Rate; 0.2

t_o - Nondimensional Acceleration Time; 0.5

x_o - Pivot Axis Location Measured from Airfoil LE; 0.25

SUMMARY

- Developed Navier-Stokes Analysis for forced unsteady separated flow using stream function and vorticity; the latter is the variable of the greatest physical significance.
- Based on the present analysis. Here is our response to some of the questions posed.

o What is the process whereby fluid particles in the vicinity of the wall are ejected from that region and coalesce into an outer-layer vortex structure?	→ Formation of counterclockwise vortex in boundary layer leads to formation of dynamic stall vortex.
o How is this mechanism modified by transitional effects? Compressibility? Turbulence? Three-dimensionality? Surface Curvature? Suction or blowing?	→ Future work with this analysis will help to answer part of this question.
o Is the unsteady separation phenomenon associated with dynamic stall unique to rapidly pitching wings, or can it be studied on fixed surfaces as well?	→ No, the phenomenon is not unique. Our results for the stationary Joukowsky airfoil at very high angle of attack show a similar flow structure.
o Can we detect incipient breakdown of the attached shear layer in time to influence or delay detachment?	→ It appears that it is possbile to delay detachment.
o Is it realistic to hope to suppress unsteady separation, or should we be spending our effort in controlling the flow after separation has occurred?	→ ?
o Dynamic stall has been observed on airfoils experiencing leading-edge stall, as well as trailing-edge stall. Is the unsteady separation mechanism different in these two cases?	→ We would like to conduct these experiments to accurately respond to this question.
o What will we need to know about the unsteady flow development in order to actually implement control technologies for suppression of unsteady separation on rapidly pitching wings?	→ —

Computed Unsteady Flows of Airfoils at High Incidence

K.-Y. Fung, Jeffrey Currier, and S. O. Man
University of Arizona
Tucson, AZ 85721

The flow over an airfoil at an angle of attack above the static stall angle would ordinarily be massively separated. Under dynamic conditions, the onset of stall can be delayed to an angle, depending on the type of unsteadiness, the freestream Mach number and the transition process, much higher than that for static stall. The stall onset mechanisms under dynamic conditions are unclear. Due to extreme difficulties involved, experimental investigations, so far, have provided insufficient information about the flow field for the identification of the onset mechanisms. A course of classical boundary layer analysis augmented with numerical experiments and measured data is chosen here instead, with the hope that the identification of onset mechanisms can be more systematic and quantitative.

To avoid confusion in terminology, the onset of stall, for the cases studied here, is defined as the conditions at which the peak suction on the airfoil attains the maximum value before the airfoil reaches the maximum angle of attack in a course of upward pitching motions. It is found that the onset of stall is delayed with increased frequency of oscillation as long as the flow remains subsonic. Once the flow is locally supercritical, the onset of stall becomes much less sensitive to increased frequency but has a strong dependency on the freestream Mach number. The dependency of the onset on the Mach number is not affected by the airfoil geometry as much as its dependency on the reduced frequency is. Before the onset of stall, the instantaneous pressure distributions over the airfoil can be considered quasi-steady, and are predictable using inviscid theory.

Two airfoils, the NACA 0012 and the Vr7, which have different dynamic stall characteristics are chosen for our study here. An analysis of the boundary layers on these two airfoils at various conditions suggests that separation bubble bursting, or the failure of reattachment of the separating boundary layer, deserves more investigations and attention as a key onset mechanism than it has been given. This analysis, which is based on computed inviscid flows

and classical theories for static stall, suggests that once the flow becomes locally supersonic, the onset of stall is a result of the interaction between the forming shock and the steepening laminar boundary layer. It also gives an explanation to the differences between the onset characteristics of the two airfoils.

The sensitivity of stall onset on transition is studied by computing the flow over an airfoil at conditions near stall and varying the switch-on location of the turbulence model for the Reynolds averaged Navier-Stokes code used for this study. Figure 1a shows a computed lift history of the NACA 0012 airfoil for the a freestream Mach number of 0.301 and at a stationary incidence angle of 11.5 degree. A turbulence model is turned on at 2% chord. The flow is subsonic everywhere throughout the history for this lower angle of attack. Notice that a steady state is reached after roughly 1500 iterations. However, when the turbulence model is turned on at 5% chord, Figure 1b, the lift history fluctuates wildly (solid line) if nonuniform time steps are used, and periodically if a time accurate marching method (dotted line) is used. A leading edge separation bubble is observed in the boundary layer of these flows. The size of the separation bubble is directly related to the turn-on location of the turbulence model, which causes the separating boundary layer to reattach if conditions allow. A move of this location from 2% to 5% changes the stability of the flow. The fluctuations in the latter case are due to unsteady separation and subsequent reattachment of the bubble. A change of incidence angle from 11.5 to 12.5 has a drastic effect on the lift history. With the turbulence model turned on at 2%, not only does the lift not reach a steady value as for the lower incidence case, it fluctuates periodically with large amplitudes, Figure 1c. As the lift reaches a high value, a local supersonic region is form near the leading edge. The separation bubble beneath this region interact strongly with the supersonic flow. A separation vortex is formed when the supersonic region reaches a certain size. The vortex then interacts as it moves with the boundary layer, causing the lift to drop to a value below zero, where another cycle of lift fluctuation begins. For 12.5 degrees, a stable solution can be found if the turbulence model is turned on before 1% chord. For an even higher angle of attack close to the static stall value, at 13.25 degrees, a mere change of transition locations from 1.25 to 1.35%, which differ by one grid point and are before and after the computed shock location respectively, causes the flow from reattachment to massive separation. For a lower freestream Mach number, 0.185, separation is less sensitive to the transition location as the angle of attack is increased.

Figure 1a, M=0.301 Alpha=11.5 T.P.@ 2%

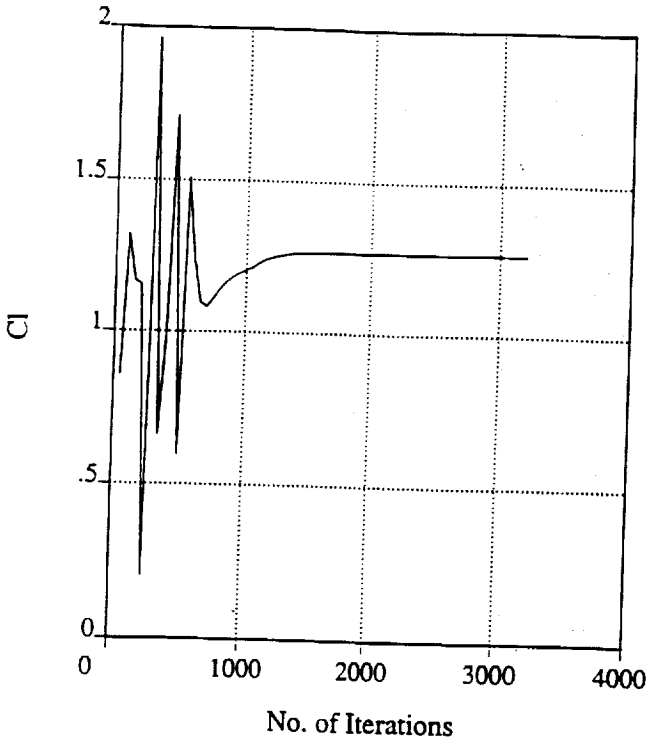

Figure 1b, M=0.301 Alpha=11.5 T.P.@ 5%

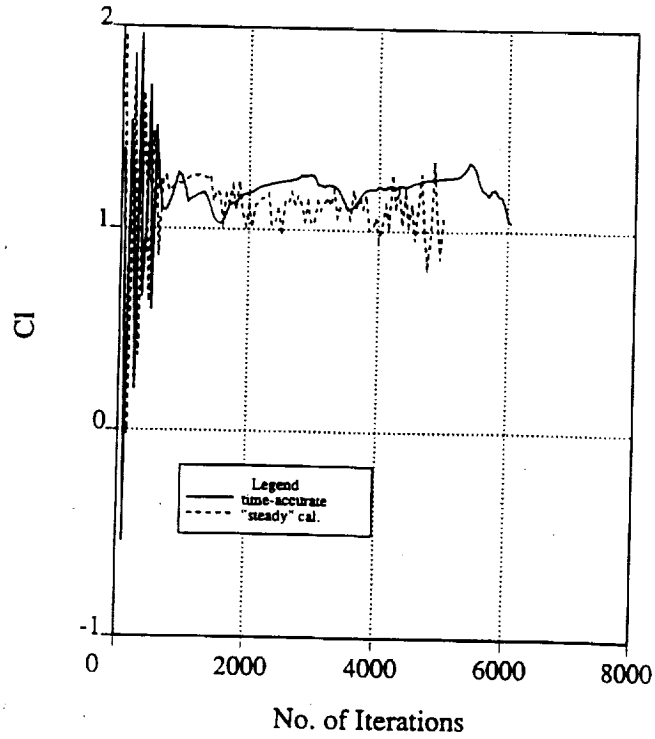

Figure 1c, M=0.301 Alpha=12.5 T.P.@ 2%

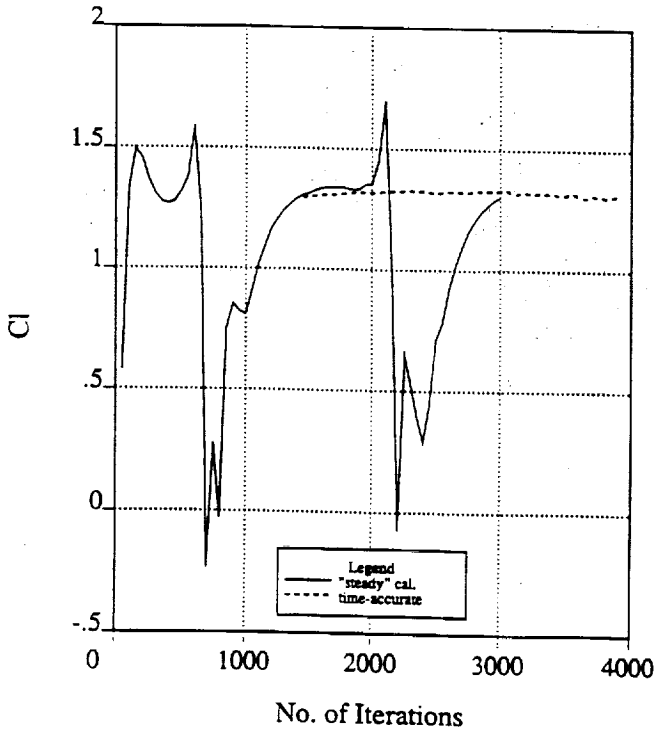

Figure 1, Lift history computed using a Navier-Stoke solver with the turbulence turned on at different locations.

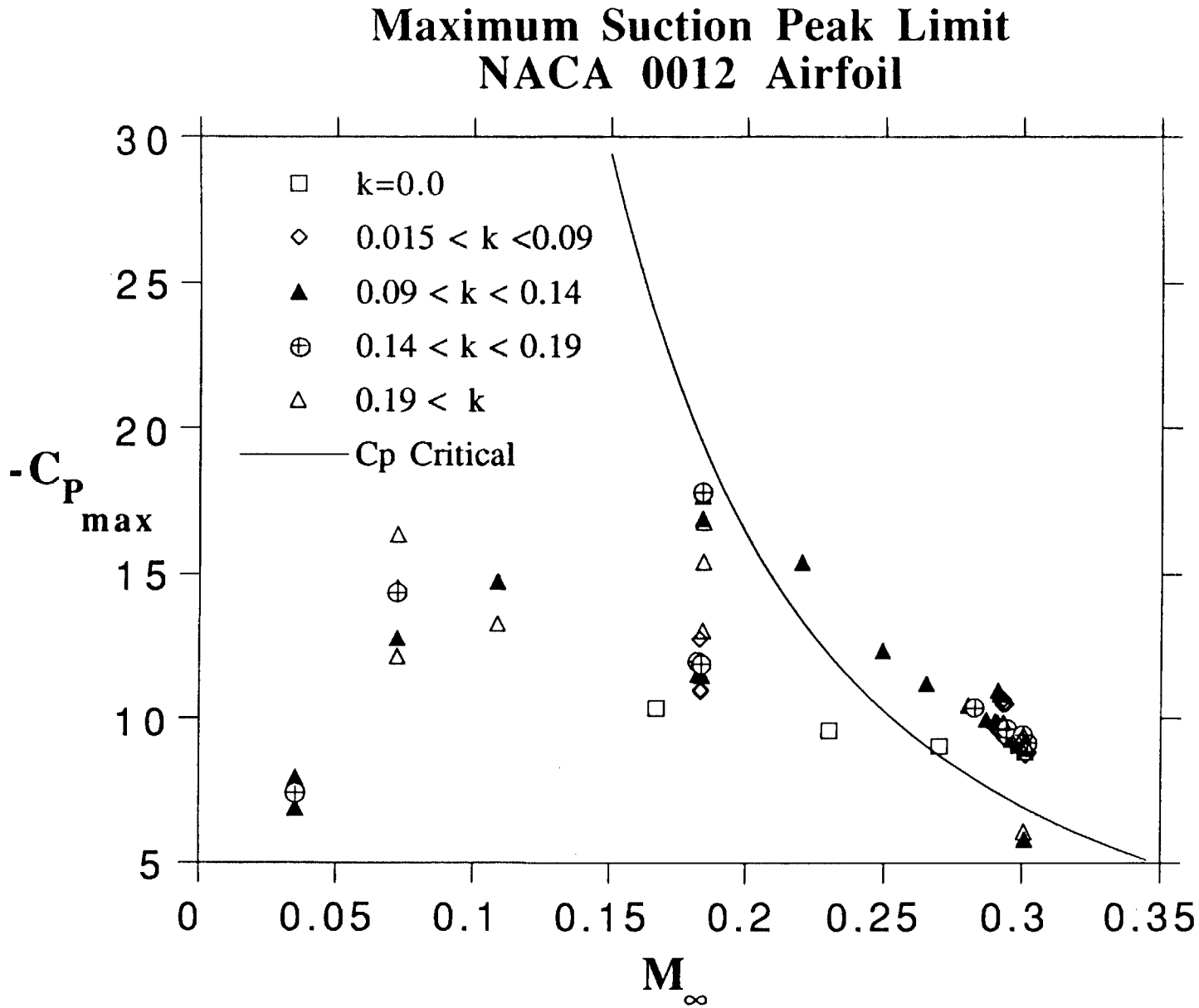
Maximum Suction Peak Limit
NACA 0012 Airfoil
k=0.0
0.015 < k <0.09
0.09 < k < 0.14
0.14 < k < 0.19
0.19 < k
Cp Critical
-C_P max
M_∞
30
25
20
15
10
5
0
0.05
0.1
0.15
0.2
0.25
0.3
0.35

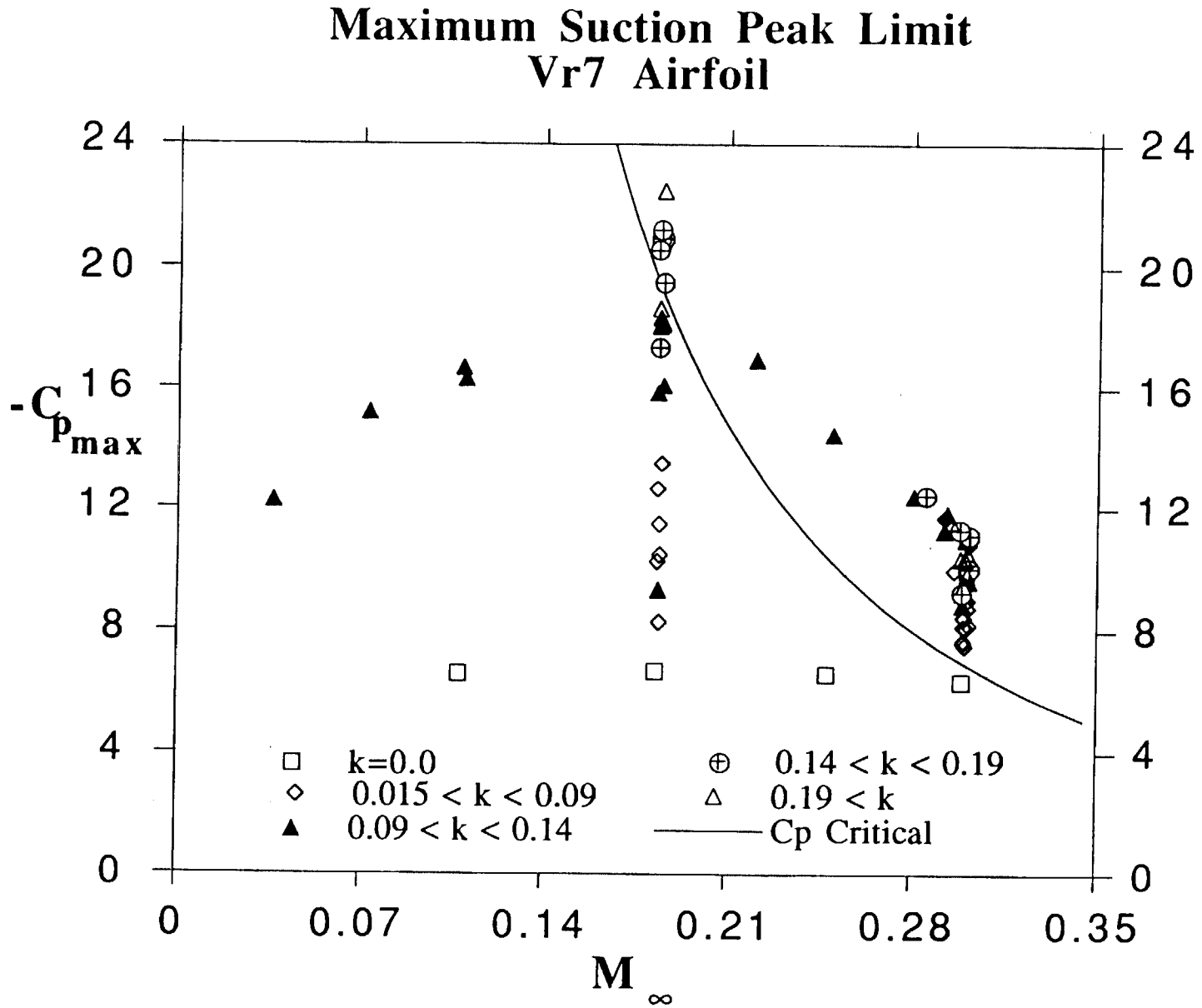
Maximum Suction Peak Limit
Vr7 Airfoil
-Cp max
M ∞
0
4
8
12
16
20
24
0
0.07
0.14
0.21
0.28
0.35
k=0.0
0.015 < k < 0.09
0.09 < k < 0.14
0.14 < k < 0.19
0.19 < k
Cp Critical

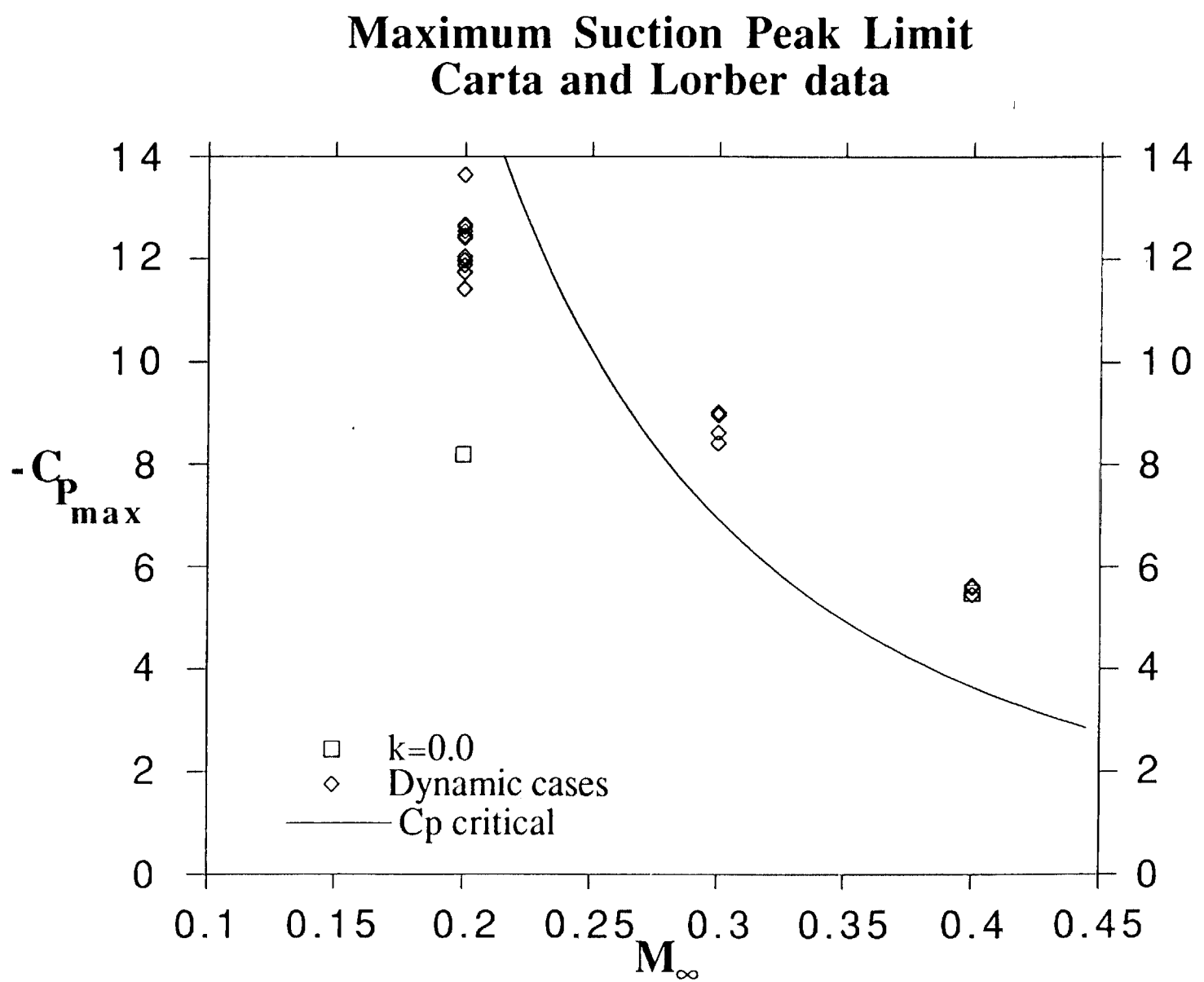
Maximum Suction Peak Limit
Carta and Lorber data
-C_Pmax
M∞
k=0.0
Dynamic cases
Cp critical
0
2
4
6
8
10
12
14
0.1
0.15
0.2
0.25
0.3
0.35
0.4
0.45

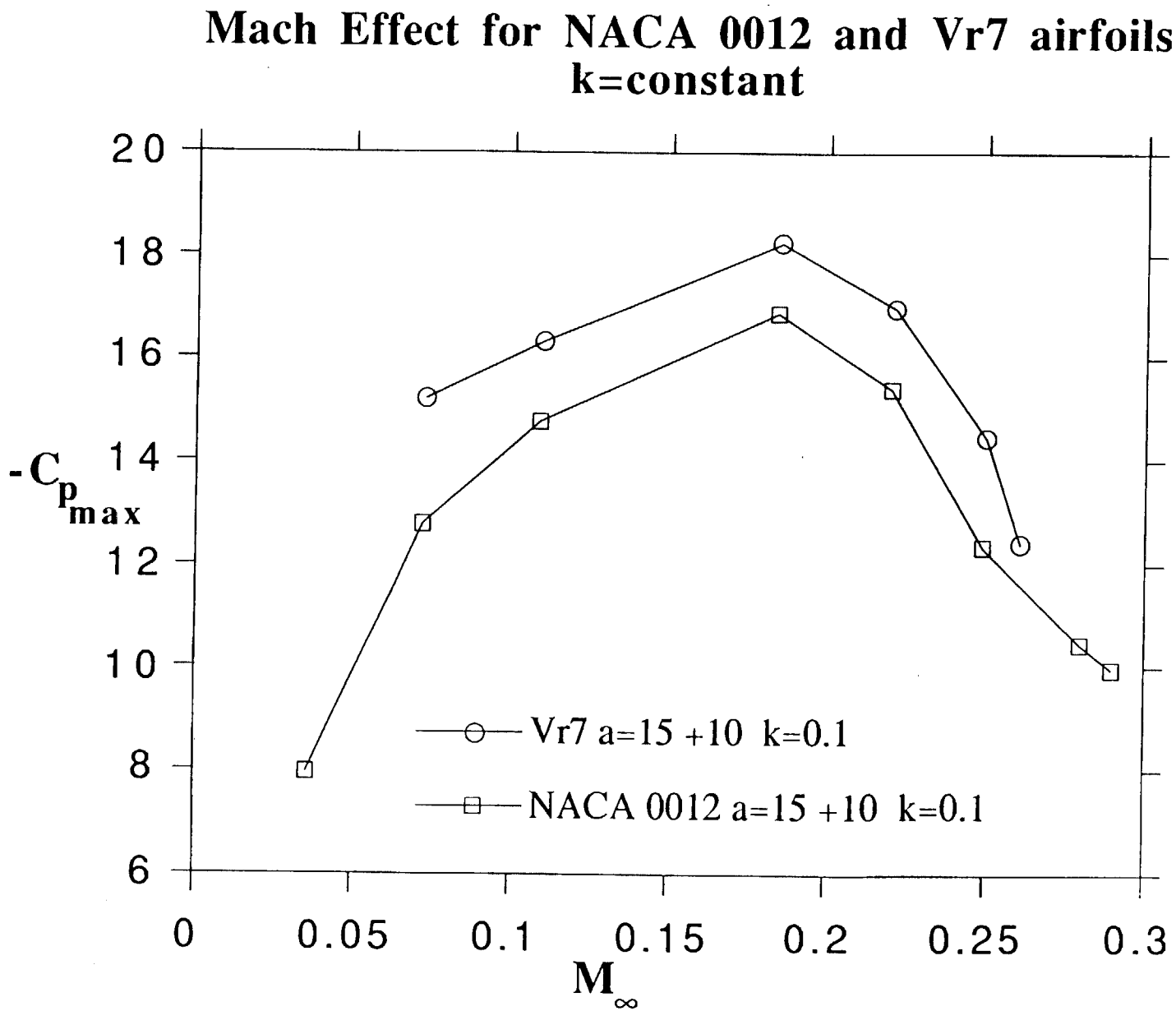
Mach Effect for NACA 0012 and Vr7 airfoils
k=constant
20
18
16
14
12
10
8
6
-Cp max
0
0.05
0.1
0.15
0.2
0.25
0.3
M∞
Vr7 a=15 +10 k=0.1
NACA 0012 a=15 +10 k=0.1

Frequency Effect for NACA 0012 and Vr7 airfoils

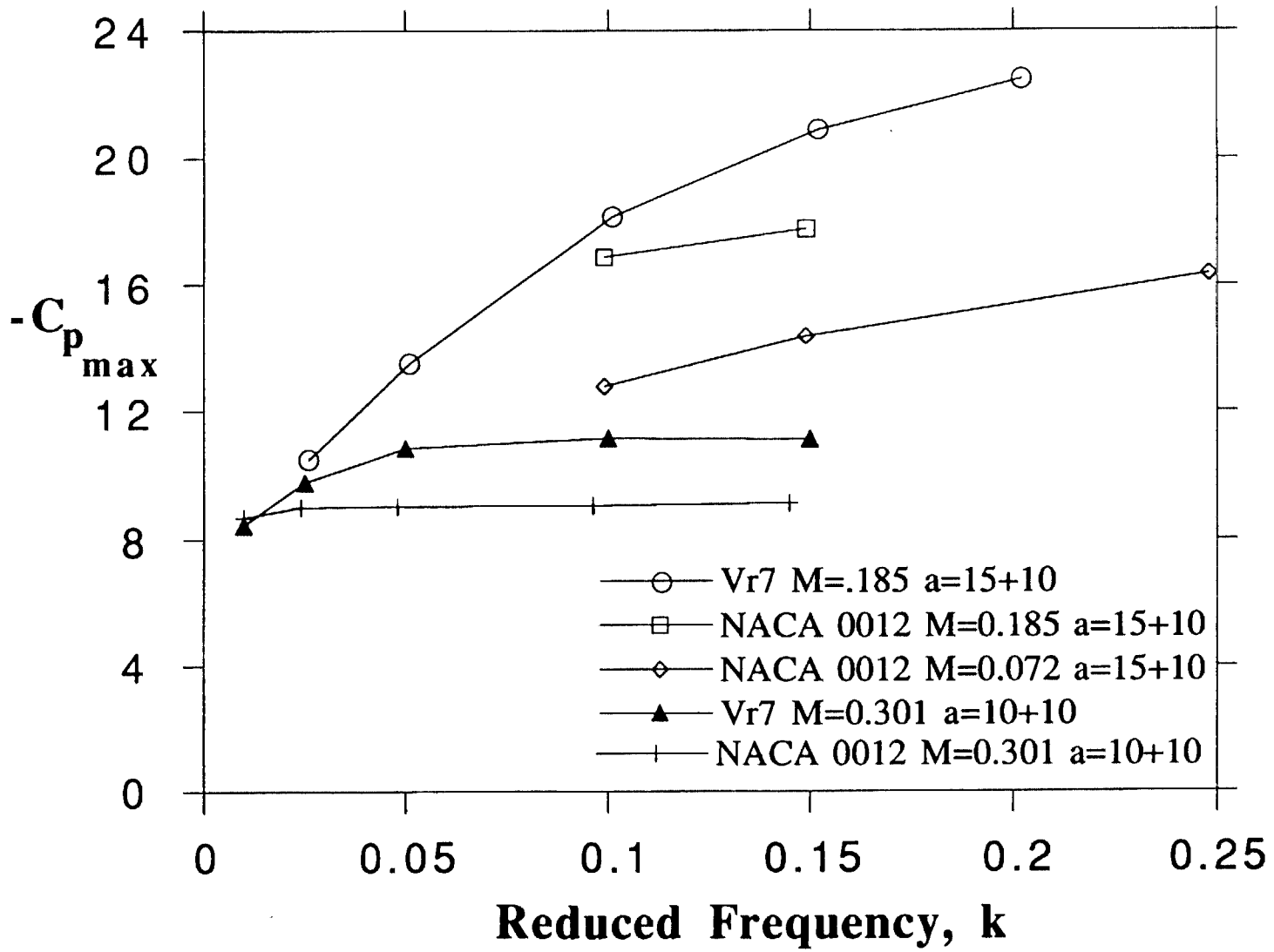

THE SUCTION PEAK ANALYSIS

- THE ONSET OF STALL IS THE CONDITION AT WHICH THE PEAK SUCTION ON THE AIRFOIL ATTAINS THE MAXIMUM VALUE BEFORE THE AIRFOIL REACHES THE MAXIMUM ANGLE OF ATTACK IN A COURSE OF UPWARD PITCHING MOTIONS PAST THE STATIC STALL ANGLE

OBSERVATIONS

- MAXIMUM SUCTION PEAK INCREASES WITH k FOR MACH-SUBCRITICAL FLOW
- DECREASES WITH MACH NUMBER FOR MACH-SUPERCRITICAL FLOW
- QUASI-STEADY FLOW BEFORE STALL ONSET

WHAT ARE THE SEPARATION MECHANISMS?

- SHOCK INDUCED SEPARATION
- SEPARATION BUBBLE BURSTING
- TURBULENT SEPARATION

Experimental and Computed Pressures

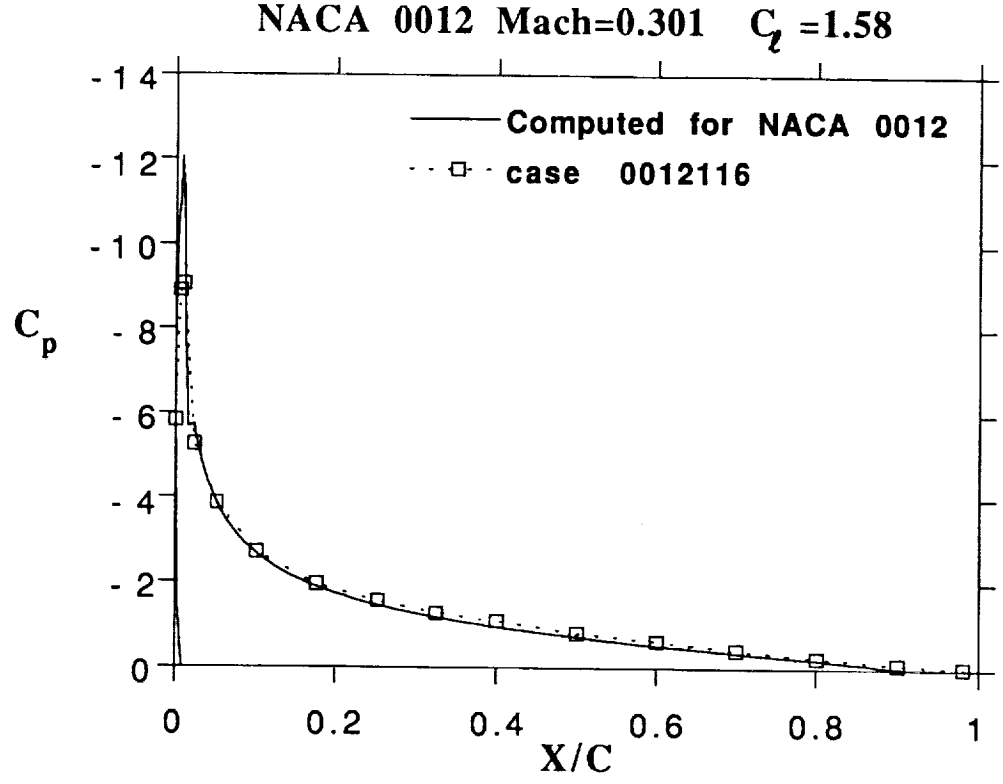

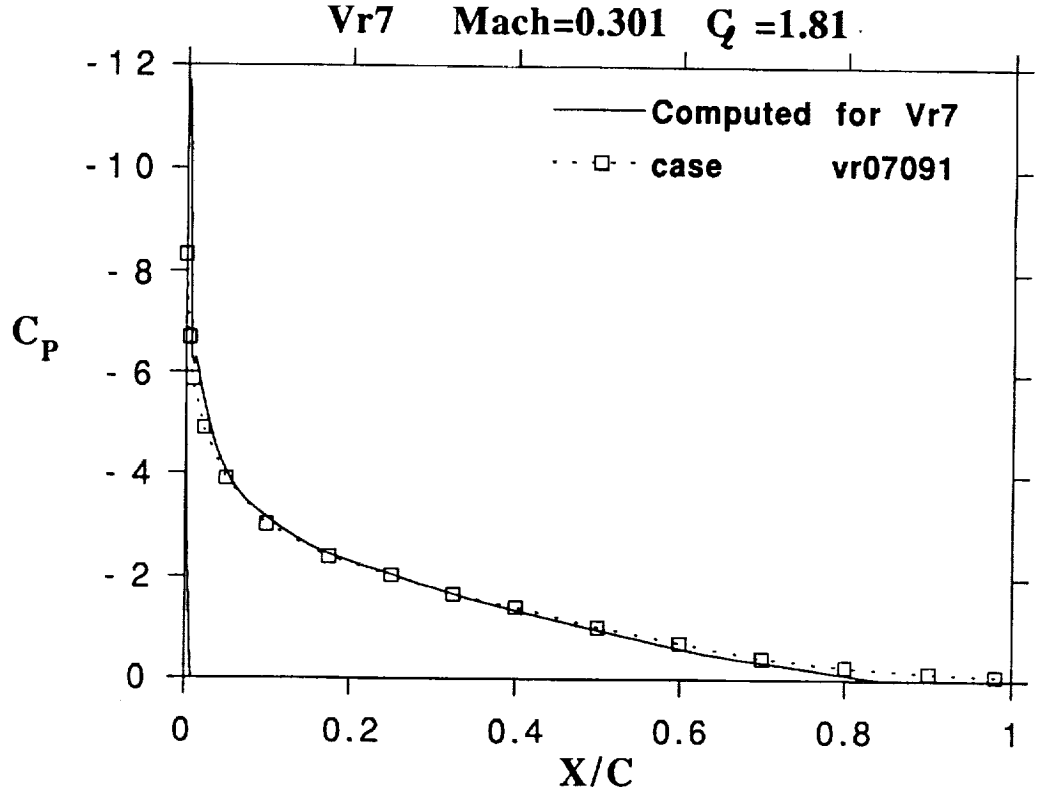

MOMENTUM THICKNESS AT SEPARATION

$$\delta_{s'} = 3.7\sqrt{\frac{0.441}{R}\left(\frac{U}{U_\infty}\right)^{-6}\int_0^{S'}\left(\frac{U}{U_\infty}\right)^{5} d\left(\frac{S'}{c}\right)}$$

CURLE AND SKAN'S BURSTING PARAMETER **K**

$$K = \frac{R_{\delta_{S'}}}{\sqrt{R}} \qquad R_{\delta_{S'}} = \frac{U_{S'}\delta_{S'}}{\upsilon}$$

Curle and Skan's Bubble Bursting Criterion

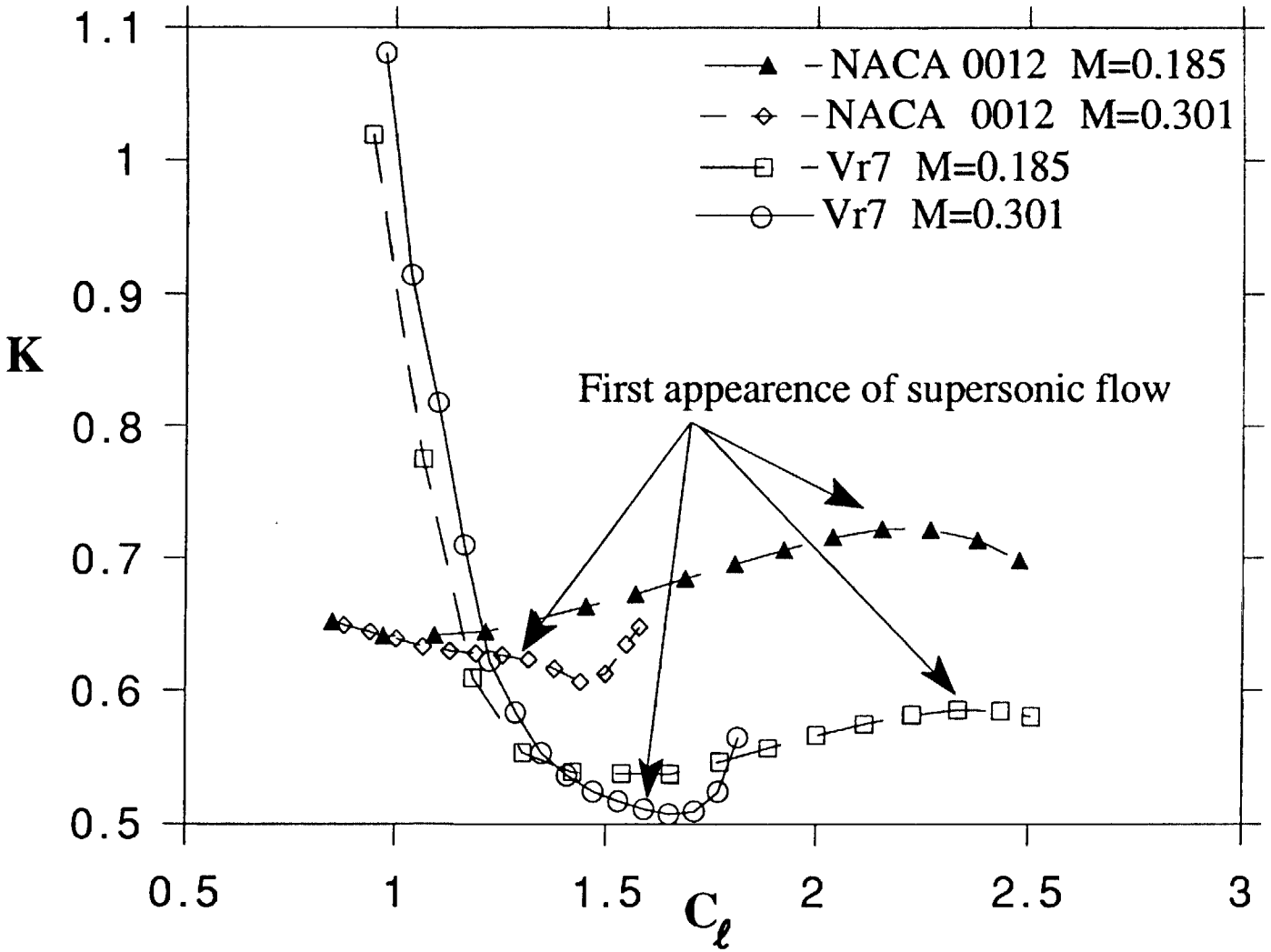

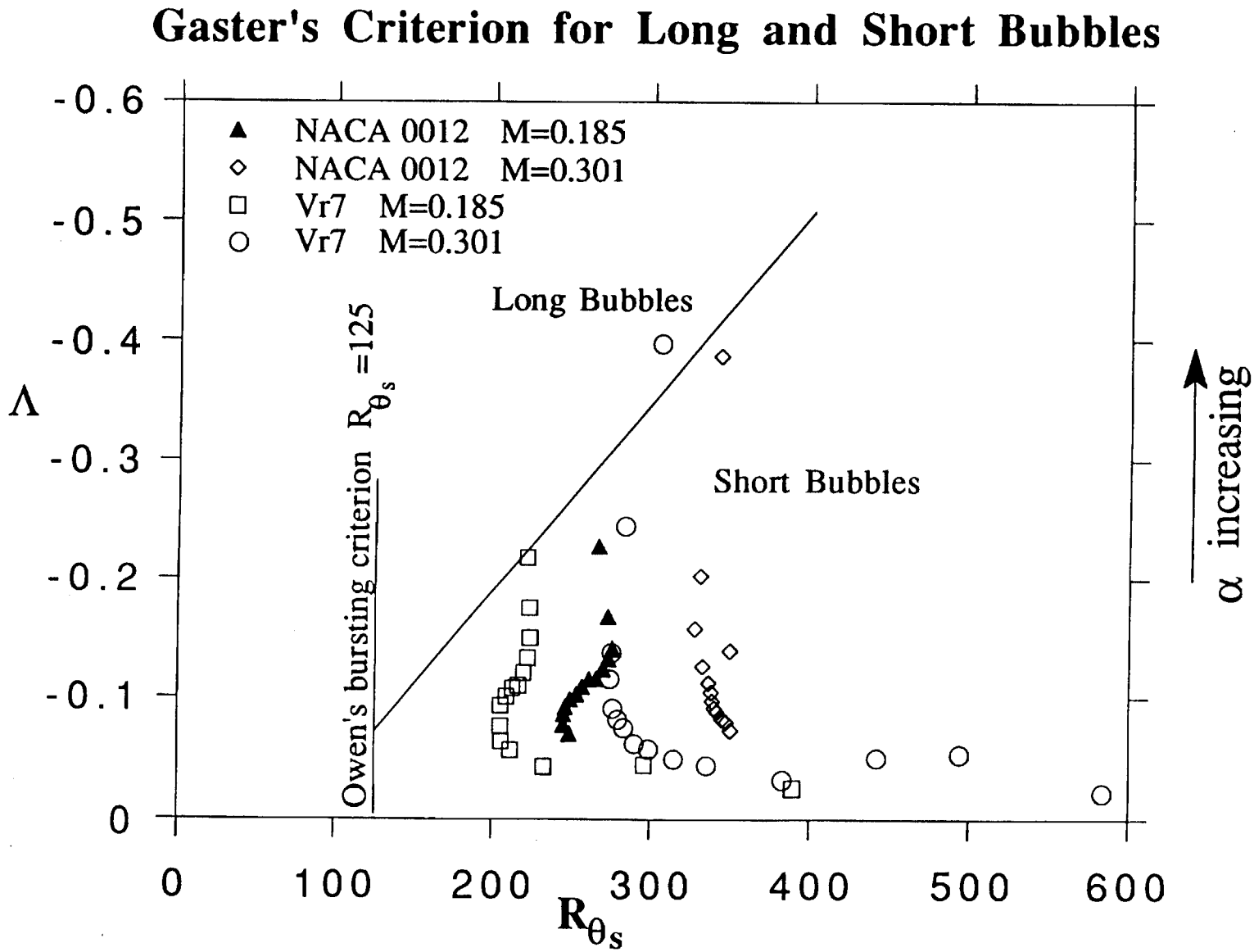
Gaster's Criterion for Long and Short Bubbles
NACA 0012 M=0.185
NACA 0012 M=0.301
Vr7 M=0.185
Vr7 M=0.301
Long Bubbles
Short Bubbles
Owen's bursting criterion R_{θ_s} =125
α increasing
Λ
$R_{\theta s}$
-0.6
-0.5
-0.4
-0.3
-0.2
-0.1
0
0
100
200
300
400
500
600

CONCLUSIONS

- The maximum suction peak is limited by shock formation
- The shape of the leading edge determines the effect of unsteadiness on stall onset
- Before onset of stall the flow can be predicted by quasi-steady theory
- Transition point placement is not sensitive when the angle of attack is below the static stall value
- Transition point placement in supercritical flows is sensitive to movements of only one grid line

Will the Real Dynamic Instability Mechanism Please Be Recognized!

L. E. Ericsson

Lockheed Missiles & Space Company, Inc.
Sunnyvale, California

There is a richness of flow mechanisms that can cause dynamic instability. Only after asking the right questions and carefully considering the answers can the fluid dynamic source of the observed dynamic instability be recognized. This will be illustrated by two carefully chosen examples.

In an aeroelastic test of a 25° swept wing with a symmetric airfoil section[1] (Fig. 1), violent oscillations in the first bending mode occurred if the location of boundary layer transition was not fixed (Fig. 2). The oscillations were of the limit cycle type, the typical result of nonlinear, negative aerodynamic damping (Fig. 3). What is the source of this dynamic instability?

The authors [1] propose a quasi-steady flow mechanism, which would require[2] that the transition-induced effect produces a net negative lift slope over at least the outboard wing sections. That is

$$C_{\ell\alpha} = (C_{\ell\alpha})_{FT} - (\Delta^i C_{\ell\alpha})_{TR} < 0 \qquad (1)$$

where $(C_{\ell\alpha})_{FT}$ is the lift slope with fixed transition and $(\Delta^i C_{\ell\alpha})_{TR}$ is the lift loss due to free transition, which acts similarly to trailing edge stall (Fig. 4). The correct question to ask now is: "Can the resulting slope $C_{\ell\alpha}$ become negative and reach the magnitude needed to cancel the structural damping present in the test?" The experimental results for trailing edge stall[3] (Fig. 5) show that negative lift slope results only at very high angles of attack, $\alpha > 12°$ in Fig. 5. Even if the plunging-induced sectional angle of attack, $\dot{z}/U_\infty$ exceeds the static stall angle, it is varying from $\alpha = 0$ to this maximum value beyond $\alpha = 12°$, and positive damping is produced at $\alpha < 12°$. As a matter of fact, even in the case of the much larger lift loss associated with leading edge stall (midgraph in Fig. 5), negative damping in plunge is only measured when the time average trim angle of attack α_0 is close to the static stall angle[4] (Fig. 6), i.e., $\alpha_o \approx \alpha_s$, not $\alpha_o = 0$ as for the results in Figs. 2 and 3.

In order to find the real dynamic instability mechanism causing the divergent oscillations in Fig. 3 one needs to follow-up on the dynamic stall/dynamic transition analogy. Starting with the conceptually simpler case of pitch oscillations, accounting for the circulation lag and the effect on flow separation of the unsteady boundary layer edge conditions makes it possible tp predict the measured negative damping at stall[4] (Fig.7a). However, the results[6] in Fig.7b show that this dynamic flow mechanism is incomplete. It cannot explain how a 6° pitch oscillation at $\alpha_o = 22°$ can cause the flow to attach to generate time-average lift high above static lift maximum, obtained at $\alpha \approx 10°$. A dynamic flow mechanism is needed that can

energize the boundary layer developed between flow stagnation and separation points to the extent needed to prevent flow separation. The "leading-edge-jet" effect[7] illustrated in Fig. 8 provides such a flow mechanism. As the airfoil leading edge moves upward during the "upstroke", the boundary layer is strengthened by the wall-jet-like moving wall effect and is more difficult to separate. The "rolling leading edge," used in Fig. 8 to illustrate the "leading edge jet" effect, has been investigated in detail[8].

The moving wall effect is of significant magnitude only in the region near the stagnation point, where the boundary layer is thin and, therefore, very sensitive to this wall-jet-like action. A similar moving wall effect on boundary layer transition has been observed on airfoils. Figure 8 illustrates how the plunging and pitching airfoils will have opposite moving wall effects for increasing effective angle of attack, $\dot{z}/U_\infty$ and θ. respectively. Carta's hot film response data[9] (Fig. 9)* show how the adverse (upstream) moving wall effect $\dot{z}(t)$ promotes transition and causes the plunging airfoil to have a longer run of attached turbulent flow prior to stall. As a result, the flow stays attached past 7.5% chord, whereas flow separation occurs forward of 5% chord on the pitching airfoil, which has a shorter turbulent run before stall due to the opposite, transition-delaying, moving wall effect. In addition to showing the opposite moving wall effects for pitching and plunging oscillations, Fig. 9 also demonstrates that the moving wall effect completely dominates over the accelerated flow effect, i.e., the effect of the lessened leeside pressure gradient adversity[8], which is the same for pitching and plunging oscillations. This dominance is found in numerous flow situations both in two-dimensional and three-dimensional flow[10].

The plunging airfoil section of the wing in Figs. 1-3 will experience a transition-promoting moving wall effect on the top side during the "down stroke" of the bending oscillation. On the bottom side, the moving wall effect is the opposite, delaying transition. As a result,a negative lift component is generated which drives the oscillation (Fig. 10). The question one now must ask is: "How can the transition asymmetry generated by the moving wall effect produce a negative load that dominates over the attached flow load, $C_{\ell\alpha}\ \dot{z}/U_\infty$, when it could not in the quasi-steady case discussed earlier, (Eq. (1)?" In the latter case, transition reacts to the change of the pressure gradient at the boundary layer edge due to $\dot{z}/U_\infty$. The test results[9] in Fig. 9 show that the (viscous) moving wall effect completely dominates over this inviscid pressure gradient effect, providing the answer to the question raised.

Wing bending oscillations of the limit cycle type, similar to those for the 25° swept wing (Figs. 1-3), have also been observed on a highly swept wing[11] (Fig. 11). The measured damping shows that the dominant dynamic flow mechanism changed when decreasing the wing sweep to Λ = 55° or less (Fig. 12). The characteristics shown in Fig. 13 rule out shock-induced flow separation as a source of the self-excited oscillation, as was also concluded in Ref. 11, where it was suggested that one or both of the following vortex-induced effects was the source (see Fig. 14). In one case (left diagram), the suggested source is the changing strength of the leading-edge vortex with increasing angle of attack, which due to the associated phase lag can generate a dynamically destabilizing lift component. The mechanism would

*The amplitudes of $\dot{z}(t)/U_\infty$ and $\theta(t)$ are of the same magnitude.

be similar to that for the "spilled" leading-edge vortex in dynamic airfoil stall[7,12]. In the other case (right diagram), the suggested flow mechanism is the breakdown of the leading-edge vortex.

The obvious question that must be answered affirmatively before suggesting candidate flow mechanisms, such as those shown in Fig. 14, is if they can produce the observed data trends (Figs. 12 and 13). In the present case they cannot. The "spilled" leading edge vortex(left diagram in Fig. 14) should cause a dynamically destabilizing effect that increases with increasing angle of attack, as the vortex strength increases. The start of cross flow separation occurs much earlier than at $\alpha = 7°$, where the dynamic instability occurs. That is, the proposed flow mechanism could not produce the observed critical dependence upon angle of attack,limiting the dynamic instability to $7° < \alpha < 10°$ (Fig. 12). The vortex breakdown mechanism (right diagram in Fig. 14) will have a critical angle of attack associated with it; the angle at which breakdown starts occurring on the wing. However, this angle is well beyond $\alpha = 10°$ for $\Lambda \geq 65°$, according to the results obtained by Lambourne and Bryer[13] for a swept wing (Fig. 15). One additional requirement would have been that the phase lag is 180° larger than in the first case (left diagram), as vortex burst causes a loss of lift. Thus, none of the suggested flow mechanisms can have caused the observed self-excited bending oscillations of the highly swept wing.

The photograph of the model[11] (Fig. 16) shows that the variable-sweep, thin outboard wing is preceded by a fixed sweep (67.5°) thick inboard wing or glove. The difference in leading edge radii is illustrated further by the cross-sectional diagram in Fig. 17. Even for the same leading edge sweep angle, the inner and outer wings will start generating leading edge vortices at different angles of attack because of the difference in their leading edge roundness[14]. Using the stall angles for 12 and 9% thick airfoils[3] to represent the inner and outer wings, respectively, one finds that for 67.5° L.E. sweep the respective wings should start developing leading edge vortices at 6.3 and 4.5°. Compressibility-induced apparent sharpening of the leading edge could probably make the very thick inner wing glove (Fig. 17) act as a 12% thick airfoil in incompressible flow, whereas the leading edge of the outer wing becomes practically sharp, causing vortex development to start at $\alpha > 0$. Thus, considering that the inner vortex must gain some strength before it can interact with the outer wing vortex, one can see how the critical α-value shown in Fig. 13 can result. That leading edge roundness does delay the generation of a leading edge vortex, in the manner described in Ref. 14, was shown by comparison with experimental results[15].

When the inner wing starts developing a leading edge vortex, it will trail inboard of the already existing leading edge vortex on the outer wing. That is, the situation is similar to the one existing for a double-delta wing[16] (Fig. 18). The figure shows how the oil flow visualization results are correlated with the position of the (primary) leading edge vortices from outer and inner delta wing leading edges. The measured suction peaks indicate the locations of the vortices. When the angle of attack is increased above a certain critical value, the outer and inner leading edge vortices start to interact with each other, as is illustrated by the oil flow pictures[17] in Fig. 19. At $\alpha = 5°$, the two vortices are separate, as in Fig. 18. At $\alpha = 7°$, however, the two vortices have started to interact (Fig. 19b), and at $\alpha = 10°$ (Fig. 19c) they have combined into one vortex.

When one compares the flow visualization pictures for the double-delta wing planform (Fig. 19) with the oil flow visualization for the swept wing[11] one can see certain similarities. However, a more direct comparison, quantitative rather than qualitative, can be made by comparing the experimental pressure distributions for the double-delta plan form[19] (Fig. 20) and the swept wing[17] (Fig. 21). Figure 20 shows that the inner delta wing vortex, when it interacts with the vortex on the outer wing, causes the sectional loading to increase and shift its center inboard. Noticing that to the spanwise inboard movement for the delta wing[17] (Fig. 20) corresponds a chordwise aft movement on the swept wing[1] (Fig. 21), one can conclude that the inner-outer vortex interactions do indeed cause very similar changes in the load distributions. The oscillation occurred when the load distribution in Fig. 21 changed from that typical for a single leading edge vortex (α = 6.9°) to that typical for the interaction discussed earlier (α = 8°) .

The interaction between inner and outer wing vortices, described above, fits the experimental facts in regard to the observed bending oscillation of the swept wing[11] (Fig. 12). Thus, it produces a critical α - range in which the single vortex loading is being transformed to that resulting from the two interacting vortices. At higher angles of attack, the two vortices are merged into one vortex, and no self-excited bending oscillation will result. Furthermore, the large amplitude pressure oscillations are localized to the wing region where one expects the interaction between the two corotating vortices to take place[11] (Fig. 22).

Figure 23 shows the measured[1] spanwise variation of the local, streamwise angle of attack for Λ = 67.5° and a fuselage angle of attack of α = 7.38°. The solid line shows the variation due to static loads, and the dash-dot lines shows the extreme values $\alpha_o + \Delta\alpha$ and $\alpha_o - \Delta\alpha$ during the down- and up-stroke portions of the bending oscillations. The inner, thick wing-glove is at the constant angle of attack α_o. Consequently, the effective apex of the outer wing does not move, and the only effect of the leading edge vortex is the entrainment-enhancement of the attached flow loads.[18] If one approximates the α_o - curve in Fig. 23 with a straight line, one could apply the analysis method of Ref. 18 directly. In any case, the single leading edge vortex will increase the damping in pitch for the rigid delta wing and the damping in bending for the present swept wing at a rate proportional to sin α . This is essentially the single vortex data trend exhibited in Fig. 12. The deviation is the interaction at 7° < α < 9° between inner and outer vortices. It is also likely to be minor variations due to shock-boundary layer interaction[19]. Thus, what remains is to describe how the vortex interaction at 7 < α < 9° can cause negative aerodynamic damping. Although the interaction is likely to generate a forcing function (buffet) due to general flow unsteadiness, the large amplitude response is caused by negative aerodynamic damping.

Whereas the single vortex effect is almost exclusively due to changing vortex strength, at least in regard to longitudinal aerodynamics, such as the pitch damping for a delta wing[18] or the damping in bending for the present swept wing, in the case of the outer-inner vortex interaction the spanwise movement of the leading edge vortex on the outer wing becomes important. It has been shown by Randall[20] that the leading edge vortex describes spanwise oscillations around its static position (Fig. 24). Thus, during the α - increasing part of the pitch oscillation, the vortex is outboard of its

static position, and during the α-decreasing part it is inboard. The spanwise location of the leading edge vortex for stepwise changing angle of attack is shown in Fig. 25 for a very slender delta wing.[21] The figure shows that for the moderate angle of attack range of interest in the present case, the spanwise location of the vortex is very sensitive to angle of attack. This explains the narrow α-range for outer-inner vortex interaction of the present swept wing.

With the aid of Figs. 21, 23 and 24 one can see how, when the wing angle of attack is increasing, the load distribution will change toward the front-loaded one for the undisturbed wing leading edge vortex. Conversely, the change will be towards the aft-loaded one, generated by the interaction from the glove vortex, when the angle of attack is decreasing. Figure 23 shows that the streamwise angle of attack of the swept wing is decreasing during the bending upstroke, $0 < \omega t > \pi$, and increasing during the bending downstroke, $\pi < \omega t > 2\pi$, with the extreme values reached at $\omega t = \pi/2$ and $\omega t = 3\pi/2$, respectively. Because the apex of the outer wing leading edge is not moving, the phase lags involved will be small. Consequently, the load distribution extremes will occur close to $\omega t = \pi/2$ and $\omega t = 3\pi/2$, and can be illustrated by the results in Fig. 26. Thus, during the bending upstroke, the lift is increased and thereby the bending moment, whereas during the downstroke lift and bending moment are decreased by the vortex interaction. In both cases the dynamic effect is destabilizing, driving the bending oscillations, in agreement with the experimental results[11].

It is essential that the designer recognize and understand the flow mechanism(s) causing dynamic instability for his particular vehicle. In the case of the transition-induced wing bending oscillations[1] (Figs. 1-3) it was suggested that this was a problem relegated to low Reynolds number flows, as on small high-performance gliders, or large transport aircraft with suction to achieve laminar flow. Quite to the contrary, the results[1] are in complete agreement with the general experience in regard to moving wall effects in both two- and three-dimensional flows[10], showing that the closer the flow conditions are to the critical one, the higher the potential of the moving wall effect is. Consequently, the laminar flow extent was not extensive when the divergent oscillations occurred. Instead, transition to turbulent flow took place around mid-chord or earlier, and the problem becomes especially acute for high performance fighter-type aircraft with "flat-top" pressure distributions.

In the case of the bending wing oscillations caused by the interaction between two leading-edge vortices[11] (Figs. 11-13), not recognizing and understanding the flow mechanism causing the oscillation, the investigators focused all efforts on the outer, variable-sweep wing, trying numerous modifications (Fig. 27) without any success whatsoever. If the leading-edge stall strip had been applied to the inner wing glove and not the outer wing, chances are that the wing bending problem would have been eliminated, avoiding the present red-lining of the performance envelope of the aircraft.

When pondering the fact that the misinterpretation of the test results was in both cases made by people with impeccable technical qualifications, one realizes how great the need is for informal meetings of the work-shop-type, such as the present meeting.

REFERENCES

1. Mabey, D. G., Ashill, P. R. and Welsh, B. L., "Aeroelastic Oscillations Caused by Transitional Boundary Layers and Their Attenuation," J. Aircraft, Vol. 24, July 1987, pp. 463-469.

2. Ericsson, L. E., "Comment on Aeroelastic Oscillations Caused by Transitional Boundary Layers and their Attenuation," J. Aircraft, Vol. 25, Oct. 1988, pp. 975-976.

3. McCullough, G. B. and Gault, D. E., "Examples of Three Representative Types of Airfoil - Section Stall at Low Speed," NACA TN2502, 1951.

4. Liiva, J., Davenport, F. J., Gray, L. and Walton, I. C., "Two-Dimensional Tests of Airfoils Oscillating Near Stall," TR 68-13, April 1968, U.S. Army Aviation Labs, Fort Eustis, VA.

5. Ericsson, L. E. and Reding, J. P., "Stall Flutter Analysis," J. Aircraft, Vol. 10, Jan. 1973, pp. 5-13.

6. Halfman, R. L., Johnson, H. C. and Haley, S. M., "Evaluation of High-Angle-of-Attack Aerodynamic Derivative and Stall Flutter Prediction Techniques," NACA TN 2533, 1951.

7. Ericsson, L. E. and Reding, J. P., "Fluid Mechanics of Dynamic Stall, Part I. Unsteady Flow Concepts," J. Fluids and Structures, Vol. 2, 1988, pp. 1-33.

8. Modi, V. J. and Mokhtarian, F., "Joukovski Airfoil with Circulation Control," AIAA Paper No. 85-1772-CP, Aug. 1985.

9. Carta, F. O., "A Comparison of the Pitching and Plunging Response of an Oscillating Airfoil," NASA CR-3172, Oct. 1979.

10. Ericsson, L. E., "Moving Wall Effects in Unsteady Flow," J. Aircraft, Vol. 25, Nov. 1988, pp. 977-990.

11. Dobbs, S. K., Miller, G. D., and Stevenson, J. R., "Self-Induced Oscillation Wind Tunnel Test of a Variable Sweep Wing," AIAA Paper 85-0739-CP, April 1985.

12. Ericcson, L. E. and Reding, J. P., "Dynamic Stall at High Frequency and Large Amplitude," J. Aircraft, Vol. 17, No. 3, March 1980, pp. 136-142.

13. Lambourne, N. C. and Bryer, D. W., "The Bursting of Leading-Edge Vortices - Some observations and Discussion of the Phenomenon," Aer. Res. Council of Great Britain, R&M No. 3282 (1962).

14. Ericsson, L. E. and Reding, J. P., "Approximate Nonlinear Slender Wing Analysis," J. Aircraft, Vol. 14, No. 12, Dec. 1977, pp. 1107-1204.

15. Woodgate, L., "Measurements of the Oscillatory Pitching Moment Derivatives on a Delta Wing with Rounded Leading Edges in Incompressible Flow," Aer. Res. Council, Great Britain, R&M No. 3628, Pt 1, July 1968.

16. Krogmann, P., "Experimentelle und Theoretische Untersuchungen an Doppeldeltaflügeln," Bericht 68A35, Aerodynamische Versuchsanstalt, Göttingen, West Germany, July 1968.

17. Wendts, W. J. Jr. and McMahon, M.C., "An Experimental Investigation of the Flow Fields About Delta and Double-Delta Wings at Low Speeds," NASA CR-521, Aug. 1966.

18. Ericsson, L. E. and Reding, J. P., "Unsteady Aerodynamics of Slender Delta Wings at Large Angles of Attack," J. Aircraft, Vol. 12, No. 9, Sept. 1975, pp. 721-729.

19. Ericsson, L. E., "Dynamic Effects of Shock-Induced Flow Separation," Journal of Aircraft, Vol. 12, No. 2, February 1975, pp. 86-92. (ERRATA, J. Aircraft, Vol. 18, No. 7, July 1981, p.608)

20. Randall, D. G., "Oscillating Slender Wings with Leading-Edge Separation," The Aer. Quarterly, Vol. XVII, Nov. 1966, pp. 311-331.

21. Werlé, H., "Vortices from Very Slender Wings," La Recherche Aérospatiale, No. 109, Nov.-Dec. 1965, pp. 1-12.

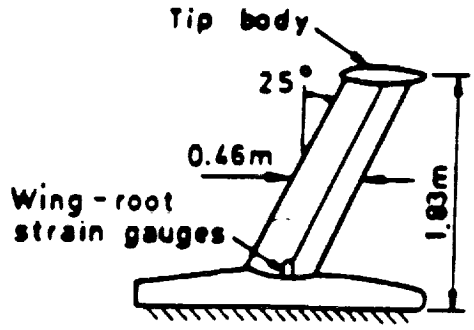

Fig. 1

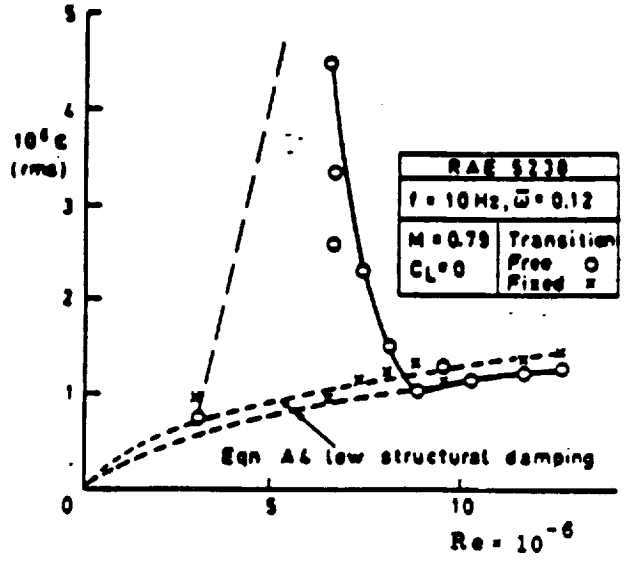

Fig. 2

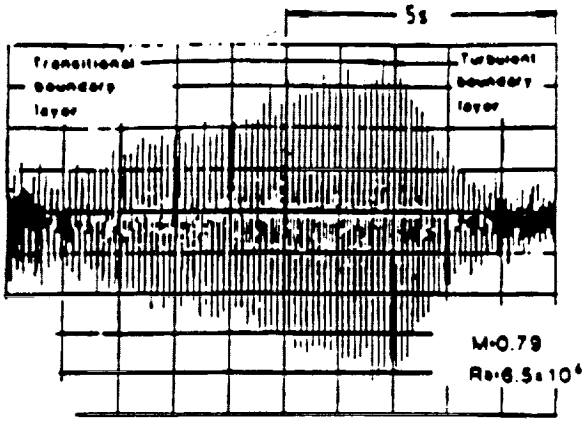

Fig. 3

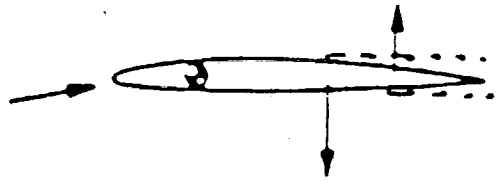

Fig. 4

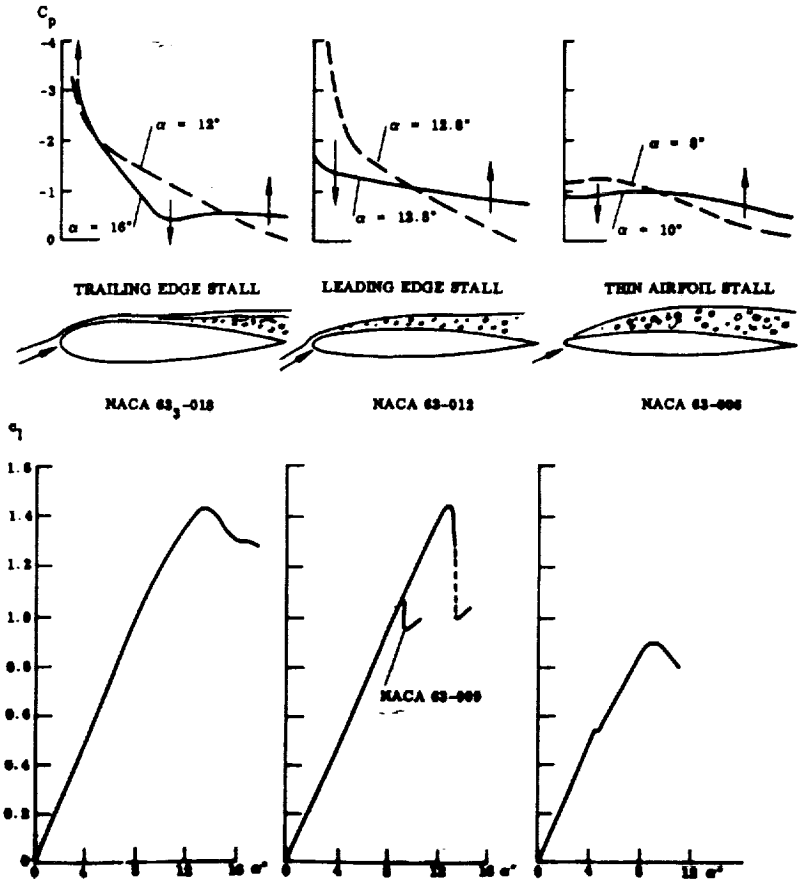

Fig. 5

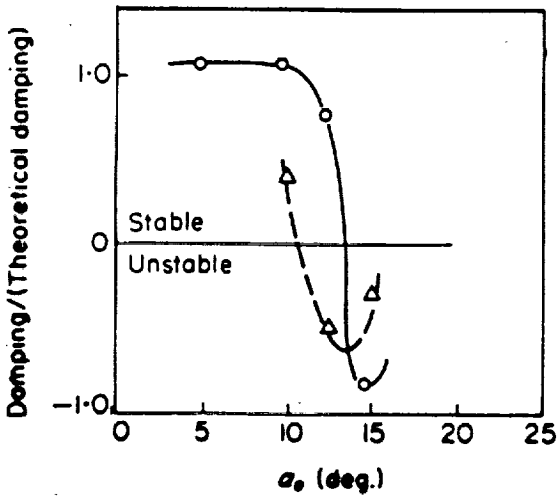

Fig. 6

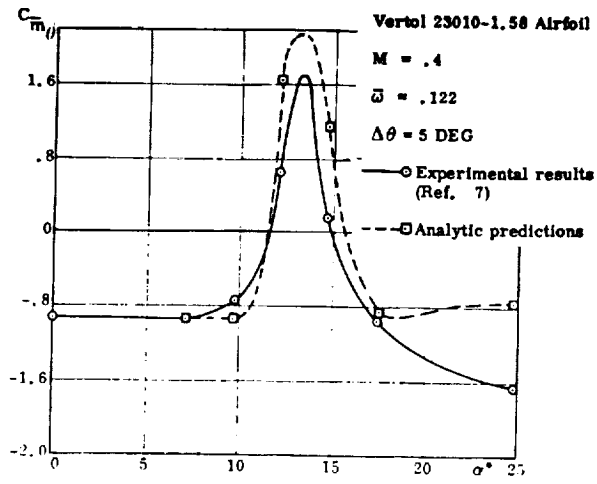

Fig. 7a

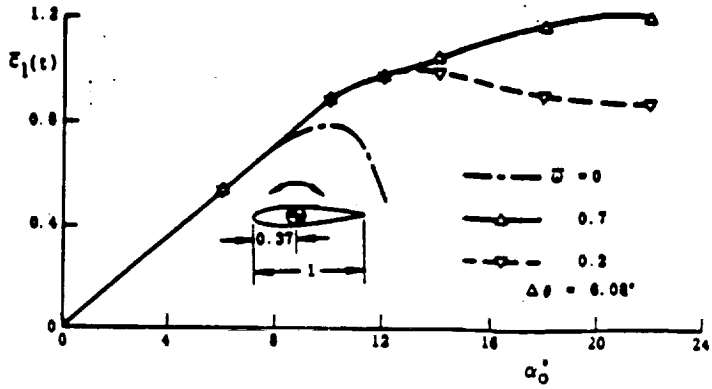

Fig. 7b

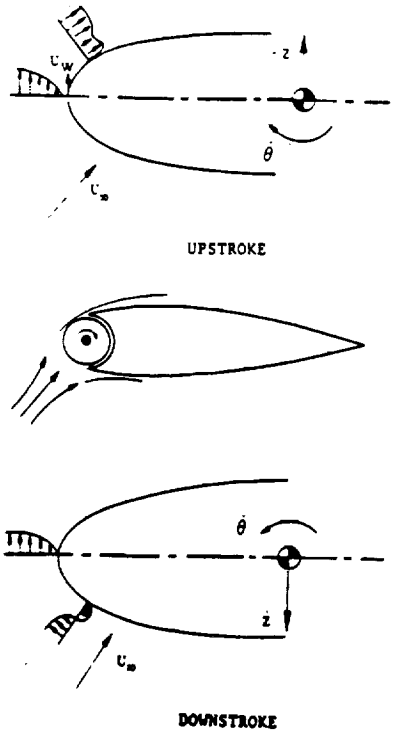

Fig. 8

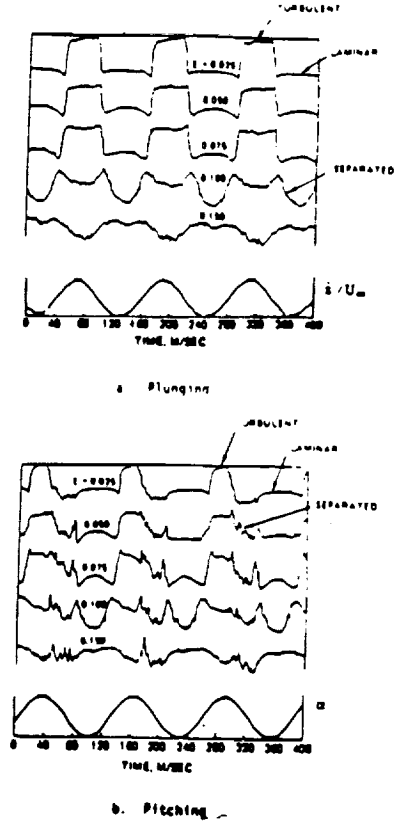

Fig. 9

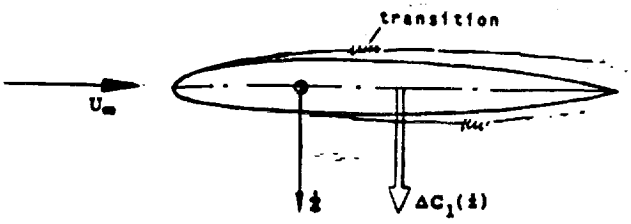

Fig. 10

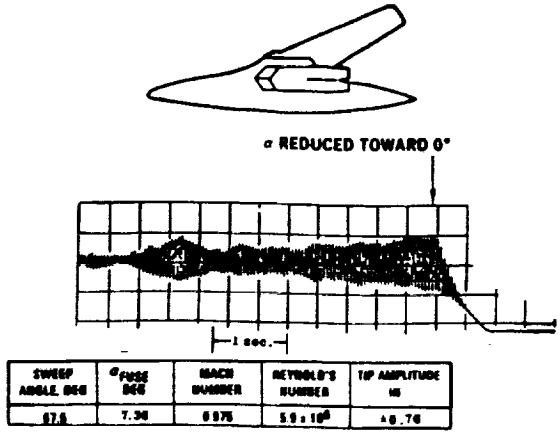

SWEEP ANGLE, DEG	α_{FUSE} DEG	MACH NUMBER	REYNOLD'S NUMBER	TIP AMPLITUDE IN
67.5	7.36	0.975	5.9×10^6	±0.76

Fig. 11

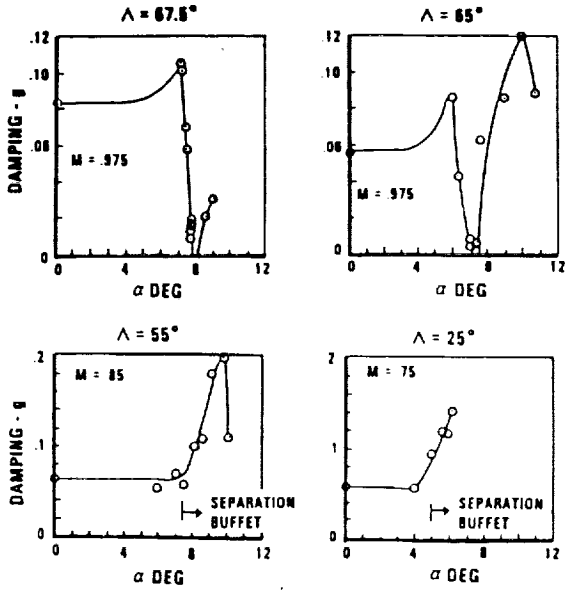

Fig. 12

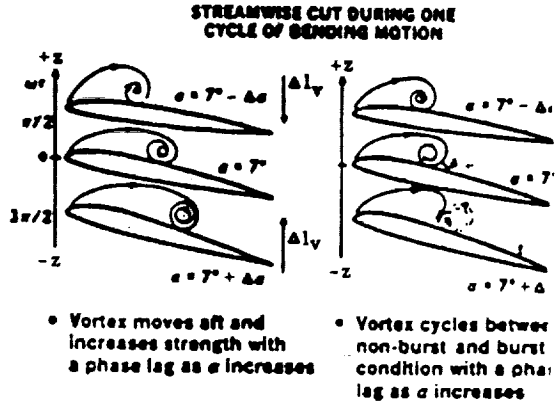

Fig. 14

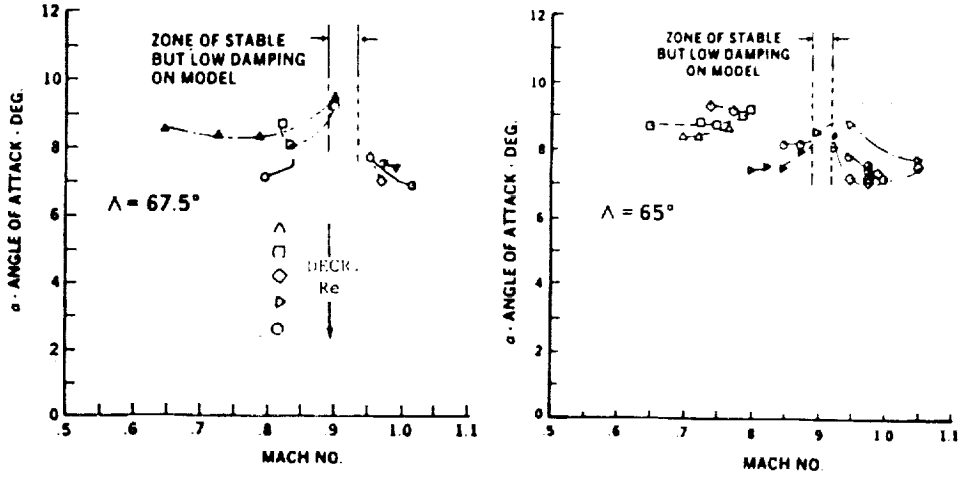

Fig. 13

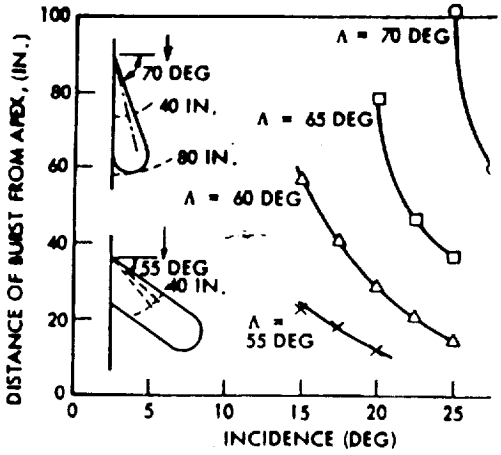

Fig.15

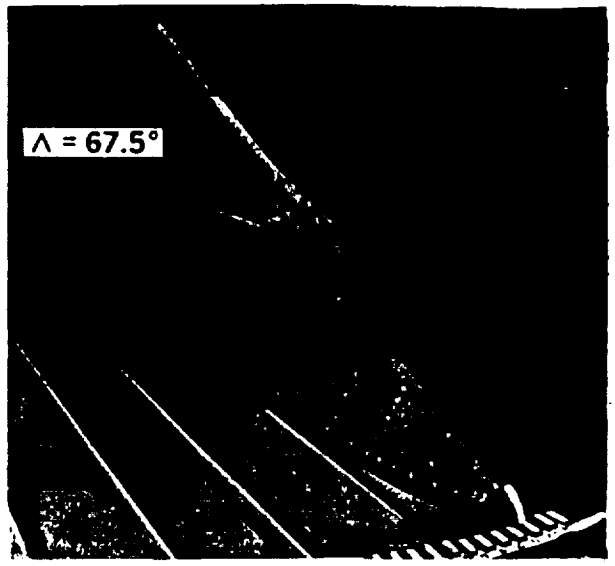

Fig. 16

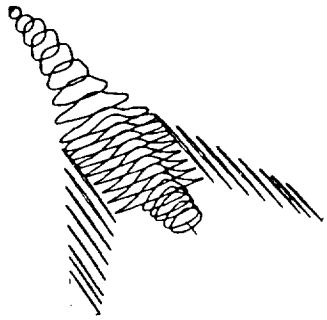

Fig. 17

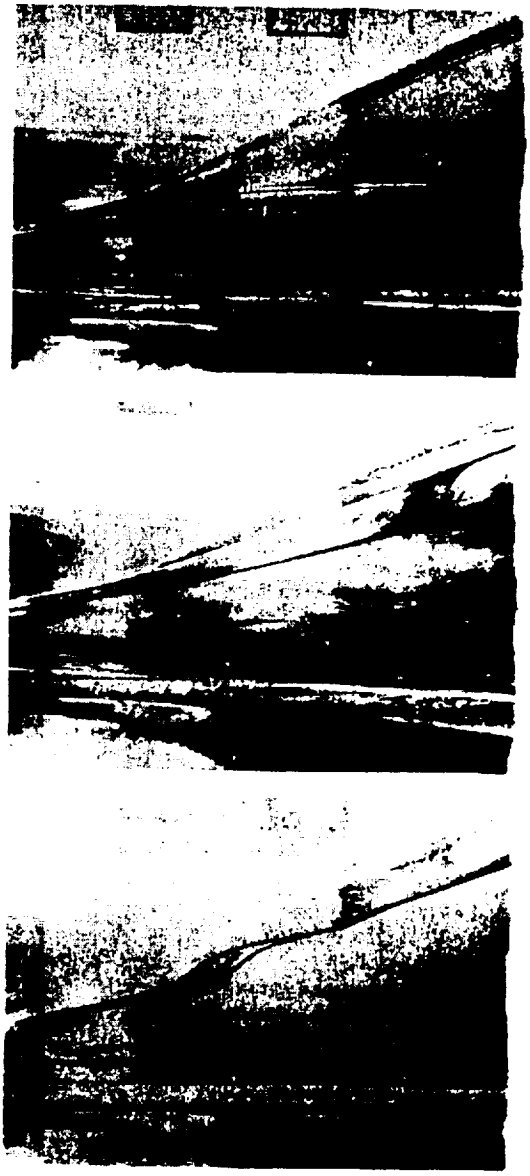

Fig. 19

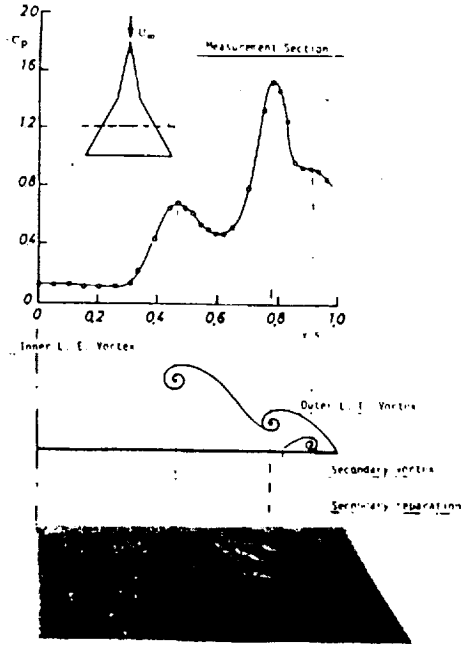

Fig.18

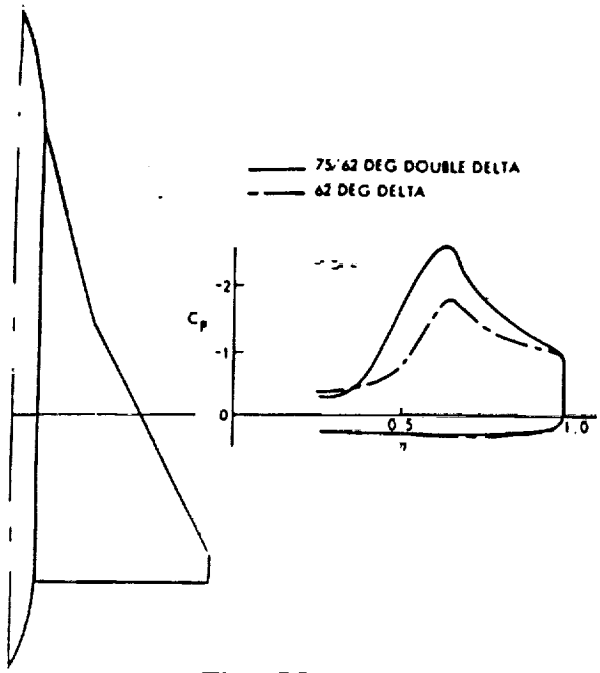

Fig. 20

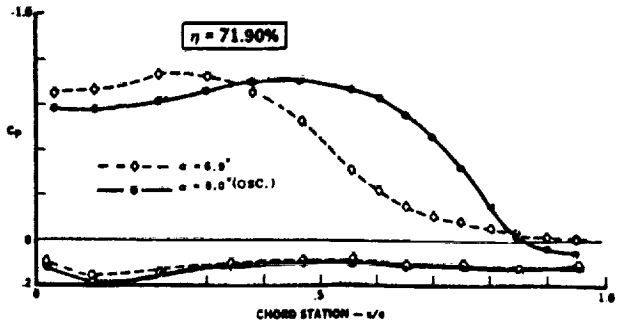

Fig. 21

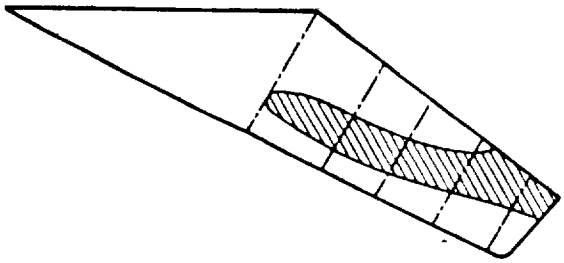

Fig. 22

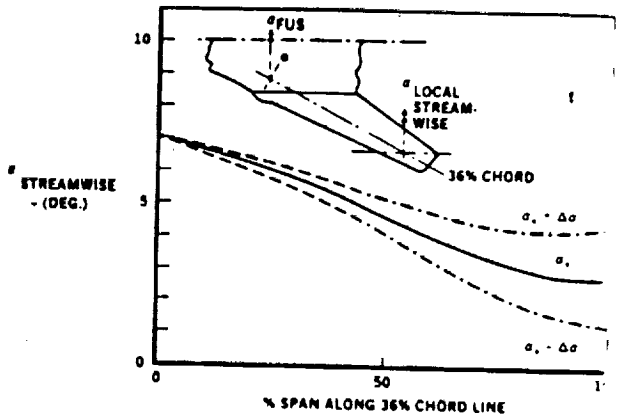

Fig. 23

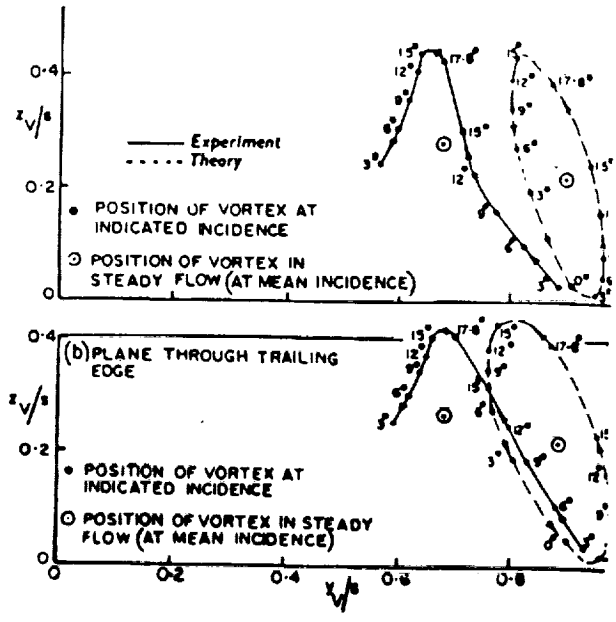

Fig. 24

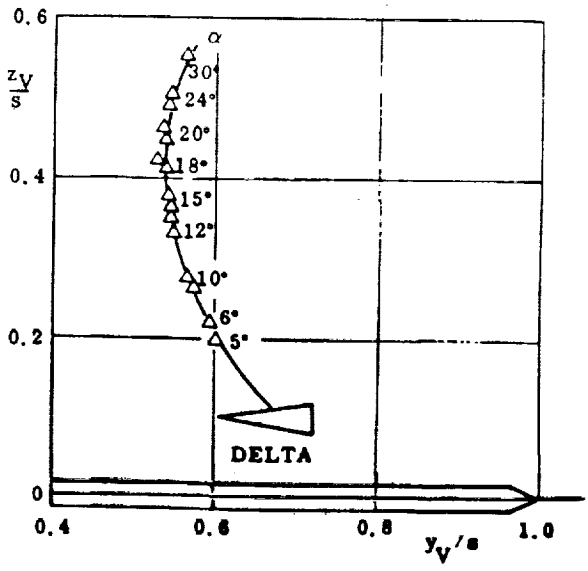

Fig. 25

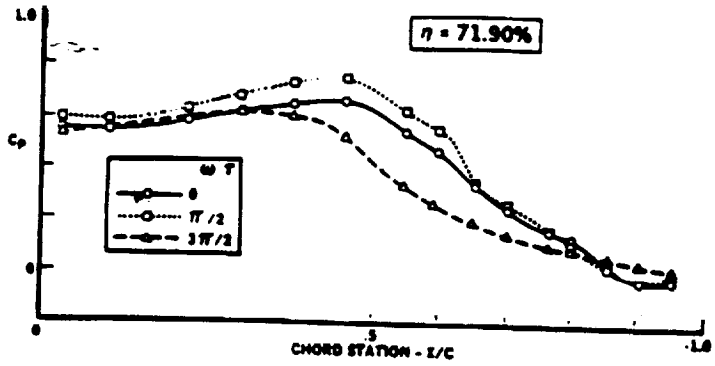
η = 71.90%
C_p
ω T
0
π/2
3π/2
CHORD STATION - X/C

Fig. 26

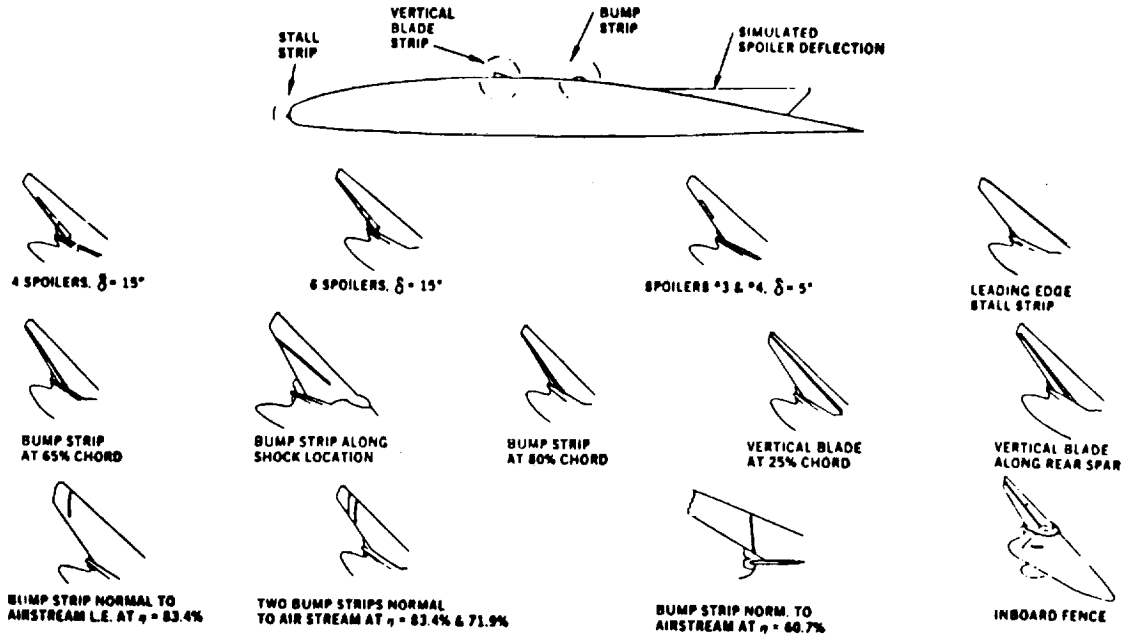
STALL STRIP
VERTICAL BLADE STRIP
BUMP STRIP
SIMULATED SPOILER DEFLECTION
4 SPOILERS, δ = 15°
6 SPOILERS, δ = 15°
SPOILERS #3 & #4, δ = 5°
LEADING EDGE STALL STRIP
BUMP STRIP AT 65% CHORD
BUMP STRIP ALONG SHOCK LOCATION
BUMP STRIP AT 80% CHORD
VERTICAL BLADE AT 25% CHORD
VERTICAL BLADE ALONG REAR SPAR
BUMP STRIP NORMAL TO AIRSTREAM L.E. AT η = 83.4%
TWO BUMP STRIPS NORMAL TO AIR STREAM AT η = 83.4% & 71.9%
BUMP STRIP NORM. TO AIRSTREAM AT η = 60.7%
INBOARD FENCE

Fig. 27

Paper Proposed for Presentation to the
Workshop on Physics of Forced Unsteady Separation
to be held at
NASA Ames Research Center April 17–19, 1990

COMPUTATION OF UNSTEADY FLOWS OVER AIRFOILS

J. A. Ekaterinaris
Navy–NASA Joint Inst. of Aeronautics
Dept. of Aeronautics and Astronautics
Naval Postgraduate School
NASA–Ames Research Center
Mail Stop 258-1
Moffett Field, CA 94035

M. F. Platzer
Navy–NASA Joint Inst. of Aeronautics
Dept. of Aeronautics and Astronautics
Naval Postgraduate School
Monterey, CA 93943

SUMMARY

Two methods are described for calculating unsteady flows over rapidly pitching airfoils. The first method is based on an interactive scheme in which the inviscid flow is obtained by a panel method. The boundary layer flow is computed by an interactive method that makes use of the Hilbert integral to couple the solutions of the inviscid and viscous flow equations. The second method is based on the solution of the compressible Navier–Stokes equations. The solution of these equations is obtained with an approximately factorized numerical algorithm, and with single block or multiple grids which enable grid embedding to enhance the resolution at isolated flow regions. In addition, the attached flow region can be computed by the numerical solution of compressible boundary layer equations. Unsteady pressure distributions obtained with both methods are compared with available experimental data.

ABSTRACT

The present paper addresses the prediction of unsteady airfoil boundary layer flows by two methods. These two methods are briefly described in the following section. The first is based on the extension of the steady interactive boundary–layer method of [1] and the second on the Navier–Stokes method of [2].

1.1 Viscous–Inviscid Interaction Method: The interactive method for steady high Reynolds number incompressible flows is described in [1] and [3], respectively, and makes use of an inverse boundary–layer method coupled to a panel method with an interactive formula suggested by Veldman [4]. The extension of this method to unsteady incompressible flows, again makes use of a panel method [5], which is similar to that of Hess and Smith [6]. This method utilizes the procedure of Basu and Hancock [7] to model the wake. The wake is represented by a series of free vortices shed from the trailing edge in response to incidence changes so that the total vorticity in the field is conserved. The airfoil's lift response then is obtained by subdividing the incidence history into sufficiently small time steps and computing the source and vorticity distributions for each time step. The unsteady interactive method is described in full detail in Refs. 5 and 8.

The unsteady boundary–layer equations are expressed in terms of an eddy viscosity, ϵ_m, so that continuity and momentum equations

$$\frac{\partial u}{\partial x} + \frac{\partial v}{\partial y} = 0 \tag{1}$$

$$\frac{\partial u}{\partial t} + u\frac{\partial u}{\partial x} + v\frac{\partial u}{\partial y} = \frac{\partial U_e}{\partial t} + U_e\frac{\partial U_e}{\partial x} + \frac{\partial}{\partial y}\left[(\nu + \epsilon_m)\frac{\partial u}{\partial y}\right] \tag{2}$$

are solved subject to the boundary conditions

$$y = 0, \quad u = v = 0; \qquad y \longrightarrow \infty, \quad u \longrightarrow U_e(x,t) \tag{3}$$

on the airfoil and with y = 0 denoting the dividing streamline that separates the upper and lower parts of the inviscid flow in the wake, subject to the following conditions

$$y \longrightarrow \pm\infty, \qquad u \longrightarrow U_e(x,t); \qquad y = 0, \qquad v = 0 \tag{4}$$

with $U_e(x,t)$ given by $U_e = U_e^o + \delta U_e(x,t)$. The eddy viscosity formulation of Cebeci and Smith [9] is used with special emphasis on the transitional region.

1.2 Navier–Stokes Methods : The Navier -Stokes method is briefly described in this paragraph. The full, unsteady, two–dimensional, compressible Navier–Stokes equations were solved. In a curvilinear coordinate system ξ, η the governing equations are:

$$\frac{\partial \hat{\mathbf{q}}}{\partial t} + \frac{\partial \hat{\mathbf{F}}}{\partial \xi} + \frac{\partial \hat{\mathbf{G}}}{\partial \eta} = \frac{1}{Re}\left(\frac{\partial \hat{\mathbf{R}}}{\partial \xi} + \frac{\partial \hat{\mathbf{S}}}{\partial \eta}\right) \tag{5}$$

where $\hat{\mathbf{q}}$ is the conservative variable vector $\mathbf{q} = (\rho, \rho u, \rho v, e)^T$, and $\hat{\mathbf{F}}$, $\hat{\mathbf{G}}$ are the nonlinear inviscid terms, and $\hat{\mathbf{R}}, \hat{\mathbf{S}}$ are the viscous terms.

The integration is performed with the finite difference factored Beam–Warming algorithm [10]. The approximately factorized form of the algorithm is:

$$\begin{aligned}&\left[I + (\Delta t/2)\left(\delta_\xi A^n_{j,k} + (D_{impl})_\xi\right)\right] \times \\ &\left[I + (\Delta t/2)\left(\delta_\eta B^n_{j,k} + (D_{impl})_\eta\right)\right] \Delta \mathbf{q}^n_{j,k} = (RHS)^n\end{aligned} \tag{6}$$

where

$$(RHS)^n = \Delta t(-\delta_\xi \mathbf{F}^n_{j,k} - \delta_\eta \mathbf{G}^n_{j,k} + \delta_\xi \mathbf{R}^n_{j,k} + \delta_\eta \mathbf{S}^n_{j,k} - \epsilon_{expl}(D_{expl})^n_{j,k}) \tag{7}$$

Solutions with embedded grid which provide enhanced grid resolution at isolated flow regions are possible. Thus, high grid resolution can be provited at critical flow regions, such as the leading edge region, where supersonic flow conditions and possible shock formation may occur even at moderate free stream subsonic speeds ($M = 0.45 - 0.50$) as the angle of attack increases. The option of solving the attached flow region with the compressible boundary–layer equations on an embedded grid is also provided. The boundary–layer equations for a generalized coordinates system [11] are:

continuity

$$\frac{\partial}{\partial t}\left(\frac{\rho}{J}\right) + \frac{\partial}{\partial \xi}\left(\frac{\rho U}{J}\right) + \frac{\partial}{\partial \eta}\left(\frac{\rho V}{J}\right) = 0 \tag{8}$$

ξ momentum

$$\rho\frac{\partial u}{\partial t} + \rho U\frac{\partial u}{\partial \xi} + \rho V\frac{\partial v}{\partial \eta} + \left(\xi_x\frac{\partial p}{\partial \xi} + \eta_x\frac{\partial p}{\partial \eta}\right) = J\frac{\partial}{\partial \xi}\left[\tau_{xx}\xi_x + \tau_{xy}\xi_y\right] + J\frac{\partial}{\partial \eta}\left[\tau_{xx}\eta_x + \tau_{yx}\eta_y\right] \tag{9}$$

normal momentum

$$\frac{\partial p}{\partial \eta} = 0 \tag{10}$$

energy

$$\begin{aligned}&\rho\frac{\partial H}{\partial t} - \frac{\partial p}{\partial t} + \rho u\frac{\partial H}{\partial \xi} + \rho v\frac{\partial H}{\partial \eta} = \\ &J\frac{\partial}{\partial \xi}\left\{\xi_x[\tau_{xx}u + \tau_{xy}v + K\left(\frac{\partial a^2}{\partial x}\right)] + \xi_y[\tau_{xy}u + \tau_{yy}v + K\left(\frac{\partial a^2}{\partial y}\right)]\right\} + \\ &J\frac{\partial}{\partial \eta}\left\{\eta_x[\tau_{xx}u + \tau_{xy}v + K\left(\frac{\partial a^2}{\partial x}\right)] + \eta_y[\tau_{xy}u + \tau_{yy}v + K\left(\frac{\partial a^2}{\partial y}\right)]\right\}\end{aligned} \tag{11}$$

Here $H = \frac{e+p}{\rho}$ is the enthalpy per unit volume, and the other quantities have the same definitions as before. Eqs. 8–11 are supplemented by the equation of state,

$$\frac{\rho}{\rho_\infty} = \frac{pT_\infty}{Tp_\infty} \tag{12}$$

or

$$\frac{T}{T_\infty} = \frac{(\gamma-1)}{a_\infty^2}\left[H - \frac{u^2+v^2}{2}\right] \tag{13}$$

Viscous or inviscid solutions can be obtained for the global grid by marching in time from an initial condition. Steady solutions are obtained by marching in time from free stream initial conditions until convergence to the steady–state. Similarly, unsteady flows are computed by marching in time from a steady flow initial condition. After the global grid solution is computed the boundary layer equations can be solved in the secondary grid using as initial condition at the inflow the velocity profile obtained by the viscous flow solution. Boundary conditions at the edge of the boundary layer domain are provided by the pressure and velocity distribution of a viscous or inviscid global flow solution for the outer region. Grid refinement is applied for the boundary–layer calculation and the values of the flow parameters at the extra boundary points are obtained by simple interpolation of the flow variables obtained from the viscous solution. For unsteady calculations the boundary layer equations are solved at each time step.

2.0 RESULTS AND DISCUSSION

The unsteady flow calculations for the NACA–0012 airfoil subject to ramp–type motion, as described in detail in [12], were performed by using both interactive and Navier–Stokes methods for a Reynolds number of 2.7×10^6 and for a non–dimensional pitch rate k defined by $k = \dot{\alpha}c/2U_\infty = 0.0127$. The airfoil chord was 10.16 cm, the pitch rate 1280 degrees/sec, pitching from 0^o to 15.54^o, at a free-stream Mach number of M = 0.3. The experimental data include upper and lower surface pressure distributions for incidence angles of 2.9, 5.8, 8.9, 11.7 and 15.5 degrees.

Figures 1 and 2 compare measured and calculated distributions of pressure coefficients for incidence angles of 2.9, 5.8, 8.9, 11.7 and 15.5 degrees, with Figure 1 showing the predictions of the interactive method and Figure 2 those of the Navier–Stokes method. In both methods, the flow was assumed to be fully turbulent due to the lack of experimental data about the location of transition, and the ramp change in the angle of attack was assumed to be given by

$$\alpha(t) = -\frac{2\alpha_{max}}{T^3}t^3 + \frac{3\alpha_{max}}{T^2}t^2 \tag{14}$$

where T is the nondimensional time required to complete the ramp motion from 0° to α_{max}. It is useful to point out that while the interactive method is based on the assumption of incompressible flow, the Navier–Stokes method is for a compressible flow. Calculations performed with the Navier–Stokes equations for a Mach number of 0.2 and 0.3, however, showed no effect of compressibility on the results.

Figures 1 and 2 show that the predictions of both methods are in good agreement with the experimental data,although the Navier–Stokes computations slightly underpredict the suction peaks at the lower incidence. Figures 3 and 4 present a comparison between the velocity profiles computed by both methods at two chordwise locations corresponding to $x/c = 0.5$ and $x/c = 0.9$ at several angles of incidence. While there is reasonably good agreement at low incidences, the two profiles begin to deviate significantly at higher incidences. Figure 4e shows, however, that both procedures predict the onset of flow reversal at $\alpha = 15.5°$ for $x/c = 0.9$. Unfortunately, there is no experimental data available to verify this prediction and to assess the accuracy of the two methods.

3.0 CONCLUSIONS

Two methods are described and applied to study the effects of low Reynolds number and flow unsteadiness on blade boundary layers. The first is based on an interactive boundary layer scheme in which the inviscid flow is computed by a panel method and the boundary layer flow by an inverse method that makes use of the Hilbert integral to couple the solutions of the inviscid and viscous flow equations. The second method is based on the solution of the compressible Navier–Stokes equations which employs an embedded grid technique for accurate boundary layer calculations with small computational cost. Calculated results obtained with both methods for a NACA–0012 airfoil subject to a ramp type motion at relatively high Reynolds number also indicate good agreement with experimental data. These results suggest that unsteady blade boundary layers can be computed accurately with either method provided the location of transition is computed interactively with the e^n–method and the transitional region is modelled properly. Future work will be directed at the systematic study of the effect of Reynolds number, transition modeling, reduced frequency and the effect of the airfoil leading edge geometry. In addition upwinding and TVD schemes will be used to enable accurate capturing of possible shock formation at the leading edge.

Acknowledgment: This work was supported by the Naval Air Systems Command, and NASA Ames Research Center.

References

[1] Cebeci, T., Clark, R. W., Chang, K. C., Halsey, N. D., and Lee, K., "Airfoils with Separation and the Resulting Wakes," *J. Fluid Mech.*, No. 163, pp. 323–347, 1986.

[2] Ekaterinaris, J. A., "Compressible Studies on Dynamic Stall," AIAA Paper 89-0024, 27th Aerospace Sciences Meeting, Reno NV, Jan. 1989.

[3] Cebeci, T., "Essential Ingredients of a Method for Low Reynolds Number Airfoils," To be published in the AIAA journal 1989.

[4] Veldman, A. E. P., "New Quasi–Simultaneous Method to Calculate Interactively Boundary Layers," *AIAA Journal,*, No. 19, 1981, p. 769.

[5] Teng, N. H., "The Development of a Computer Code (U2DIIF) for the Numerical Solution of Unsteady, Inviscid and Incompressible Flow over an Airfoil," M.S. Thesis, Naval Postgraduate School, Montery CA, 1987.

[6] Hess, J. L., and Smith, A. M. O., "Calculation of Potential Flow about Arbitrary Bodies," *Progress in Aeronautical Sciences*, Pergamon Press, Oxford, Vol. 8, 1966, pp 1–138.

[7] Basu, B. C., and Hancock, G. J. "The Unsteady Motion of a Two–Dimensional Airfoil in Incompressible Inviscid Flow," *Journal of Fluid Mech.*, Vol. 87, 1987, pp. 157–168.

[8] Jang , H. M., "A Viscous–Inviscid Interactive Method for Unsteady Flow," *Ph.D. Thesis, University of Michigan*, Ann Arbor, Michigan 1989.

[9] Cebeci, T, and Smith, A. M. O., "Analysis of Turbulent Boundary Layers," *Academic Press* , New York, 1974.

[10] Beam, R. M. and Warming, R. F., "An Implicit Factored Scheme for the Compressible Navier–Stokes Equations," *AIAA Journal*, Vol. 16, No. 4, April 1978, pp. 393–402.

[11] Steger, J. L, VanDalsem, W. R., Panaras, A. G., and Rao, K. V., "A Formulation for the Boundary–Layer Equations In General Coordinates," NASA Technical Memorandum 100079, June 1988.

[12] Landon, R. H., "NACA 0012 Oscillatory and Transient Pitching," AGARD Report No. 702, 1981.

Figure Captions

Figure 1. Pressure Coefficient at $\alpha = 2.9^o, 5.8^o, 8.9^o, 11.7^o, 15.5^o$ predicted by the viscous–inviscid interaction method. ($Re = 2.7 \times 10^6, k = 0.0127$)

Figure 2. Pressure Coefficient at $\alpha = 2.9^o, 5.8^o, 8.9^o, 11.7^o, 15.5^o$ predicted by the Navier–Stokes solution. ($Re = 2.7 \times 10^6, k = 0.0127$)

Figure 3. Comparison of the boundary–layer profiles computed with both methods, at $\alpha = 2.9^o, 5.8^o, 8.9^o, 11.7^o, 15.5^o$ for the 50% chord. ($Re = 2.7 \times 10^6, k = 0.0127$)

Figure 4. Comparison of the boundary–layer profiles computed with both methods, at $\alpha = 2.9^o, 5.8^o, 8.9^o, 11.7^o, 15.5^o$ for the 90% chord. ($Re = 2.7 \times 10^6, k = 0.0127$)

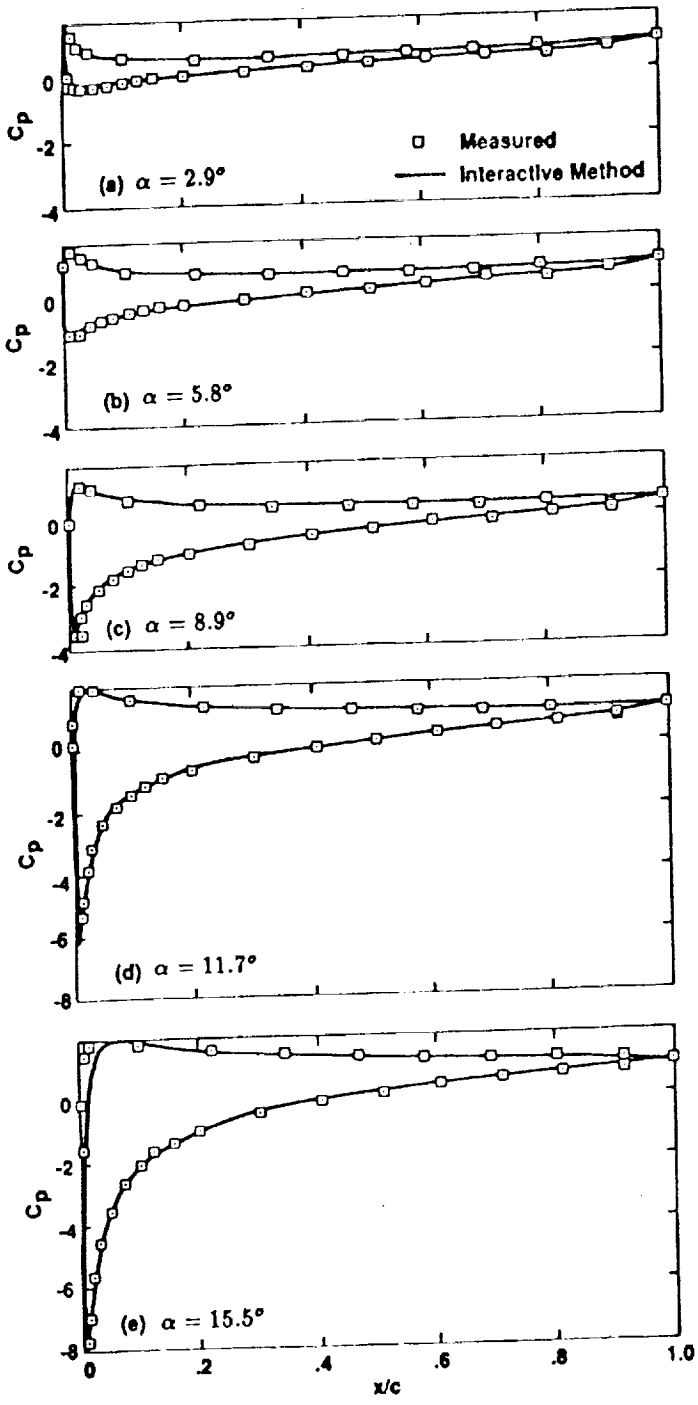

Figure 1 Pressure coefficient distributions predicted by the interactive method: ($Re = 2.7 \times 10^6, k = 0.0127$).

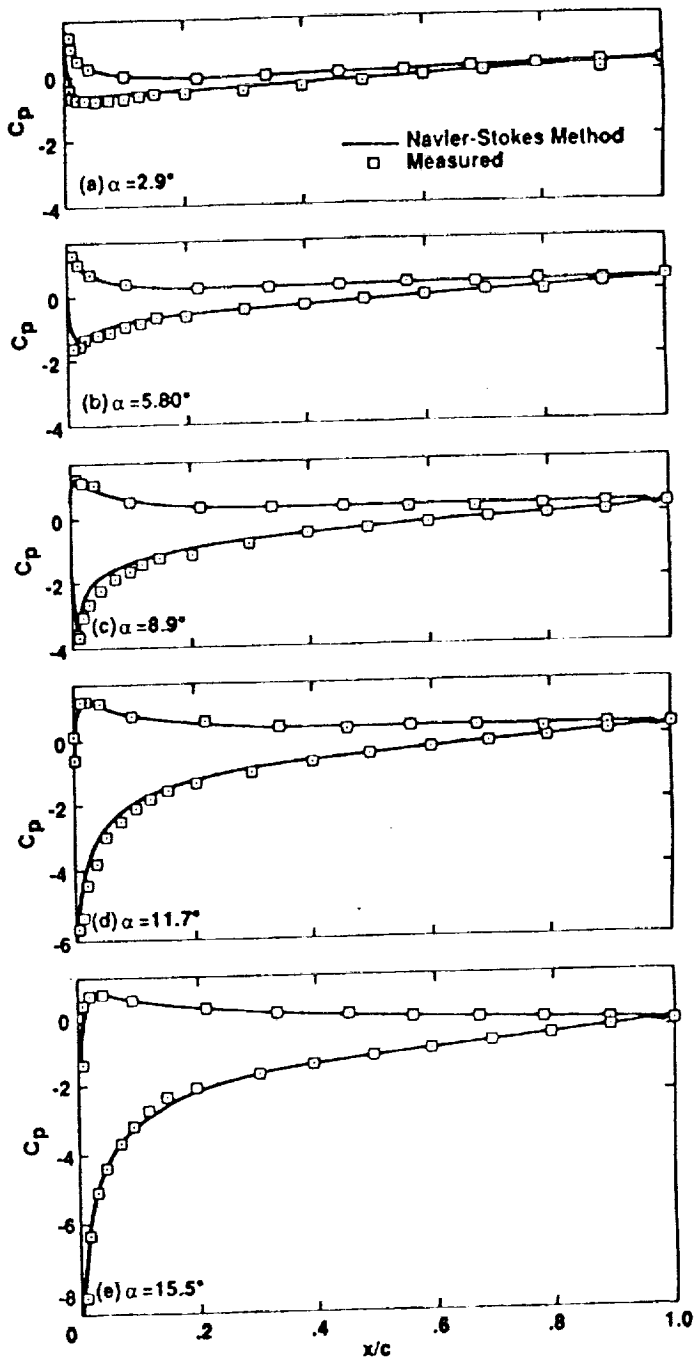

Figure 2 Pressure coefficient distributions predicted by the Navier-Stokes method: ($Re = 2.7 \times 10^6, k = 0.0127$).

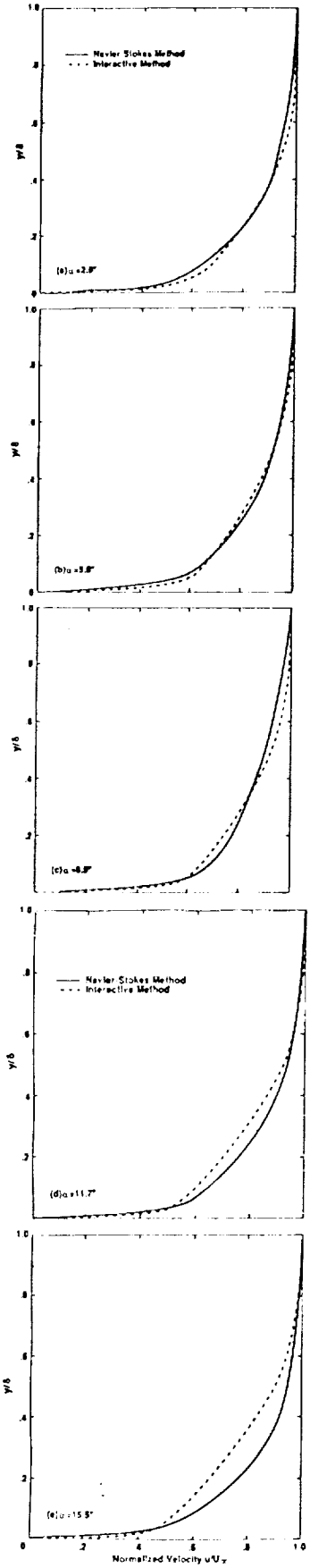

Figure 3 Comparison of the boundary layer profiles computed with both methods, for the 50% chord: ($Re = 2.7 \times 10^6, k = 0.0127$).

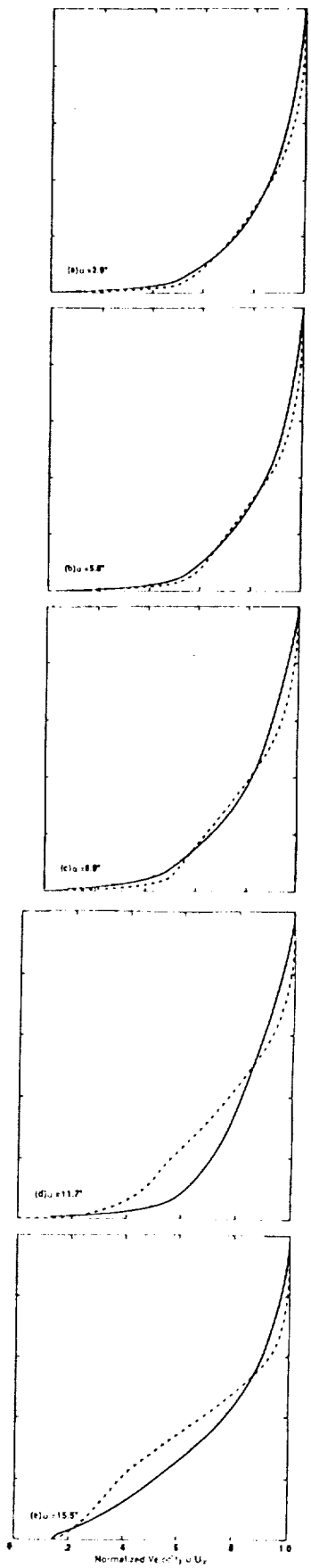

Figure 4 Comparison of the boundary layer profiles computed with both methods, for the 90% chord: ($Re = 2.7 \times 10^6, k = 0.0127$)

PREDICTION OF UNSTEADY AIRFOIL FLOWS AT LARGE ANGLES OF INCIDENCE

by

Tuncer Cebeci* and H. M. Jang** and H. H. Chen†

Aerospace Engineering Department

California State University, Long Beach

Abstract

The effect of unsteady motion of an airfoil on its stall behavior is of considerable interest to many practical applications including the blades of helicopter rotors and of axial compressors and turbines. Experiments with oscillating airfoils, for example, have shown that the flow can remain attached for angles of attack greater than those which would cause stall to occur in a stationary system. This result appears to stem from the formation of a vortex close to the surface of the airfoil which continues to provide lift. It is also evident that the onset of dynamic stall depends strongly on the airfoil section and as a result great care is required in the development of a calculation method which will accurately predict this behavior.

In principle, the prediction of dynamic stall can be accomplished by solving the Reynolds-averaged Navier-Stokes equations or their reduced forms. A turbulence model is required and is presumed, with reasonable supporting evidence to be uninfluenced by the imposed unsteadiness. Several papers have been prepared with calculations of this type and involve the solution of equations with two diffusion terms as well as parabolized forms and thin-layer approximations. An alternative is to make use of interactive boundary-layer

---

*Professor and Chairman.

**Research Associate.

†Assistant Professor.

theory whereby inviscid and boundary-layer equations are solved and allowed to influence each other by an iterative scheme.

Extensive investigations with an interactive approach have been reported by Cebeci et al.[1] and show that the incompressible flow and performance characteristics of airfoils can be predicted accurately and efficiently for high and low Reynolds numbers and for a range of angles of attack up to and including stall. At incidence angles higher than stall, however, this procedure, was unable to predict the airfoil performance due to relatively large regions of flow separation on the surface and in the wake. Near stall, the value of the trailing edge displacement thickness approached 10% of the chord and the numerical method could not provide converged solutions. The predictions of this interactive boundary-layer are similar to those obtained from solutions of thin-layer Navier-Stokes by the ARC-2D method for angles of attack up to and including stall. It has been shown in Ref. 1 that the interactive flow calculations without the wake effect and for angles of attack greater than that of stall, yielded lift coefficients which increased with incidence angle almost in the same way as those computed with the thin-layer Navier-Stokes approach with the wake effect included. When the wake effect was included in the interactive boundary-layer calculations, the results agreed more closely with measurements but could not be extended beyond the stall angle.

More recently, the interactive method has been improved to permit calculations for angles of attack greater than that of stall and the results have been shown to have the correct behavior. To achieve this, modifications were made to the iterative procedure and to the method of calculating the wake. These improvements are described in Ref. 2 and are necessary where results are required at angles of attack corresponding to stall and post stall.

The interactive boundary-layer method for steady flows has also been extended to study the laminar separation and reattachment near the leading edge of a thin oscillating airfoil[3], but the calculation of flow over practical airfoils involves laminar and turbulent flows and the inclusion of the upstream influence of the wake requires careful step-by-step development and evaluation, as has been done for steady flows. The use of a quasi-steady approach to unsteady flows represents an essential building block in a progression towards an interactive calculation method which solves unsteady equations even though the latter is likely to represent a much wider range of oscillation frequencies. The extent of the differences can be quantified only by comparing results from both.

Our presentation will describe the extension of the steady interactive boundary-layer method of Cebeci et al.[1] to unsteady flows over practical airfoils subject to a ramp-type motion. The method makes use of the unsteady panel method developed by Platzer and his student, Teng[4], and is able to compute flows with large regions of flow separation. By solving the quasi-steady and unsteady boundary-layer equations in an interactive method, the quasi-steady method will be assessed over a range of angles of attack and frequency in terms of convenience, accuracy, and the computational cost. The calculations will encompass airfoil and wake flows at angles of attack close to the start of the dynamic stall and will provide insight into the development of dynamic stall as a result of the trailing edge separation.

References

1. Cebeci, T., Clark, R.W., Chang, K.C., Halsey, N.D. and Lee, K.: Airfoils with Separation and the Resulting Wakes. J. Fluid Mech., Vol. 173, pp. 323-347, 1986.

2. Cebeci, T., Jau, J., Vitiello, D. and Chang, K.C.: Prediction of Post-Stall Flows on Airfoils. In Numerical and Physical Aspects of Aerodynamic Flows, IV (ed. T. Cebeci), Springer-Verlag, N.Y., 1990.

3. Cebeci, T., Khattab, A.A. and Schimke, S.M.: Separation and Reattachment Near the Leading Edge of a Thin Oscillating Airfoil. J. Fluid Mech., Vol. 188, 1988, pp. 253-274.

4. Teng, N.G.: The Development of a Computer Code for the Numerical Solution of Unsteady Inviscid, and Incompressible Flow Over an Airfoil. M.S. Thesis, Naval Postgraduate School, Monterey, CA, 1987.

PURPOSE

TO DEVELOP AN INTERACTIVE BOUNDARY-LAYER (IBL) METHOD CAPABLE OF COMPUTING UNSTEADY FLOWS ON AIRFOILS INCLUDING DYNAMIC STALL.

APPROACH

EXTENSION OF AN ACCURATE METHOD FOR COMPUTING STALL AND POST STALL ON AIRFOILS IN STEADY FLOWS.

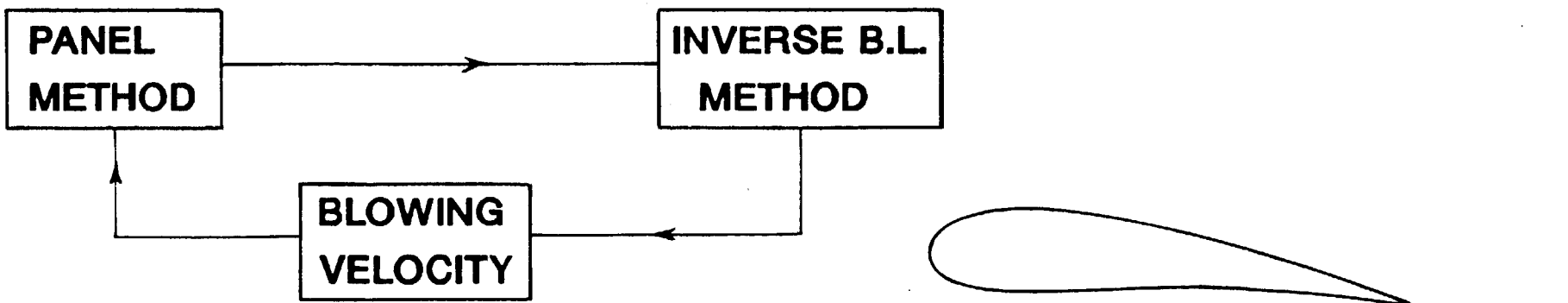

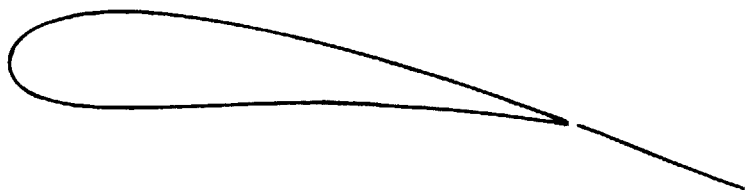

CALCULATIONS ON THE AIRFOIL AND IN THE WAKE

STEPS IN THE DEVELOPMENT OF THE PROCEDURE, 1

1. UNSTEADY PANEL METHOD + QUASI-STEADY BOUNDARY-LAYER METHOD

2. UNSTEADY PANEL METHOD + UNSTEADY BOUNDARY-LAYER METHOD

   PANEL METHOD WITH AND WITHOUT VISCOUS EFFECTS

   - EXTENSION OF THE HESS-SMITH PANEL METHOD TO UNSTEADY FLOWS, BY M.F. PLATZER AND HIS STUDENT TENG.
   - INCLUSION OF VISCOUS EFFECTS, BY H.M. JANG.

STEPS IN THE DEVELOPMENT OF THE PROCEDURE, 2

UNSTEADY BOUNDARY-LAYER METHOD

$$\frac{\partial u}{\partial x} + \frac{\partial v}{\partial y} = 0$$

$$\frac{\partial u}{\partial t} + u\frac{\partial u}{\partial x} + v\frac{\partial u}{\partial y} = \frac{\partial u_e}{\partial t} + u_e\frac{\partial u_e}{\partial x} + \frac{\partial}{\partial y}\left[(\nu + \varepsilon_m)\frac{\partial u}{\partial y}\right]$$

$$y = 0: \qquad u = v = 0$$

$$y = \delta: \qquad u_e(x) = u_e^o(x) + \delta u_e(x)$$

$$\delta u_e(x) = \frac{1}{\pi}\int_{x_a}^{x_b} \frac{d}{d\sigma}(u_e\delta \times)\frac{d\sigma}{x - \sigma}$$

SOME FEATURES OF THE METHOD FOR STEADY FLOWS, 1

1. COMPARISONS WITH NS SOLUTIONS AND WITH EXPERIMENT

NACA 0012 AIRFOIL, $R_c = 6 \times 10^6$

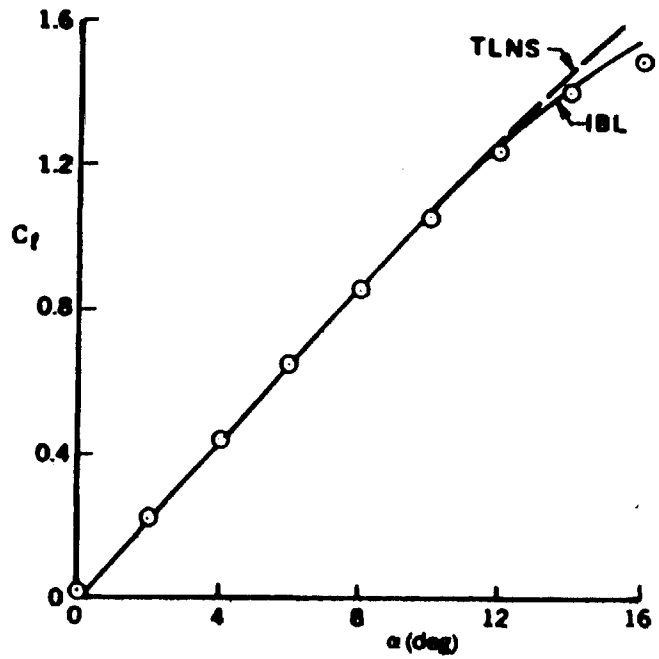

GA(W)-2, $R_c = 4.3 \times 10^6$

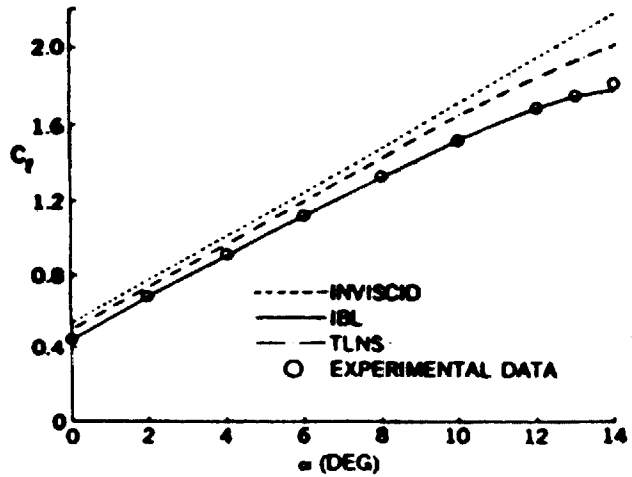

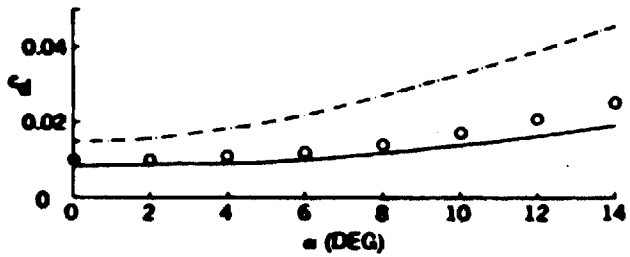

SOME FEATURES OF THE METHOD FOR STEADY FLOWS, 2

2. EFFECT OF WAKE

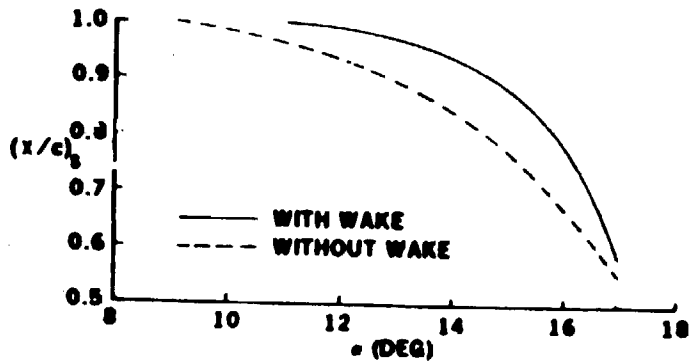

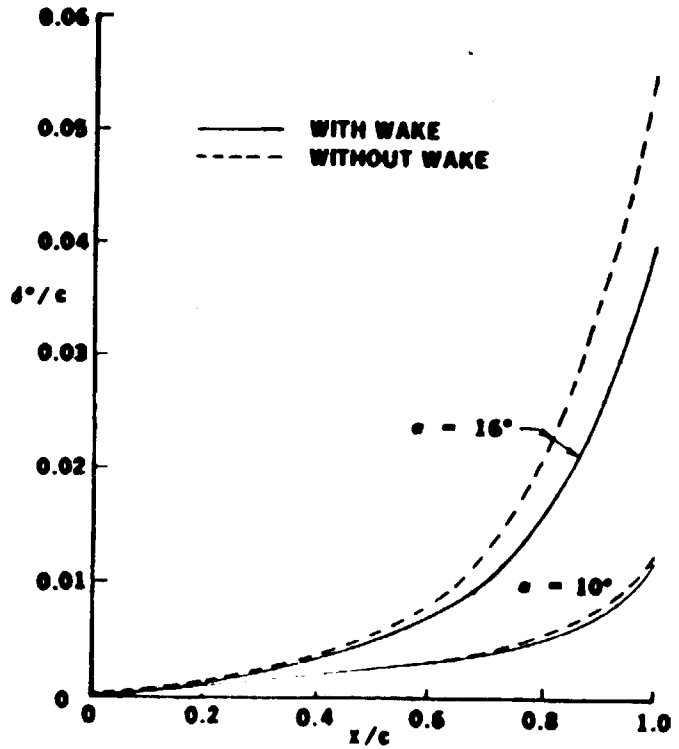

SOME FEATURES OF THE METHOD FOR STEADY FLOWS, 3

3. RECENT WORK AND IMPROVEMENTS FOR POST-STALL FLOWS

- SOLUTIONS ARE SENSITIVE TO
  - TRANSITION AT HIGH ANGLES OF ATTACK, AND
  - LARGE FLOW SEPARATION,ESPECIALLY IN WAKE
    i.e. NEAR STALL, AT THE TRAILING EDGE

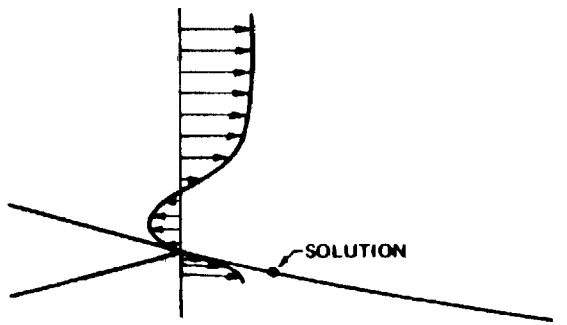

CONTINUATION METHOD

$u = u_{ref} + n(u_e - u_{ref})$ $n = 0, 0.1, 0.2, ..., 1.0$

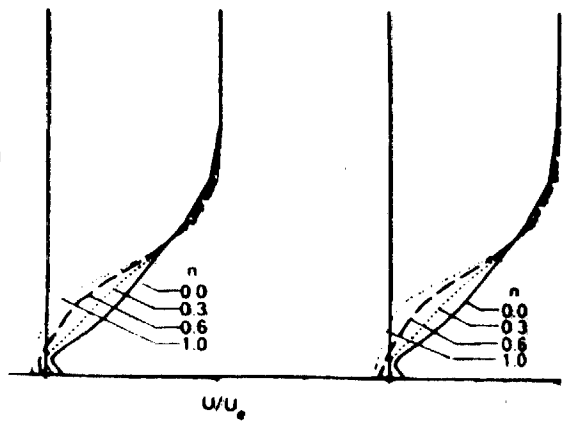

SOME FEATURES OF THE METHOD FOR STEADY FLOWS, 4

NACA 0012 AIRFOIL, $R_c = 6 \times 10^6$

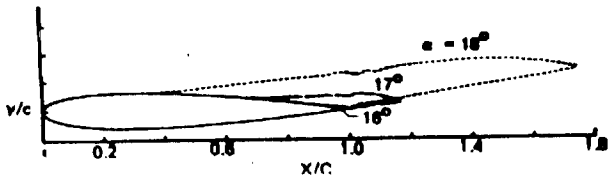

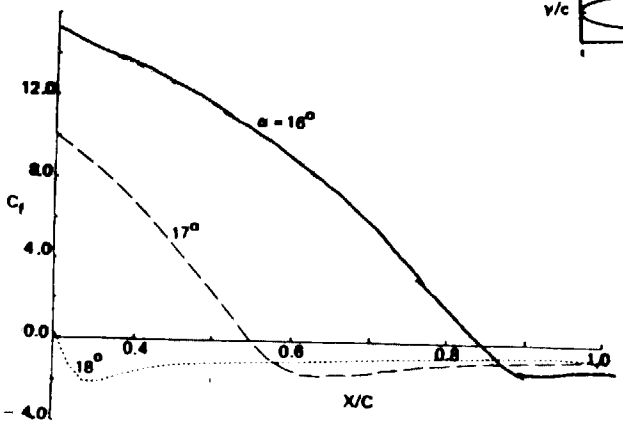

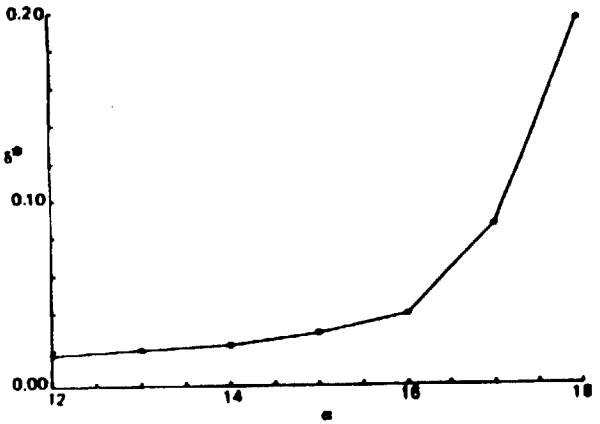

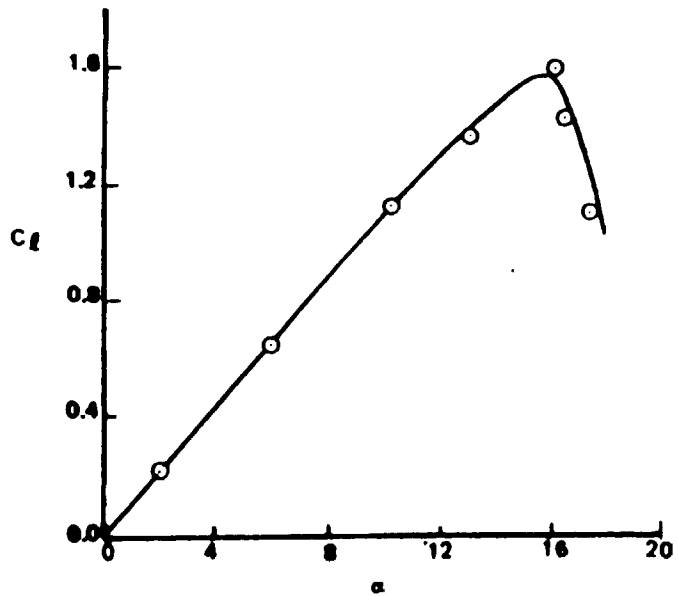

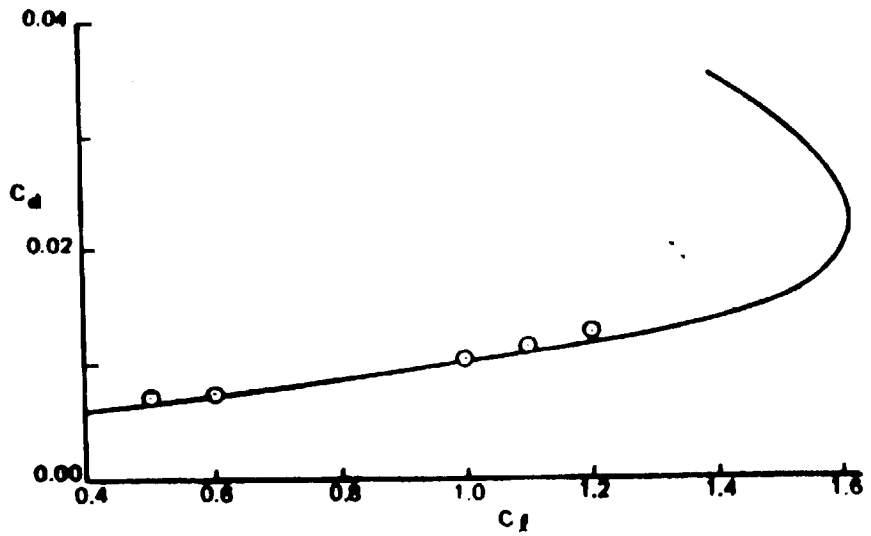

SOME FEATURES OF THE METHOD FOR STEADY FLOWS, 5

NACA 23012 AIRFOIL, $R_c = 6 \times 10^6$

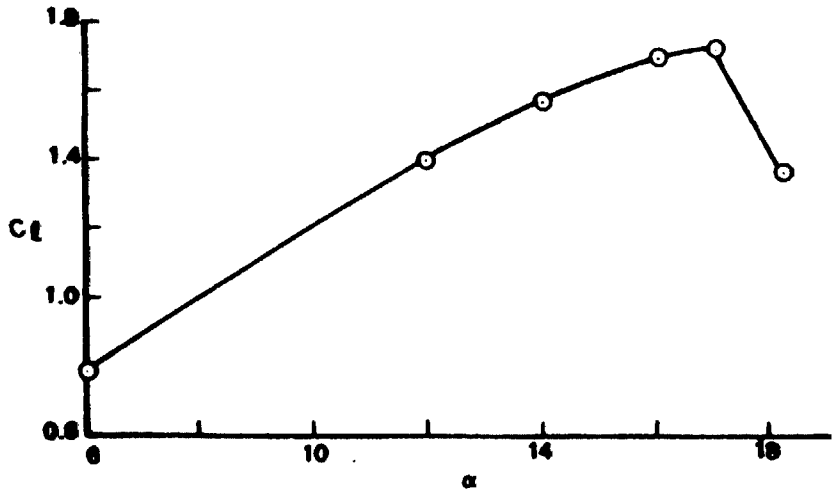

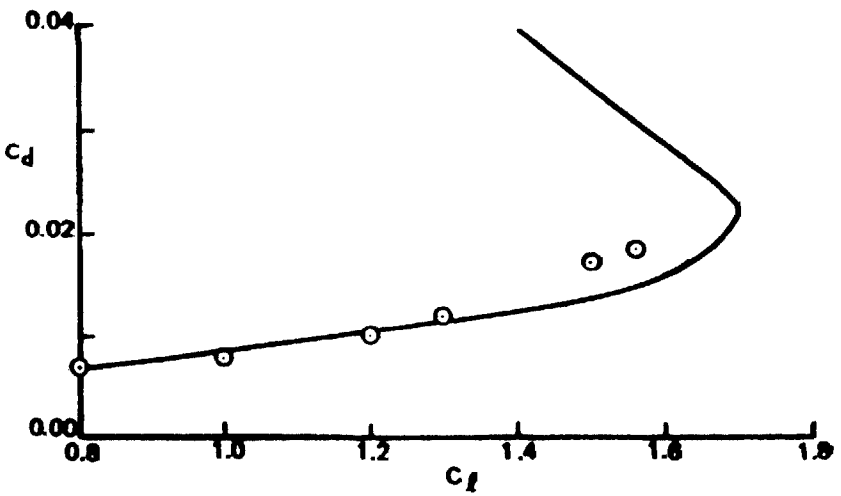

RESULTS FOR $\alpha = 5 + 10 \sin \omega t$

TRANSIENT EFFECTS

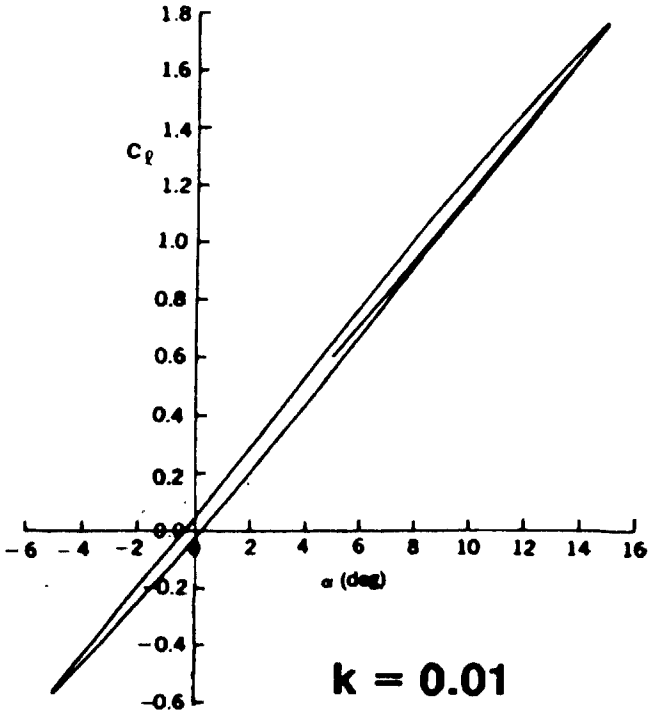

k = 0.01

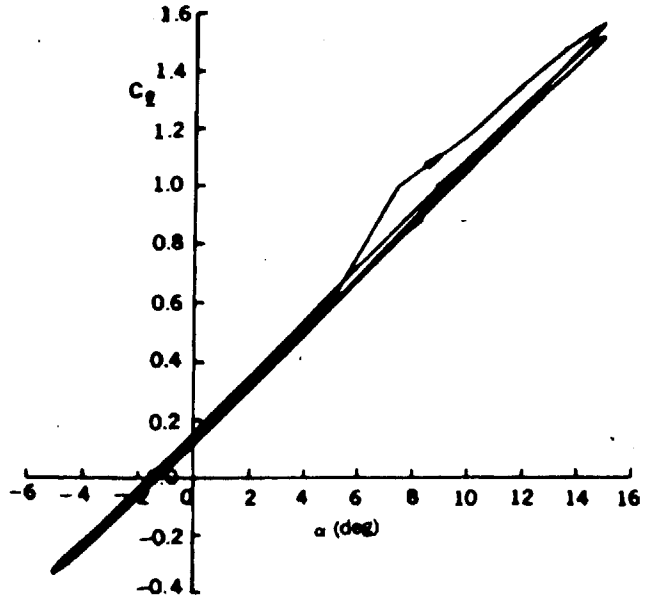

k = 0.15

VARIATION OF THE WAKE LOCATION FOR k = 0.01

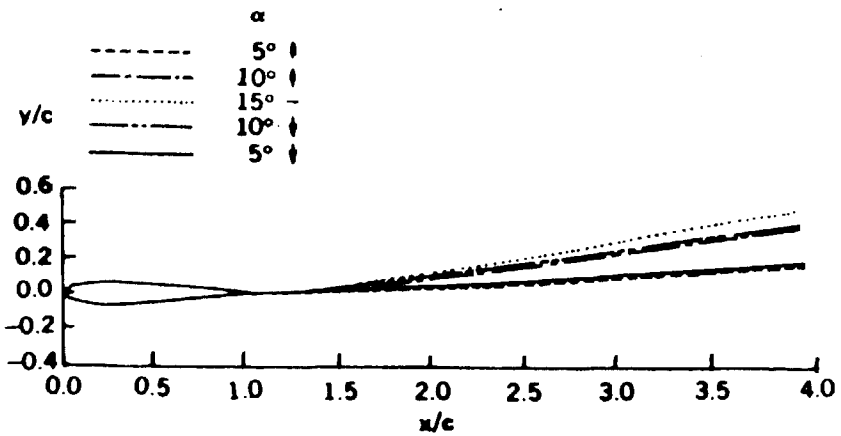

EFFECT OF PITCH RATE ON THE LIFT COEFFICIENT OF THE SSC-A09 AIRFOIL

$$R_c = 2 \times 10^6$$

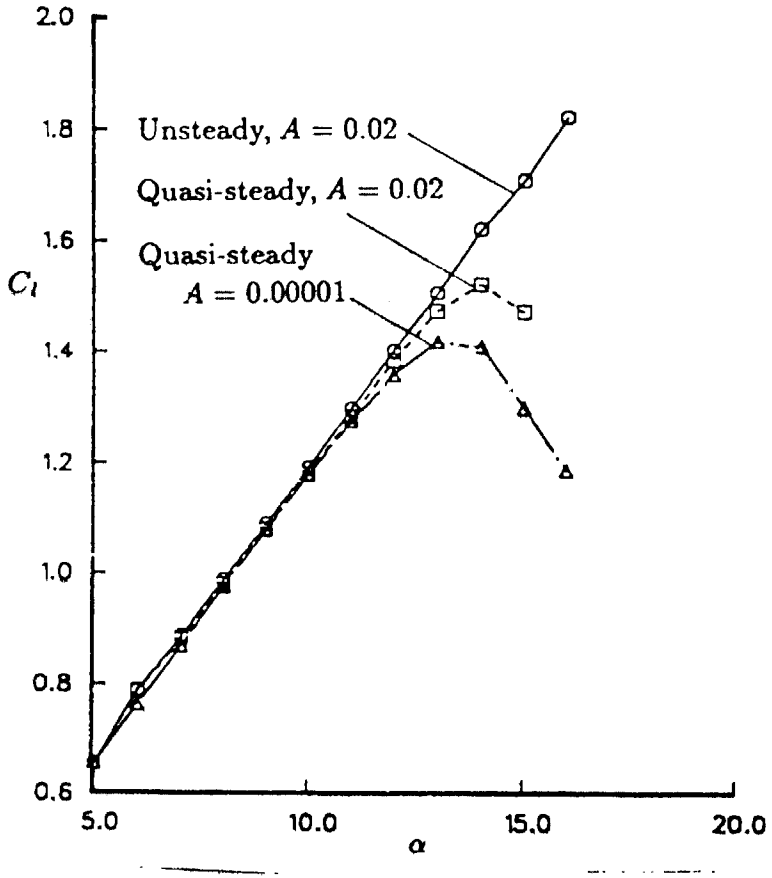

STEADY STATE

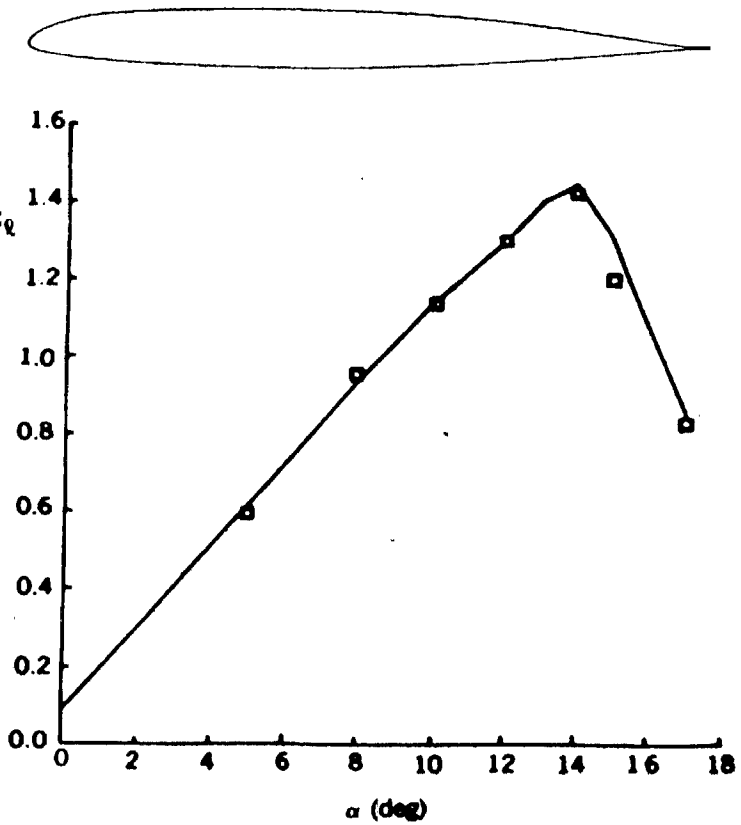

EFFECTS OF PITCH RATE ON THE DISPLACEMENT THICKNESS DISTRIBUTION OF THE SSC-A09 AIRFOIL

$$R_c = 2 \times 10^6$$

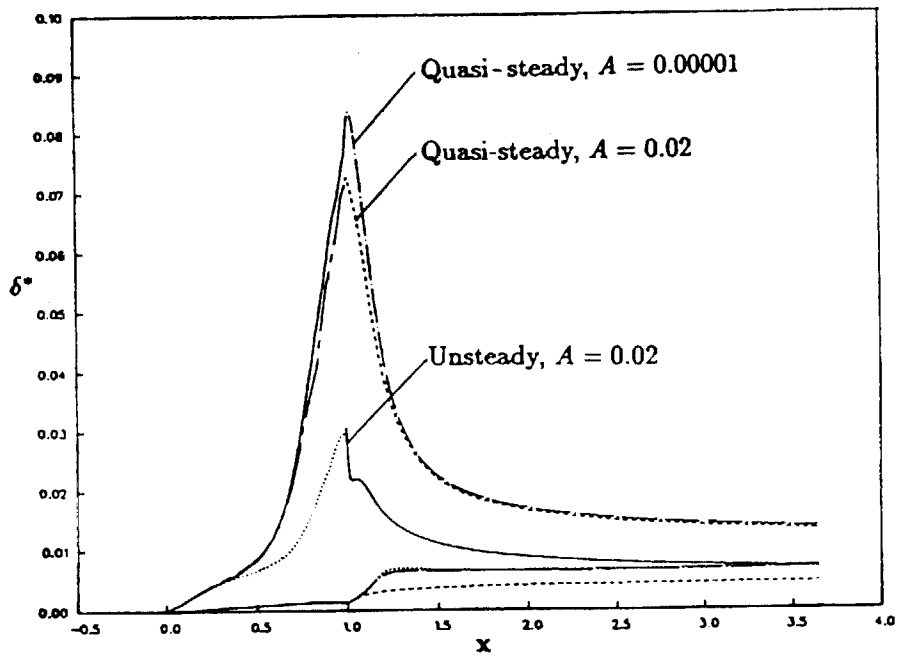

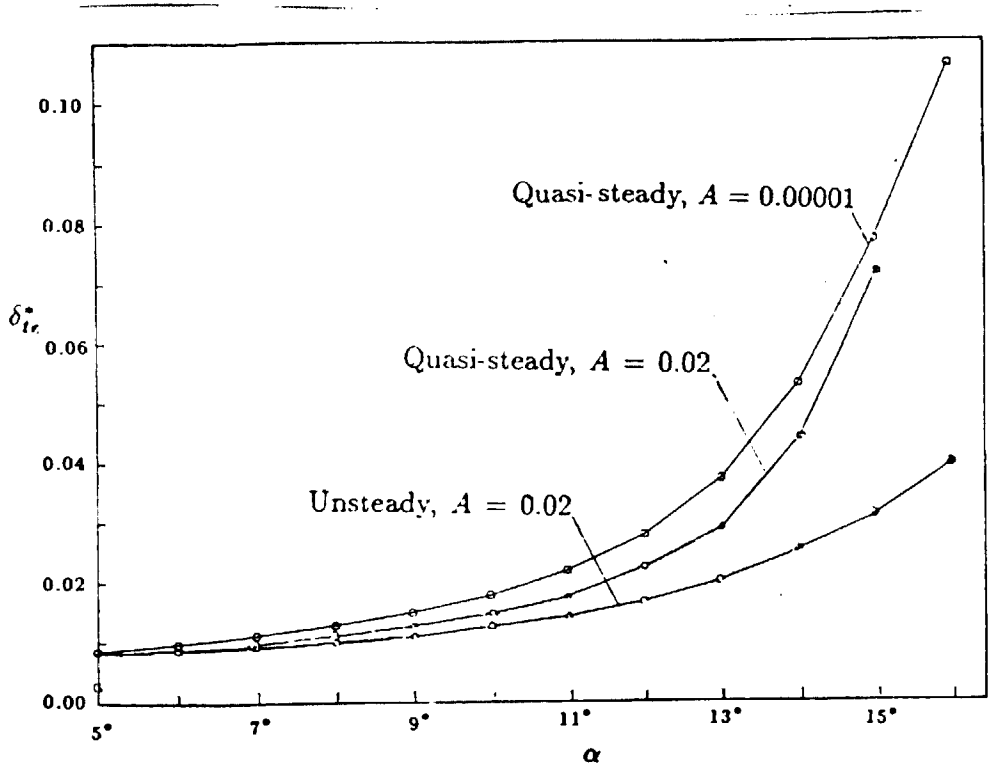

SOME ASPECTS OF UNSTEADY SEPARATION

by

C. R. Smith and J. D. A. Walker
Department of Mechanical Engineering and Mechanics
Lehigh University
Bethlehem, Pennsylvania 18015

Unsteady separation can be forced in a variety of ways and in this presentation two fundamental means will be considered, namely (1) the introduction of convected vorticular disturbances into the flow and (2) the influence of a specific type of three-dimensional geometry. In both situations a response of the viscous flow near the wall is provoked wherein the fluid near the surface abruptly focusses into a narrow region that erupts from the surface into the mainstream. In two-dimensional flows the eruption takes the form of narrow explosively-growing spike, while in three-dimensional situations, examples are presented which indicate that the eruption is along a narrow zone in the shape of a crescent-shaped plume. The nature of the three-dimensional flow near a circular cylinder, which is mounted normal to a flat plate, is also examined in this study. Here the three-dimensional geometry induces complex three-dimensional separations periodically. The dynamics of the generation process is studied experimentally in a water channel, using hydrogen bubble wires and a laser sheet, and the main features of the laminar regime through to transition are documented.

Discussion

Unsteady viscous-inviscid interactions between an effectively inviscid outer flow and a viscous region near a surface occur in a variety of important applications such as the flows occurring in turbomachinery and on moving airfoil surfaces. Many examples occur in quite different physical environments but nevertheless exhibit a common type of behavior. At a certain stage, a viscous layer near a wall, which has been hitherto passive and which to this point is well described by conventional boundary-layer theory, begins to develop strong outflows over a zone which is very narrow in the streamwise direction. As this eruptive behavior develops, it culminates in the ejection of boundary-layer fluid away from the wall into the outer inviscid flow. The process is known as an unsteady viscous-inviscid interaction; it is generally distinguished by the eruptive nature of the phenomenon as well as the fact that discrete "chunks" of vorticity are torn from the region near the surface and abruptly introduced into the outer flow.

Such unsteady interactions can be induced in a number of ways, one of which occurs whenever a vortex is convected close to a solid surface. A vortex near a solid wall induces a moving region of adverse pressure gradient on the viscous flow near the surface and, provided the vortex is near the wall for a sufficient period of time, all moving vortices will ultimately provoke a boundary-layer eruption. Well-documented examples include the flow induced near a ground-plane by aircraft-trailing vortices (Harvey and Perry, 1971), the boundary layer induced by a vortex ring moving toward a plane wall (Walker et al., 1987) and the so-called "secondary instability" of Goertler vortices that develop in the boundary layer on a concave wall (Ersoy and Walker, 1985). In all of these situations, recirculating eddies develop in the boundary layer near the wall as a consequence of the pressure distribution induced by the parent vortex. With the evolution of these secondary vortices, strong updrafts begin to develop and the boundary layer evolves rapidly toward interaction with the outer flow. The nature of the interaction is such that a boundary-layer eruption occurs in a focussed band which is narrow in the streamwise direction, with the result that the secondary eddies are ejected from the boundary layer into the external flow (Walker et al., 1987).

Similar processes occur within the turbulent boundary layer (Walker et al., 1989; Walker, 1989) wherein the flow in the region near the wall breaks down violently and intermittently. The breakdown process always initiates near a low-speed streak and results in a strong, unsteady viscous-inviscid interaction with the outer layer motion. Recent studies (Haji-Haidari, 1990; Smith et al., 1990, and Walker, 1990) show that the streaks and the eruptive behavior are due to moving hairpin vortices which are convected near the surface. This represents the fundamental regenerative process in a turbulent boundary layer where new vorticity from the wall region is continually introduced into the outer part of the boundary layer through intermittent eruptions of the wall layer.

One objective of the present work was to develop algorithms to compute the evolution of strongly interacting boundary-layer flows and to this end a model problem was considered, namely the unsteady boundary layer induced by a two-dimensional vortex above a plane wall in an otherwise stagnant fluid. A zone of recirculation in the boundary layer is soon produced due to the pressure field associated with the vortex (Walker, 1989), and strong updrafts then evolve on one side of the recirculating eddy. As the boundary-layer flow starts to focus toward an eruption, it is not possible to track the phenomenon using conventional numerical methods based on the Eulerian formulation of the flow problem and in this study Lagrangian methods were used. In the latter approach, the trajectories of a large number of individual fluid particles are evaluated and, as the boundary-layer focusses toward an eruption, the fluid

particles move naturally into the erupting region, which is consequently well-resolved. Some calculated results for displacement thickness are shown in Figure 1, which is taken from Peridier and Walker (1989). Initially, the displacement thickness grows progressively after the motion is initiated (from an impulsive start), with the greatest growth occurring near $x = 0.5$ near the recirculating secondary eddy, that develops in the boundary layer for $t > 0.28$. However, at around $t = 0.85$ a corner starts to appear in δ^* and very rapidly the boundary layer focusses into a "needle-like" eruption. The dynamics of this process, which are believed to be generic for all two-dimensional flows, will be discussed.

For moving three-dimensional vortices, the induced flow patterns near the wall are much more complex but a narrow, focussed eruption is also produced. Experimental studies of the flow provoked by a moving hairpin vortex will be presented. The hairpin vortex is created in an otherwise laminar boundary layer and the nature of the flow induced downstream is documented. It is found that a discrete eruption of fluid from the wall region is produced. In three-dimensions, the erupting boundary layer first appears in the shape of a crescent-like ridge and then rolls over into a secondary hairpin vortex. This behavior is essentially predicted by the general three-dimensional theory of unsteady separation recently described by Van Dommelen and Cowley (1990).

Lastly, the nature of the flow near a three-dimensional corner is investigated experimentally using the configuration depicted schematically in Figure 2. In this situation, horseshoe vortices are observed to form periodically upstream of the cylinder; as they are swept outboard of the cylinder, sharp eruptive responses from the flow near the wall are seen. The flow regime is investigated thoroughly using hydrogen bubble wire flow visualization as well as a laser sheet. The separation processes are very complex but can be understood in terms of the basic influence of a vortex on a viscous flow.

References

Ersoy, S. and Walker, J. D. A. (1985), "Viscous Flow Induced by Counterrotating Vortices", *Physics of Fluids*, Vol. 28, pp. 2687-2698.

Harvey, J. K and Perry, F. J. (1971), "Flowfield Produced by Trailing Vortices in the Vicinity of the Ground", *AIAA Journal*, Vol. 9, pp. 1659-1660.

Peridier, V. J. and Walker, J. D. A. (1989), "Vortex-Inducing Boundary-Layer Separation", Report FM-13, Department of Mechanical Engineering and Mechanics, Lehigh University, October.

Van Dommelen, L. L. and Cowley, S. J. (1990) "On the Lagrangian Description of Unsteady Separation", to appear in *Journal of Fluid Mechanics*; see also NASA Technical Memorandum

102026.

Walker, J. D. A. (1989), "Wall-Layer Eruptions in Turbulent Flows", NASA Technical Memoranda 102362, ICOMP-89-26.

Walker, J. D. A. 1990 "Models Based on the Dynamical Features of the Wall Layer", to appear in *Applied Mechanics Reviews*, Proceedings of XI U. S. National Congress of Applied Mechanics, University of Arizona, Tucson, AZ, May 21-25, 1990.

Walker, J. D. A., Abbott, D. E., Sharnhorst, R. K. and Weigand, G. G. (1989), "Wall-Layer Model for Velocity Profile in Turbulent Flows", *AIAA Journal*, Vol. 27, pp. 140-149.

Walker, J. D. A., Smith, C. R., Doligalski, T. L. and Cerra, A. W. (1987), "Impact of a Vortex Ring on a Wall", *Journal of Fluid Mechanics*, Vol. 181, pp. 99-140.

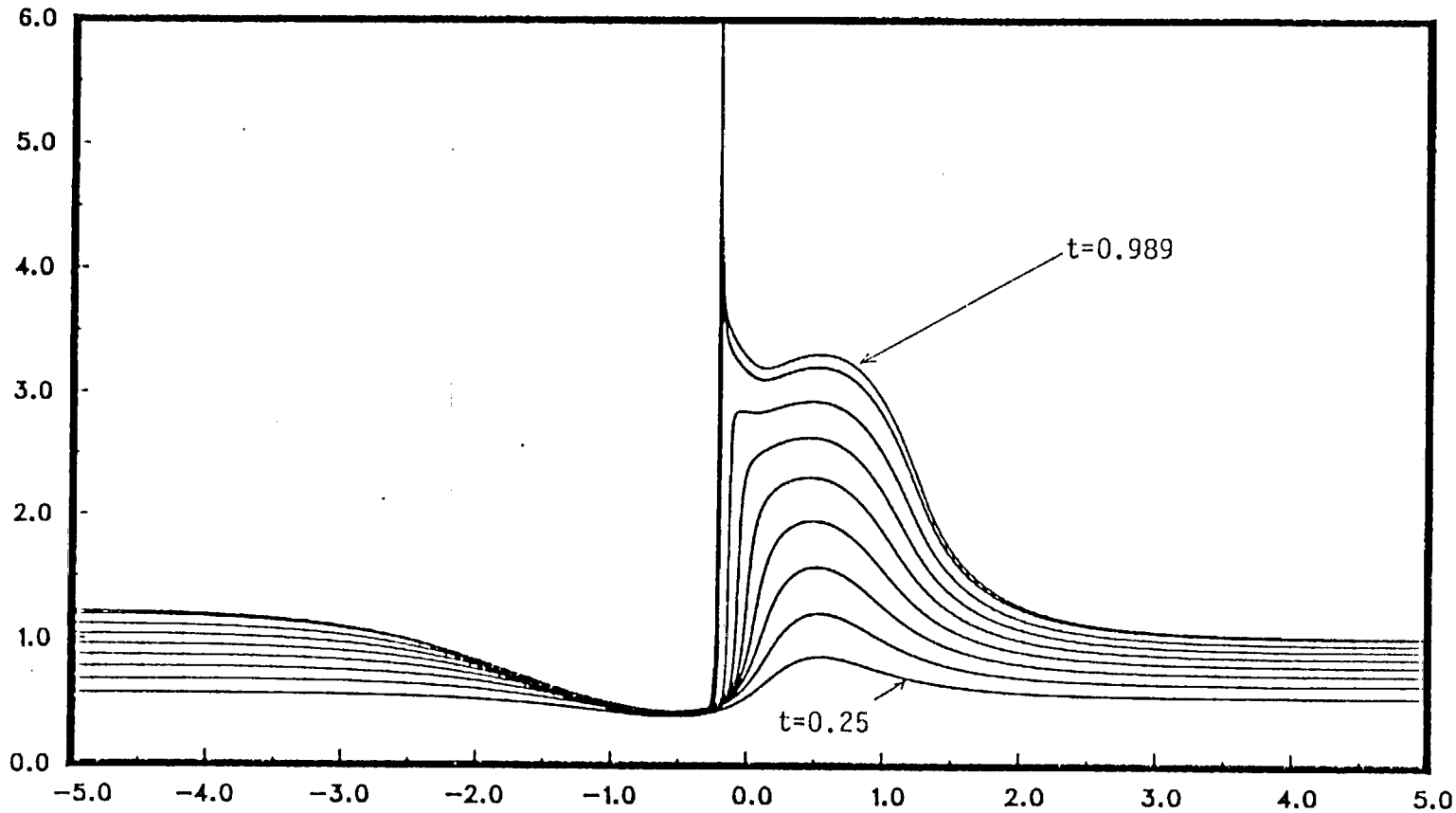

Figure 1: Temporal development of the displacement thickness δ^*; plotted curves at t = 0.25, (0.10), 0.95 and $t_s = 0.989$.

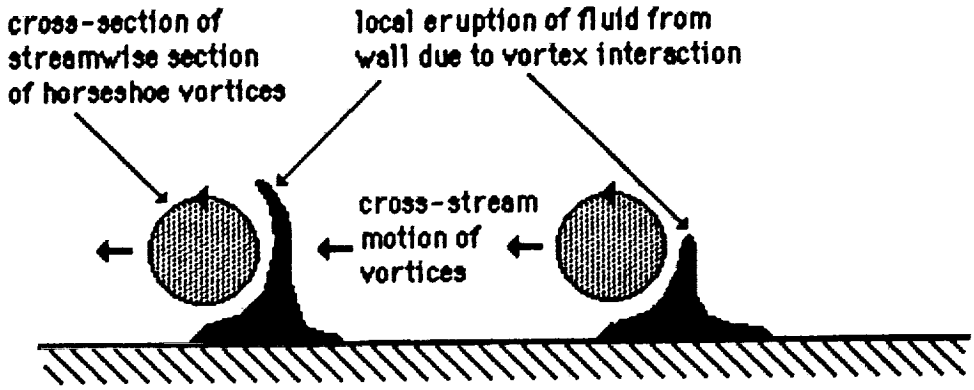

View A-A

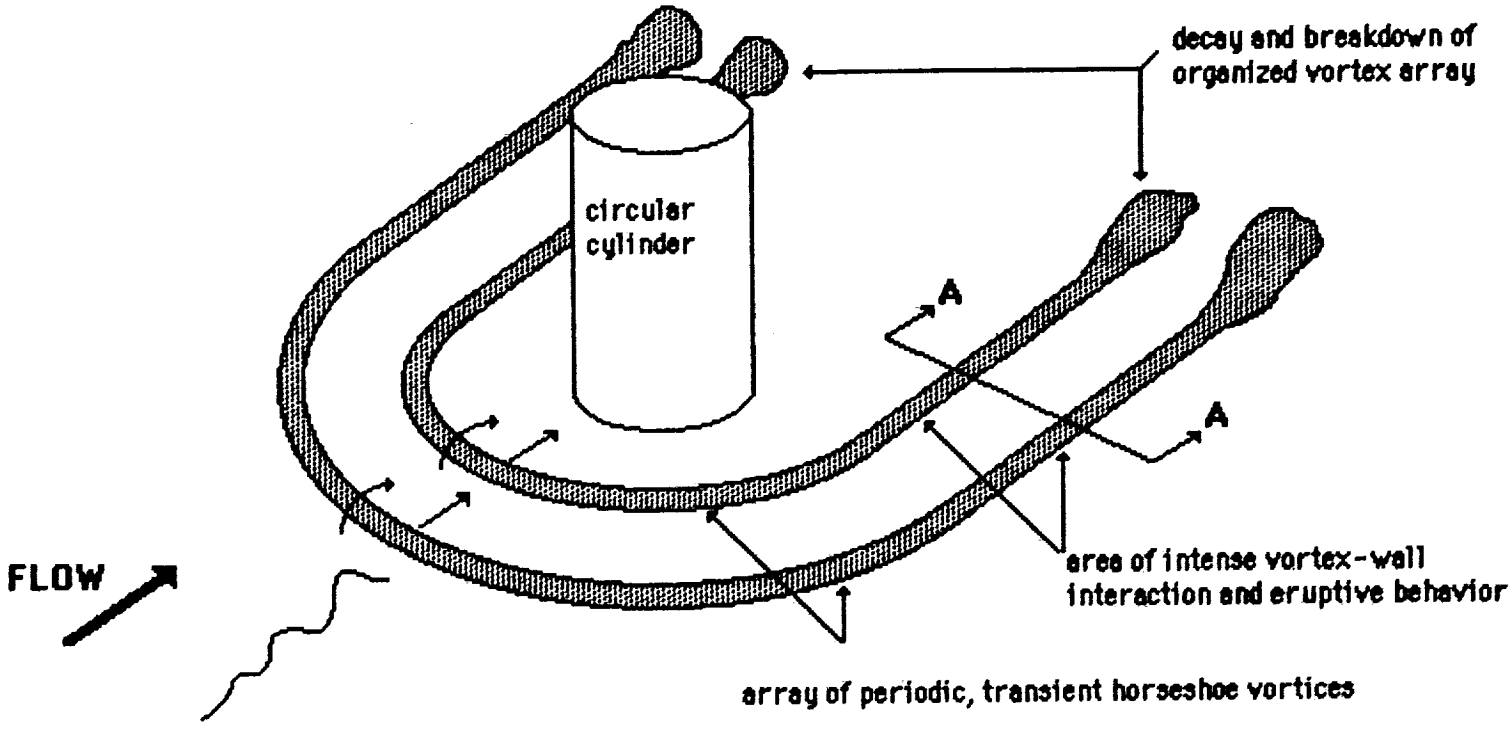

Figure 2: The development of a transient, three-dimensional horseshoe vortex array in a laminar boundary layer impinging on a cylinder. Note sharp eruptive behavior stimulated by vortex-wall interaction of the streamwise portion of the horseshoe vortices.

Departure Solutions of the Unsteady Thin-Layer and Full Navier-Stokes Equations Solved Using Streamline Curvature Based Iteration Techniques

M. Barnett
United Technologies Research Center
East Hartford, Connecticut

D. Turner and A. P. Rothmayer
Iowa State University
Ames, Iowa

Abstract

The development of a thorough understanding of the mechanisms for vortex eruptions from viscous layers, which are believed to be associated with phenomena such as dynamic stall onset and transition, is crucial if accurate models of such phenomena are to be formulated. The development of such models may, in turn, allow for the possibility that such effects could be accounted for during the design of various aerodynamic devices such as wings, helicopter rotors and turbomachinery blading and thus lead to designs which are stall free or stall resistant and which have better stall-recovery properties. The present investigation is being conducted as part of an effort to develop analytical and numerical tools which can be used to help improve our understanding of the vortex-eruption mechanism at high Reynolds numbers. The addition of the normal-momentum equation to the classical unsteady boundary-layer equations is crucial, according to recent asymptotic analyses of the vortex-eruption problem, and is a key feature of the analyses being developed by the present authors. The purpose of this paper is, first, to describe departure solution behavior observed when using unsteady, streamline-curvature based solution procedures in which nontrivial transverse pressure gradient effects are included and, second, to show that special treatment of the time-derivative of the normal velocity is needed to eliminate the ill-posed solution behavior, which is observed when small spatial and temporal step sizes are used.

Introduction

A number of recent analytical studies have been directed towards understanding the fundamental physics associated with the development and subsequent eruption of concentrated regions of vorticity from the boundary layer (e.g., van Dommelen and Shen (1980), Elliott, *et al* (1983), Peridier, *et al* (1988) and Smith (1988)). This event is believed to be associated with well-known physical phenomena, such as the onset of airfoil dynamic stall and transition from laminar to turbulent flow. The cumulative observation of the above-mentioned and other studies seems to indicate that the classical boundary-layer equations are insufficient to completely describe the vortex eruption phenomenon. Even if strong viscous-inviscid interaction is allowed, it appears likely that normal pressure gradient effects must be accounted for in some form. The present paper describes part of an overall effort directed towards the development of unsteady analyses capable of addressing high Reynolds number flows in which normal pressure gradients are important and ultimately, it is hoped, where vortex eruptions occur, as well.

The important work of van Dommelen and Shen (1980) first documented the existence of a finite-time singularity in the solution of the non-interacting, classical, unsteady boundary-layer equations for flow past an impulsively started circular cylinder. Later work (e.g., Peridier, *et al* (1988)) showed that, if the boundary-layer equations are allowed to interact with the inviscid flow, the van Dommelen and Shen singularity can be bypassed. However, another finite-time singularity, which cannot be removed through interaction alone, arises shortly thereafter. The recent asymptotic study of Smith (1988) indicates that normal pressure gradient effects must be included in order to avoid the latter (interactive) finite-time singularity. This provides the motivation for the present work, which addresses the issue of how various terms in the unsteady normal-momentum equation must be numerically treated within the framework of a globally iterated space- and time-marching solution algorithm, in order to avoid ill-posed behavior of the solutions. Globally iterated solution algorithms for steady and unsteady flows have been employed extensively in both asymptotic (*i.e.*, infinite Reynolds number) and finite Reynolds number investigations, where they have proven to be computationally

efficient. Streamline curvature techniques have been demonstrated in a number of studies, for example, see Smith *et al* (1984), Presz (1985), Rothmayer (1989, 1990) and Power (1990) – many other examples can be found in the literature. Thus, this approach is being pursued here in the hope that the use of a boundary-layer like numerical approach will lead to a computationally efficient technique to solve the vortex-eruption problem.

External Flow Analysis – Flow Past a Flat Plate

The particular concern of this paper is an issue which arose while the first author was developing a numerical solution scheme for the equation set consisting of the classical, unsteady, incompressible boundary-layer equations supplemented with the inviscid form of the normal-momentum equation. Note that these equations are essentially identical to the leading-order terms in the Incompressible form of the "Thin-Layer" Navier-Stokes equations, and will therefore be referred to here as the ITLNS equations, for convenience. For two-dimensional flows these equations are given by

$$\frac{\partial u}{\partial x} + \frac{\partial v}{\partial y} = 0 \ , \tag{1}$$

$$\frac{\partial u}{\partial t} + u\frac{\partial u}{\partial x} + v\frac{\partial u}{\partial y} = -\frac{\partial P}{\partial x} + \frac{\partial^2 u}{\partial y^2} \tag{2}$$

and

$$\frac{\partial v}{\partial t} + u\frac{\partial v}{\partial x} + v\frac{\partial v}{\partial y} = -Re\frac{\partial P}{\partial y} \ , \tag{3}$$

where u and v are the velocity components in the x- and y-directions, respectively, with x oriented tangent to the body surface and y normal to it, and P is the static pressure. In this section, the body is assumed to be a semi-infinite flat plate, so that x and y are Cartesian coordinates. Standard low-speed, external flow nondimensionalizations have been used and the y-coordinate and v-velocity component have been scaled with the square root of the Reynolds number as follows: $u = u^*/U^*_\infty$, $v = v^*\sqrt{Re}/U^*_\infty$, $P = (P^* - P^*_\infty)/\rho^* U^{*2}_\infty$, $x = x^*/L^*_{ref}$, $y = y^*\sqrt{Re}/L^*_{ref}$ and $t = t^*/(L^*_{ref}/U^*_\infty)$. Asterisks denote dimensional quantities, the subscript ∞ denotes a quantity evaluated in the uniform far field upstream flow and Re is the Reynolds number defined as $Re = U^*_\infty L^*_{ref}/\nu^*$, where ν^* is the upstream value of the kinematic viscosity which, along with the density ρ^*, is assumed to be constant.

The ITLNS equations can be solved in the primitive variable form given above, or they can be solved after transforming to Görtler variables – the latter approach has been used in this study. However, to simplify the present discussion, the primitive variable form of these equations will be considered, after using the stream function ψ, defined by the relations $u = \partial\psi/\partial y$ and $v = -\partial\psi/\partial x$, to replace v. Substituting for v in Eq. (3) yields

$$-\frac{\partial^2\psi}{\partial x\partial t} - u\frac{\partial^2\psi}{\partial x^2} + \frac{\partial\psi}{\partial x}\frac{\partial^2\psi}{\partial x\partial y} = -Re\frac{\partial P}{\partial y} \ . \tag{4}$$

The boundary conditions on the surface ($y = 0$) are the no-slip, zero injection conditions: $u(x,0) = 0$ and $\psi(x,0) = 0$ for $t \geq 0$. At the outer edge of the boundary layer ($y \to \infty$) the edge condition on u is $\lim_{y\to\infty} u(x,y;t) \to U_e(x,t)$ and the pressure P satisfies the unsteady Bernoulli relation. The equations can either be solved in direct mode (edge conditions specified) or inverse mode (displacement thickness specified). The additional boundary condition needed for the latter is given by the following relationship between the edge value of ψ and the displacement thickness δ^*,

$$\psi(x, y_e; t) = U_e(x,t)(y_e - \delta^*(x,t)) \ , \tag{5}$$

where y_e is the value of y at the boundary-layer edge and U_e is treated as an unknown. In addition, both upstream and downstream boundary conditions are needed – the latter is required because the introduction of the inviscid normal-momentum equation makes the inviscid form of the governing equations equivalent to the unsteady incompressible Euler equations, which are elliptic-like in space at any time t, as explicitly evidenced by the presence of the ψ_{xx} term in Eq. (4), which represents the streamline curvature. For the simple problem to be considered here, the upstream and downstream profiles for u and ψ are assumed to

correspond to the Blasius (flat-plate) profile. Finally, the initial condition which is needed at time $t = 0$ is assumed to correspond to the Blasius solution along the entire plate surface.

The ITLNS equations are numerically solved using fully implicit discretizations which are first-order accurate for the x- and t-derivatives and second-order accurate for the y-derivatives. All y-derivatives are central differenced and all x- and t-derivatives are backward differenced with respect to the solution point (at (x_i, y_j, t_n)) with the exception of the ψ_{xx} term in the normal-momentum equation, which is central differenced, thus introducing unknown information from the upstream point at x_{i+1}. This information is obtained by initially guessing ψ_{i+1}, using the value from the previous time step, and then performing multiple, global spatial sweeps at each time level until the ψ-field converges. An acceleration scheme has been used to improve the convergence properties of this procedure but will not be discussed here, however, as it is not relevant to the present focus. Initially the authors believed that central differencing of the ψ_{xx} term would properly (and fully) account for the elliptic-like nature of the governing equations at each time step, as demonstrated in applications of similar approaches to steady flows (e.g., see Presz (1985)). However, this was not found to be the case, as will be discussed below.

The issue which is of concern here arises when attempting to solve the above system of equations for a specified time-dependent displacement-thickness distribution (i.e., the inverse method). Consider the simplest possible case, where the displacement thickness is assumed to be that for a steady flat-plate flow for all time $t \geq 0$. Thus, the inverse solution procedure should yield the Blasius solution at all values of x and t, with a small perturbation (depending on the specified value of the Reynolds number) due to normal pressure gradient effects. This has been found to be the case here when the spatial and temporal step sizes Δx and Δt, respectively, are not chosen to be "too small." However, as Δx and Δt are decreased, it has been observed that, during the first time step, the solution departs from its anticipated behavior in a manner reminiscint of that observed when attempting to solve a boundary-value problem using an initial-value technique. This occurs despite the use of central differencing for the ψ_{xx} term. That is, for a fixed, constant spatial stepsize Δx below some minimum value, there appears to be a *minimum* temporal step size Δt, below which the space-marching solution behaves as if it is ill-posed with respect to x.

Examples of the departure solutions are shown in Figs. 1A and 1B, where the skin-friction coefficient, $C_f = 2\tau_w^* \sqrt{Re}/\rho^* U_\infty^{*2}$, and wall pressure P_w, respectively, are plotted as functions of distance along the plate for a Reynolds number of 1×10^6 based on a reference length $L_{ref} = 1$. This case was calculated starting at $x = 1.0$ with a fixed value of $\Delta x = 0.001$ and three different values of Δt, namely 0.0010, 0.0009 and 0.0001. This value of Δx is below the minimum for which departures have been observed, and the three values of Δt are near the boundary between departure-free solutions and departing solutions. Note that the solution goes from being well-behaved at the largest value of Δt to growing in an oscillatory exponential manner for the middle value to monotonic exponential growth for the smallest value. Similar departure behavior was subsequently observed in the solutions obtained from a different numerical code which uses a similar streamline-curvature based technique to solve the full Navier-Stokes equations, for internal flows, as discussed in the next section.

Before continuing, it should be noted that a consistency check on the finite-difference form of Eq. (4) was carried out. The equations were found to be consistent in the sense that as Δx and Δt are independently reduced to zero, Eq. (4) is identically recovered. Thus, the possibility that truncation errors associated with the discretized equations have changed the mathematical character of the governing differential equations has been eliminated as a possible source for the branching behavior.

Calculations to establish the "departure boundary" for three different Reynolds numbers were performed, namely $Re = 1 \times 10^6$, 1×10^7 and 1×10^8. The results are consistent, and indicate that the value of Δt for which the solution crosses over from "departure-free" to "departing" is a function of Reynolds number, as might be anticipated. The fact that there is a minimum Δx above which solutions remain departure-free for any value of Δt is not surprising – once Δx becomes large enough, the solution probably oversteps the streamwise length scale of the physical mechanism governing the behavior.

The branching behavior of the small step size solutions of the ITLNS equations obtained using the present numerical solution procedure has been examined in detail by the authors in an effort to understand its source. As a result of this investigation, the term responsible for the departure solutions has been found to be the v_t term appearing in the normal-momentum equation. That is, it has been found that, regardless of the values used for Δx and Δt, if the v_t term is *neglected*, then the solution will *never* exhibit the departure behavior described above, so long as the ψ_{xx} term is not backward differenced, but is instead central differenced.

Further, this behavior is found to be independent of the numerical treatment used for the convective terms in the normal-momentum equation.

Recall that in the present study, the v_t term has been written using the stream function definition, i.e., $v_t = -\psi_{xt}$. In the numerical algorithm described above, this term was discretized using a backward difference for the x-derivative, leading to the following form at all y-locations, where the subscript i and superscript n denote the x-index and the t-index, respectively, with (i, n) at the current station in both space and time and Δx assumed to be uniform:

$$\psi_{xt} \approx \frac{1}{\Delta t \Delta x}\left[(\psi_i^n - \psi_{i-1}^n) - (\psi_i^{n-1} - \psi_{i-1}^{n-1})\right] . \tag{6}$$

The apparent ill-posedness exhibited by the numerical solutions, and the fact that the v_t term has been found to be responsible, suggests an alternative discretization for the ψ_{xt} term wherein a *forward* difference in x with respect to the solution station is used. That is, ψ_{xt} is discretized in the form

$$\psi_{xt} \approx \frac{1}{\Delta t \Delta x}\left[(\psi_{i+1}^n - \psi_i^n) - (\psi_{i+1}^{n-1} - \psi_i^{n-1})\right] . \tag{7}$$

With this modification, the ill-posed behavior which is observed when a backward difference is used no longer arises, regardless of the values of Δx and Δt that are specified. A case for which violent branching occurs when using a backward difference for the x-derivative in ψ_{xt}, which was presented in Fig. 1, has been recalculated using a forward difference with the same spatial and temporal stepsizes, i.e., $\Delta x = 0.001$ and $\Delta t = 0.0001$. The resultant solution is departure free and virtually identical to the backward-difference solution for $\Delta t = 0.001$, which did not branch because the value of Δx was too large.

The precise reason that forward-differencing of the x-derivative in the ψ_{xt} term is needed to prevent the ill-posed behavior of the small step-size solutions of these equations is unknown at the present time. One possiblity is that the responsible mechanism is somehow related to physical boundary-layer instability mechanisms. Another possibility is that the mechanism is purely inviscid in nature, as is the case leading to the requirement for central differencing of the ψ_{xx} term. Both of these possiblities are currently under investigation, and it is hoped that this issue will be resolved in the near future.

Internal Flow Analysis – Pulsatile Flow Through a Channel

Here the governing equations are taken to be the unsteady Navier-Stokes equations. This set of equations is non-dimensionalized by the method of Smith (1976). The final equations are: conservation of mass,

$$u_x + v_y = 0 ; \tag{8}$$

conservation of x-momentum,

$$u_t + Re(uu_x + vu_y) = -P_x + \underline{u_{xx}} + u_{yy} ; \tag{9}$$

and conservation of y-momentum,

$$\underline{v_t} + Re[u(v_x - v_T) + \underline{vv_y}] = -P_y + \underline{v_{xx}} + \underline{v_{yy}} . \tag{10}$$

The v_T term is a pseudo-time derivative introduced to accelerate convergence of the global-iteration scheme at each time-level t. The Reynolds number, Re, is defined here by $Re = L^{*3}g^*/\rho^*\nu^{*2}$, where L^* is the dimensional channel width, ρ^* is the density, ν^* is the kinematic viscosity and $-g^*$ is the local applied pressure gradient driving the basic flow. This set of equations is solved in a two-dimensional channel where the upstream flow is a pulsatile Poiseuille flow driven by the pressure gradient

$$\frac{\partial P}{\partial x}(-\infty, y) = -1 + \gamma_0 \cos \beta t . \tag{11}$$

The corresponding velocity profile is

$$u(-\infty, y) = u_0^s + u_0^u , \tag{12}$$

where

$$u_0^s = \frac{1}{2}y(1-y) \quad , \quad u_0^u = c_1 e^{\sqrt{\beta}e^{\frac{i\pi}{4}}y} + c_2 e^{\sqrt{\beta}e^{\frac{5i\pi}{4}}y} - \frac{\gamma_0}{2i\beta} , \tag{13}$$

with

$$c_1 = \frac{e^{\sqrt{\beta}e^{\frac{5\pi i}{4}}}}{2i\beta\left[1+e^{\sqrt{\beta}e^{\frac{5\pi i}{4}}}\right]} \quad , \quad c_2 = \frac{\gamma_0}{2i\beta\left[1+e^{\sqrt{\beta}e^{\frac{5\pi i}{4}}}\right]} \tag{14}$$

and $v(-\infty, y) = 0$. No-slip boundary conditions are applied along the upper and lower walls and the downstream boundary conditions are $u_x = 0$ and $v_x = 0$.

For the case where the streamwise length scale is the same order as the channel width, the minimal system of equations needed to reproduce the unsteady asymptotic structure of Smith (1976) is the parabolized Navier-Stokes (PNS) equations (Eqs. (8)–(10) with all underlined terms neglected). Bearing this in mind, a Navier-Stokes algorithm is formulated by first developing a PNS algorithm and then iterating on the additional (underlined) terms. It is well-known that, when solving the *steady* PNS equations, departure solutions can be suppressed either by neglecting the streamwise pressure-gradient term P_x, or the streamline-curvature term (the uv_x term, see Rothmayer (1989, 1990)). In this study, the streamline-curvature term uv_x is used to suppress departure solutions in the steady single-pass version of the algorithm, and also to provide a mechanism for upstream propagation of information in the steady and unsteady global-iteration algorithms.

The streamline-curvature term uv_x is treated as a known source term and is forward-differenced in space relative to the current solution point. The pseudo-unsteady term uv_T (introduced to accelerate convergence as in Davis (1984) and Barnett and Davis (1986)) is included implicitly using a standard backward difference in time (see Rothmayer (1989, 1990)). Note that two unsteady effects are present – the real unsteady terms u_t and v_t and the pseudo-unsteady term v_T. The latter is driven to zero during multiple sweeps through the solution domain at each real time level t.

The algorithm described above, without the addition of the Navier-Stokes terms (i.e., underlined terms in Eqs. (8)-(10)) is similar to that described in the section on external flows, where the ITLNS equations are solved. As with that algorithm, a number of implicit/explicit PNS-like algorithms were tested. The full Navier-Stokes version of the internal-flow solution technique treats the underlined terms as source terms calculated from the solution at the previous iteration, although algorithms with implicit treatment of v_t were also tested. The reader is referred to Rothmayer (1990) for further details.

The above-described Navier-Stokes solution algorithm has been used to solve for the flow through a flat channel with the pulsatile pressure gradient given by Eq. (11) and the upstream boundary conditions given by Eqs. (12–14). Fig. 2A shows a comparison between the wall shear stress computed using the present analysis at a downstream location along with that given by the analytical Poiseuille solution – the agreement is excellent. The departure solutions, to be discussed next, were triggered by introducing a very small indentation in the channel wall (typical height $h = 1 \times 10^{-6}$).

As with the previously described external-flow analysis, it has been found that the present solution algorithm experiences departure-solution behavior when a minimum spatial/temporal step-size restriction is violated, with solutions like that shown in Fig. 1. Figure 2B shows how the minimum allowable time step, Δt_s, changes with varying streamwise step size, Δx, for a Reynolds number of 10 million. For a streamwise step size above a critical value ($\Delta x \approx 0.207$) the numerical scheme is free of departure solutions for all values of Δt examined. As found with the external-flow analysis, neglecting the v_t term leads to departure-free solutions for all values of Δx and Δt.

A similar departure-solution behavior was also observed when solving the PNS equations numerically. As with the Navier-Stokes algorithm, the unsteady PNS method displayed the spatial/temporal step-size constraints. These departure solutions could again be eliminated by neglecting the v_t term. These observations hold even if the normal-momentum equation is reduced to the very simple form $v_t = -P_y$.

In the external-flow analysis, branching of the numerical solution was suppressed by spatially forward-differencing the v_t term, after re-expressing in terms of the stream function. A similar approach was attempted in the internal-flow analysis. The $-\psi_{xt}$ term was forward and backward differenced in space, and treated both implicitly and explicitly in both cases, in an attempt to eliminate the departure solutions. Of the four methods, the backward-differenced explicit method had the least severe time-step restriction for a given value of Δx. However, for sufficiently small time steps, all four algorithms exhibited the departure-solution behavior previously discussed. This is in contrast with the external-flow analysis, where branching could be completely eliminated by spatial forward-differencing of the $-\psi_{xt}$ term. It is not clear at this time

why this difference between the internal- and external-flow analyses exists. Fortunately, the pseudo time step ΔT can be optimized so that the time scales for the observed departure solutions fall below the scales of the Navier-Stokes regime (which constitute a likely absolute lower bound on the temporal time step needed for practical calculations). However, if a judicious choice of ΔT is not made, then departure solutions may be encountered even at the large values of Δt associated with the interactive boundary-layer regime of Smith (1976) (see Fig. 2C).

Another interesting, and currently unexplained, phenomena observed in both the internal- and external-flow analyses is that departure solutions can be eliminated by neglecting the v_t term in certain local transverse regions, while retaining this term outside of those regions. The five points labeled A1, A2 and B1 through B3 on Fig. 2B are points at which the solution has been stabilized by neglecting v_t in the various regions indicated. Fig. 2D shows the location of these regions for each point. It can be seen from this group of figures that the size and location of these regions are sensitively dependent on both the spatial and temporal stepsizes. For all values of Δx there appears to exist a Δt below which v_t must be neglected across the entire channel to ensure departure-free solutions.

Concluding Remarks

The objective of this paper has been, first, to describe departure solution behavior observed when using streamline-curvature based solution procedures which are being developed to study high Reynolds number vortex-eruption phenomena, second, to indicate the responsible term in the governing equations and, finally, to show how the departure solutions can be eliminated. We have shown that the time-derivative of the normal velocity, $v_t = -\psi_{xt}$, appearing in the normal-momentum equations, is responsible for the branching behavior, which only occurs for small spatial and temporal step sizes. The ill-posed behavior has been eliminated in the external-flow analysis by forward differencing the spatial-derivative appearing in the $-\psi_{xt}$ term. It should be noted that the step sizes for which the observed ill-posed behavior arises turn out to be within the range needed to capture many important unsteady viscous-inviscid interaction phenomena, such as dynamic stall onset. Therefore, this mechanism should not be ignored if accurate solutions are to be obtained. The implication is that special differencing procedures may be needed to properly account for the mechanisms responsible for the elliptic-like character of the governing equations at each time level of a time-marching algorithm, possibly even for non-streamline-curvature techniques. A more complete description of the responsible mechanism is currently being pursued by the authors, and will be reported when it is available.

Acknowledgements

The authors wish to acknowledge the helpful discussions of Dr. Frank Smith of University College, London and Mr. Robert LaBarre of UTRC. We also wish to gratefully acknowledge the funding of this research by the United Technologies Corporation and by the National Science Foundation Presidential Young Investigator Award of A. P. Rothmayer. Finally, the authors would like to acknowledge the computational resources provided by the Iowa State University Computation Center.

References

Barnett, M. and Davis, R. T., 1986, "Calculation of Supersonic Flow with Strong Viscous-Inviscid Interaction," *AIAA J.*, **24**, pp. 1949–1955.

Davis, R. T., 1984, "A Procedure for Solving the Compressible Interacting Boundary-Layer Equations for Subsonic and Supersonic Flows," AIAA Paper 84–1614.

Elliott, J. W., Cowley, S. J. and Smith, F. T., 1983, "Breakdown of Boundary Layers: (i) On Moving Surfaces, (ii) In Semi-Similar Unsteady Flow, (iii) In Fully Unsteady Flow," *Geophys. and Astrophys. Fluid*

Dyn., **25**, pp. 77–138.

Peridier, V. J., Smith, F. T. and Walker, J. D. A., 1988, " Methods for the Calculation of Unsteady Separation," AIAA paper 88–0604.

Power, G. D., 1990, "A Novel Approach for Analyzing Supersonic High Reynolds Number Flows with Separation," AIAA Paper 90–0764.

Presz, W. M., 1985, "A Numerical Method for Duct Flow with Boundary-Layer Separation," AIAA Paper 85–1410.

Rothmayer, A. P., 1989, "The Computation of Separated Flows in Symmetric Channels," Proceedings of the Fourth Symposium on Numerical and Physical Aspects of Aerodynamic Flows, Long Beach, CA.

Rothmayer, A. P., 1990, "Solution of the High Reynolds Number Navier-Stokes Equations by Global Streamline Curvature Iteration," to appear in *Eur. J. Mech.*

Smith, F. T., 1976, "Flow Through Constricted or Dilated Pipes and Channels: Parts 1 and 2," *Q. Journal Mech. Appl. Math.*, **29(3)**, pp. 343–364.

Smith, F. T., 1979, "On the Non-Parallel Flow Stability of the Blasius Boundary Layer," *Proc. Roy. Soc.* **A366**, pp. 91–109.

Smith, F. T., 1988, "Finite-Time Breakup Can Occur in any Unsteady Interacting Boundary Layer," *Mathematika*, **35** pp. 256–273.

Smith, F. T., Papageorgiou, D. and Elliott, J. W., 1984, "An Alternative Approach to Linear and Nonlinear Stability Calculations at Finite Reynolds Numbers," *J. Fluid Mech.*, **146**, pp. 313–330.

van Dommelen, L. L. and Shen, S. F. 1980, "The Spontaneous Generation of the Singularity in a Separating Laminar Boundary Layer," *J. Comp. Phys.*, **38**, 125.

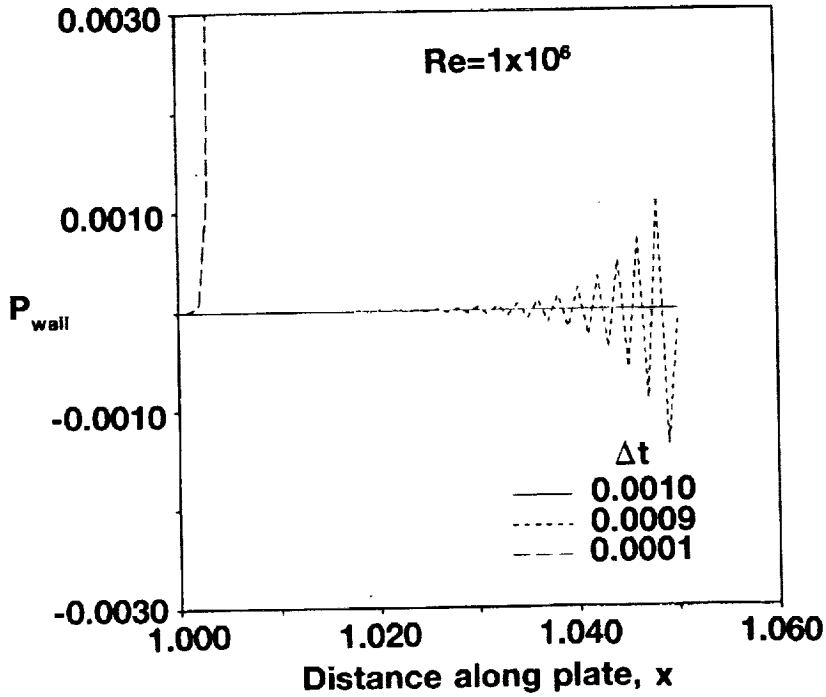

Fig. 1A. Wall pressure along plate for three values of Δt, Δx=0.001.

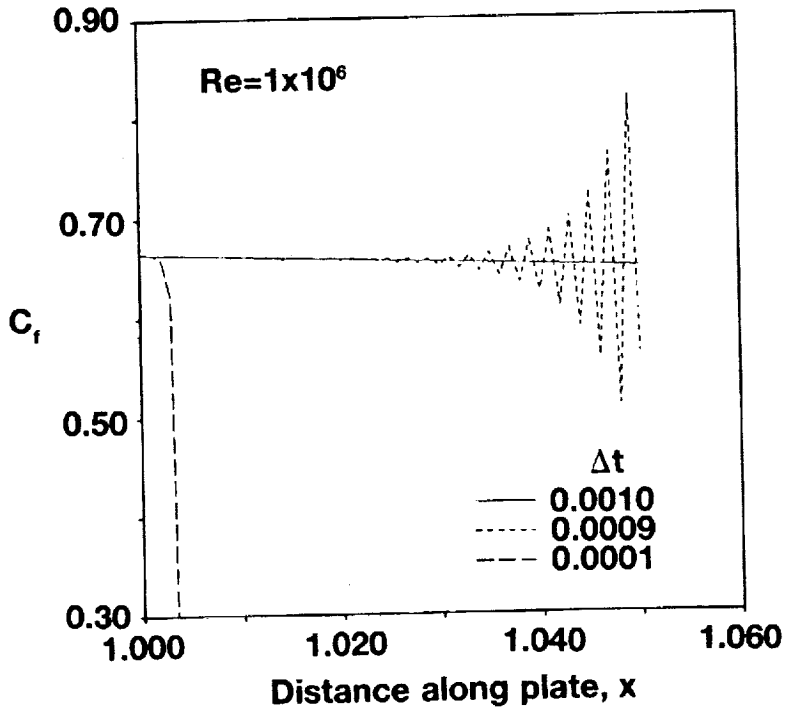

Fig. 1B. Skin-friction coefficient along plate for three values of Δt, Δx=0.001.

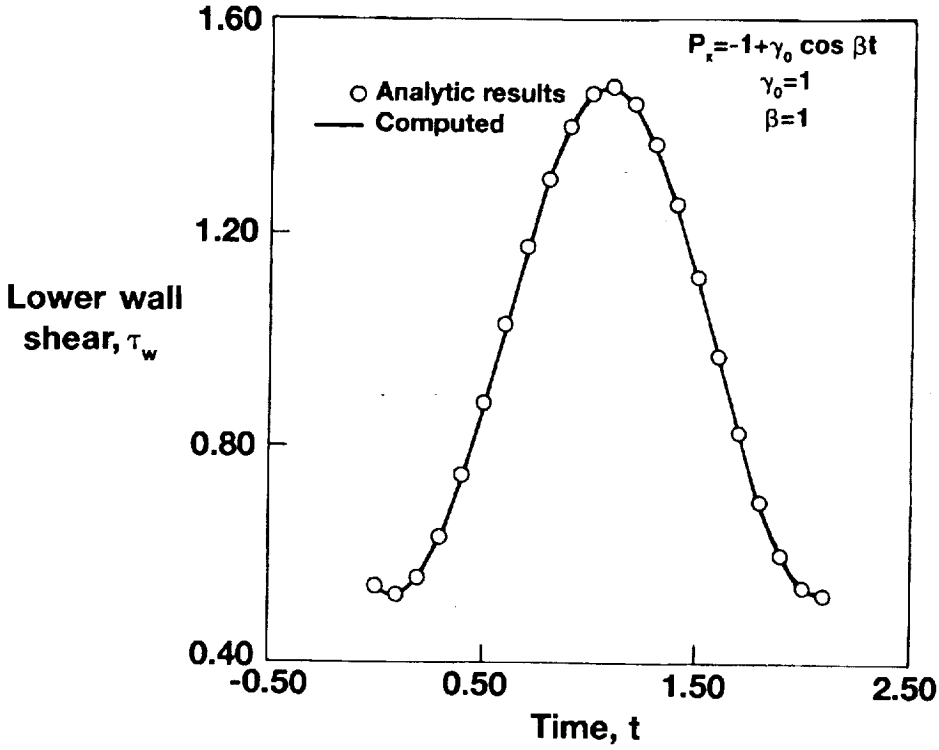

Fig. 2A. Comparison of analytical and calculated wall shear with the solution driven by a pulsatile pressure gradient.

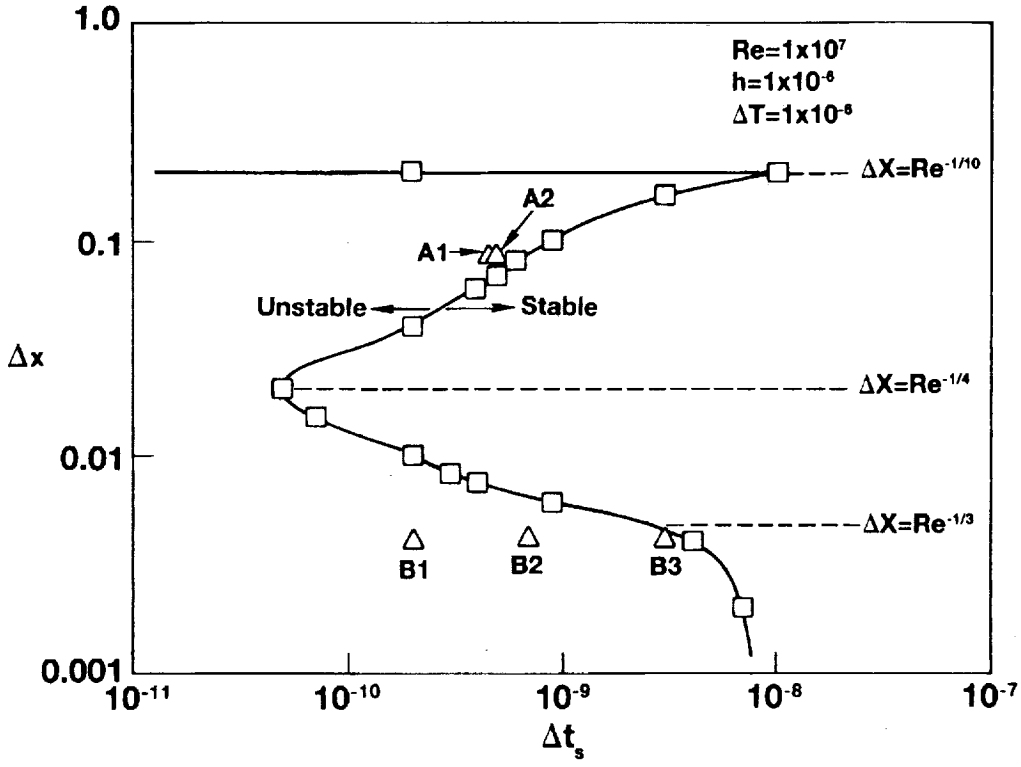

Fig. 2B. Stability boundary for the internal flow algorithm.

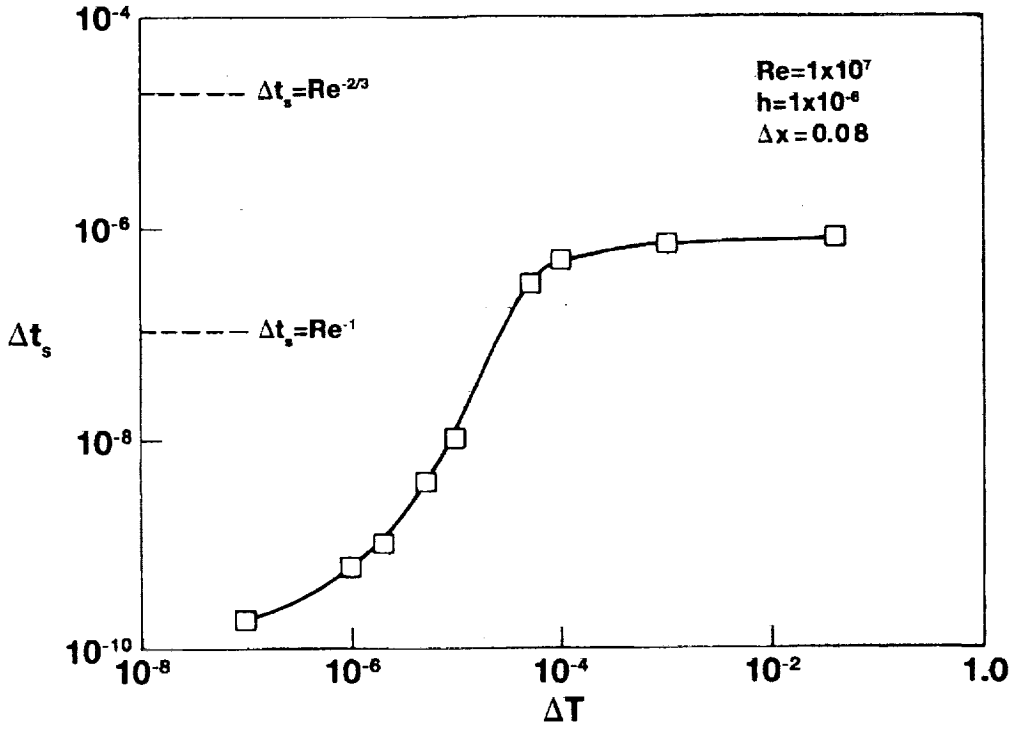

Fig. 2C. Variation of minimal time step constraint with changing pseudo time step.

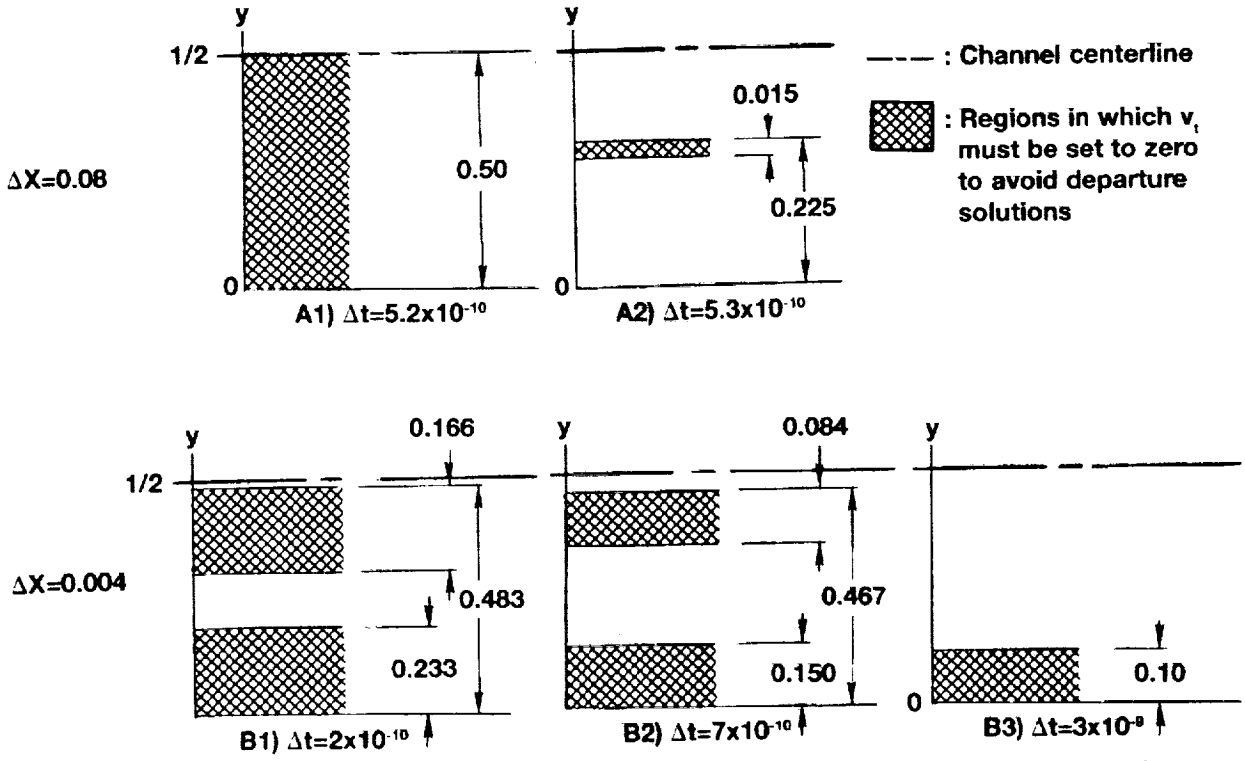

Fig. 2D. Illustration of regions where neglecting V_t suppresses branching.

N94- 34981

Experiments on an Unsteady, Three-dimensional Separation

R.W. Henk*, W.C. Reynolds† , and H.L. Reed‡
Stanford University, Stanford, California

Unsteady, three-dimensional flow separation occurs in a variety of technical situations, including turbomachinery and low-speed aircraft. An experimental program at Stanford in unsteady, three-dimensional, pressure-driven laminar separation has investigated the structure and time-scaling of these flows; of particular interest is the development, washout, and control of flow separation. Results reveal that a two-dimensional, laminar boundary layer passes through several stages on its way to a quasi-steady three-dimensional separation. The quasi-steady state of the separation embodies a complex, unsteady, vortical structure.

This talk will describe the experimental facility, the means of generating separation, and the stages of the development of an unsteady, three-dimensional separation.

Background

A working definition for three-dimensional separation has been adopted according to Legendre (1982) and Tobak and Peake (1982). Legendre (1982) succinctly states that a "line of separation ... has no local property. Its only characteristic is to pass through a saddle point." The definition stipulates that the reference frame is that of the surface and that the saddle point of the flow is on the surface. The three-dimensional separation generated in our experiment evolves into the type Owl face of the first kind according to the classification scheme by Perry and Hornung (1984). This separation has a clearly identifiable saddle point which was seen in visualizations of our flowfield. In this experiment the separation is seen to develop and decay in the reference frame of a fixed flat plate.

This experiment differs markedly from those by Didden and Ho (1985) and Koromilas and Telionis (1980). Didden and Ho report on an axisymmetric vortex traveling close to a wall. The MRS condition calls the contortions that the wall-jet boundary layer assume a *downstream-moving* separation (see Didden and Ho, 1985). In our experiment, *downstream-moving separation* refers to the decay of the separation as the sluggish fluid is sheared back into an unseparated velocity profile. The most important physics during this process is the diffusion of vorticity in the separated shear layer back to the surface.

Koromilas and Telionis (1980) documented the development of a two-dimensional separation. In their experiment, separation developed at the Howarth-flow section, where the test surface underwent deformation over time. A time-variation of the leading-edge vorticity and the test boundary layer accompanied this deformation. In our experiment, upstream conditions and the contours of the test surface remained constant. Our well-documented initial conditions and boundary conditions aid comparison with direct numerical simulations such as Pauley, *et al.* (1988).

---

* Graduate Student, Department of Mechanical Engineering, Stanford University.

† Professor, Department of Mechanical Engineering, Stanford University.

‡ Associate Professor, Department of Aeronautical and Mechanical Engineering, Arizona State University.

Experimental Facility and Experimental Conditions

The experimental facility is a closed-circuit water tunnel, figure 1, in which water flows from an overhead tank through the test section and then to a sump tank. Turbulence attenuation by honeycomb, screens, and acceleration through a nozzle provides a low turbulence freestream to the test section. A fresh boundary layer then develops under a zero pressure gradient until it reaches the unsteady portion of the test section. At this point, the boundary layer encounters either (1) a steady, zero or adverse pressure gradient, or (2) a computer-controlled, time-varying pressure gradient, as determined by the valves draining flow through the wall opposite the test surface. The water is continually pumped from the sump to the overhead tank to close the circuit.

The freestream flow is controlled by a bank of manual and computer-controlled valves located on the wall opposite the test surface. Typically the flow sees a zero pressure gradient. When instructed by the computer, some valves may be opened proportionately to create a local, adverse pressure gradient. The flowrate drained through each valve, and hence the imposed freestream flow, can be steady or unsteady. Any waveform may be imposed on the freestream flow. A square wave was chosen for these experiments.

For these experiments one upstream valve and one downstream valve are commanded to operate 180 degrees out of phase, producing a steady, zero pressure gradient flow in the upstream portion of the test section while the downstream flow sees an unsteady adverse pressure gradient. This ensures constant initial conditions for the test boundary layer; for example, leading-edge vorticity does not vary .

The test surface, a flat plate $2.7m$ long, forms the top wall of the test section. On the lower surface of the test surface, a fresh boundary layer is grown for investigation.

Laminar and turbulent boundary-layer experiments are performed in this tunnel. These laminar studies took place over the first meter of the test surface. The range of chord Reynolds numbers for the separation experiments extends from $1x10^5$ through $2x10^5$. Table 1 lists some of the flow parameters and geometry for this particular experiment.

Two laser doppler anemometer (LDA) systems measure velocities through the water tunnel. At the entrance to the test section, a single-component Helium-Neon LDA monitors the inlet flow. Downstream, the second LDA measures the velocity of the separated flow. This two-component Argon-Ion LDA is mounted on a traverse that permits movement of the measuring volume in all spatial directions. Motion normal to the test surface is automated for velocity surveys, which can continue for days without intervention.

Results: Stages in the development of a three-dimensional separation

The developing three-dimensional separation evolved through four distinct stages on its way to steady shedding. The four stages are the initial inviscid response, the breakaway of the shear layer, initiation of large-scale unsteadiness, and the quasi-steady state. Some zones of the separation structure experienced all of the stages as the separation develops under an impulsively imposed adverse pressure gradient.

Nomenclature for this section will use these special symbols: $\langle ??? \rangle$ refers to a phase-averaged quantity, where ??? is either a phase-mean velocity or double product term; LP:# refers to a measurement station along the centerline of the tunnel. Measurement

stations are shown in figure 2 with respect to tunnel geometry and the three-dimensional separation. Flow parameters and dimensions for tunnel geometry are listed in table 1.

The extent of each stage can be seen in a plot of the momentum-thickness histories at various locations along the centerline, figure 3. In the following subsections, the important features of each stage will be described more thoroughly.

Initial inviscid response. As is expected for an elliptic incompressible flow, flow through the entire tunnel responds instantaneously to the changes in the pressure gradient. Significant influence of the nonstationary, adverse pressure gradient is confined to downstream of $x \approx 0.55m$.

Breakaway of shear layer from the surface. The breakaway of the shear layer is part of the viscous response to the newly imposed adverse pressure gradient. It also contains aspects of an inviscid response as the near-wall flow is accelerated in the upstream direction. This can be modeled by taking the base case of a Blasius boundary layer and superimposing the potential flow correction.

It takes about $0.25s$ for the viscosity to catch up with the initial inviscid response. This stage at LP:1 lasts until $t \approx 4.5s$. The entire flow is remarkably quiescent throughout this stage of development. Figures 4a and 4b show phase-averaged $\langle U \rangle$-velocity profile histories at stations LP:1 and LP:2 respectively. The process that is taking place during this time is the displacement of the wall-bounded shear layer away from the surface as downstream and spanwise fluid is convected underneath, that is, into the separation wake. The separation wake extends from station LP:A through LP:2, as is shown in the separation cross-section, figure 2b.

Initiation of large-scale unsteadiness. At $t \approx 4.5s$, the shear-layer instability catches up with the viscous response. The shear layer rolls up and sheds in a dramatic and vigorous fashion (figures 4a and 4b). Accordingly, $\langle u'u' \rangle$-profile histories exhibit a pronounced alteration at this time.

Arrival at quasi-steady state. The $\langle U \rangle$-velocity profile histories, figures 4a and 4b, reveal an almost unchanging profile from $t \approx 7.5s$ until the end of the cycle, when suction is released. Although these profiles appears steady, they conceal perpetual unsteadiness in the steady-state structure of three-dimensional separation. Details of the physics and structure of the separation are better understood by considering profile histories of double product terms.

After $t \approx 7.5s$, the broad $\langle u'u' \rangle$-profile at LP:1 (figure 5a) has collapsed to a narrow peak. The narrow peak could be indicative of regular vortex roll-up or of flapping of the shear layer in the y-direction. The $\langle v'v' \rangle$- and $\langle u'v' \rangle$-profile plots (figures 6a and 7a, respectively) convince us of the latter explanation. For example, were vortex roll-up the dominant mechanism, then the $\langle v'v' \rangle$-profiles at LP:1 should show a peak similar to $\langle u'u' \rangle$ during the quasi-steady state. A low-frequency flapping of the shear layer at this location would result in the observed peak in $\langle u'u' \rangle$-profiles and flat $\langle v'v' \rangle$- and $\langle u'v' \rangle$-profiles.

In contrast, downstream at the location at LP:2, the broad peak in the $\langle u'u' \rangle$-profile persists throughout the quasi-steady state (figure 5b). This broad peak also appears in $\langle v'v' \rangle$- and $\langle u'v' \rangle$-profiles (figures 6b and 7b). The consistent peak throughout the double product profiles confirms that at this streamwise location, vigorous activity in the x- and y-directions trades high-velocity fluid in the outer flow with low-velocity fluid that was near the wall. In other words, spanwise vortices are passing through this streamwise

location. Evidently, the location of vortex roll-up has traveled downstream of LP:1 to a final position upstream of LP:2.

Thus the quasi-steady state includes a regular roll-up and shedding of vorticity from the separated shear layer that occurs between LP:1 and LP:2. Flow visualization confirmed that well-defined vortices began to roll up near LP:1 and shed through LP:2.

Conclusions

This experimental study on the fluid dynamics of unsteady, three-dimensional flow separation has broadened the understanding of the time behavior of these flows.

A definition for unsteady and three-dimensional separation has been adopted that is consistent for all such flows. This definition follows the suggestions of Legendre, Tobak and Peake. Although a controversy has arisen because of the differing definitions, it is found that all phenomena are adequately addressed by all.

The dominant processes of the development of a three-dimensional separation can be divided into four stages for various zones of the flow structure. Some of these zones experience all of the stages as the separation develops under an impulsively imposed adverse pressure gradient.

The four stages in the development of three-dimensional separation are the initial inviscid response, the breakaway of the shear layer, initiation of large-scale unsteadiness, and the quasi-steady state.

Acknowledgements

The authors gratefully acknowledge support by the Office of Naval Research under contract N00014-84-K-0232, which was monitored by Dr. S. Lekoudis.

Bibliography

DIDDEN, N. & HO, C.M. 1985 'Unsteady separation in a boundary layer produced by an impinging jet.' *Journal of Fluid Mechanics,* **160**, pp. 235-256.

KOROMILAS, C.A. & TELIONIS, D.P. 1980 'Unsteady laminar separation: an experimental study,' *J. Fluid Mech.* **97**, part 2, pp. 347-384.

LEGENDRE, R. 1982 'Regular or Catastrophic Evolution of Steady Flows Depending on Parameters.' *Recherche Aérospatial* 1982-4:41-49.

PAULEY, L.L., MOIN, P. & REYNOLDS, W.C. 1988 'A Numerical Study of Unsteady Laminar Boundary-Layer Separation.' Stanford University Dept. of Mech. Engineering: Thermosciences Division. Report No. TF-34.

PERRY, A.E. & HORNUNG, H. 1984 'Some Aspects of Three-dimensional Separation, Part II: Vortex Skeletons.' *Zeitschrift für Flugwissenschaften und Weltraumforschung.* **8**, Heft 2:155-160.

TOBAK, M. & PEAKE, D.J. 1982 'Topology of Three-Dimensional Separated Flows.' *Annual Review of Fluid Mechanics.* **14**: 61-85.

Tunnel Geometry		
Dimension	Value	Comments
L, x-Length (total)	3.66 m	
x to LP:B, chord	0.575 m	
x to LP:D	0.613 m	Suction port begins
x to LP:1	0.651 m	Suction port ends
x to LP:2	0.689 m	
H, y-Depth (total)	0.129 m	
W, z-Span (total)	0.356 m	
width of suction port	38.1 mm	Port centered in span

Flow Conditions		
Quantity	Value	Comments
U_0	0.217 m/s	Inlet flow velocity
Q, (total)	0.0100 m^3/s	Volume flowrate
for Zero Pressure Gradient		
θ at LP:B	0.00125 m	Momentum thickness
θ at LP:1	0.00139 m	
θ at LP:2	0.00143 m	
for Suction		~16%
Q	0.00156 m^3/s	Volume flowrate
dU	0.0334 m/s	Least-squares fit
max. dC_p/dx	2.52 $1/m$	Gradients of Press. Coeff.
max. dC_p/dz	0.266 $1/m$	from potential flow est.

Table 1. Tunnel geometry and flow conditions.

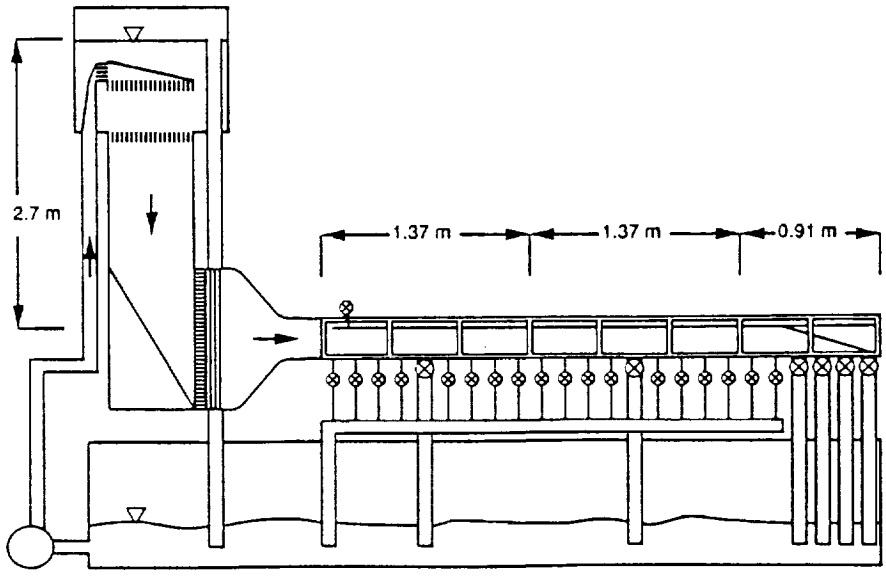

Figure 1: The Stanford unsteady boundary-layer research water tunnel.

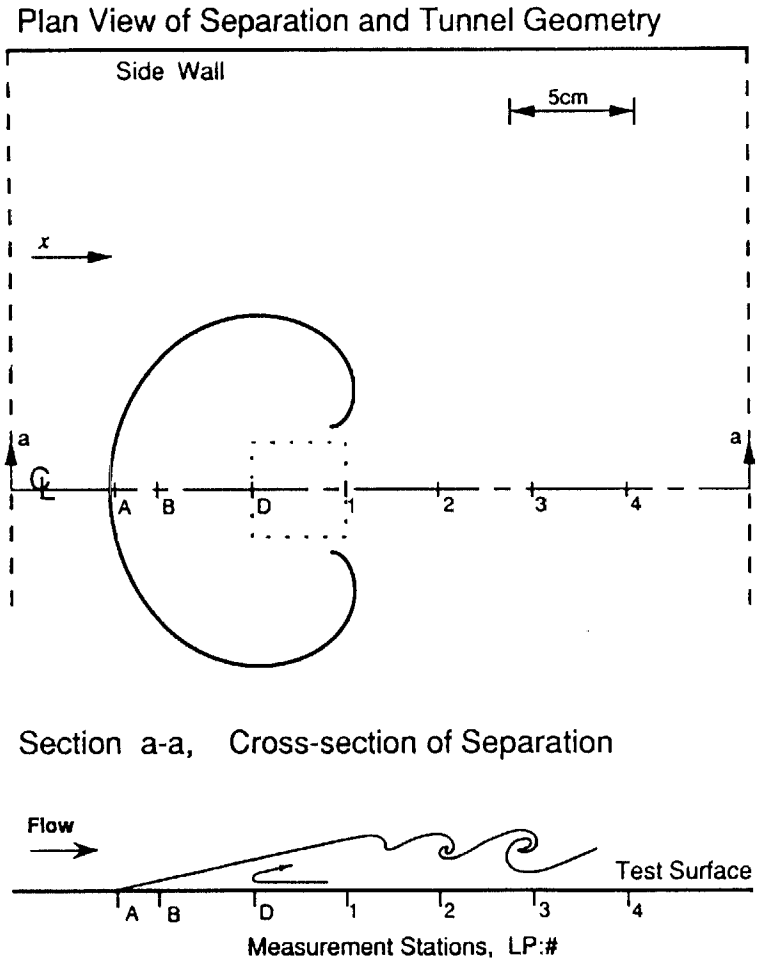

Figure 2: A schematic of tunnel geometry and separation structure shows location of measurement stations. The separation wake, composed of sluggish fluid, resides within the Owl-face structure between stations A and 1.

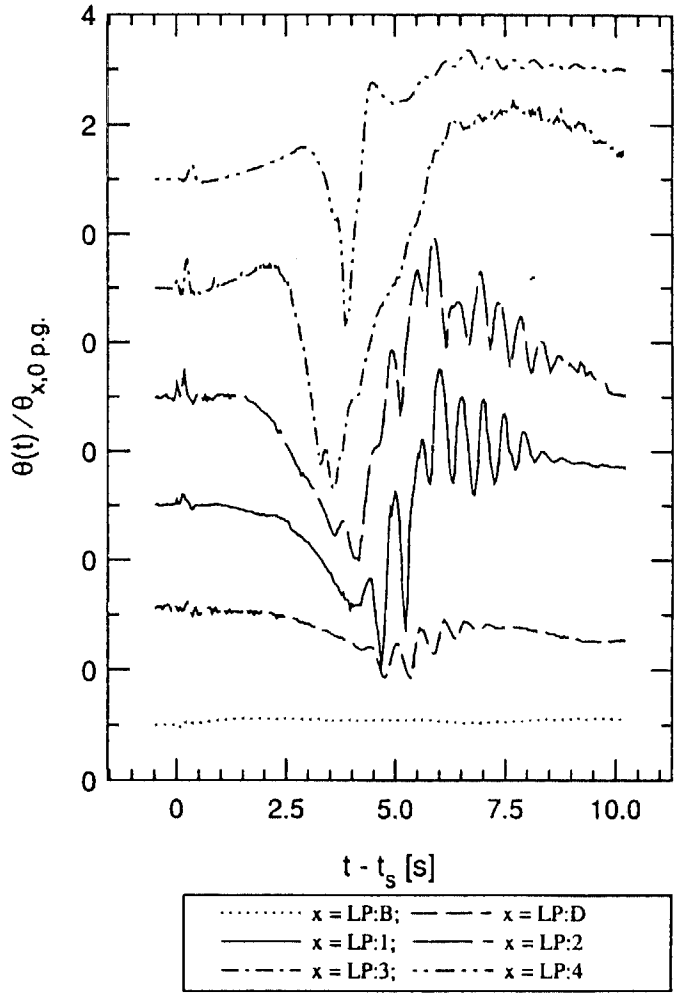

Figure 3: Histories of the momentum thickness, θ, along the centerline of the developing separation. The instantaneous momentum thickness becomes negative at several locations. Values are normalized to the value of the local momentum thickness during zero pressure-gradient conditions.

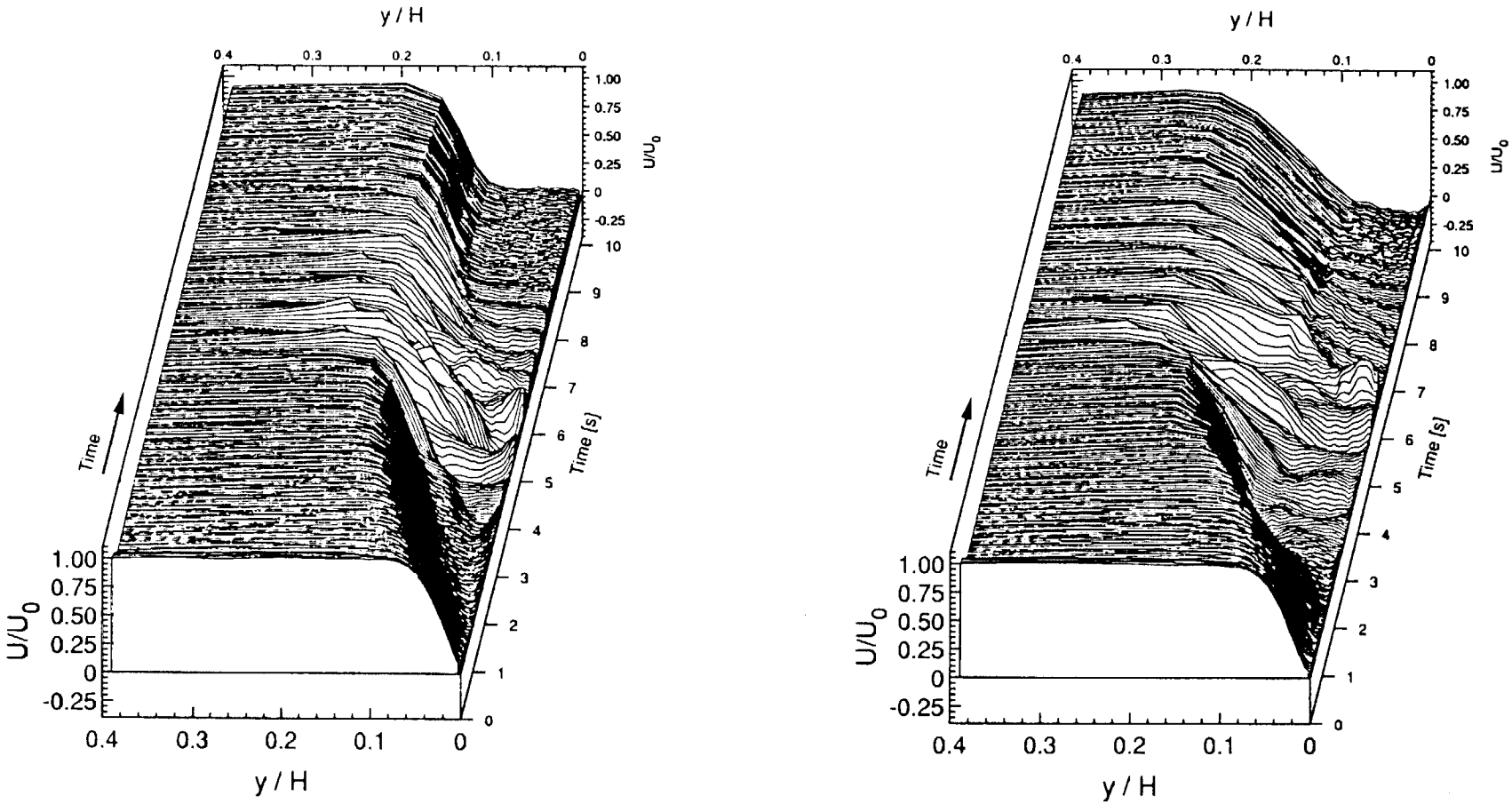

Figure 4: Evolution of the phase-averaged $\langle U \rangle$-velocity profiles from the instant the adverse pressure gradient is applied: (a) is at LP:1, (b) is at LP:2.

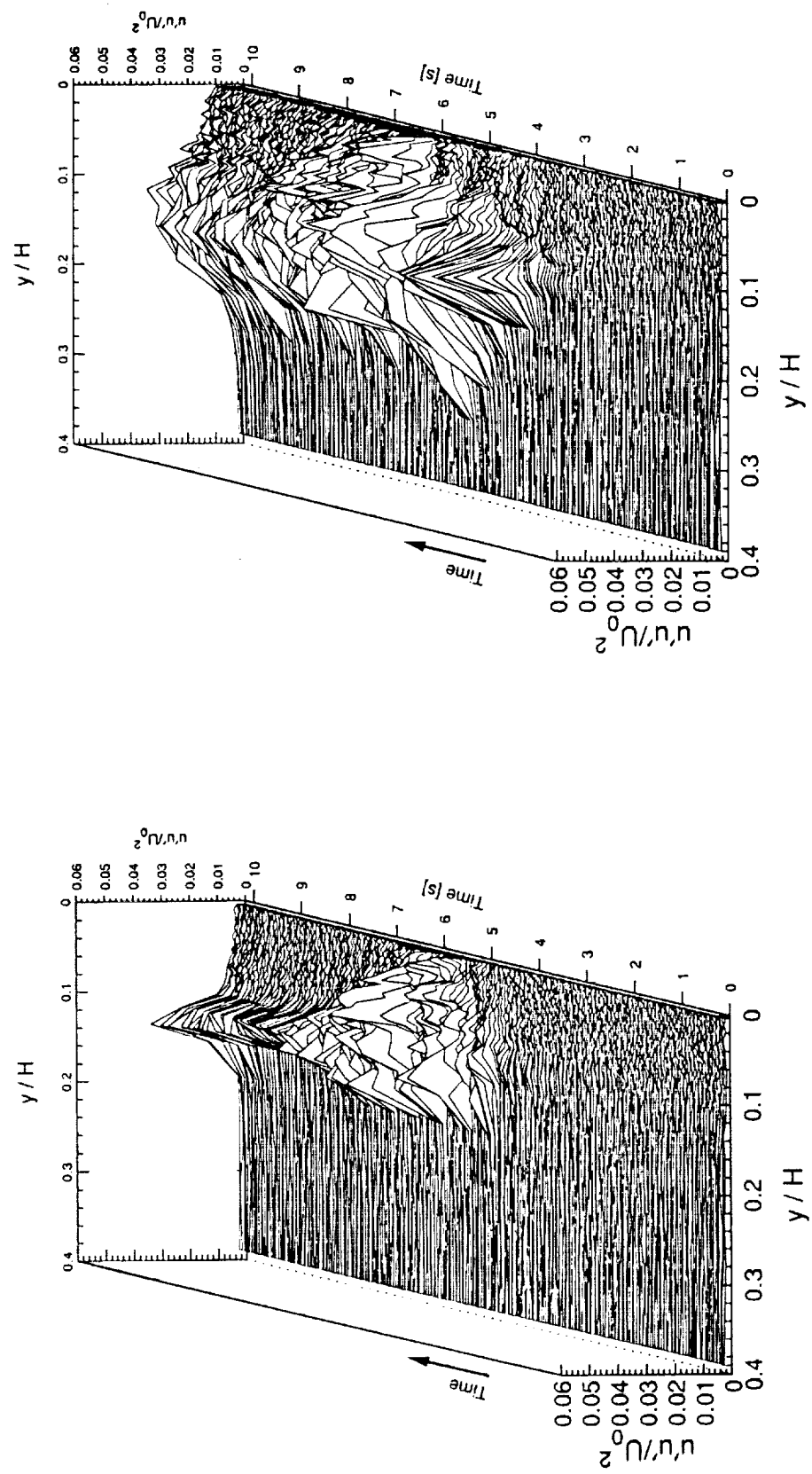

Figure 5: Evolution of the phase-averaged $\langle u'u' \rangle$-velocity profiles from the instant the adverse pressure gradient is applied: (a) is at LP:1, (b) is at LP:2.

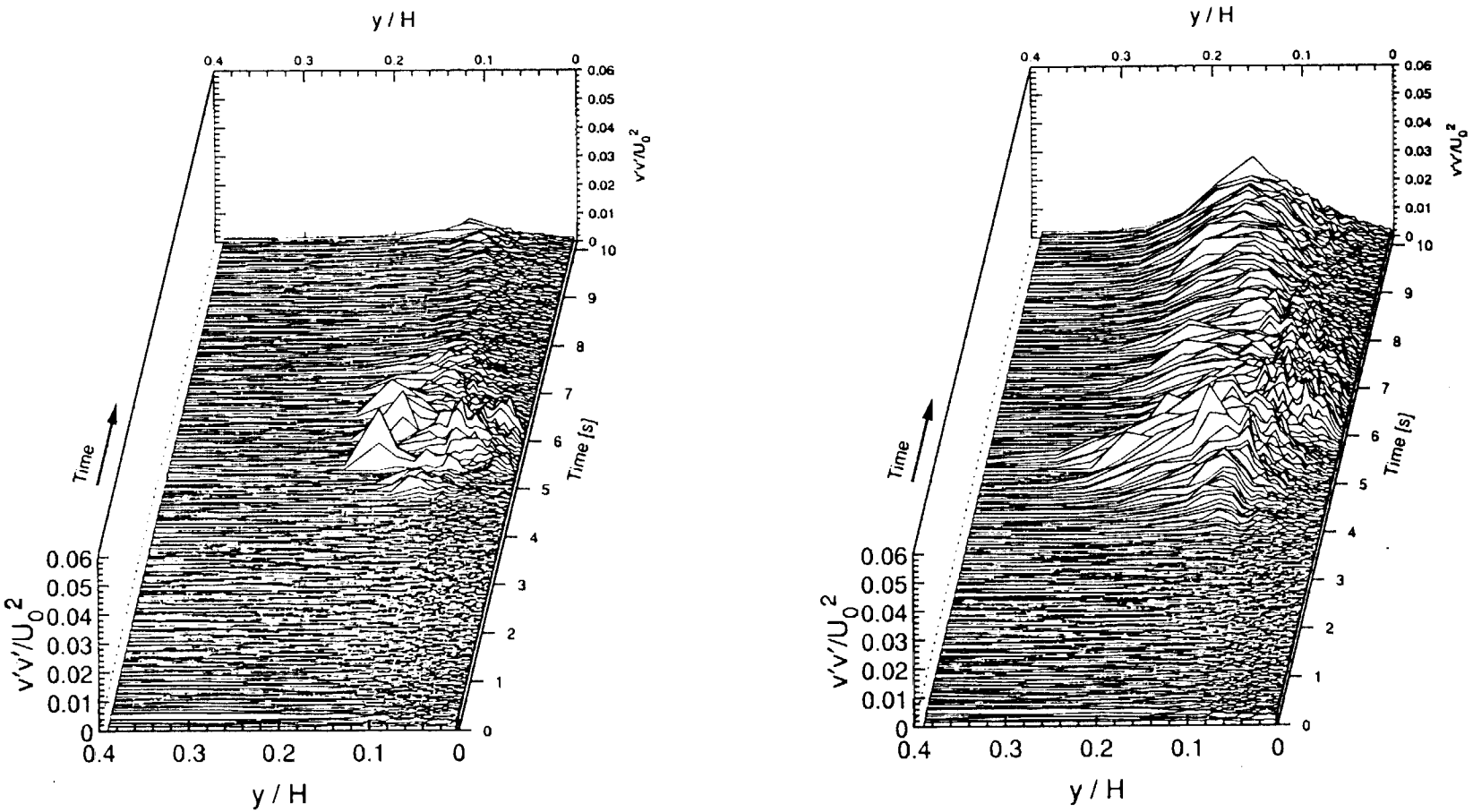

Figure 6: Evolution of the phase-averaged $\langle v'v' \rangle$-velocity profiles from the instant the adverse pressure gradient is applied: (a) is at LP:1, (b) is at LP:2.

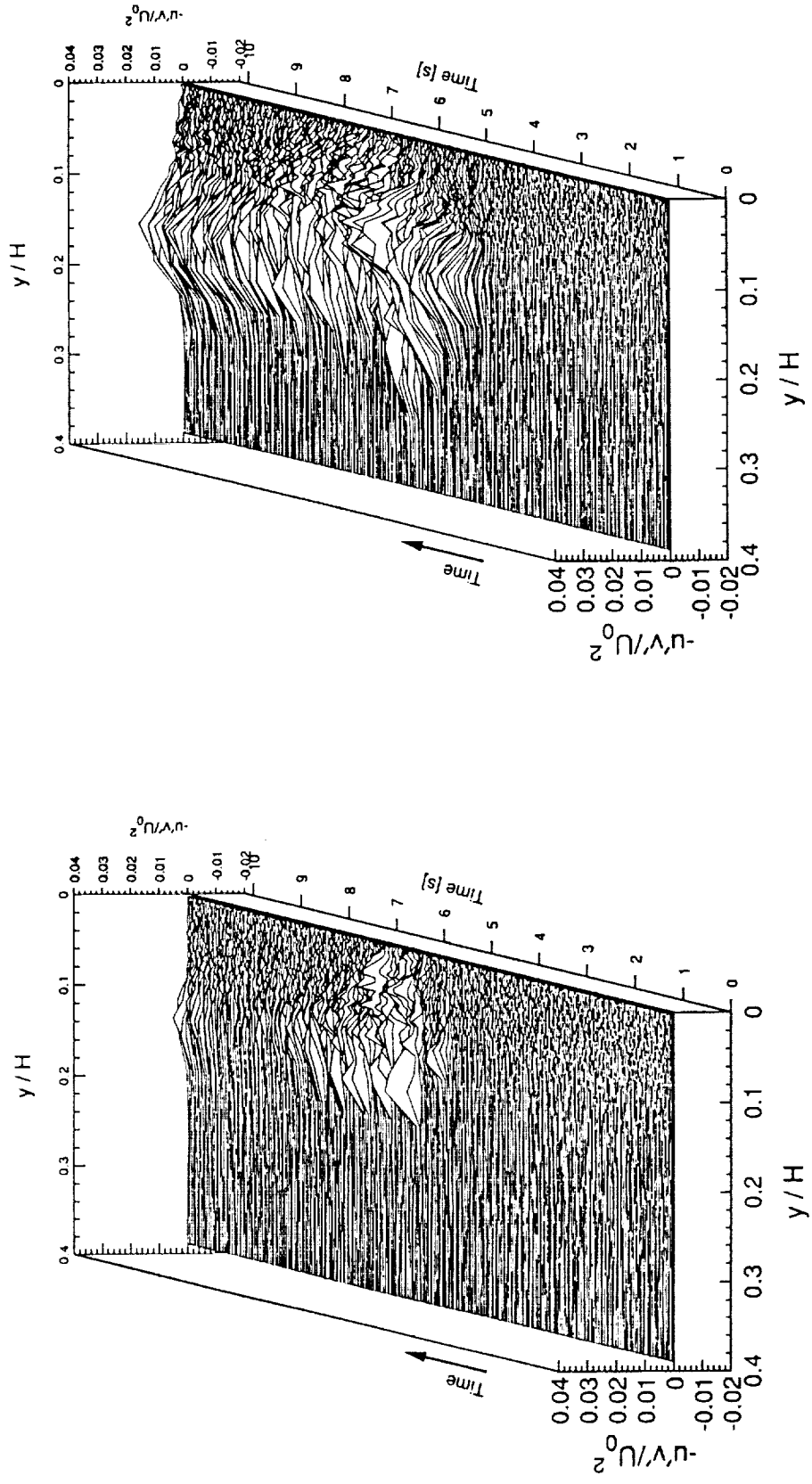

Figure 7: Evolution of the phase-averaged $(u'v')$-velocity profiles from the instant the adverse pressure gradient is applied: (a) is at LP:1, (b) is at LP:2.

Non-Local Sub-Characteristic Zones of Influence in Unsteady Interactive Boundary-Layers

A.P. Rothmayer
Department of Aerospace Engineering
Iowa State University

Abstract

The properties of incompressible, unsteady, interactive, boundary layers are examined for the model hypersonic boundary layer of Brown *et al* (1974,1975) and internal flow past humps or, equivalently, external flow past short-scaled humps. Using a linear high frequency analysis, it is shown that the domains of dependence within the viscous sublayer may be a strong function of position within the sublayer and may be strongly influenced by the pressure displacement interaction, or the prescribed displacement condition. Detailed calculations are presented for the hypersonic boundary layer. This effect is found to carry over directly to the fully viscous problem as well as the nonlinear problem. In the fully viscous problem, the non-local character of the domains of dependence manifests itself in the sub-characteristics. Potential implications of the domain of dependence structure on finite difference computations of unsteady boundary layers are briefly discussed.

1. Introduction

The phenomena of unsteady separation and vortex eruption appear to involve a number of possible high Reynolds number structures, including: classical boundary layers and singularities (Van-Dommelen & Shen (1980), Smith & Burggraf (1985)), interactive boundary layers and interactive singularities (Brotherton-Ratcliffe & Smith (1987), Smith (1988)), and the introduction of inviscid effects and normal pressure gradients (Elliott *et al* (1983)). As noted above, at some point the vortex eruption may pass through a stage in which viscous-inviscid interaction becomes important, although it is now generally accepted that viscous-inviscid interaction does not suppress the ultimate boundary-layer singularity leading to vortex eruption. However, the interactive stage may certainly be one segment of the vortex eruption and could be used as a means of controlling the development of the singularity. This, of course, assumes that marginal states could be found and that some form of artificially induced interaction could be used to control those marginal states (a suggestion which seems reasonable given recent computations). It seems clear that computational methods may have to accommodate the viscous-inviscid interaction at some point in the vortex eruption and such interactions may include artificially induced interactions if an attempt is made to control the development of the unsteady flow. It is important, therefore, to understand any factors which may complicate the theory and computation of these interactive structures - which brings us to the crux of the present study.

In 1985, Smith & Burggraf showed that two-dimensional Tollmien-Schlichting waves can pass into a high frequency regime with elevated amplitudes in which the wave is predominantly inviscid. Viscous effects are confined to a sublayer which is governed by classical unsteady boundary layer equations and is driven by the slip velocity of the inviscid sublayer. As such, the viscous sublayer could admit the Van-Dommelen & Shen (1980) singularity and burst into the outer layers (see also Elliott *et al* (1983)). However, with this exception, the viscous sublayer is decoupled from the rest of the structure. The inviscid sublayer is found to be governed by nonlinear thin-layer Euler equations and it is this layer which feels the effect of the pressure-displacement interaction. For hypersonic flows, the predominantly inviscid flow is governed by a modified inviscid Burgers equation

$$A_T + (A-1)A_X = 0 \quad . \tag{1.1}$$

This equation also governs the unsteady initial value problem for high frequency, large amplitude, short-scaled waves introduced into the original viscous interactive boundary-layer. Additional implications of eqn. (1.1), especially as regards finite-time singularities, are addressed by Brotherton-Ratcliffe & Smith (1987) and Smith (1988).

From the Smith & Burggraf (1985) model, eqn. (1.1), several interesting observations can be made. Linear waves propagate upstream, finite-time shocks are inevitable at finite wave amplitudes, and at sufficiently high amplitudes the characteristics change direction. This suggests that the differencing of at least the streamwise convective term uu_x and pressure gradient, which produce the $(A-1)A_X$ term, is not a simple matter, but depends on an interplay between the deviation from a "mean flow profile" and the pressure displacement interaction.

Most finite difference methods for calculating high Reynolds number unsteady viscous flows tend to rely on upwinding schemes based on the sign of the streamwise velocity (see for example Keller (1978)). However, the above observations suggest that traditional differencing techniques may not be appropriate in some unsteady interactive boundary-layer computations. The present study indicates that in non-parallel, unsteady, hypersonic boundary layers – and in a wide variety of zero-displacement boundary layers – the zones of influence are determined by a subtle interplay between the convective effects, the pressure-displacement interaction and the nonparallel (possibly separated) flow – *throughout the entire viscous sublayer.*

2. Governing Equations

The principal problem to be addressed in this study is the linear unsteady flow superimposed upon an originally nonlinear steady hypersonic boundary layer. The equations governing a high Reynolds number unsteady interactive hypersonic boundary layer may be found in a number of studies, including: Brown *et al* (1974,1975) and Gajjar & Smith (1985). The governing equations, with the Prandtl transposition, are found to be: the conservation of mass equation,

$$U_X + V_Y = 0 \tag{2.1}$$

and the conservation of streamwise momentum equation,

$$U_T + UU_X + VU_Y = -P_X(X,T) + U_{YY} \quad , \tag{2.2}$$

with no-slip boundary conditions at the wall and

$$U(X,Y,T) \to Y + F(X) + A(X,T) \qquad as\ Y \to \infty . \tag{2.3}$$

The pressure displacement relation in the hypersonic flow of Brown *et al* (1974,1975) is simply P=–A. Here F(X) is a prescribed steady hump/indentation shape. For the unsteady internal flow of Smith (1976) and Duck (1979,1985), as well as the short-scale hump in a Blasius boundary layer (Smith *et al* (1981)), the P=–A law is replaced by A=0. The primary issue of interest here is the numerical integration of the above system of equations using a finite difference procedure. This issue, as will be shown in this study, may not be as simple as it might first appear.

3. High Frequency Limit

Suppose that a nonlinear steady state solution has been calculated for equations (2.1) through (2.3) – say a hump induced separation. This may be easily done using a variant of the Davis (1984) alternating direction explicit (ADE) method (see also Brotherton-Ratcliffe (1987)). A linear unsteady disturbance is superimposed upon this steady base solution:

$$[U,V] - [U_0,V_0](X,Y) + \bar{\epsilon}\,[\hat{u}_1,\hat{v}_1,](X,Y,T) + O(\bar{\epsilon}^2) \qquad (\bar{\epsilon} \ll 1) \quad . \tag{3.1}$$

Equations (2.1) and (2.2) will be further simplified by letting the time scale become short, or

$$\frac{\partial}{\partial T} = \Omega \frac{\partial}{\partial t_0} \qquad (\Omega \gg 1) \ . \tag{3.2}$$

The reader will note that this approach follows very closely the work of Smith & Burggraf (1985), Tutty &

Cowley (1986), Brotherton-Ratcliffe & Smith (1987) and Smith (1988). The lower deck is found to break up into two distinct regions (I and III in Fig. 1). For purposes of discussion, and comparison with Smith & Burggraf (1985), an extra region, II, will be introduced. Region II can be derived as a limit of Region III. The entire structure is found to be confined to a neighborhood of a point X_0 within the lower deck, with

$$X = X_0 + \Omega^{-1} x_0 \quad , \tag{3.3}$$

and viscous effects are found to be confined to a thin classical Stokes layer, Region I, where $Y = \Omega^{-1/2}\overline{Y}$. The Stokes layer equations are solved subject to the no-slip boundary conditions at the wall and matching with Region III. It should be noted that Region I is decoupled from Region III. In Region III we take Y to be O(1) and the governing equations are found to be

$$\hat{u}_{1_{x_0}} + \hat{v}_{1_Y} = 0 \quad \text{and} \quad \hat{u}_{1_{t_0}} + U_0(Y)\hat{u}_{1_{x_0}} + U'_0(Y)\hat{v}_1 = -\hat{p}_{1_{x_0}} \quad , \tag{3.4a,b}$$

where $U_0(Y)$ is the local steady velocity profile. Upon integration of equation (3.4b), application of the tangency boundary condition, and the hypersonic pressure displacement relation, the entire problem is reduced to:

$$\hat{u}_{1_{t_0}} + U_0(Y)\hat{u}_{1_{x_0}} - U'_0(Y)\int_0^Y \hat{u}_{1_{x_0}}(x_0, \eta, t_0)d\eta = \hat{a}_{1_{x_0}} \quad , \tag{3.5}$$

subject to $\hat{u}_1 \to \hat{a}_1$ as $Y \to \infty$. Equation (3.5) will form the basis of the numerical calculations presented later in this study. It may be shown that in the limit as Y becomes large eqn. (3.5) reduces to the linear version of the Smith & Burggraf (1985) wave equation (1.1), but with a non-trivial displacement effect from region III:

$$\hat{a}_{1_{t_0}} + (F_0 + A_0 - 1)\hat{a}_{1_{x_0}} = -\delta \quad . \tag{3.6}$$

Further details of this structure may be found in Tutty & Cowley (1986) and Rothmayer (1990).

4. Zones of Influence for the Unsteady Linear and Nonlinear Viscous Sublayer

Although the numerical results of this study will be for the high frequency limit of section 3, this approach may be generalized to other cases. First consider an integrated form of equations (2.1) and (2.2) for the fully nonlinear problem:

$$U_T + UU_X - U_Y\int_0^Y U_X(X, \eta, T)d\eta = -P_X(X, T) + \underline{U_{YY}} \quad , \tag{4.1}$$

where P(X,T) is fixed from the appropriate pressure displacement law and the u-matching condition (2.3). Linearized problems may be considered, in which case, given an expansion of the form of eqn. (3.1), equation (4.1) becomes

$$u_T + U_0 u_X + \underline{uU_{0_X}} + \underline{V_0 u_Y} - U_{0_Y}\int_0^Y u_X(X, \eta, T)d\eta = -p_X(X, T) + \underline{u_{YY}} \quad , \tag{4.2}$$

subject to no-slip at the wall and $u(X, \infty, T) = a + f$ as $Y \to \infty$. The high frequency limit of Rothmayer (1990) results in a parallel flow approximation and neglecting viscous effects in the main portion of the boundary layer. Equivalently, the high frequency equation is simply equation (4.2) without the underlined terms, for linear flows, or equation (4.1) without the underlined terms, for nonlinear flows. Equation (4.2) may be evaluated on the Y grid $Y_j = (j-1)\Delta Y$ using, say, a central difference approximations for u_Y and u_{YY} and a trapezoidal rule quadrature for the integral in (4.2). As will be shown in section 5, equation (4.2) may be reduced to the form

$$\mathbf{u}_T + \mathbf{A}\mathbf{u}_X = \mathbf{B}\mathbf{u} + \mathbf{g} \quad \text{or} \quad [\hat{\mathbf{u}}_1]_{t_0} + \mathbf{A}[\hat{\mathbf{u}}_1]_{x_0} = 0 \tag{4.3a,b}$$

when a high frequency approximation is used (see eqn. (3.5), also Rothmayer (1990)) and the underlined

terms in equation (4.2) are neglected. This equation assumes that a suitable pressure displacement relation has been used to relate the pressure to some combination of the velocities on the vertical grid (see Rothmayer (1990)). For example, the hypersonic interaction law gives $\hat{p}_1 = -\hat{u}_{1_{iN}}$ whereas the prescribed displacement law (A=0) may be used, in which case the high frequency approximation gives:

$$p_x = -g + \sum_{j=2}^{N-1} u_{jx}\Delta Y \quad \text{and} \quad g(x,t) = f_t + (Y_N + A_0 + F_0 - 1/2)f_x \quad . \quad (4.4)$$

The vector $\mathbf{g}$ is given by $\mathbf{g} = [g...g]^T$ while the matrix $\mathbf{A}$ is given in Rothmayer (1990) for the high frequency limit. The same analysis may be applied to equation (4.1), but now in terms of $\mathbf{U} = [U_{i1}, ..., U_{iN}]^T$ and the coefficient matrix $\mathbf{A}$ is a function of the solution. Equation (4.3a) is simply an N-dimensional wave equation which may be solved by standard means using the method of characteristics. Note that the viscous effect as well as the nonparallel effects (i.e. all underlined terms in (4.2)) only contribute to $\mathbf{B}$ and so do not affect the sub-characteristic analysis. The primary difference between the present study and the standard method of sub-characteristics is that the characteristics cannot be determined via a local analysis, due to the pressure displacement interaction P=-A (or the A=0 law). The eigenvalues of the coefficient matrix $\mathbf{A}$ can readily be calculated and satisfy $|\mathbf{A} - \lambda_i \mathbf{I}| = 0$, and the eigenvectors are found from $\mathbf{A}\mathbf{v}_i = \lambda_i \mathbf{v}_i$. The actual method used in this study for finding the eigenvalues and eigenvectors is a nonlinear Newton-Raphson method (which is discussed in Rothmayer (1990)). It is not assumed that the eigenvectors have been normalized. Using classical methods (see John (1971)), a new solution vector $\mathbf{u} = \mathbf{V}\tilde{\mathbf{u}}$ is defined, where $\mathbf{V}$ is an NxN matrix whose columns are the eigenvectors, i.e. $\mathbf{V} = [\mathbf{v}_1...\mathbf{v}_N]$. Substitution into equation (4.3a) and multiplication by the inverse of $\mathbf{V}$ diagonalizes eqn. (4.3a), and gives

$$\tilde{\mathbf{u}}_T + \Lambda\tilde{\mathbf{u}}_X = \tilde{\mathbf{B}}\tilde{\mathbf{u}} + \tilde{\mathbf{g}} \quad , \quad (4.5)$$

where $\tilde{\mathbf{B}} = \mathbf{V}^{-1}\mathbf{B}\mathbf{V}$, $\tilde{\mathbf{g}} = \mathbf{V}^{-1}\mathbf{g}$ and Λ is the diagonal eigenvalue matrix $\Lambda = diag(\lambda_1, ..., \lambda_N)$. Equation (4.5) can be easily integrated along its characteristics for $\tilde{\mathbf{u}}$, and then the $\tilde{\mathbf{u}}$ can be converted back to $\mathbf{u}$. Direct integration of (4.3a) requires a differencing formulation which correctly incorporates the diagonalization transformation $\mathbf{u} = \mathbf{V}\tilde{\mathbf{u}}$.

5. A Solution of the Non-Local High-Frequency Characteristic Problem

As in the preceding section, consider a quadrature of the integral in equation (3.5) on the vertical grid $Y_j = (j-1)\Delta Y$ with j=1,...,N. A trapezoidal rule will be employed here, although other quadratures may be used, in which case:

$$\hat{u}_{1_{j_{t_0}}} - \left(\frac{1}{2}\Delta Y U'_{0_j}\right)\hat{u}_{1_{1_{x_0}}} - \sum_{L=2}^{j-1} \Delta Y U'_{0_j}\hat{u}_{1_{L_{x_0}}} + \left(U_{0_j} - \frac{1}{2}\Delta Y U'_{0_j}\right)\hat{u}_{1_{j_{x_0}}} - \hat{u}_{1_{N_{x_0}}} = 0 \quad , \quad (5.1)$$

keeping in mind that $\hat{u}_{1_N} = \hat{a}_1$. Equation (5.1) is applied at the points j=3,...,N. At j=2 the summation from L=2,...,j-1 is removed from the equation, while at j=1 equation (5.1) is replaced by $\hat{u}_{1_{1_{t_0}}} - \epsilon\ \hat{u}_{1_{N_{x_0}}} = 0$. The above equations are just the single matrix wave-equation (4.3b) where $[\hat{\mathbf{u}}_1] = \left[\hat{u}_{1_1} \quad ... \quad \hat{u}_{1_N}\right]^T$ and the coefficient matrix $\mathbf{A}$ is given in Rothmayer (1990). The characteristic slopes, λ_j, are the eigenvalues of $\mathbf{A}$, and satisfy $|\mathbf{A} - \lambda_i \mathbf{I}| = 0$, where $\lambda = \partial x_0/\partial t_0$. The Riemann invariant Γ_j associated with the λ_j eigenvalue satisfies (see Chorin & Marsden (1979)):

$$A^T\left[\frac{\partial \Gamma_j}{\partial \hat{u}_{1_i}}\right] = \lambda_j\left[\frac{\partial \Gamma_j}{\partial \hat{u}_{1_i}}\right] \quad . \tag{5.2}$$

In general there are N eigenvalues, and it turns out that the first N−1 are roughly the slope of the U_0 velocity at a particular j gridpoint (for the particular solution being calculated in this study). The last eigenvalue, λ_N, does not appear to have any simply determined value and must be found via numerical computation. These eigenvalues have associated with them the Γ_j Riemann invariants, each of which is constant along the characteristic with slope λ_j. Therefore at each (x_0,t_0,Y) gridpoint a system of N equations in the N $\hat{u}_{1_j}$'s needs to be solved, namely

$$\sum_{i=1}^{N}\left(\frac{\partial \Gamma_j}{\partial \hat{u}_{1_i}}\right)\hat{u}_{1_i} = (\Gamma_j)_0 \quad , \tag{5.3}$$

where $(\Gamma_j)_0$'s are the Riemann invariants evaluated along the initial data plane. The equations (5.3) may be inverted to give:

$$[\hat{u}_1] = \left[\frac{\partial \Gamma_j}{\partial \hat{u}_{1_i}}\right]^{-1}\left[(\Gamma_j)_0\right] \quad . \tag{5.4}$$

This is effectively the diagonalization process of equation (4.5). Equation (5.4) gives the dependence of each $\hat{u}_{1_j}$ on the Riemann invariant Γ_j associated with the λ_j eigenvalue. Therefore the inverse of the Jacobian matrix of the Riemann invariants gives the domain of dependence of the streamwise velocity at each jth gridpoint in terms of the j characteristics with slope λ_j, providing that the Riemann invariant multiplying a given row element of the inverse is non-zero. In the general case, there is no reason to expect the domains of dependence to be simple.

For purposes of computation, an idealized flow will be considered. The velocity field is assumed to take the form:

$$U_0(Y) = Y + A\left(1 - e^{-Y}\right) \quad , \tag{5.5}$$

where A is taken as an independent parameter, in lieu of A_0+F. The wall shear stress is given by $\tau_w = U_0'(0) = 1 + A$, indicating that the flow is attached for A>−1 and separated for A<−1. The case A=0 gives an undisturbed sublayer. Velocity profiles for various values of A are shown in Figs. 2 through 4, along with the eigenvalue and eigenvector calculations. In addition, a new function, Θ_i, will be defined, which is the product of a row *element* in the inverse eigenvector matrix and the corresponding *element* of the Riemann invariant vector:

$$\Theta_i = \left[\frac{\partial \Gamma}{\partial \hat{u}_1}\right]^{-1}_{ij}[\Gamma_j]_0 \quad . \tag{5.6}$$

The results of these calculations are shown in Figs. 5 through 8, assuming constant perturbation velocities on the initial data plane. The results for A=0 are in agreement with the linear results of the Smith & Burggraf (1985) study. The solution at any vertical point in the grid depends only on the j=N eigenvalue which has slope −1. The results of the above calculations for an accelerated flow are shown in Figs. 6 and 7. Consider the schematic interpretation of Figs. 5 through 7, shown in Fig. 8. This figure is a qualitative interpretation only and is not meant to convey accurate quantitative data. At low amplitudes (i.e. A near 0) all of the characteristics point downstream with slope −1. As the flow is accelerated (i.e. A increasing) a region of dependence begins to emerge for small values of j, and the slope of the downstream-directed characteristic begins to decrease. A

typical case, say A=5, now has the j=N eigenvalue competing with the eigenvalues which are approximately the velocities near the bottom of the boundary layer. Note that this only occurs in the outer portion of the boundary layer (i.e. for j large). The eigenvalues associated with small j's have characteristics which point upstream and so the tendency in the outer portion of the boundary layer is for the upstream directed characteristics to begin competing with, and eventually overtaking, the downstream directed characteristic. The overall picture is that the characteristics in the outer portion of the sublayer appear to change direction for increasing A, whereas the characteristics in the lower portion of the sublayer do not. This means that the characteristics are not pointing in the same direction throughout the sublayer when the change in the direction of the characteristics does occur, but vary with vertical position.

7. Conclusion and Implications for Finite Difference Computations

In this study it has been shown that the sub-characteristics in an unsteady interactive viscous flow are not simply determined by the convective velocity, but rather are fixed by an interplay between the convective terms, the pressure displacement interaction, and the nonparallel base flow. In addition, the sub-characteristics may vary throughout the entire viscous sublayer and may possess a complex structure. These results seem to be in accord with the work of Smith & Burggraf (1985) on nonlinear hypersonic waves, which suggests that the characteristics will change direction at sufficiently large disturbance amplitude. Is it worthwhile to perform the domain of dependence calculation before proceeding to the finite difference solution? This of course depends on the results for a particular case. A simple differencing scheme may correctly capture the physics of the problem in question. However, the present study indicates that it is possible for an unsteady flow to possess complicated domains of dependence, and hence to require complex differencing schemes. It is anticipated that problems related to incorrectly modeling the domains of dependence in a finite-difference method will manifest themselves either as a CFL (Courant-Friedrichs-Lewy) condition or as spurious oscillations in the solution.

Acknowledgement

This research was supported by a grant from the United Technologies Research Center and by a National Science Foundation Presidential Young Investigator Award.

References

Brotherton-Ratcliffe, R.V., & Smith, F.T., 1987, "Complete Breakdown of an Unsteady Interactive Boundary Layer (Over a Surface Distortion or in a Liquid Layer)," *Mathematika*, 34, pp. 86-100.

Brotherton-Ratcliffe, R.V., 1987, Ph.D Thesis, Univ. of London.

Brown, S.N., Stewartson, K., and Williams, P.G., 1975, "Hypersonic Self-Induced Separation," *Physics of Fluids*, 18(6), pp. 633-639.

Brown, S.N., Stewartson, K., and Williams, P.G., 1974, "On Expansive Free-Interactions in Boundary Layers," *Proc. Roy. Soc. Edinburgh*, 74A(21), pp. 271-283.

Chorin, A.J., & Marsden, J.E., 1979, *A Mathematical Introduction to Fluid Mechanics*, Springer-Verlag.

Davis, R.T., 1984, "A Procedure for Solving the Compressible Interacting Boundary Layer Equations for Subsonic and Supersonic Flows," AIAA Paper 84-1614.

Duck, P.W., 1985, "Pulsatile Flow Through Constricted or Dilated Channels: Part II," *Q. J. Mech. Appl. Maths*, 38, pp. 621-653.

Duck, P.W., 1979, "Viscous Flow Through Unsteady Symmetric Channels," *J. Fluid Mech.*, 95, pp. 635-653.

Elliott, J.W., Cowley, S.J., & Smith, F.T., 1983, "Breakdown of Boundary Layers: (i) On Moving Surfaces, (ii) In Semi-Similar Unsteady Flow, (iii) In Fully Unsteady Flow," *Geophys. and Astrophys. Fluid Dyn.*, 25, pp. 77-138.

Gajjar, J., & Smith, F.T., 1983, "On Hypersonic Self-Induced Separation, Hydraulic Jumps and Boundary Layers with Algebraic Growth," *Mathematika*, 30, pp. 77–93.

John, F., 1971, *Partial Differential Equations*, 4th ed., Springer–Verlag.

Keller, H.B., 1978, "Numerical Methods in Boundary–Layer Theory," *Ann. Rev. Fluid Mech.*, 10, pp. 417–433.

Rothmayer, A.P., 1990, "Zones of Influence in a Two–Dimensional, Unsteady, Hypersonic, Boundary Layer," to appear in *Proc. Roy. Soc., 1990.*

Smith, F.T., 1988, "Finite–Time Breakup can Occur in any Unsteady Interacting Boundary Layer," *Mathematika*, 35, pp. 256–273.

Smith, F.T., & Burggraf, O.R., 1985, "On the Development of Large–Sized Short–Scaled Disturbances in Boundary–Layers," *Proc. Roy. Soc.*, A399, pp. 25–55.

Smith, F.T., Brighton, P.W.M., Jackson, P.S., & Hunt, J.C.R., 1981, "On Boundary–Layer Flow Past Two–Dimensional Obstacles," *J. Fluid Mech.*, 113, pp. 123–152.

Smith, F.T., 1976, "Flow Through Constricted or Dilated Pipes and Channels, Parts 1 and 2," *Q. J. Mech. Appl. Math.*, 29, pp. 343–364.

Tutty, O.R., & Cowley, S.J., 1986, "On the Stability and the Numerical Solution of the Unsteady Interactive Boundary–Layer Equation," *J. Fluid Mech.*, 168, pp. 431–456.

Van Dommelen, L.L., & Shen, S.F., 1980, "The Spontaneous Generation of the Singularity in a Separating Laminar Boundary Layer," *J. Comp. Phys.*, 38, pp. 125–140.

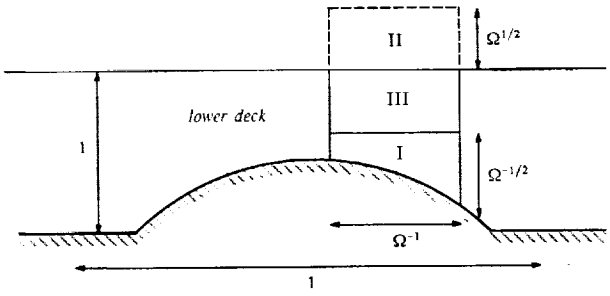

Figure 1. Asymptotic structure for a high frequency unsteady linear disturbance in a nonparallel viscous sublayer.

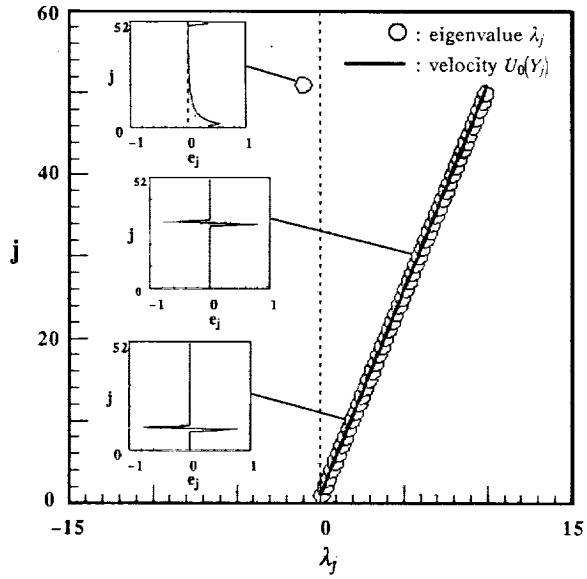

Figure 2. Eigenvalues, eigenvectors and the velocity profile for A=0 and N=51. e_j is the eigenvector associated with λ_j.

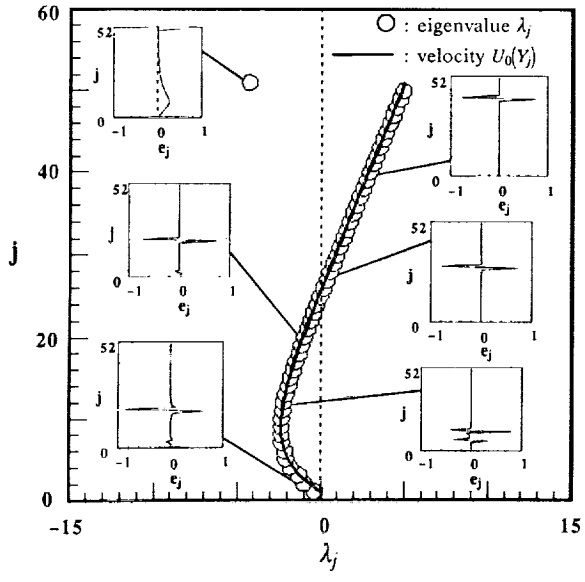

Figure 3. Eigenvalues, eigenvectors and the velocity profile for a model separated flow (A=-5, N=51).

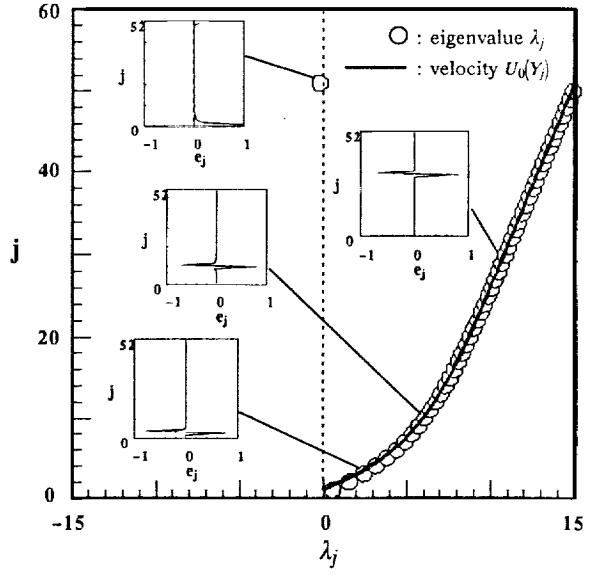

Figure 4. Eigenvalues, eigenvectors and the velocity profile for a model accelerated flow (A=5, N=51).

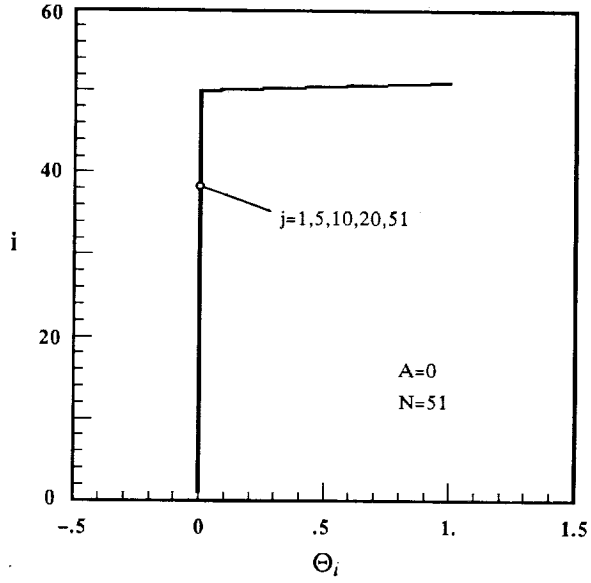

Figure 5. Domains of dependence for vertical positions in the grid and A=0.

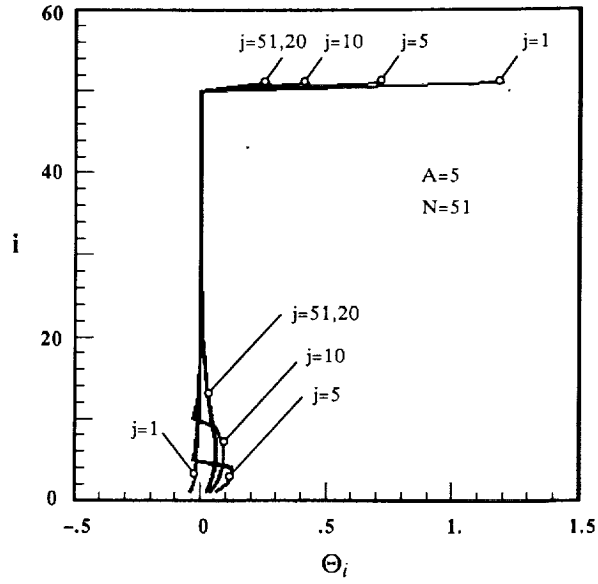

Figure 6. Domains of dependence for various vertical positions in the grid and A=5.

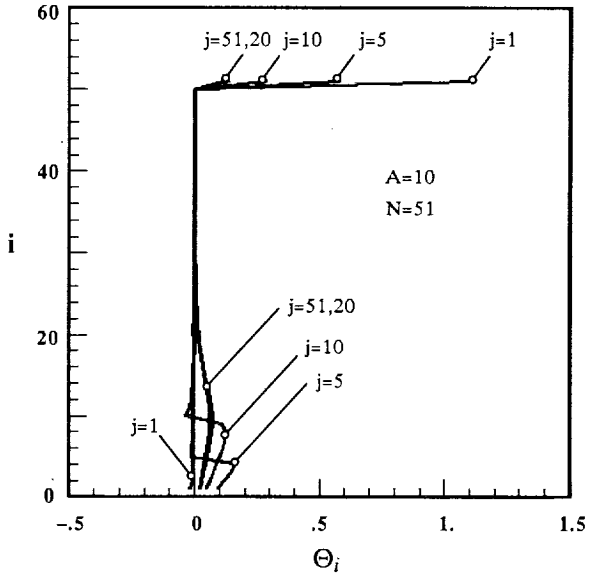

Figure 7. Domains of dependence for various vertical positions in the grid and A=10.

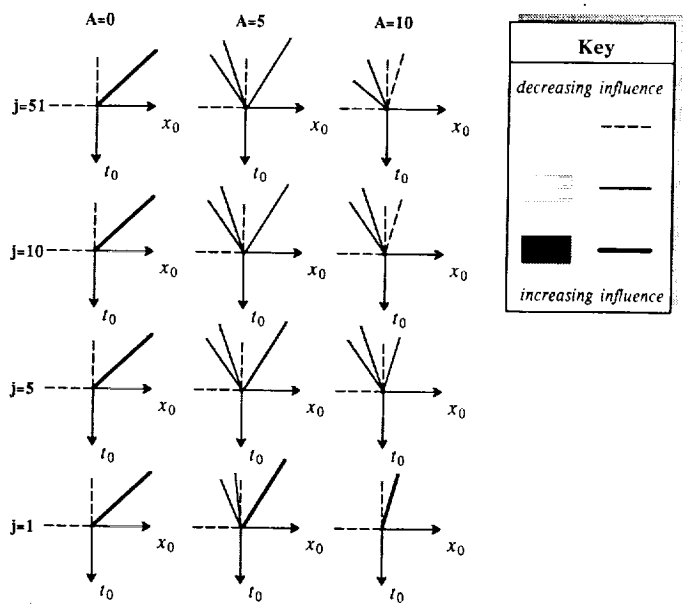

Figure 8. Schematic diagram of the domains of dependence given by Figs. 5 through 7. Results are qualitative only.

Forced Unsteady Deceleration of a Turbulent Boundary Layer from a Temporal Perspective.

G. J. Brereton
Department of Mechanical Engineering and Applied Mechanics,
The University of Michigan, Ann Arbor, MI 48109

Introduction

The behavior of a turbulent boundary layer which has been subjected to a local ramp-like deceleration in the external velocity field, which leads to forced separation, has been studied experimentally.[1] The data of this study are re-interpreted in light of more recent findings concerning the temporal nature of boundary-layer turbulence[2] in the presence of forced unsteady shear. In particular, the robustness of the near-wall turbulent motions to organized deformation is recognized. Their resilence to unsteady shearing action promotes continued efficient turbulent mixing and rapid redistribution of turbulent kinetic energy during forced transients. In aerodynamic problems, the rapid nature of the adjustment of the turbulence field to a new temporal boundary condition necessitates equally rapid remedial measures to be taken if means of control/prevention of forced unsteady separation are to be deployed to maximum effect. This requirement suggests exploration of the use of simple real-time statistical forecasting techniques, based upon time-series analysis of easily-measurable features of the flow, to help assure timely deployment of mechanisms of boundary-layer control.

This paper focuses upon the nature of turbulence in boundary layers undergoing forced deceleration which would lead to separation. A preliminary form of a forecasting model is presented and evaluated. Using observations of the previous two large eddies passing a detector, it forecasts the behavior of the future large eddy rather well.

Background

Close to the wall, the robustness of the dominant turbulent motions of boundary layers to forced unsteady deformation has been demonstrated experimentally. In a recent water-tunnel experiment,[2] measurements of the major component of the turbulence production tensor were made when the parent boundary layer was subjected to a superposed oscillatory variation in the free-stream velocity, shown in figure 1, while decelerating with increasing streamwise distance. On average, the motions of the turbulent boundary layer were extremely robust to the imposition of forced unsteadiness at any frequency. Mean values of production of $\overline{u'u'}$, and of all measured components of the Reynolds stress tensor showed no variation with frequency and scarcely differed from the equivalent steady or quasi-steady measures, as illustrated by the turbulence production data shown in figure 2.

The time-dependent response of this spatially-decelerating flow undergoing unsteady forcing was characterized by momentary measures of turbulence production of very similar shape to their time-averaged counterparts, with peak production always around $y^+ \simeq 9$ (shown in figure 3). The coincidence of the position of peak production, and the shape similarity implied that temporal production arose only as a modulation of a robust mean process, which was undisturbed by temporal variation in the local shear, over a range of frequencies. More importantly, measurements of the time lag between peaks in temporal values of $u'u'$ and $v'v'$ showed that the process of redistribution of turbulent kinetic energy from the component in which it was produced ($u'u'$) to one with negligible production ($v'v'$) took place locally over the same scales of time regardless of the frequency of unsteadiness — a process driven by motions characteristic of the mean flow. This key result is shown in figure 4 and demonstrates the importance of the robust turbulent motions of the parent boundary layer in accounting for temporal redistribution of turbulent kinetic energy, when necessitated by the superposition of oscillatory shear. It is also of considerable importance that the cycle-averaged lag between $u'u'$ and $v'v'$ reached a maximum of around only 40 viscous units in time (referenced to the mean friction velocity) — an extremely short period of time in typical aerodynamic applications — and that this time lag was greatest close to the location of maximum production of $u'u'$ and of maximum anisotropy in the Reynolds stress tensor. This short time scale, representative of temporal redistribution of turbulent kinetic energy, is indicative of the efficient turbulent mixing which appears to be unaffected by the superposition of an oscillatory shear field.

In summary, the near-wall motions of the parent turbulent boundary layer have been shown to be resilient and to sustain their steady-state character when subjected

to unsteady forcing of a sinusoidal kind. Also, they appear to dictate features of the response of temporal turbulent motions of the boundary layer during transients, and in particular, time scales of temporal redistribution of turbulent kinetic energy.

These findings, revealed from measurements of two components of the velocity field in a turbulent boundary layer undergoing sinusoidal unsteadiness, may be applied to results of an earlier study in the same apparatus,[1] in which an abrupt, ramp-like deceleration in free-stream velocity (and increase in streamwise pressure gradient) was enforced on an otherwise steady flat-plate turbulent boundary layer, in order to initiate separation. The forcing boundary condition and the normalized response of the turbulence ($u'u'$) are shown in figures 5 and 6. Once the starting transients had died out and the ramp-like deceleration had been established, the organized unsteady component of streamwise velocity followed a quasi-laminar development, as described by a viscous Stokes layer which grew outward from the wall in time. The flow was then one in which the momentary production of $u'u'$ was being reduced rapidly, through the abrupt decrease in shear strain. The concurrent reduction in $u'u'$ to values greatly below its initial level was then due to the extreme effectiveness of redistribution of turbulent kinetic energy amongst other component, as driven by the sustained presence of robust turbulent motions which originated in the boundary layer before the forced deceleration. The consistency of shape in profiles of the component of $u'u'$ deviatoric from its initial state, when normalized by the component of free-stream velocity deviatoric from its initial value, concurs with the interpretation that it is the sustained presence of the dominant motions of the boundary layer before imposition of forcing which account for this rapid, efficient turbulent mixing and adjustment of the boundary layer during the transient. The sustained presence of these turbulent motions during unsteady deformation may be an important factor in understanding the kinds of hysteresis observed frequently in unsteady flows of this kind.

It is worthwhile noting that $u'u'$ is reduced by 25% of its value in a time of 28 viscous units (referenced to the friction velocity of the initially undisturbed flow) which corresponds to 0.8 seconds of transient behavior shown in figure 6. A time scale of this order represents an extremely rapid transient if a means of boundary-layer control is to be deployed after detection of a related event, in order to control the subsequent evolution of the boundary layer. Moreover, if the proposed mode of boundary-layer control were one in which vorticity (or equivalently, shear strain) were reintroduced at the wall, it would be most effective if deployed during the transient, while there were still appreciable levels of Reynolds stress near the surface, in order to regenerate turbulent kinetic energy through the interaction of Reynolds stress and shear strain.

Since finite actuation times for devices for control of boundary layers (pop-up delta surfaces, localized suction, surface acceleration etc.) are a necessity, the practical utility of these devices may well depend upon the ability to forecast conditions under which the process of separation might be forced by the external flow. Based on the physical picture portrayed in this section of a turbulent boundary layer undergoing forced deceleration towards separation, a time series model describing the temporal behavior of streamwise velocity in the decelerating turbulent boundary layer is presented, with a view to testing its capabilities for predicting future velocity conditions at which separation would be anticipated, and control devices deployed.

Forecasting of non-stationary turbulent processes

There are a number of statistical forecasting techniques which may be used to continually update a limited time series of information, with a view to predicting a future value of the time series with some degree of confidence. Most of these techniques follow the parametric approach of seeking models for observation data, and well-known examples include ARMA[3] (autoregressive moving-average) models, for stationary stochastic processes, and ARIMA[3] (autoregressive integrated moving-average) models, for non-stationary stochastic processes. In the spirit of Box & Jenkins,[3] the models deemed most desireable are those which follow the principle of parsimony and provide adequate representations of observation data with the smallest possible number of parameters. This point is of particular importance if the eventual goal is real-time forecasting from sequential data. The time series of the measured velocity (at $y^+ = 400$) in a turbulent boundary-layer shown in figure 7, for the case of rapid deceleration which leads to separation, was used for model selection and testing. A second time series of streamwise velocity data recorded under steady conditions was used for concurrent testing, since any robust non-stationary forecasting scheme for a finite series of sequential data should also perform satisfactorily for stationary data.

After considerable methodical testing of a range of orders of ARMA and ARIMA models, the most suitable appeared to be a model in which the time series was represented by a locally-stationary first-order autoregressive stochastic process, superimposed upon a non-stationary process modeled only by its level and slope with respect to time. Physically, this model may be thought of as a decomposition of the velocity field into two distinct kinds of motion, *i.e.*

$$u(t) = u(t)_{\text{n-s}} + u(t)_{\text{s}} \tag{1}$$

The non-stationary component $u(t)_{\text{n-s}}$ is modeled as:

$$u(t)_{\text{n-s}} = \overline{U} + \frac{\Delta U}{\Delta T} t \tag{2}$$

where $\overline{U}$ is a short-time mean of u and $\frac{\Delta U}{\Delta T}$ the short-time estimate of the gradient in time, from a linear fit to data. The stationary component $u(t)_{\text{s}}$ is modeled as:

$$[u(t)_{\text{s}} - \mu(t)] - \phi[u(t-1)_{\text{s}} - \mu(t-1)] = a(t) \tag{3}$$

where $\mu(t) = \overline{U} + \frac{\Delta U}{\Delta T} t$, ϕ is the single autoregressive parameter of the model, and $a(t)$ is a white-noise process, uncorrelated from one time to the next.

The non-stationary scale represents the local velocity as a large eddy, which carries the short-time-mean level of velocity, its short-time-mean gradient with respect to time, and represents the memory of the fluid. The superposed stationary scale is a Markoff stochastic process, whose past has no influence on the future if its present is specified. It therefore represents the less coherent aspects of turbulent motions. The parameters $\overline{U}$, $\frac{\Delta U}{\Delta T}$, ϕ and a, which characterize these scales of motion for short time series, are continually updated by new information, and are therefore adaptive in time.

The reasonableness (and parsimony) of this representation may be demonstrated by considering the power spectrum of a Markoff stochastic process. This spectral estimate is shown in figure 8 for a stationary time series of turbulent velocity data, in which a smoothed, windowed Fourier transform spectral estimation is also included for purposes of comparison. Although the windowed Fourier representation admittedly provides a more detailed description of the power spectrum, the Markoff model only requires fitting the data to a single parameter ϕ (though autoregressive processes of higher order could be modeled if desired). Moreover, the importance of autoregressive spectral estimation in other engineering applications is such that a number of efficient adaptive parameter-estimation schemes have been developed for real-time application (*i.e.* the Widrow algorithm[4] for which each estimate of an updated autoregressive parameter requires only a very small number of add or multiply computations).

The model of (1), (2) and (3) is implemented by taking a short part of a time series (say, 25 points) and fitting the parameters of the model to the data of the time series. Forecasts of expected future values of u may be made by evaluating (1), (2) and (3) for future times, for any expected future value $a(t)$ assumed to be zero.[3] Values of forecasts and their associated confidence levels may then be made. In a real-time sequential algorithm, new data would then displace the oldest data

from a shift register, new values of adaptive parameters would be estimated, and new forecasts made.

In preliminary tests of this model, the length of the past time series upon which the model parameters were chosen was based on the time scales of large eddies of boundary layer. A forecasting target of the time scale of one large eddy into the future was chosen, with a 95% confidence level placed on that future forecast. The time series was sampled at a rate of approximately $1/t^+$ Hz, and slower sampling rates could be experimented with by considering every other data point, etc. Comparisons of forecasts made 25 observations into the future, with the measured data at these times, are shown in figure 9. These representative data describe the outcome of choosing a model which is tuned by (or estimates its parameters from) the previous two large eddies (50 observations, in this case) and forecasts the behavior of the flow one large eddy (25 observations) into the future. Estimates of the associated confidence limits of the forecast are also shown. Given the simplicity of the model, its forecasts appear remarkably good.

Some very general observations from other preliminary tests indicated that forecasting more than two large eddies into the future was very much more uncertain, regardless of how many previous large eddies were used to tune the model. There was also a small improvement in the forecasts if they were tuned to the previous four large eddies, though at the expense of a greater time requirement for estimating parameters of the model.

Summary

Modeling of non-stationary turbulent velocity data as a superposition of coherent (in local velocity and its time gradient) and incoherent (Markoff) motion yields surprisingly good forecasts of the future behavior of a turbulent velocity time series given its past. Since coherent motions are known to play important roles in the transient behavior of turbulent boundary layers, and are of particular importance in a variety of separation phenomena,[5] time-series methods of this kind appear to have the capability of playing very important roles in schemes aimed at the active control of separation of turbulent boundary layers.

References

1. Brereton, G. J., Carr, L. W. & Reynolds, W. C.

Unsteady turbulent boundary-layer experiments with rapidly changing free-stream conditions.

Proceedings of the AGARD Conference on Unsteady Aerodynamics, Göttingen, 1985.

2. Brereton, G. J., Reynolds, W. C. & Jayaraman, R.

Response of a turbulent boundary layer to sinusoidal free-stream unsteadiness.

Journal of Fluid Mechanics, accepted for publication, December 1989.

3. Box, G. E. P., & Jenkins, G. M. 1976

Time Series Analysis: Forecasting and Control, Holden-Day, Oakland, California.

4. Papoulis. A. 1984

Probability, Random Variables and Stochastic Processes, McGraw-Hill, New York, New York.

5. Gad-el-Hak. M. 1987

Unsteady separation on lifting surfaces, Applied Mechanics Review, **40**, 4.

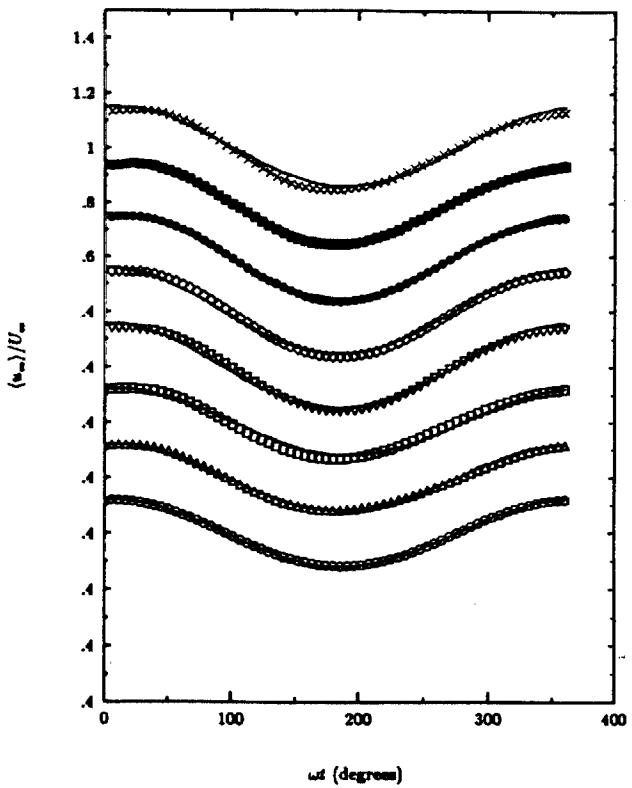

Figure 1. The external forcing condition of sinusoidal variation of free-stre velocity with phase angle, beyond the turbulent boundary layer; ——— $1 + A\cos\omega t$; ○, quasi-steady; △, 0.1 Hz; □, 0.2 Hz; ▽, 0.5 Hz; ◇, 0.8 H ●, 1.0 Hz; ■, 1.6 Hz; ×, 2.0 Hz. Note the shifted ordinate; the upperm graph corresponds to the uppermost numerical legends.

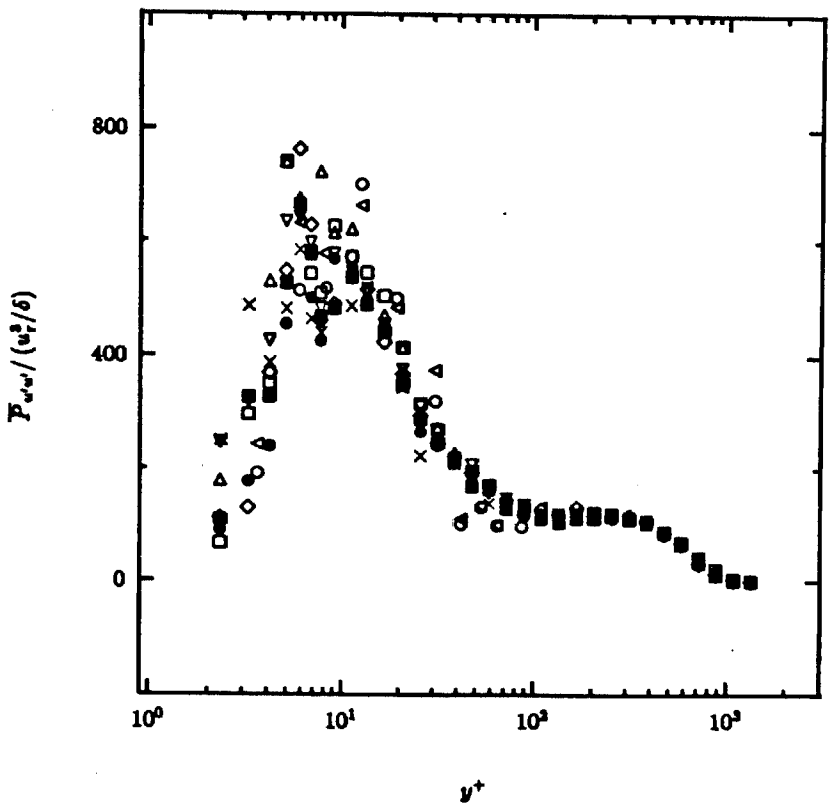

Figure 2. Boundary-layer profiles of production of $\overline{u'u'}$, for the case of forced sinusoidal unsteadiness; ×, 2.0 Hz; ■, 1.6 Hz; ●, 1.0 Hz; ◇, 0.8 Hz; ▽, 0.5 Hz; □, 0.2 Hz; △, 0.1 Hz; ○, quasi-steady, ◁, steady.

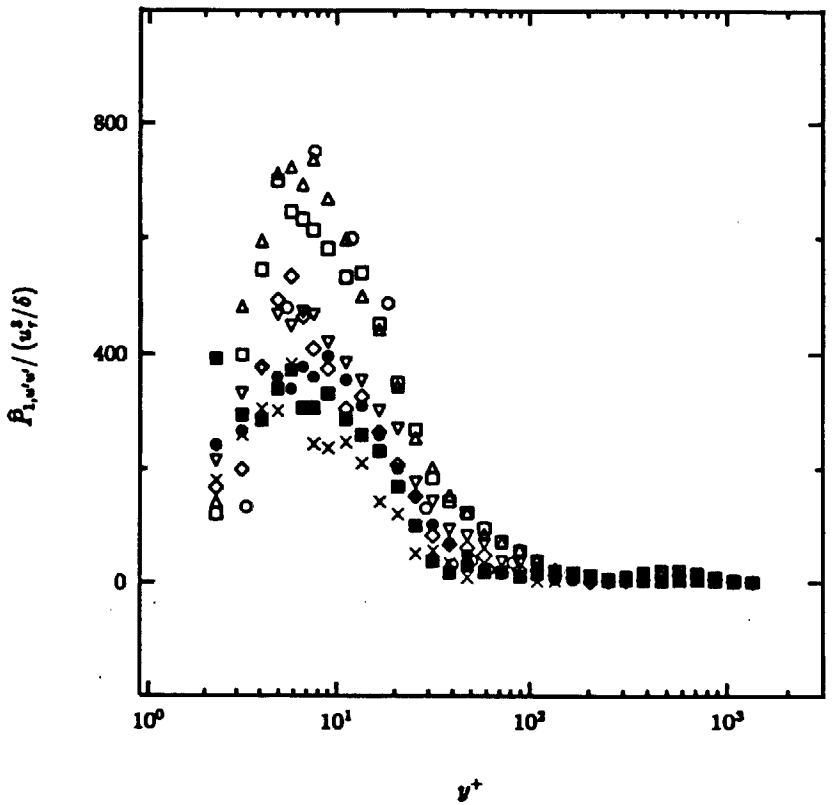

Figure 3. Boundary-layer profiles of the amplitude of production of $\langle u'u' \rangle$ at its first harmonic, for the case of forced sinusoidal unsteadiness; $\times$, 2.0 Hz; $\blacksquare$, 1.6 Hz; $\bullet$, 1.0 Hz; $\diamond$, 0.8 Hz; ∇, 0.5 Hz; $\square$, 0.2 Hz; $\triangle$, 0.1 Hz; $\circ$, quasi-steady.

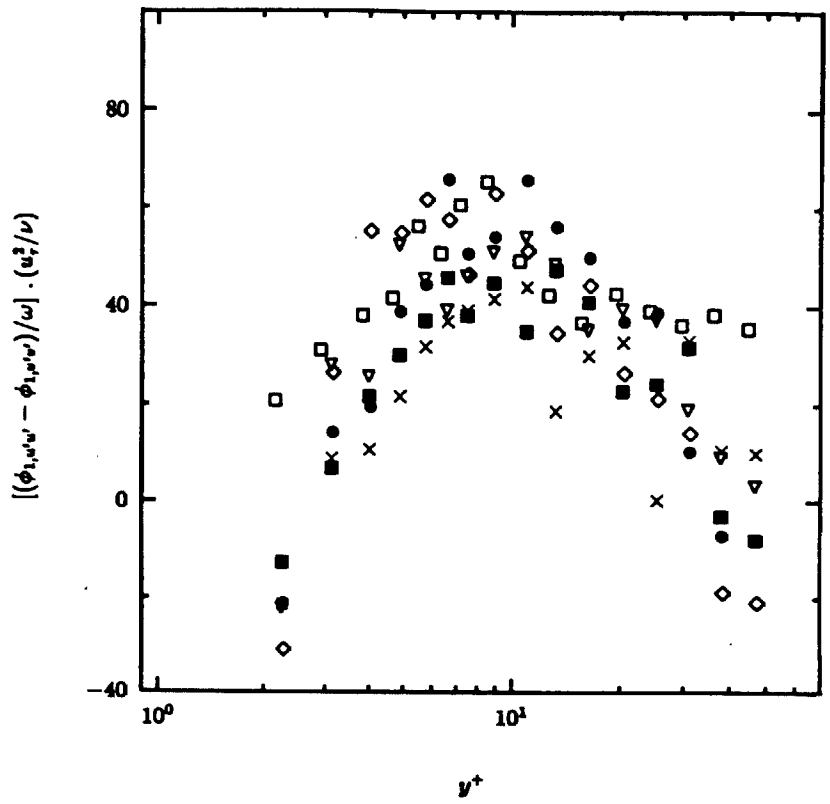

Figure 4. Near-wall profiles of the normalized time lag between peaks in $\langle u'u' \rangle$ and $\langle v'v' \rangle$, for the case of forced sinusoidal unsteadiness; $\triangle$, 0.2 Hz; $\square$, 0.5 Hz; $\diamond$, 1.0 Hz; $\bullet$, 1.6 Hz; $\blacksquare$, 2.0 Hz. Note that ω is the circular frequency of oscillation and that the time lag is in viscous time units, referenced to the mean friction velocity.

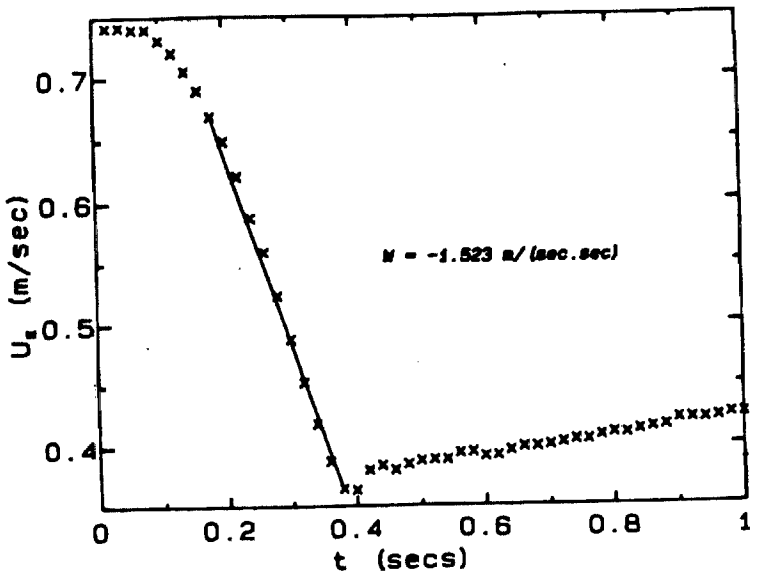

Figure 5. The external forcing condition of a ramp deceleration in free-stream velocity with time, beyond the turbulent boundary layer.

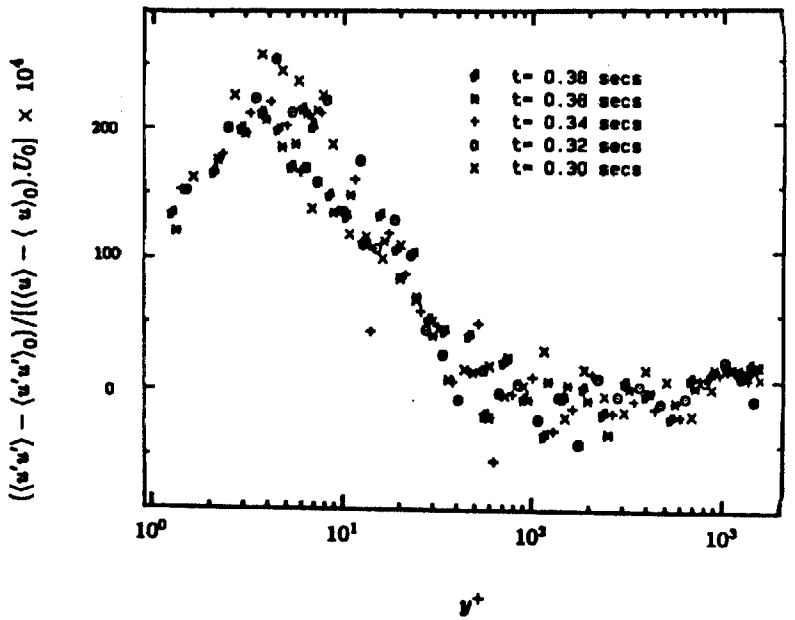

Figure 6. Evolution of the turbulence field during the ramp deceleration in free-stream velocity. The turbulence field is plotted as the deviation of $\langle u'u' \rangle$ from its initial value $\langle u'u' \rangle_0$, normalized by the deviation of $\langle u \rangle$ from its initial value $\langle u \rangle_0$. Abscissa normalization is referenced to the initial friction velocity.

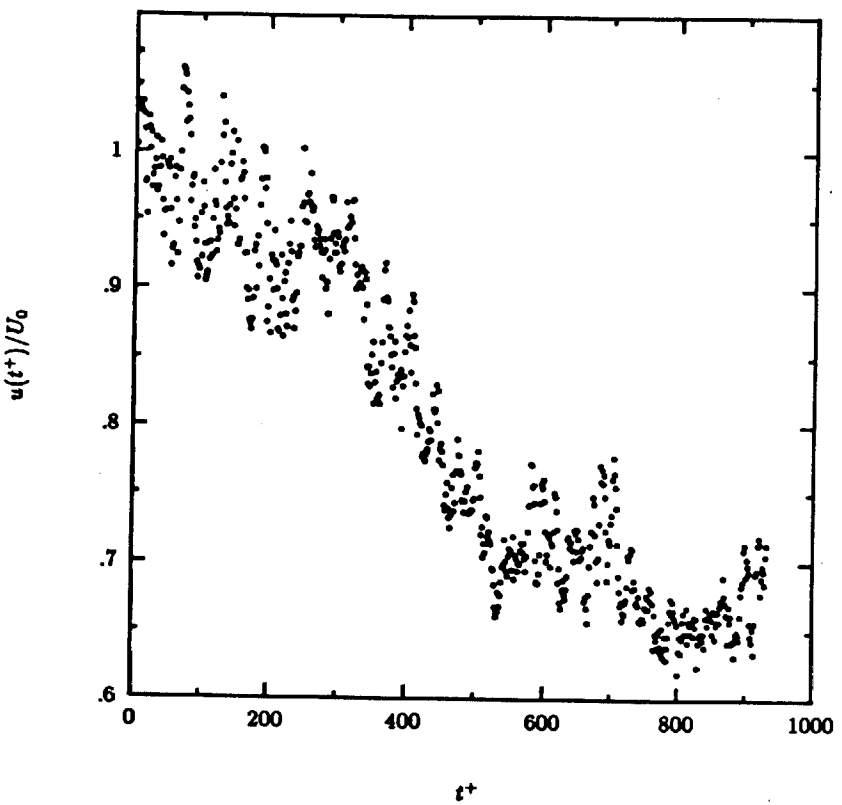

Figure 7. A time series of velocity data at $y^+ = 400$, recorded during forced deceleration of a turbulent boundary layer. Normalization in viscous units is with reference to the initial friction velocity, before initiation of the deceleration transient.

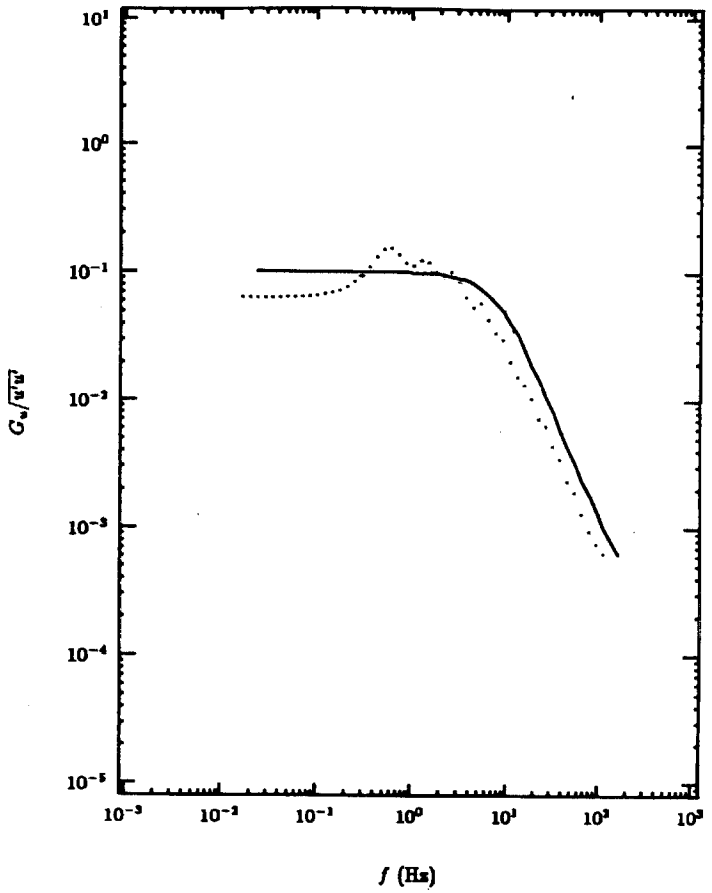

Figure 8. Comparison of a windowed Fourier transform power spectral estimate and a first order autoregressive model to the same stationary turbulent data.

· , Fourier transform, ———— , autoregressive.

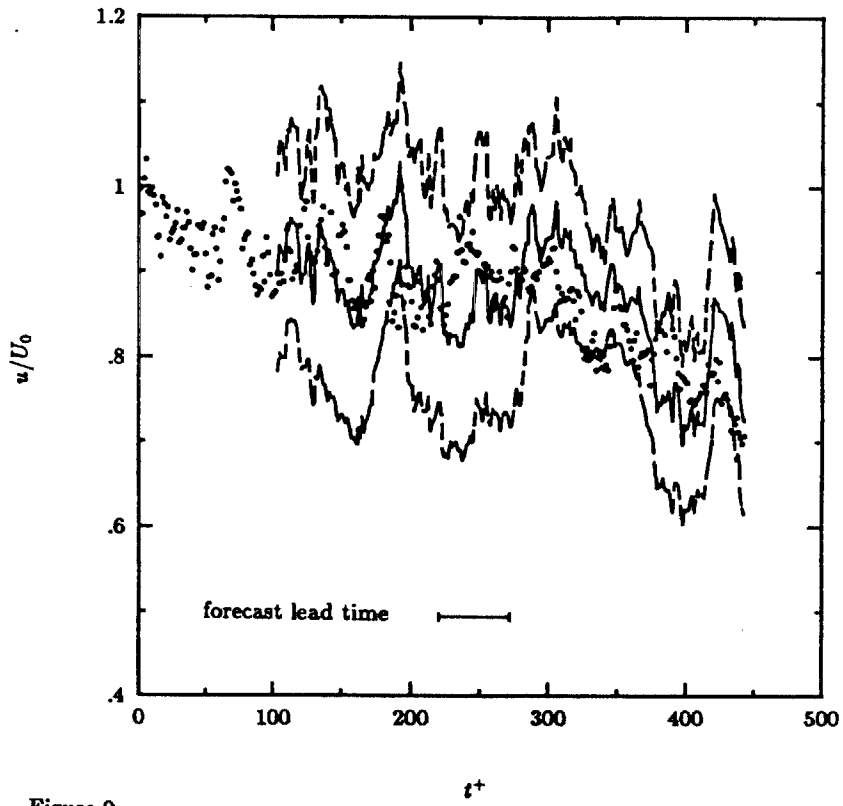

Figure 9.

Comparison of forecast and measured data for abrupt forced deceleration. • , measured experimental data; ————, forecast of future data values; — — — — , limits for 95% confidence in forecast. The model is adaptive over the previous 50 observations and forecasts 25 observations ahead.

Mechanical Engineering Dept

Stanford, CA 94305-3030

Turbulence modelling for unsteady separated flows -

abstract for NASA/AFOSR/ARO Workshop on Unsteady Separation

Peter Bradshaw, Feb. 1990

1. Unsteadiness

The exact transport equations for turbulent (Reynolds) stresses have left-hand sides representing the "substantial derivatives" of the Reynolds stresses, i.e. the rates of change of stress with respect to time, as seen by an observer following the mean motion of the fluid. Here the "mean" is a statistical average for the turbulent motion, distinguished from the ordered unsteadiness on which it is superimposed: for a turbomachine blade or a cyclically-pitching airfoil, the mean is a phase average (Fig. 1: see Ref. 1 for a practical discussion). Written in coordinates fixed with respect to a solid surface, the substantial derivative appears partly as an Eulerian time derivative at given spatial coordinate position and partly as a spatial derivative.

If the Reynolds-stress transport equations are modelled term by term ("stress-transport" or "second-order" models), the left-hand sides are left in exact form. The right-hand sides of the exact equations contain no time derivatives and there is no justification for introducing them in a model. Therefore the applicability of a stress-transport model to unsteady flow can be judged on its performance in steady flow: a model that behaves well in steady flows with rapid streamwise changes in stress (implying a large substantial derivative on the left-hand side) will behave equally well in unsteady flows where the left-hand side is equally large because of rapid timewise and/or streamwise changes.

This conclusion is true only of stress-transport models: models which ignore or approximate the left-hand sides cannot be judged in this way, but are necessarily suspect in any flow where the left-hand is large. It seems inescapable that the only candidates for rapidly-changing unsteady flows are stress-transport models (e.g. Refs. 2, 3). Any model based on eddy viscosity relates the turbulent stresses to the local mean velocity gradients, which amounts to ignoring the left-hand sides of the Reynolds-stress transport equations. (This is true even for two-equation models, which use transport equations for turbulent energy and dissipation

rate.) Algebraic stress models are based on an approximation to the left-hand sides which can easily be shown to be poor in rapidly-changing flows.

Clearly, unsteadiness can lead to secondary effects (e.g. appearance of concentrated spanwise vortices in a boundary layer or vortex street) which would defeat a turbulence model even in steady flow, so that passing the "left-hand-side" test is necessary but not sufficient.

2. Separation

Separation presents two specific problems to a turbulence model:--

(i) Prediction of the flow near separation depends critically on the "near-wall" part of the turbulence model. Several workers are currently studying this problem (Refs. 4-9), but all are using conventional models for the correlations between the pressure fluctuation and the velocity-gradient fluctuations. These correlations redistribute contributions to the Reynolds-stress tensor among the different components, and their modelling is a key part of any transport-equation method. Current practice is to relate the "redistribution" terms to local turbulence quantities and mean-flow gradients, but this is essentially risky because the pressure fluctuation at a point depends on an integral of the velocity fluctuations over a nominally infinite volume. Comparison with turbulence simulation data (Ref. 10) show that this "local" assumption breaks down very badly in the viscous wall region, where turbulence quantities and mean-flow gradients are changing rapidly with distance from the surface. The models can always be forced to reproduce the "law of the wall" in attached flows, simply by making the empirical coefficients functions of a Reynolds number related to the dimensionless wall distance y^+: however the flaw in the basic assumptions suggests that the models will break down near separation where the law of the wall no longer holds.

(ii) Downstream of separation, a boundary layer changes gradually to a mixing layer. Even in the simplest case of formation of a mixing layer from the boundary layer at exit from a jet nozzle, the effects of initial conditions persist for extremely long distances downstream. If the turbulence model does not predict boundary layers and (asymptotic) mixing layers adequately with the same set of coefficients, the coefficients must be interpolated in the streamwise direction. This is the "zonal modelling" technique (Ref. 11): it is also applicable in ad hoc corrections of the defects of turbulence models in special zones like imbedded vortices or shock-wave interactions.

References (first line is author's index category and abstract)

1 ..17.1,13.0,25.6:arbitrary sub (time) gridscale cutoff*
HANKEY, W.L.; CALARESE, W.*
Reynolds stresses for unsteady turbulent flows*
AIAA J. 21, 1210*
1983. `

2 ..17.1,13.0: upgraded sublayer modelling*
KEBEDE, W.; LAUNDER, B.E.; YOUNIS, B.A.*
Large-amplitude periodic pipe flow - a second-moment closure study*
Presented at 5th Symposium on Turbulent Shear Flows, Cornell, p. 16-23*
1985. `

3 ..17.1,13.0,14.0: k, eps. and stress transport - expts suggest log law fails at high freq.*
COUSTEIX, J.; HOUDEVILLE, R.*
Modelling of unsteady boundary layers*
Presented at Zaric Memorial Seminar on Near-Wall Turbulence, Dubrovnik, Yugoslavia, May 1988 (to be published by Hemisphere)*
1988. `

4 ..13.0: wall functions mask inherent deficiencies in stress models - useful review and backstep calcs*
LASHER, W.C.; TAULBEE, D.B.*
The effect of the near-wall treatment on the behavior of Reynolds-stress turbulence models for reattaching flows*
7th Sympo. on Turbulent Shear Flows, Stanford Univ.*
1989. `

5 ..13.0: Launder collaborator - redistribution coefficients depend on anisotropy*
SHIMA, N.*
Calculation of a variety of boundary layers with a second-moment closure applicable up to a wall*
7th Sympo. on Turbulent Shear Flows, Stanford, Univ.*
1989. `

6 ..25.6,08.0,13.0: injection to simulate wavy wall with 10^6 grid points - check of LRR not good near wall*
MIYAKE, Y.; KAJISHIMA, T.*
A discussion on turbulence model by means of LES*
7th Sympo. on Turbulent Shear Flows, Stanford Univ.*
1989. `

7 ..13.0,14.0: results for rapid P-S model, and near-wall k, eps.*
MANSOUR, N.; SHIH, T.*
Advancements in turbulence modeling*
Presented at 3rd Joint ASCE/ASME Mechanics Conference*
1989. `

8 ..13.0: genuine triple-product transport--but expresses near-wall effects solely by low Re*
AMANO, R.S.; GOEL, P.; CHAI, J.C.*
Turbulence energy and diffusion transport of third-moments in a separating and reattaching flow*
AIAA J. 26, 273*
1988. `

9 ..13.0: just so - especially near-wall regions*
RODI, W.*
Recent developments in turbulence modelling*
Presented at 3rd Int. Symp. on Refined Flow Modelling and Turbulence Measurements, Tokyo*
1988. `

10 ..13.0,05.0: correlation of about - 0.5 between pressure and its Laplacian*
BRADSHAW, P.; MANSOUR, N.N.; PIOMELLI, U.*
On local approximations of the pressure-strain term in turbulence models*
Studying turbulence using numerical simulation databases, Ames/Stanford CTR-S87, p. 159*
1987. `

11 ..14.0: just so*
FERZIGER, J.H.; ET AL.*
Zonal modelling of turbulent flows - philosophy and accomplishments*
Presented at Zaric Memorial Seminar on Near-Wall Turbulence, Dubrovnik, Yugoslavia, May 1988 (to be published by Hemisphere)*
1988. `

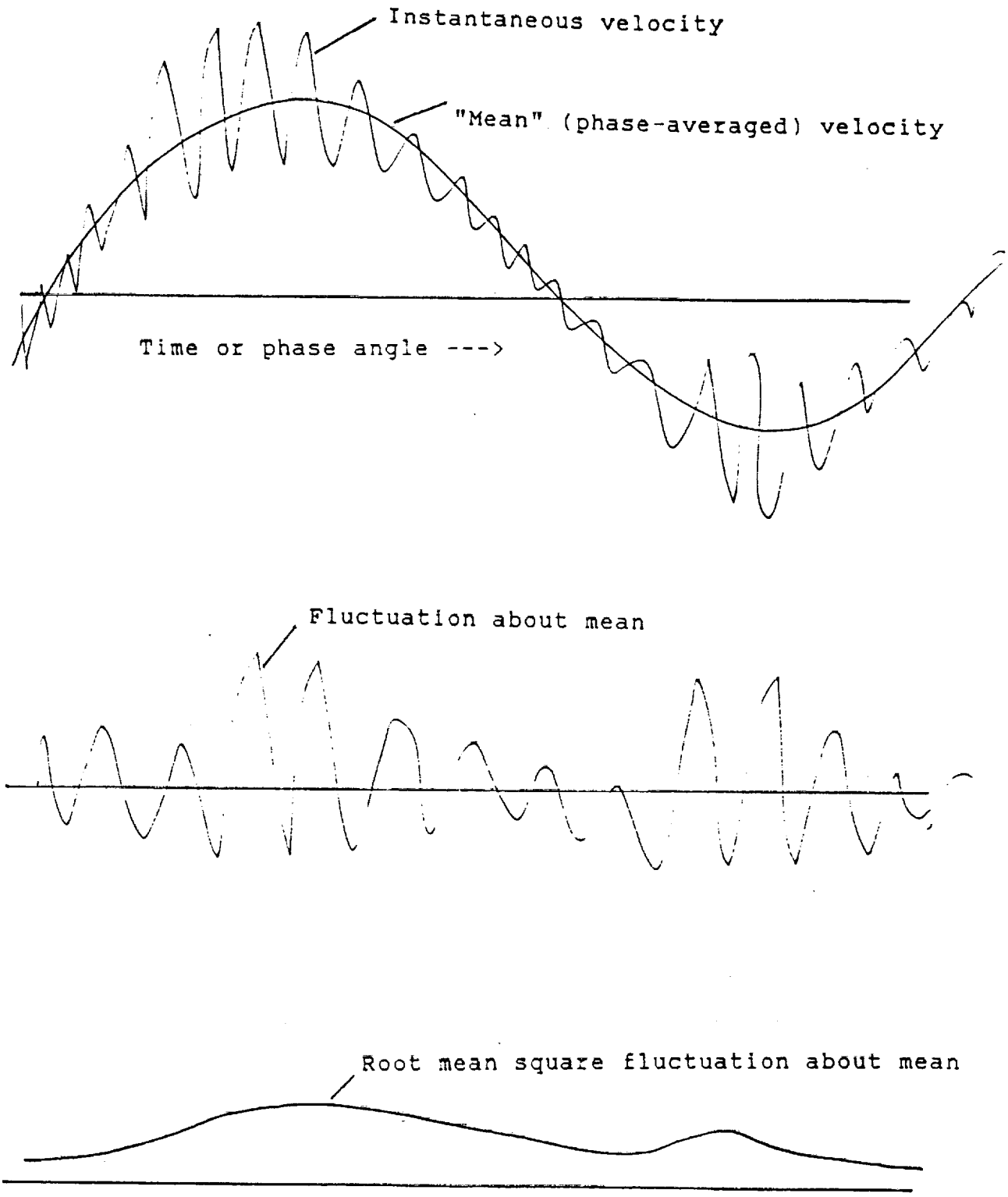

Fig. 1 Phase Averaging in Cyclically-Unsteady Flow

NASA/AFOSR/ARO Workshop on Unsteady Separation

Turbulence modelling for unsteady separated flows

Peter Bradshaw

Heat Transfer and Turbulence Mechanics Group, M.E. Dept
Stanford, CA 94305-3030, April 1990

1. Unsteadiness
1.1 Transport equations – general

• Exact "transport" equations govern turbulent (Reynolds) stresses.

• As for all transport equations, their left-hand sides represent the mean rates of change of the transported quantity with time, as seen by an observer following the mean motion of the fluid.

• Here the "mean" is a statistical average for the turbulent motion, distinguished from the ordered unsteadiness on which it is superimposed.

1.2 Definitions of averages

• For a turbomachine blade or a cyclically-pitching airfoil, we usually choose the mean to be a phase average.

• In coordinates fixed with respect to a solid surface, the mean rate of change seen by a moving observer appears as:

a time derivative at given spatial position

plus a spatial derivative (which varies with time).

1.3 Transport equations for Reynolds stresses

• In "stress-transport" or "second-order" models, the Reynolds-stress transport equations are modelled term by term.

• The rate of change of Reynolds stress on the left-hand side of each equation is left in exact form – no modelling.

• The right-hand sides of the exact equations contain no time derivatives ...

...so there is no justification for introducing time derivatives in a model of the right-hand sides!

• Because the left-hand side depends only on the sum of the time derivatives and space derivatives, the applicability of a stress-transport model to unsteady flow can be judged on its performance in steady flow...

1.4 Transport equations for Reynolds stresses – continued

• Suppose we have a model that behaves well in steady flows with rapid streamwise changes in stress (implying a large "left-hand side")...

...it should behave equally well in unsteady flows where the left-hand side is equally large, because of rapid time-wise (and/or streamwise) changes.

• This conclusion is true only of stress-transport models.

• The unsteady-flow performance of models which ignore or approximate the left-hand sides of the Reynolds-stress transport equations cannot be estimated in this way.

• Such models are necessarily suspect in any flow where the left-hand sides (rates of change of Reynolds stresses) are large.

1.5 Eddy-viscosity models

• Any model based on eddy viscosity relates the turbulent stresses to the local mean velocity gradients, which amounts to **ignoring** the left-hand sides of the Reynolds-stress transport equations.

• This is true even for "two-equation" models such as the k, ϵ model.

These models use transport equations for turbulent energy and dissipation rate but not for the individual stresses.

• Algebraic stress models were intended to improve on the assumption of isotropic eddy viscosity in the "two-equaton" models.

However they are based on an approximation to the left-hand sides which is poor in rapidly-changing flows.

1.6 Turbulence models for unsteady flows – conclusions

- It seems inescapable that the only plausible candidates for rapidly-changing unsteady flows are stress-transport models.

- Unfortunately, stress-transport models are harder to program, and taken longer to run, than eddy-viscosity models. The more independent variables you have, the bigger the computational disadvantage.

- As H.L. Mencken said *"To every difficult question there is a simple answer – which is wrong"*.

- Clearly, unsteadiness can lead to new secondary effects, e.g. the appearance of concentrated spanwise vortices in a boundary layer or vortex street.

- These might defeat a turbulence model even in steady flow, so that passing the "left-hand-side" test is necessary but not sufficient.

2. Separation

• Separation presents two specific problems to a turbulence model:–

• (i) Prediction of the flow near separation depends critically on the "near-wall" part of the turbulence model.

•(ii) Downstream of separation, a boundary layer changes gradually to a mixing layer.

2.1 Near-wall modelling

• Several workers are currently studying this problem, using stress-transport equation models. Here, the dificulty is to model transport *normal* to the surface.

•All are using conventional models for the correlations between the pressure fluctuation and the velocity-gradient fluctuations. (These correlations redistribute contributions to the Reynolds-stress tensor among the different components, and their modelling is a key part of any transport-equation method.)

•Current practice is to relate the "redistribution" terms to local turbulence quantities and mean-flow gradients.

2.2 Near-wall modelling – continued

• "Local" modelling is always risky, because the pressure fluctuation at a point depends on an integral of the velocity fluctuations over a nominally infinite volume.

• Comparisons with turbulence simulation data show that this "local" assumption breaks down very badly in the viscous wall region...

...where turbulence quantities and mean-flow gradients are changing rapidly with distance from the surface.

• Any model can be forced to reproduce the "law of the wall" in attached flows, simply by making the empirical coefficients functions of a Reynolds number related to the dimensionless wall distance y^+.

• However the flaw in the basic assumptions suggests that these attached-flow models will break down near, and after, separation where the law of the wall no longer holds.

2.3 Modelling of separated shear layers

• Even in the simplest case of formation of a mixing layer from the boundary layer at exit from a jet nozzle, the effects of initial conditions persist for extremely long distances downstream.

• If the turbulence model does not predict boundary layers and (asymptotic) mixing layers adequately with the same set of coefficients, the coefficients must be interpolated in the streamwise direction.

• This is the "zonal modelling" technique: it is also applicable in *ad hoc* corrections of the defects of turbulence models in special zones like imbedded vortices or shock-wave interactions.

• Zonal modelling – model coefficients depending on local flow type – is the only logical alternative to the dream of a "universal" turbulence model.

Conclusions

• There is a universal turbulence model – the 3D, time-dependent Navier-Stokes equations. Any simpler model is likely to be less accurate or less widely applicable!

• Turbulence modelling is caught between the Navier-Stokes equations and Mencken's Theorem.

• It will be a long time before numerically-exact Navier-Stokes simulations can produce useful results for unsteady flows in engineering geometries...

...and until then we must use the "best-buy" models.

• A major conclusion of this review is that only Reynolds-stress transport models, using PDE "transport" equations for the Reynolds stresses, can incorporate the physics of unsteady flows.

N94-34985

Toward the Optimization of Control of Unsteady Separation

S.F.Shen and Zheng-Hua Xiao, Cornell University

Abstract:

Regardless of our understanding, or the lack of it, of the complicated physical process, means can always be found to alter the occurrence and development of unsteady separation. To be able to optimize the control of separation, however, requires the identification of the critical aspects to which the intervention may be focused and achieve the desired result with minimum waste of effort. The Lagrangian analysis of unsteady boundary-layer traces the trajectories of individual fluid particles, and reveals the 'bad seeds' that, through extreme deformation in the direction normal to the wall, eventually develop into a virtual barrier and cause the ejection of boundary-layer material into the main stream. It follows logically that separation can be triggered or delayed most effectively by targeting these 'bad seeds'. Since they are normally interior points of the boundary layer, attempts to influence them through the boundary conditions are necessarily indirect. Furthermore, as the strategy has to be the modification of the growing process of the 'bad seeds', whatever may be the intervention scheme, it needs to be strong enough and early enough. In Shen and Wu (1988), examples of how acceleration/deceleration of the (2D) body, as well as the moving wall (of a rotating cylinder), may affect the development of the bad seed toward separation are shown. In fact it was mentioned therein that the results might be the first step for a feasibility study of the control of unsteady separation.

A practical difficulty of making Lagrangian calculations of the boundary layers, even in the simpler 2D case, is the loss of accuracy due to the continuing distortion of the fluid element with time. This is accentuated in airfoil-like slender bodies (Wu, 1985). More problems arise if wall suction or blowing is added. These however cause much less trouble for the more conventional Eulerian formulation. The weakness of the Eulerian scheme mainly lies in its inability to identify the 'bad seed' that ultimately leads the uprising. In the traditional marching algorithms of the Eulerian formulation, the resolution also appear to suffer in the presence of extensive reversed flow, which is typically prerequisite to unsteady separation. We have developed during the past year a time-accurate 2D boundary-layer Euler program, by formulating the unsteady boundary layer as an initial-value problem with spatial boundary conditions. It proves to be able to resolve the typical 'spike' signature of the displacement thickness at the inception of separation, which seems to be now generally accepted since the Lagrangian calculations of van Dommelen and Shen (1980). A comparison of the newly developed Eulerian vs. the earlier Lagrangian results for the bench-mark case of the impulsively-started cylinder is shown in Fig. 1. The absolute values of the spike differ because of the limited resolution of both methods at the mathematical singularity. It is the unmistakable occurrence of the spike that identifies separation.

With both the Lagrangian and the Eulerian programs as working tools, serious research on the possible control of unsteady boundary-layer separation and its optimization could actually begin. In principle we should continuously watch for the emergence and development of 'bad seeds' with the Lagrangian, and test the efficacy of various means of control to suppress the bad behavior. Other seeds turning into bad ones can also be tagged and dealt with. The 'lead time' for intervention is an equally intriguing aspect of the dynamics of separation. (It cries for a theoretical analysis, but we have yet to be able to formulate.) The Eulerian serves both as an alternate to the Lagrangian to circumvent the distortion problem, and as a possibly easier implementation of the control details. The technical aspects of switching from one code to the other are not expected to be a bottleneck but remains to be done.

Initial experimentation of control by surface suction for the impulsively-started cylinder have been reported by Shen (1990).The results substantiate the common-sense expectation that sufficient suction must be able to remove all 'bad seeds', hence separation — like massive mastectomy, while less suction is needed with earlier intervention, an indication of the role of the 'lead time'. Presented here are some additional results of applying suction to the impulsively started circular cylinder, which normally separates at (dimensionless) time t = 1.5:

Case (1) -- Fairly massive suction over the rear half, with peak at the rear stagnation point, starting from t = 1.3, as shown in sketch of Fig. 2(a). The suction is applied too late and does not capture the bad seed, as Fig. 2(b) shows substantial reduction of boundary layer thickness in the rear but the spike still appears at t = 1.5 and X = 110°, same as without suction.

Case (2) -- Less total suction but concentrated more around X = 110°, starting still from t = 1.3, Fig. 3(a). The spike appearance is delayed to t = 1.55 and X = 125° in Fig. 3(b), suggesting that the separation is now from a new group of bad seeds. There is some success with much reduced expenditure.

Case (3) -- Similar to case (2) but moving the suction region along the surface with a speed determined by a feedback from the boundary layer growth, reducing suction magnitude to a half, starting still from t = 1.3, Fig. 4(a). The spike now appears at t = 1.7 and X = 127° approximately. Thus more improvement is achieved with less effort.

The control strategy used in case (3) above is primitive, simply synchronizing the peak of the applied suction with the location of the maximum of the 'blowing velocity' $d(U\delta^*)/dx$, U being the free stream velocity at the wall and δ^* the displacement thickness. The suction strength Q is another parameter at our disposal. As a trial, we next regulate the peak suction not only to occur at the location of the calculated maximum blowing velocity but also to have exactly the same magnitude. Thus the applied suction is programmed as represented in Fig. 5 (a). The calculated displacement thicknesses, shown in Fig. 5 (b), are seen to be without the spike feature; the boundary layer remains attached for time up to t = 2.5.

These results are but crude exemples of how to optimize the applied suction and achieve some control over the time and location of the inception of unsteady separation. In practical design, other precursors of the nascent spike, such as the flow reversal point on the wall, could replace the maximum 'blowing velocity' in actuating the control, and feedback loops may be added.

Acknowledgement:

Preparation of this work has been partially supported by AFOSR-88-0229. The numerical calculation was performed by using the Cornell National Supercomputer Facility, a resource of the Center for Theory and Simulation in Science and Engineering (Theory Center), which receives major funding from the National Science Foundation and IBM Corporation, with additional support from New York State and members of the Corporate Research Institute.

References:

Shen,S.F. and Wu, T. "Unsteady Separation over Maneuvering Bodies", AIAA Paper 88-3542, 1988.

Shen, S.F. "Lagrangian View of Unsteady Separation", invited presentation at Workshop on Analytical Methods in Unsteady Separation, Columbus, OH, sponsored by U.S. Army Research Office, Jan.25-26, 1990.

Van Dommelen, L.L. and Shen, S.F. "The Spontaneous Generation of the Singularity in a Separating Laminar Boundary Layer", J. Comp. Phy., vol. 38, 1980, pp.125-140.

Wu, T. "Unsteady Incompressible Boundary-Layer Separation over a Two-Dimensional Impulsively Started Elliptic Cylinder by Lagrangian Method", MS Thesis, Cornell University, 1985.

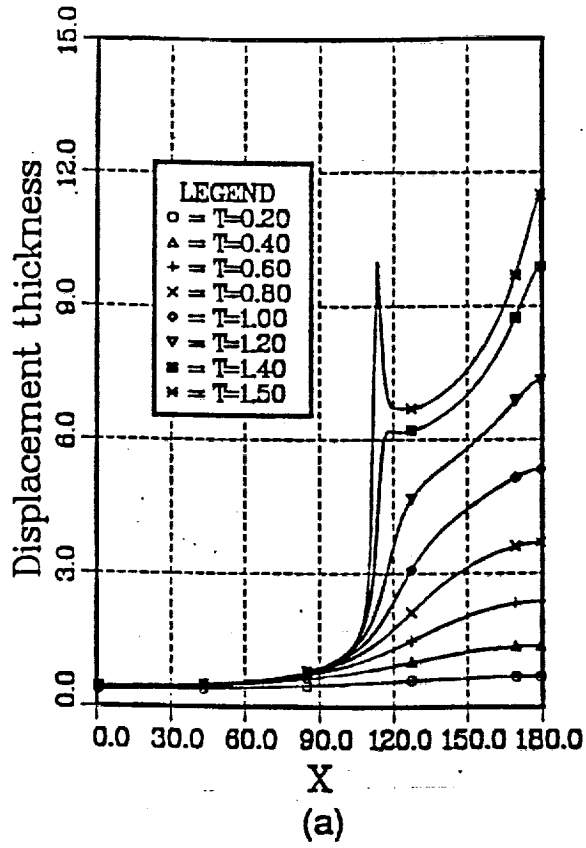

(a)

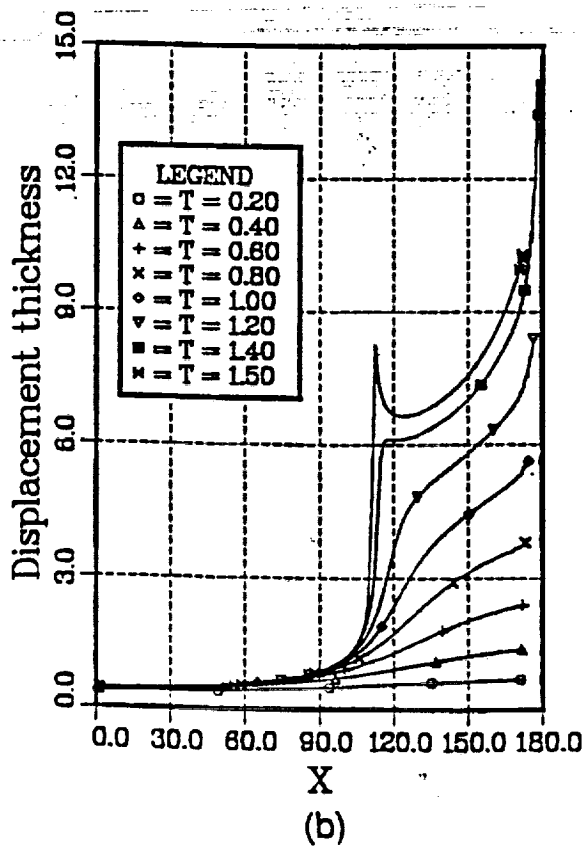

(b)

Fig. 1 Displacement Thickness on an Impulsively Started Circular Cylinder

(a) Eulerian (b) Lagrangian

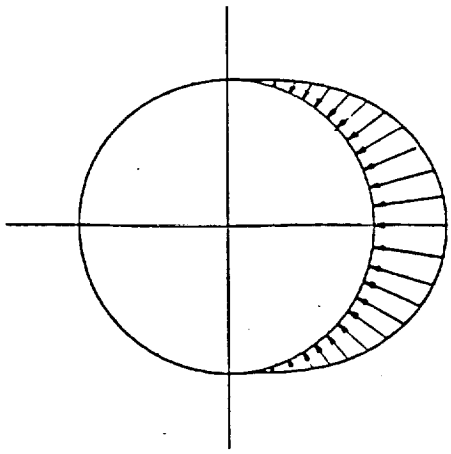

(a) Suction Distribution along the Circular Cylinder

$V_S = 0.5Q\ (1.0-\cos((X-X0)/(X1-X0)*2\pi))$

$Q = -50.0 \quad X0 <= X <= X1 \quad X0 = 90.70° \quad X1 = 269.30°$

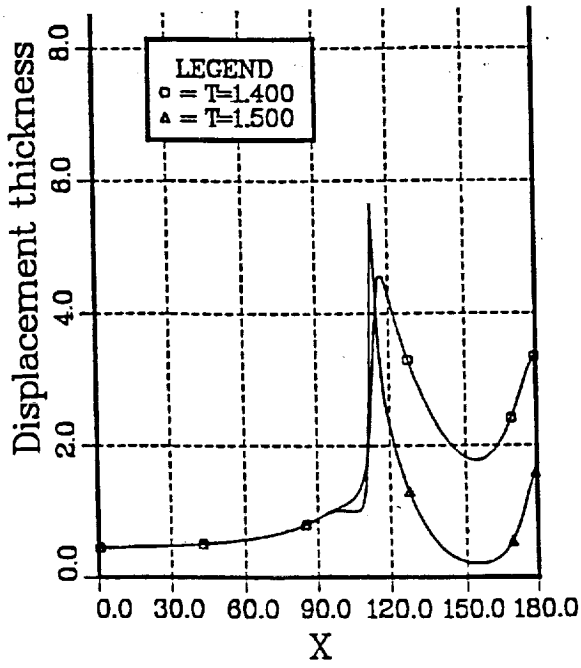

(b) Calculated Displacement Thicknesses at t = 1.4 and 1.5.

Fig. 2 Displacement Thicknesses on an Impulsively Started Circular Cylinder with Suction Imposed when t = 1.30, Case (1).

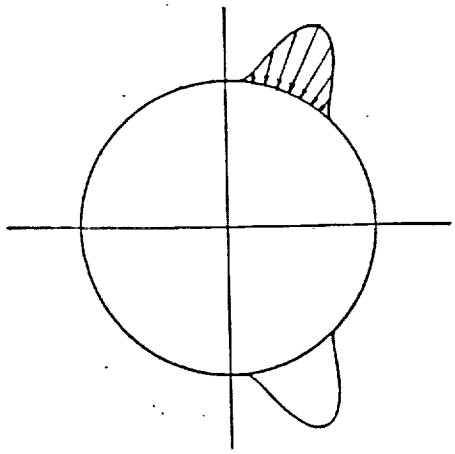

(a) Suction Distribution along the Circular Cylinder
$Vs = 0.5Q\ (1.0-\cos((X-X0)/(X1-X0)*2\pi))$
$Q = -50.0 \quad X0 <= X <= X1 \quad X1 = X0 \quad X1 = 39.38°$

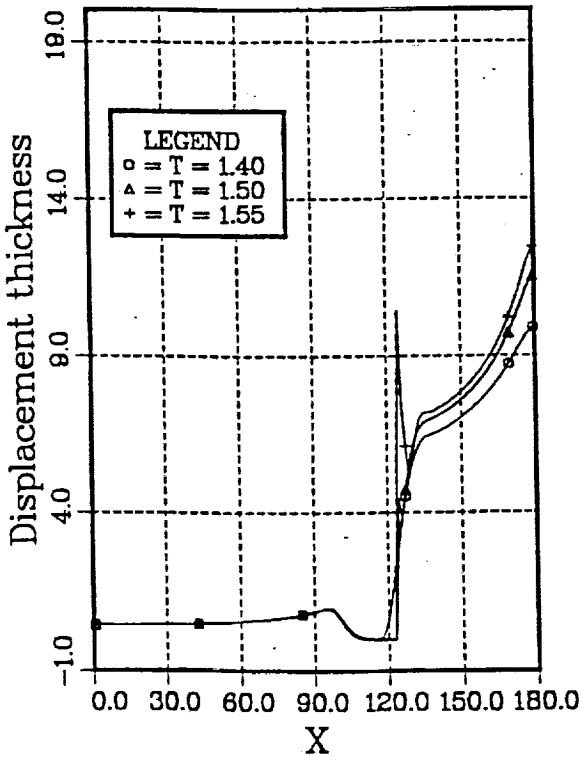

(b) Calculated Displacement Thicknesses at t = 1.4 and 1.55.

Fig. 3 Displacement Thicknesses on an Impulsively Started Circular Cylinder with Suction Imposed when t = 1.30, Case (2).

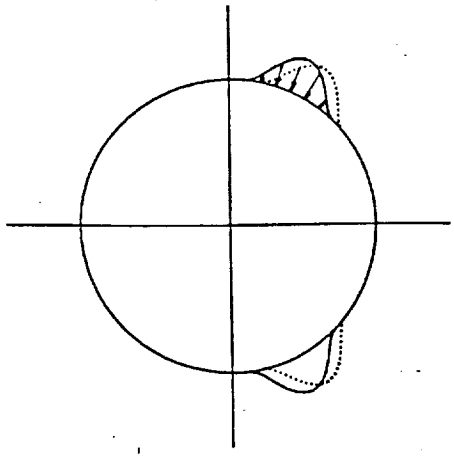

(a) Moving Suction Distribution along the Circular Cylinder
Vs = 0.5Q (1.0-Cos((X-X0)/(X1-X0)*2π))
Q = -25.0 X0 < = X < = X1 X1 = X0 X1 = 39.38°

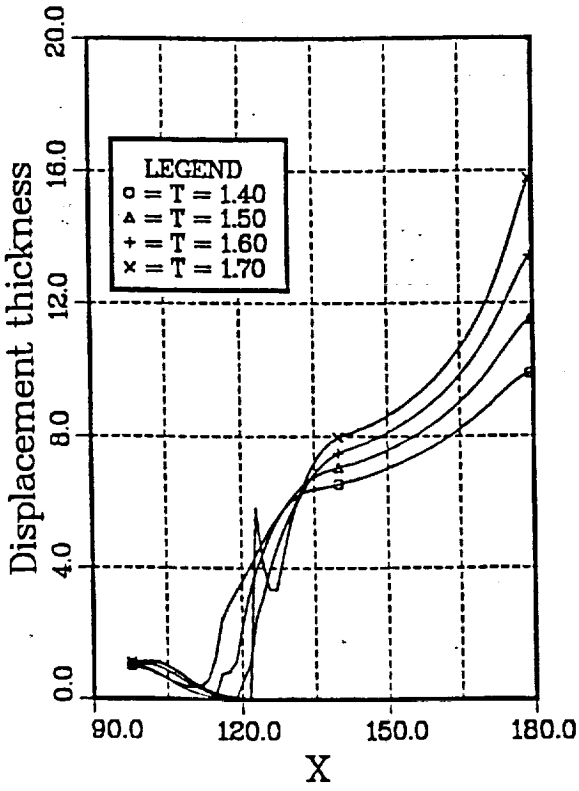

(b) Calculated Displacement Thicknesses at t = 1.4, 1.5, 1.6 and 1.7.

Fig. 4 Displacement Thicknesses on an Impulsively Started Circular Cylinder with Suction Imposed when t = 1.30, Case (3).

C-4.

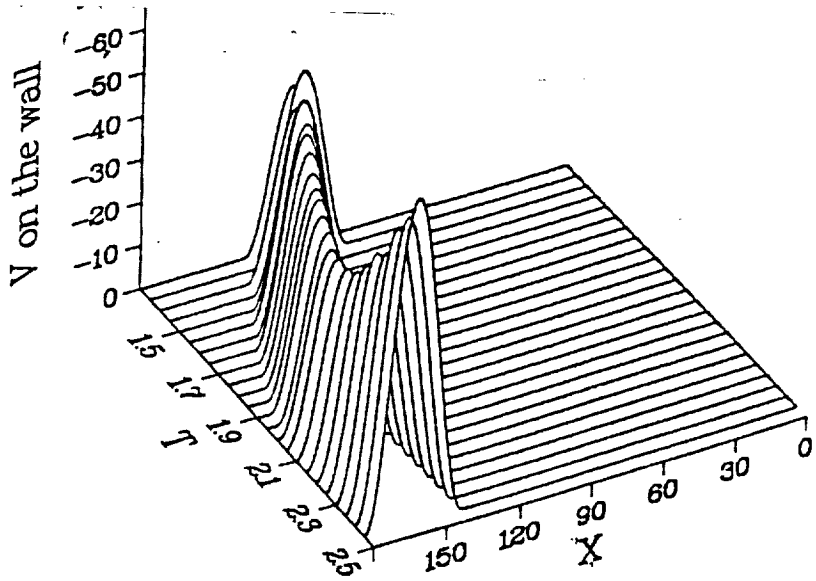

(a) Programmed Suction Distribution at Different Times
Vs = 0.5Q (1.0-Cos((X-X0)/(X1-X0)*2π))
Q = Max Blowing Velocity X0 < = X < = X1 X1-X0 = 39.38°

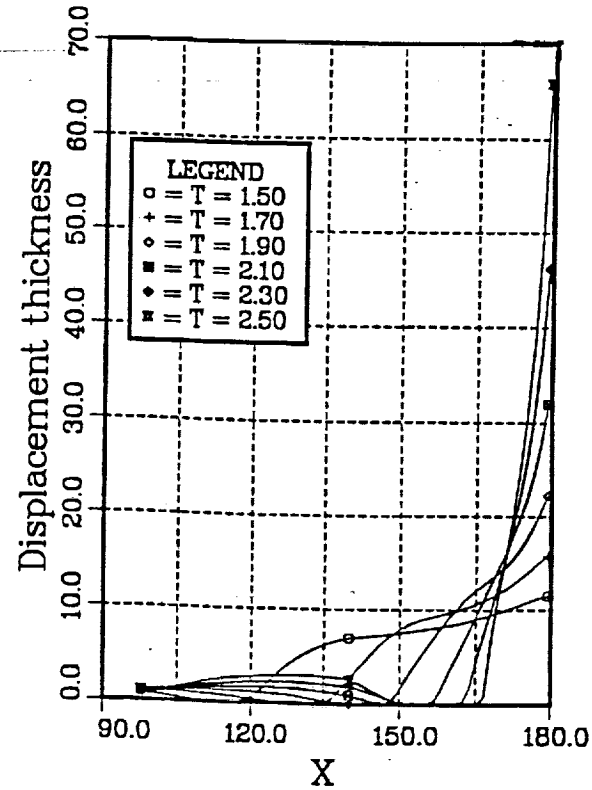

(b) Calculated Displacement Thicknesses at t = 1.5 and later.

Fig. 5 Displacement Thicknesses on an Impulsively Started Circular Cylinder with Programmed Suction, $t_s = 1.4$.

N94-34986

THE QUEST FOR STALL-FREE DYNAMIC LIFT

by

C. Tung, K.W. McAlister, L.W. Carr,
E. Duque and R. Zinner

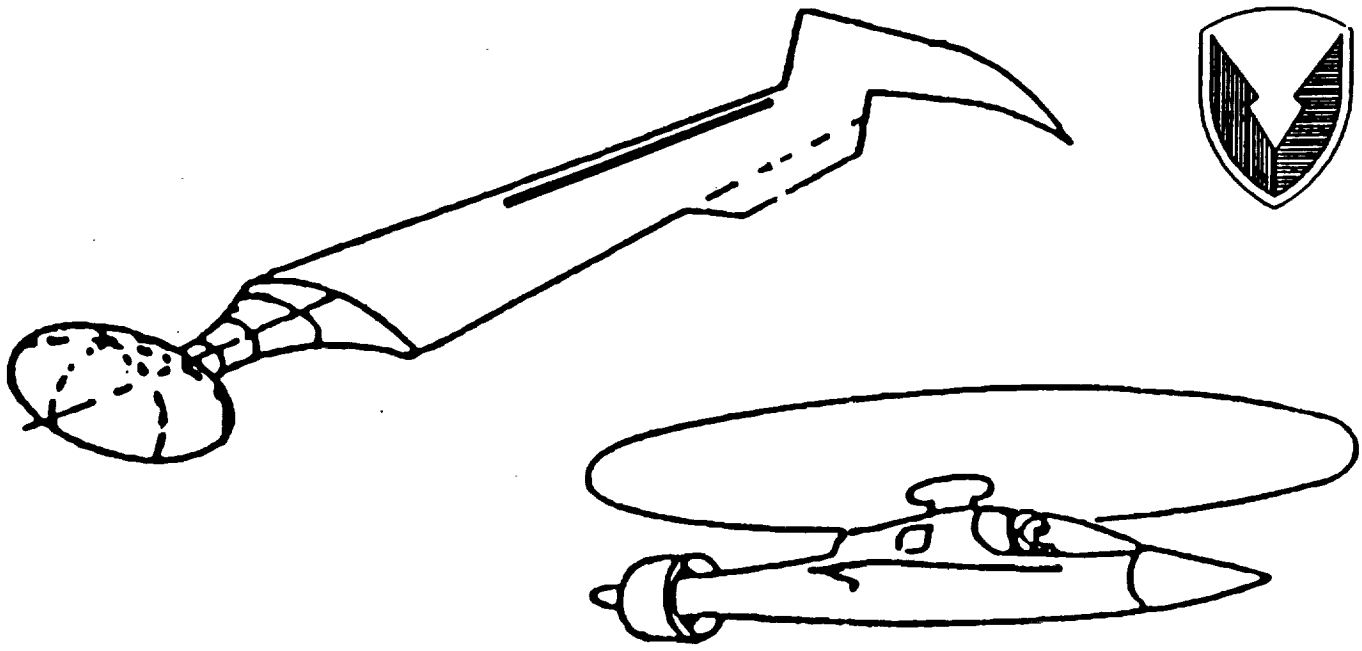

Army Aeroflightdynamics Directorate
Ames Research Center
Moffett Field, California

Presented at the Workshop On Physics Of Forced Unsteady Separation; NASA-Ames Research Center; Moffett Field, California; April 17-19, 1990.

THE QUEST FOR STALL-FREE DYNAMIC LIFT

by

C. Tung, K.W. McAlister, L.W. Carr,
E. Duque and R. Zinner

INTRODUCTION

During the past decade, numerous major efforts have addressed the question of how to control or alleviate dynamic stall effects on helicopter rotors, but little concrete evidence of any significant reduction of the adverse characteristics of the dynamic stall phenomenon has been demonstrated. Nevertheless, it is important to remember that the control of dynamic stall is an achievable goal. Experiments performed at the US Army Aeroflightdynamics Directorate more than a decade ago demonstrated that dynamic stall is not an unavoidable penalty of high amplitude motion, and that airfoils can indeed operate dynamically at angles far above the static-stall angle without necessarily forming a stall vortex. These experiments, one of them featuring a slat that was designed from static airfoil considerations, showed that unsteadiness can be a very beneficial factor in the development of high-lift devices for helicopter rotors.

The experience drawn from these early experiments is now being focused on a program for the alleviation of dynamic-stall effects on helicopter rotors. The purpose of this effort is to demonstrate that rotor stall can be controlled through an improved understanding of the unsteady effects on airfoil stall and to document the role of specific means that lead to stall alleviation in the 3-D unsteady environment of helicopter rotors in forward flight. The first concept to be addressed in this program will be a slatted airfoil. A 2D unsteady Navier-Stokes code has been modified to compute the flow around a two-element airfoil.

BACKGROUND

Dynamic stall continues to be a serious factor in modern helicopter design. The impulsive loads that are generated during helicopter airfoil stall limit high speed helicopter flight and reduce the maneuvering capability of the aircraft. The character of the dynamic stall phenomenon has been carefully studied (Refs. 1-3) and a significant body of knowledge has been acquired concerning the behavior of various airfoils during dynamic stall (Refs. 4-6). These studies have shown that deep stall is relatively insensitive to the airfoil profile; however, there are definite indications that dynamic stall inception is sensitive to the character of the boundary-layer (Ref. 3).

In order to better understand the significance of the boundary layer on the stall behavior, a variety of passive stall modifications were tested on an oscillating VR-7 airfoil (Ref. 7). In this study, a backward-facing step was installed in a attempt to control the progression of flow reversal on the airfoil and thus delay the formation of the stall vortex. Although several backward-facing step configurations were tested, no significant effect on the vortex development or the dynamic stall airloads was detected. Vortex generators were then installed at 20% chord to delay stall through boundary-layer re-energization. The vortex generators delayed the static stall significantly and even kept the boundary layer attached on the rearward portion of the airfoil under dynamic conditions. However, use of the vortex generators induced leading-edge stall in the dynamic environment and the loads were not measurably improved.

Finally, a leading-edge slat was installed in order to shift to the slat the rapid flow accelerations that normally occur near the leading edge of the basic airfoil and to re-energize the boundary layer on the main airfoil. A detailed diagram of this particular slat/airfoil combination is shown if Figure 1. This slat was found to postpone the dynamic stall to angles well above the range normally expected on helicopter airfoils, with virtually no drag penalty in the angle range associated with retreating blade aerodynamic conditions. A qualitative comparison of the slat/airfoil combination to that of the basic airfoil is presented in Figure 2. To approximate the full contribution of the slat/airfoil combination, the lift and moment curves were adjusted to match that of the basic airfoil at $\alpha = 15^o$. Figure 3 presents the lift and moment coefficients for the basic VR-7 airfoil for pitch oscillations of $\alpha = 15^o + 10^o \sin(\omega t)$ and for a range of frequencies. The dynamic

stall effects are quite evident. Figure 4 presents the same conditions for the slat/airfoil combination where it is clear that the dynamic stall vortex is no longer present. Figure 5 shows a comparison of the instantaneous pressure distributions for the basic airfoil and for the slat/airfoil combination at the same test conditions. Note the movement of the dynamic stall vortex along the chord of the basic airfoil and the complete absence of the vortex imprint in the slatted airfoil results.

APPROACH TO CONCEPT EVALUATION

The results in Reference 7 demonstrate the dramatic involvement that can be achieved by the use of a slat: the dynamic stall vortex is completely suppressed throughout the cycle of oscillation at the moderate frequencies that are compatible with helicopter forward-flight conditions. However, the slat/airfoil combination tested may not be the optimum shape nor even an acceptable configuration for a rotor application. Although the addition of the slat was effective in suppressing stall, the drag penalty is too large at the lower angles-of-attack (Fig. 6). A more acceptable design for the rotor would have to feature a retractable slat in order to avoid the high-drag penalty that would otherwise occur on the advancing side of the rotor disk. Encouraged by the success of the slat in suppressing the stall vortex, a new program called High Maneuverability and Agility Rotor and Control System (HIMARCS) has been initiated to study different techniques for increasing dynamic lift without stall. At the present time, the slat/airfoil combination is being reexamined in order to validate new CFD codes and to determine if the water tunnel can be used to qualitatively assess the performance of various high-lift concepts.

A general purpose code which solves the conservative thin-layer Navier-Stokes equations in generalized coordinates (Ref. 8) has been modified to handle the multi-element airfoil and includes an algebraic turbulence model (Ref. 9). Figure 7 compares the force and moment results for the basic VR-7 to the static results from an earlier wind tunnel experiment at $M_\infty = 0.3$ and $Re = 4.2 \times 10^6$ (Ref. 3). The computed lift coefficients show a reasonably good agreement with the test data. The moment coefficients also compare reasonably well at low angles-of-attack, but seriously under predict at high angles-of-attack. The drag coefficients are over predicted at low angles-of-attack, but are under predicted at higher angles-of-attack. This

over prediction of the drag at low angles-of-attack is expected since the computation assumed a fully turbulent boundary layer and in the experiment the boundary layer was allowed to undergo natural transition. Figure 8 compares the computed lift and drag coefficients for the basic and slatted VR-7 airfoil with the test results in Reference 7. Again the lift coefficients compare much better than the drag coefficients. Figure 9 shows the calculated Mach number and pressure coefficient contours for the slatted VR-7 airfoil at $\alpha = 15°$. The enlarged views of these contours illustrate the ability of the code to model the interaction between the slat wake and the main-element boundary layer.

The slatted VR-7 airfoil will also be tested in the water-tunnel facility where total lift, drag and pitching moment measurements can be made. These results will be used to establish the scaling law between the comparatively low Reynolds number environment in the water tunnel and the higher Reynolds numbers attainable in the wind tunnel. The water tunnel results will also to be used to complement the CFD efforts. A water-tunnel model of the VR-7 with slat has been constructed (Fig. 10) and a comparison between the experiment and the CFD calculations will be published in the near future (Ref. 10). Once greater confidence has been established in the CFD code as well as the use of the water tunnel for qualifying a candidate concept, a slotted airfoil will be designed. After the slot shape and position has been optimized, a set of slotted rotor blades will be constructed and the concept demonstrated under forward-flight conditions. The HIMARCS program will eventually address numerous high lift and control concepts as suggested in Figure 11.

REFERENCES

[1]Carr, L.W.; McAlister, K.W. and McCroskey, W.J.: "Analysis of the Development of Dynamic Stall Based on Oscillating Airfoil Experiments." NASA TN D-8382, Jan. 1977.

[2]McCroskey, W.J.; McAlister, K.W.; Carr, L.W.; Pucci, S.L.; Lambert, 0. and Indergand, R.F.: "Dynamic Stall on Advanced Airfoil Sections." J. American Helicopter Society, Vol. 26, No.3, July 1981, pp. 40-50.

[3]McCroskey, W.J.; McAlister, K.W.; Carr, L.W.; and Pucci, S.L.: "An Experimental Study of Dynamic Stall on Advanced airfoil Sections, Vol. 1,2,3." NASA TM-84245, July 1982.

[4]Ham, N.D. and Garelick, M.S.: "Dynamic Stall Considerations in Helicopter Rotors." J. of American Helicopter Society, Vol.13, No.2, April 1968, pp.49-55.

[5]Carta, F.O.; Commerford, G.L.; Carlson, R.G. and Blackwell, R.H.: "Investigation of Airfoil Dynamic Stall and its Influence on Helicopter Control Loads." USSAAMRDL TR 72-51, Sept. 1972.

[6]Liiva, J.: "Two-Dimensional Tests of Airfoils Oscillating Near Stall." J. of Aircraft, Vol. 6, No. 1, Jan. 1969 pp.46-51.

[7]Carr, L.W. and McAlister, K.W.: "The Effect of a Leading-Edge Slat on the Dynamic Stall of an Oscillating Airfoil." AIAA paper 83-2533, Oct. 1983.

[8]Steger, J.L.; Ying, S.X. and Schiff, L.N.: "A Partially Flux Split Algorithm for Numerical Simulations of Compressible Inviscid and Viscous Flow." Workshop on Computational Fluid Dynamics, Institute of Non-Linear Science, University of California, Davis, CA, 1986.

[9]Baldwin, B.S. and Lomax, H.: "Thin-layer Approximation and Algebraic Model for Separated Turbulent Flows." AIAA paper 78-257, Huntsville, Alabama, Jan. 1978.

[10]Duque, E.P.N.; Zinner, R.A. and McAlister, K.W.: "Static Stall Prediction for Single and Multi-Element Airfoils." to be published at ASME 1990 Winter Annual Meeting.

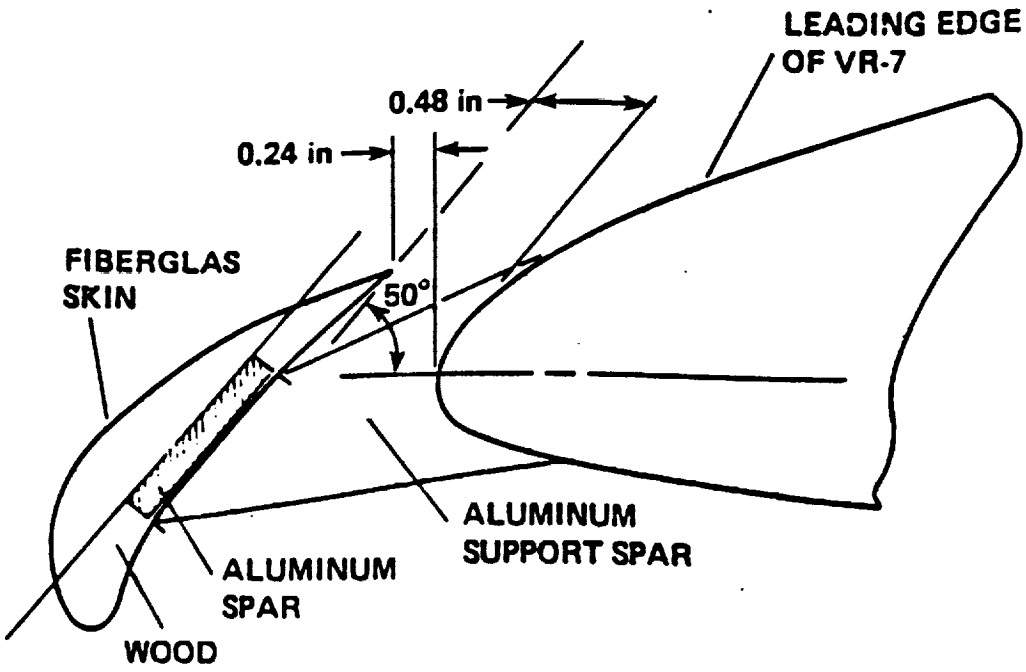

Figure 1.- Detailed sketch of VR-7 airfoil with slat.

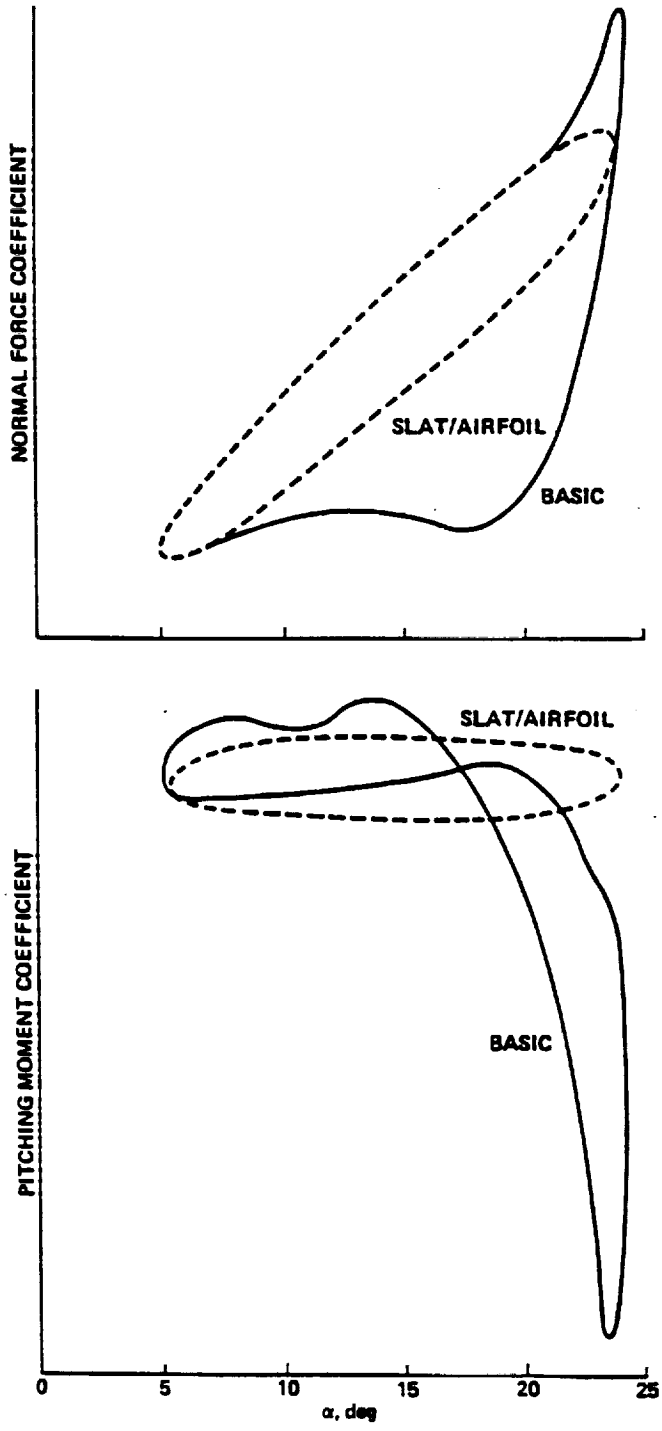

Figure 2.- Lift and moment measurements on the basic and slatted VR-7 airfoils at $k = 0.15$, $\alpha = 15^{o} + 10^{o} \sin \omega t$, $M_{\infty} = 0.185$ and $Re = 2.5 \times 10^{6}$.

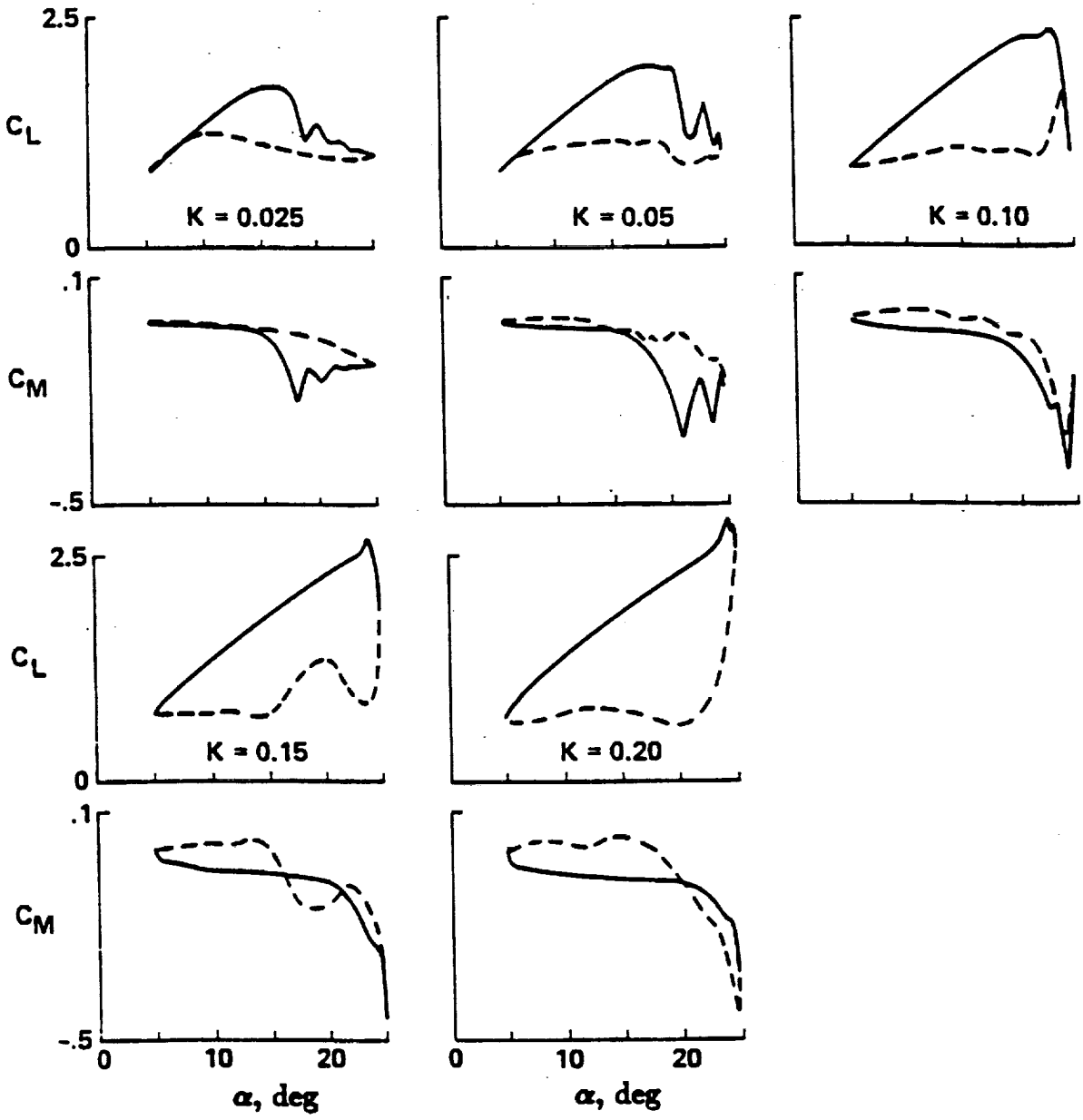

Figure 3.- Lift and moment coefficients for the basic VR-7 airfoil over a range of frequencies at $\alpha = 15° + 10° \sin \omega t$. Dashed lines indicate decreasing α.

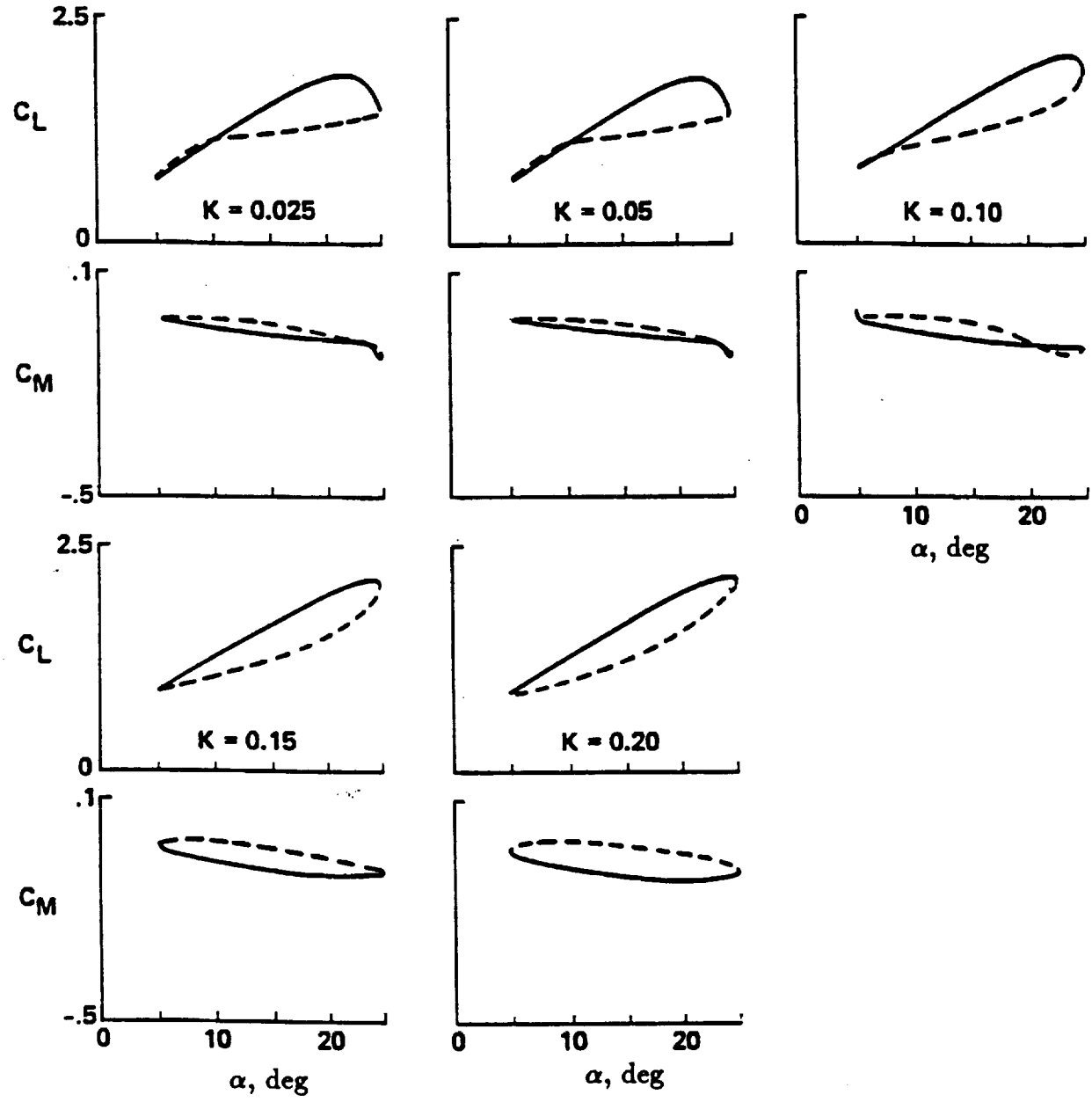

Figure 4.- Lift and moment for the VR-7 airfoil with slat for $\alpha = 15^o + 10^o \sin\ \omega t$, $M_\infty = 0.185$, $Re = 2.5 \times 10^6$ and a range of frequencies. Dashed lines indicate decreasing α.

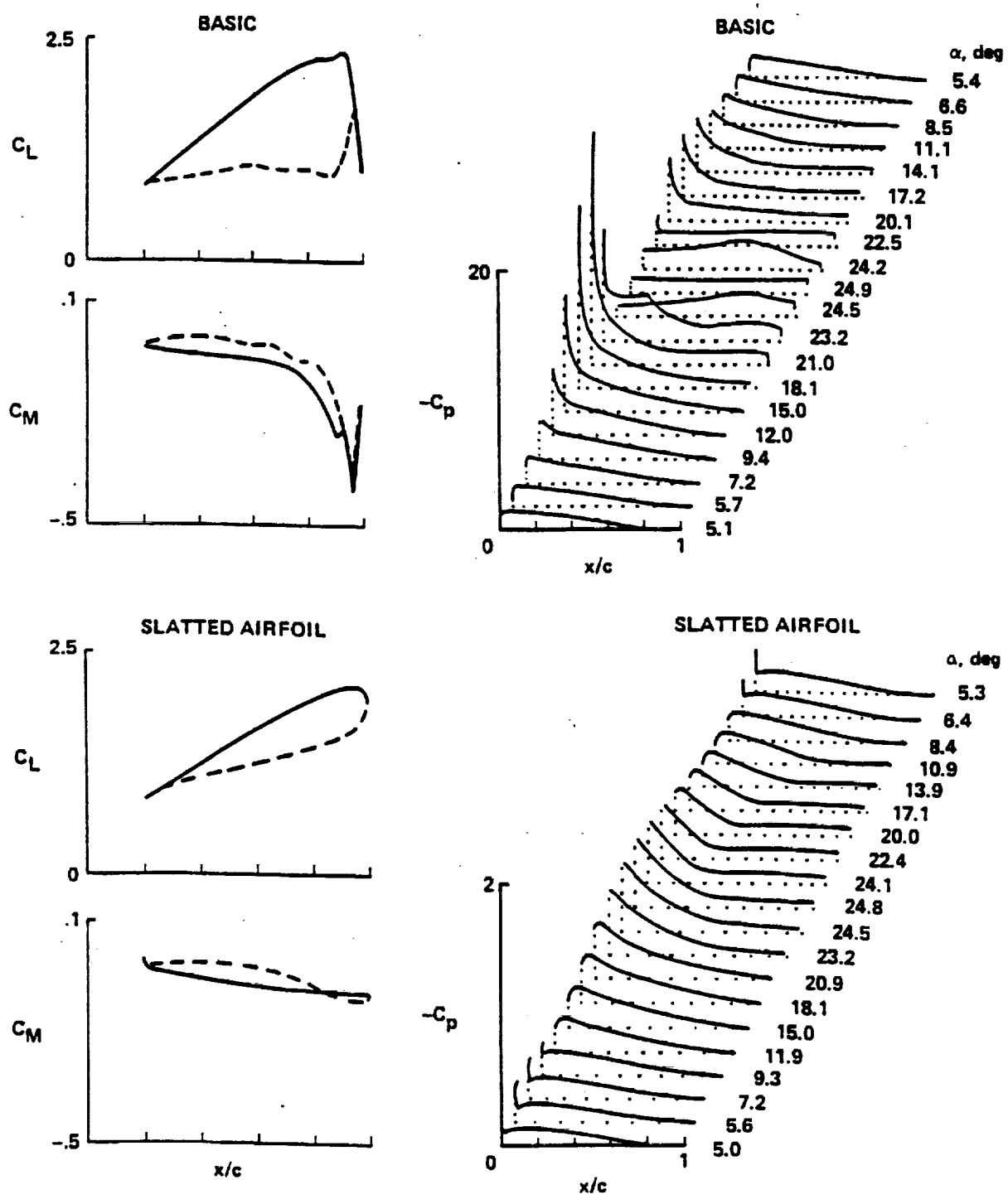

Figure 5.- Lift, moment and pressure for the basic and slatted VR-7 airfoils for $\alpha = 15^\circ + 10^\circ \sin\ \omega t$, $k = 0.1$, $M_\infty = 0.185$ and $Re = 2.5 \times 10^6$. Dashed lines indicate decreasing α.

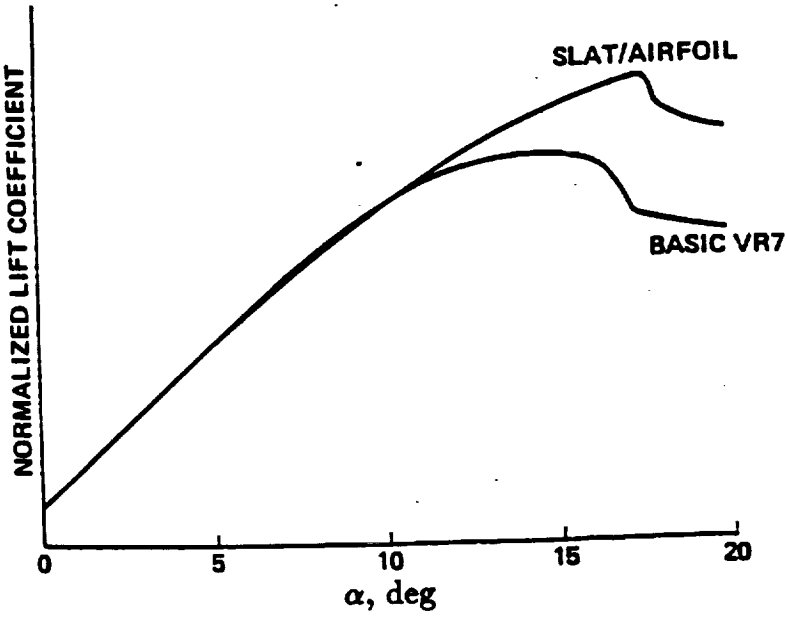

(a) Quasi-static lift.

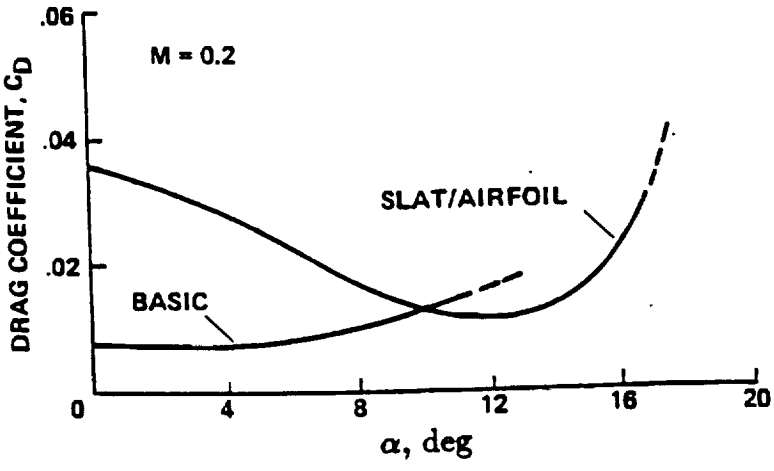

(b) Wake drag.

Figure 6.- Lift and drag measurements for the basic and slatted VR-7 airfoils a $M_\infty = 0.185$ and $Re = 2.5 \times 10^6$.

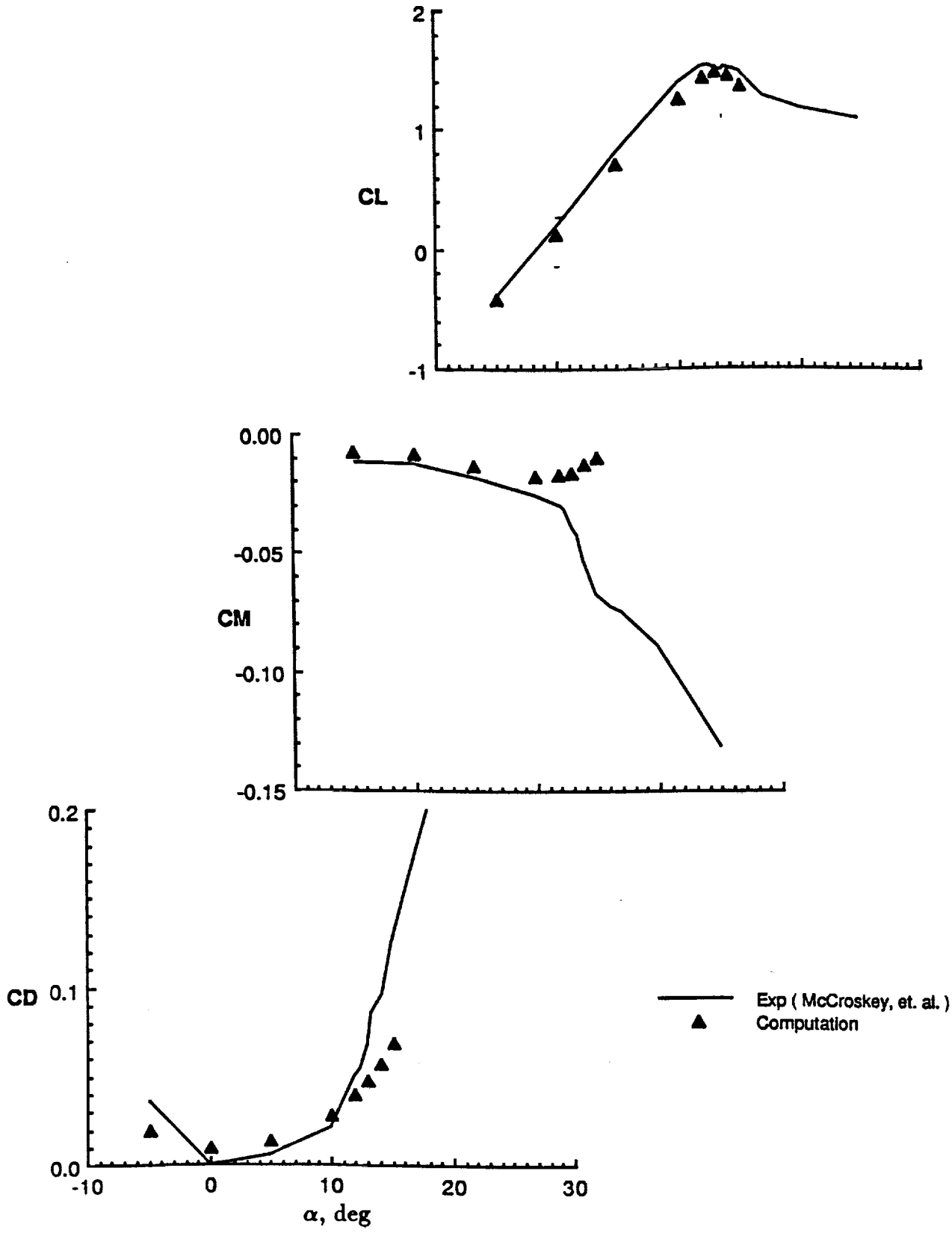

Figure 7.- Force and moment calculations for the basic VR-7 airfoil at $M_\infty = 0.3$ and $Re = 4.2 \times 10^6$.

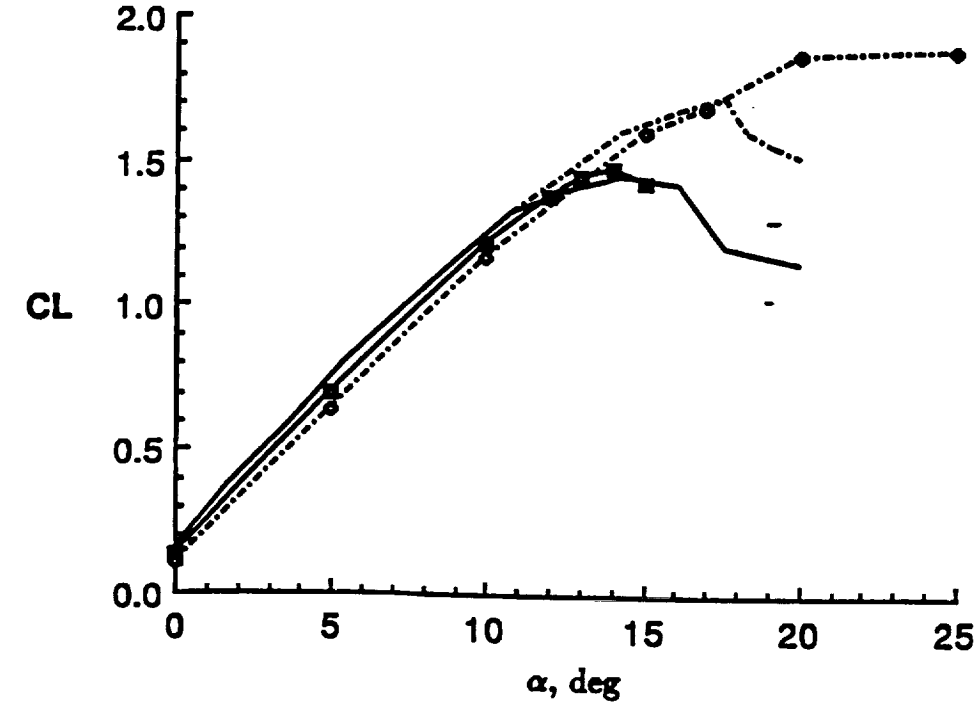

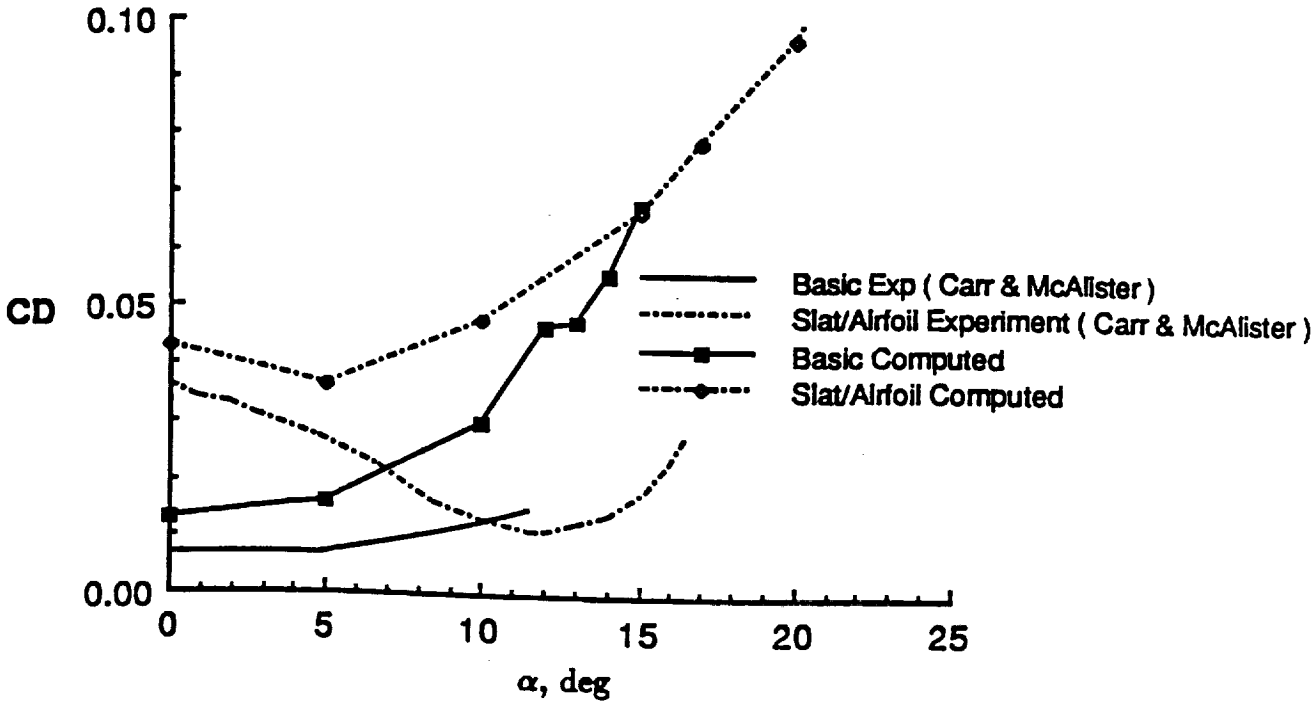

Figure 8.- Lift and drag on the basic and slatted VR-7 airfoils at $M_\infty = 0.185$ and $Re = 2.5 \times 10^6$.

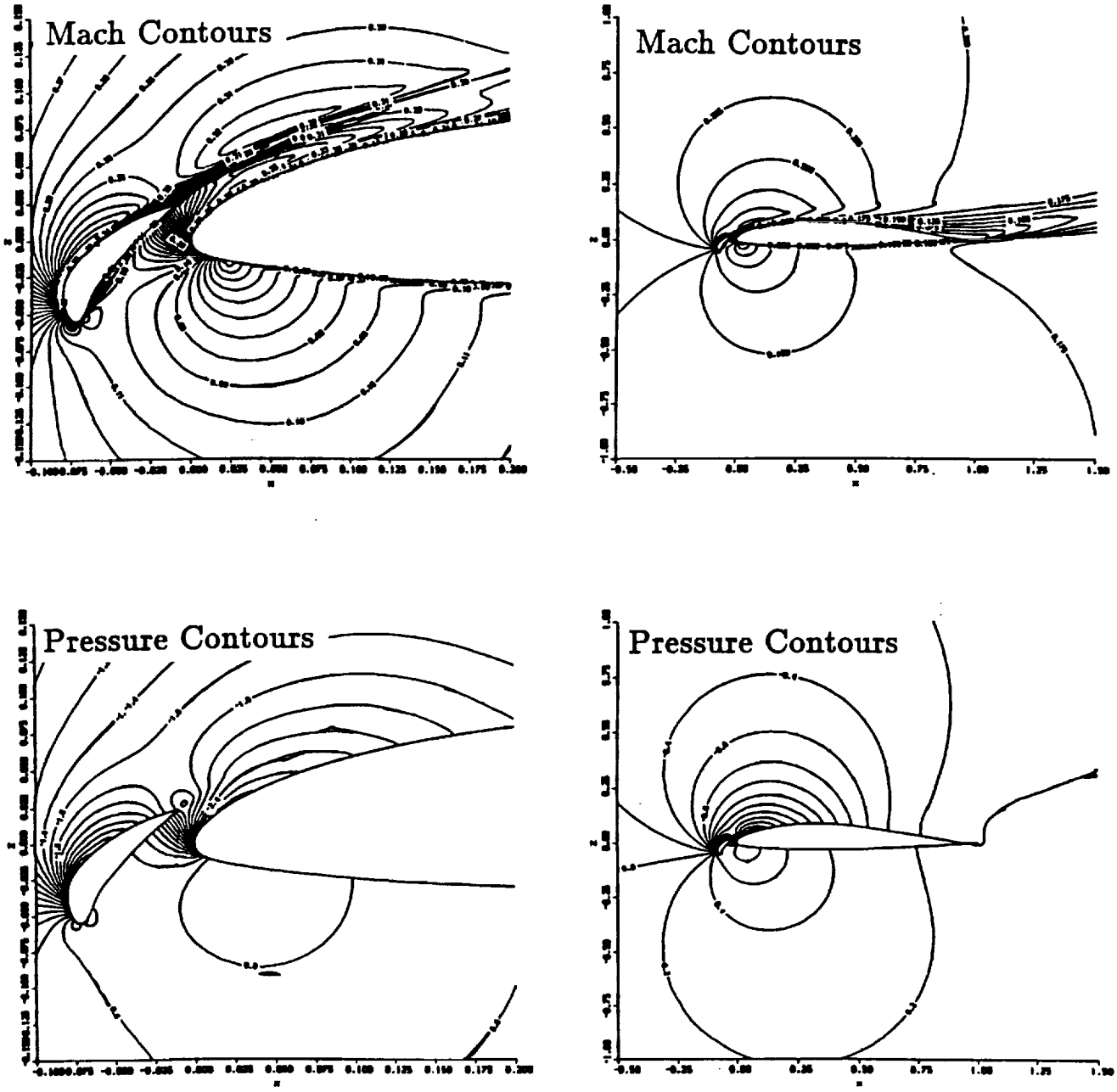

Figure 9.- Calculated Mach and pressure contours around the VR-7 airfoil with slat at $\alpha = 15^o$, $M_\infty = 0.185$ and $Re = 2.5 \times 10^6$.

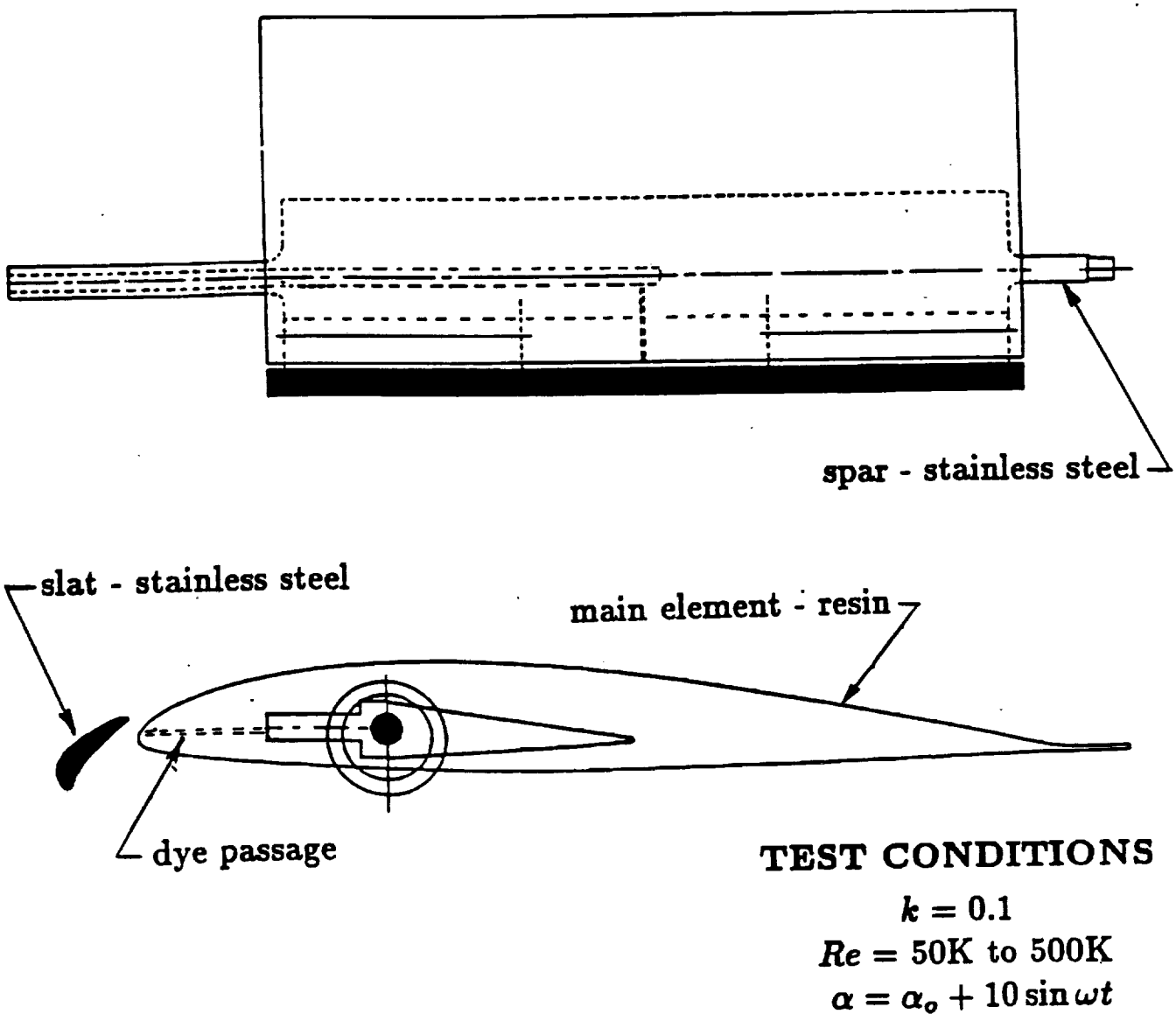

Figure 10.- Water-tunnel model of the VR-7 airfoil with slat.

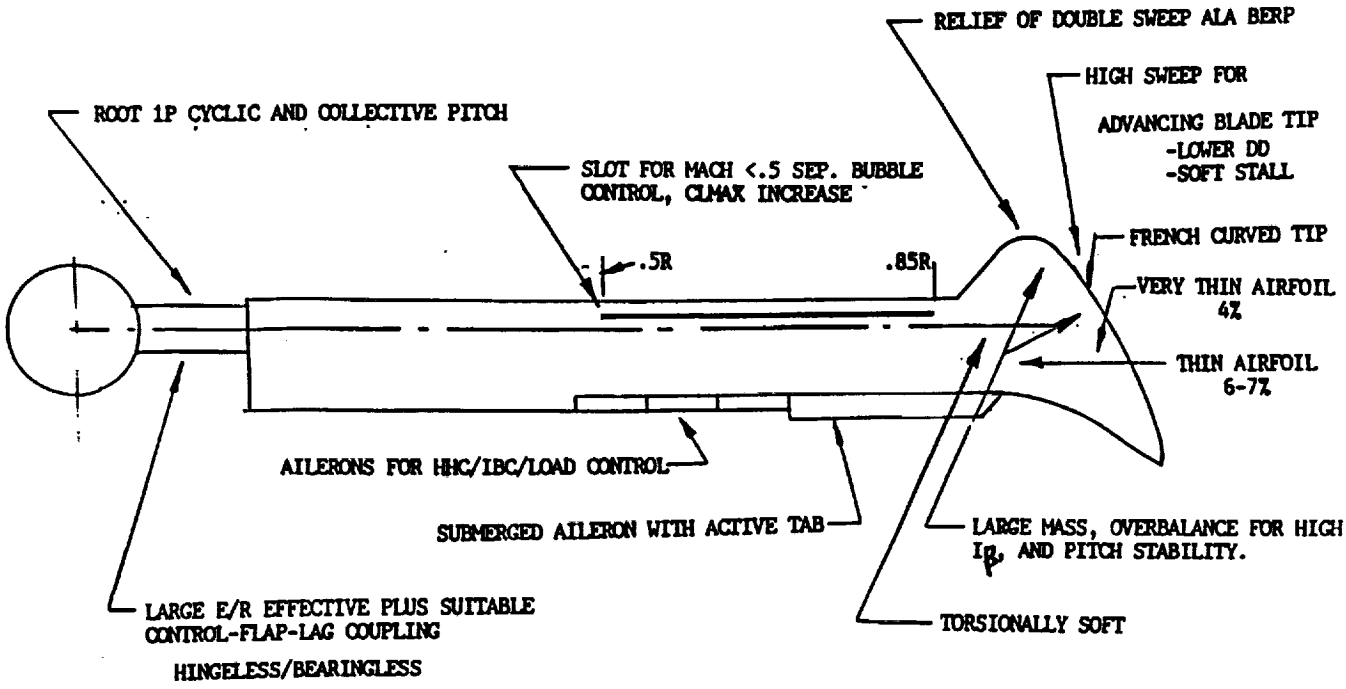

NON-LINEAR TWIST
-FOR GOOD FM
-REDUCE NEG ANGLE @ 90

HIGH CLMAX
HIGH MAX. LIFT MOMENT @ 270
HIGH LIFT MOMENT/β
INTEGRATED FLAP DAMPING

HIMARCS ROTOR
SPECULATIVE PROJECTION

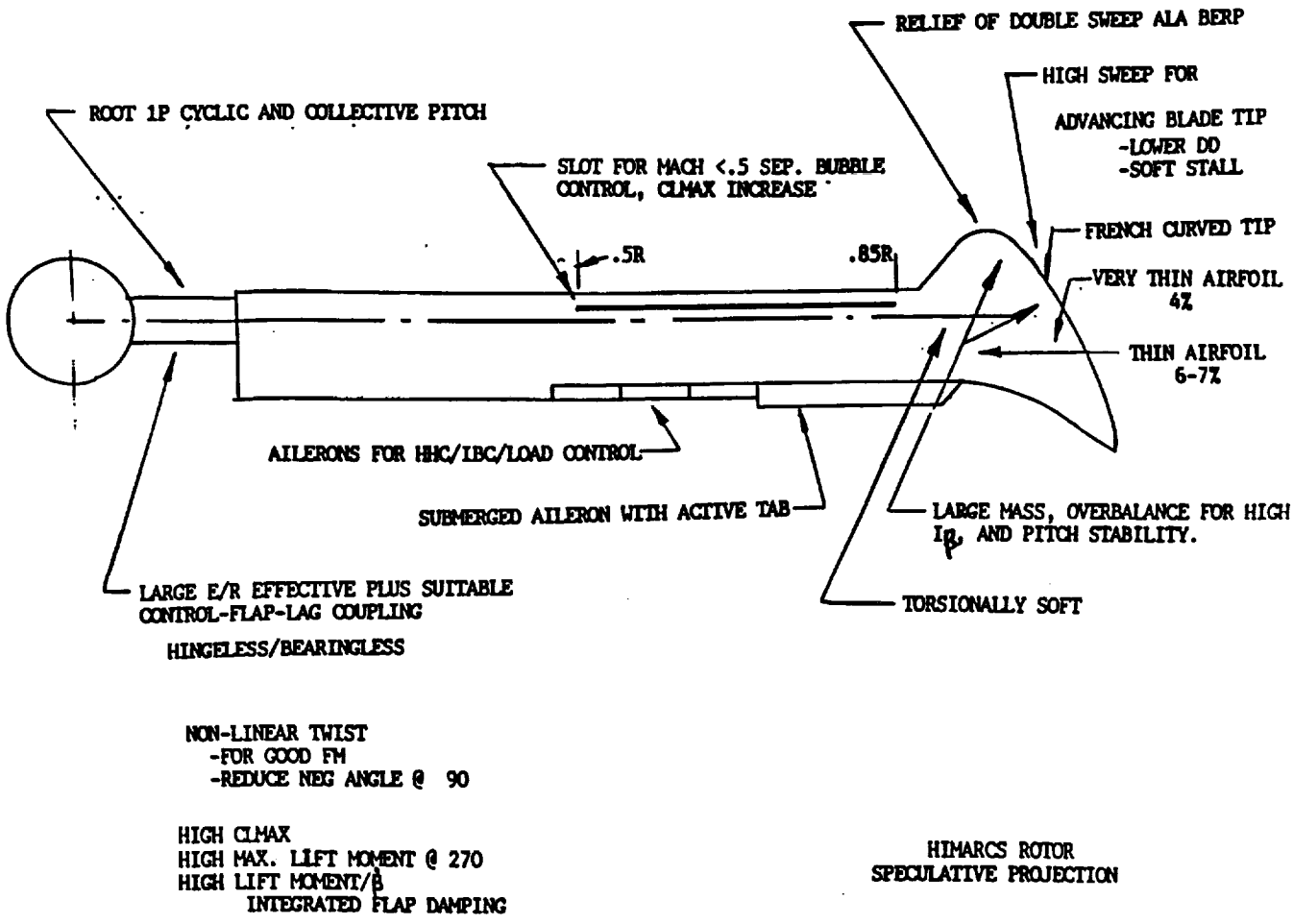

Figure 11.- Wide range of high-lift and control devices considered in HIMARCS.

Mechanisms of Flow Control with the Unsteady Bleed Technique

D.R.Williams, M.Acharya and J.Bernhardt

Fluid Dynamics Research Center
Illinois Institute of Technology
Chicago IL 60616

Introduction

The unsteady bleed technique (a.k.a. internal acoustic forcing) has been shown to be an effective method for control of separation on low Reynolds number airfoils, blunt-end cylinders aligned axially with the flow, cylinders aligned perpendicular to the flow and forebody geometries at high angles of attack. In many of these investigations, the mechanism for the control has been attributed to enhancement of the shear layer (Kelvin-Helmholtz) instability by the unsteady component of the forcing. However, this is not the only possible mechanism, nor may it be the dominant mechanism under some conditions. In this work it is demonstrated that at least two other mechanisms for flow control are present, and depending on the location and the amplitude of the forcing, these may have significant impact on the flow behavior.

Experiments were conducted on a right-circular cylinder with a single unsteady bleed slot aligned along the axis of the cylinder. The effects of forcing frequency, forcing amplitude and slot location on the azimuthal pressure distribution were studied. The results suggest that a strong vortical structure forms near the unsteady bleed slot when the slot location is upstream of the boundary layer separation point. The structure is unsteady, since it is created by the unsteady forcing. The "vortex" generates a sizeable pressure spike (Cp = -3.0) in the time-averaged pressure field immediately downstream of the slot. In addition to the pressure spike, the boundary layer separation location moves farther downstream when the forcing is activated. Delay of the separation is believed to be a result of enhancing the Kelvin-Helmholtz instability. When forcing is applied in a quiescent wind tunnel, a weak low-pressure region forms near the slot that is purely the result of the second-order streaming effect.

Background

Sigurdson and Roshko(1985) used an acoustic driver to excite the axisymmetric shear layer and separation bubble formed at the blunt end of a cylinder aligned axially with the flow. They identified two fundamentally different mechanisms by which the unsteady forcing modified the flow. In the first mechanism the unsteady forcing enhanced the Kelvin-Helmholtz instability in the separating shear layer. A second mechanism involved forcing at wavelengths comparable to the separation bubble height, which enhanced a "shedding" type of instability for the entire bubble.

Huang, Maestrello and Bryant (1987) demonstrated the effectiveness of internal acoustic forcing as a flow control technique for reattaching the separated boundary layer on a low Reynolds number airfoil at high angles of attack. Their unsteady bleed slot was located near the leading edge of the airfoil. They found that lift was enhanced and stall was delayed when the separating shear layer was perturbed by sound at frequencies comparable to those found in the shear layer.

Williams and Economou (1987) used unsteady bleed to control the Karman vortex formation behind a circular cylinder at Reynolds number 370. This work was extended by Williams and Amato (1988 a,b). The unsteady bleed was shown to generate a low pressure region near the body and momentum was added to the flow by the second-order streaming effect.

In another experiment on an airfoil, Huang, Bryant and Maestrello (1988) showed spectral evidence that the wake structure responded to the excitation frequency when the unsteady bleed slot was located near the trailing edge of the airfoil. In this case the most effective frequency was near the vortex shedding frequency. The control mechanism was attributed to the generation of large-scale vortical structures which enhanced entrainment and modified the pressure recovery region.

Williams, et al. (1989) used the unsteady bleed technique to control the forebody vortex formation around slender cone-cylinder bodies at high angles of attack. With the correct forcing conditions it was possible to eliminate the strong forebody vortex and convert the asymmetric velocity field to a symmetric velocity field. In this case, the forebody vortex is steady, so there is no natural frequency to scale the control. Therefore, the control mechanism was attributed to a direct modification of the mean flow. In particular, the rectified pressure field and the momentum addition by the streaming effect were believed to be the controlling factors.

Hsiao, et al (1989) showed that the flow around airfoils and cylinders could be influenced by forcing through a slot aligned with the cylinder axis or airfoil span. They found that the forcing was most effective when placed near the separation line. As in other experiments on airfoils and cylinders, the data indicated a sensitivity to

forcing frequency. This provided evidence that the unsteady component of the forcing enhanced entrainment and delayed separation. However, their pressure measurements on a cylinder showed a relatively large pressure spike near the unsteady bleed slot that could not be explained by enhanced entrainment.

We became interested in the nature of this pressure spike, because it represented a large percentage of the modified pressure field. The following experiment was designed to explore the mechanisms by which the unsteady bleed technique modified the flow.

Experimental Arrangement

The tests were conducted on a 6.35 cm diameter cylinder mounted vertically in an open return wind tunnel. The cross section of the wind tunnel was 40 cm by 61 cm. End plates were placed 41 cm apart, which gave an aspect ratio of 6.4 for the cylinder. The unsteady bleed forcing was generated by a 30 cm diameter loudspeaker mounted on top of the wind tunnel and connected by a pipe to the interior of the cylinder. The loudspeaker was driven by a 60 Watt Dynaco amplifier and a Hewlett-Packard 3311A function generator. Measurements of the pressure inside the cylinder showed the pressure fluctuation to be sinusoidal. The power delivered to the speaker by the amplifier was measured with an r.m.s. voltmeter and ammeter. Although the power varied with amplitude and frequency, it was always less than 25 Watts.

A schematic of the cylinder and the forcing arrangement is shown in Figure 1. The slot was 8 cm long and 0.1 cm wide and was centered along the span of the cylinder. Because the slot is the only opening in the forcing system, there is no net mass addition to the flow over the forcing cycle. For one half of the cycle fluid was ejected from the cylinder, then during the suction phase of the cycle fluid was drawn back in to the cylinder.

Results

In order to quantify the amplitude of the unsteady bleed disturbance, both velocity measurements and sound pressure level (SPL) measurements were made next to the slot in the cylinder wall with no external flow. The hot-wire anemometer probe was placed in the exit plane of the slot. Although the hot-wire experiences reverse flow during the suction side of the forcing cycle, the reverse flow signal was distinct from the outflow phase of the cycle, so the signal could be correctd. The r.m.s. velocity fluctuation level computed for this signal is shown in Figure 2a as a function of the frequency at different r.m.s. voltage levels applied to the loudspeaker. The data show that the r.m.s. velocity level does not increase monotonically with the forcing frequency. At lower voltage amplitudes to the speaker, the r.m.s. velocity decreases as the frequency is increased from 20 Hz to

120 Hz.

The sound pressure level was measured under the same forcing conditions with a B&K sound pressure level meter placed perpendicular to the exit plane of the slot. The data shown in Figure 2b have a monotonic increase with frequency from 20 Hz to 240 Hz.

The differences in the trends with increasing frequency allow us to separate the effect of the SPL from the velocity fluctuations. The data presented in Figure 3 show the pressure distribution around the azimuth of the cylinder at two different forcing frequencies 40 Hz and 140 Hz where the r.m.s. voltage of the speaker was kept constant at 2.0 volts r.m.s. The freestream speed was 5.27 m/s. Although the effect of the forcing produces a significant change in the pressure distribution, it is clear that very little difference occurred between the two pressure distributions. From Figures 2a and 2b we see that the velocity amplitude decreases slightly from 6.0 m/s to 5.5 m/s, while the SPL increases from 95 dB to 106 dB at the corresponding forcing conditions. It is apparent from this comparison that the control effect follows the behavior of the velocity fluctuations more closely than the SPL. It is highly unlikely that sound plays a significant role in the flow control mechanism.

Effect of Forcing on Azimuthal Pressure Distribution

The term "acoustic forcing" implies that the control mechanism occurs by a linear wave process. However, the following results indicate that this is not the case. Figure 4 shows pressure measurements taken with forcing at 240 Hz, SPL at 121 dB and the r.m.s. velocity fluctuation level at 14 m/s, but with *no flow* in the wind tunnel. (The pressure coefficient has been normalized in this plot by a dynamic pressure of 0.06694 in. w.c. for comparison with the other data.) It is clear that the mean pressure field around the slot is lower than the ambient pressure. This is a nonlinear effect resulting from the rectification of the unsteady pressure signal, and is analogous to the streaming phenomenon. A discussion of the rectification effect can be found in the paper by Williams and Amato (1988b).

The disturbances created by the loudspeaker must couple somehow with the flow field to create the vortical disturbances that enhance entrainment and delay separation. The r.m.s. velocity fluctuation level associated with a 120 dB sound wave is only 0.05 m/s. In contrast, the velocity fluctuation measured by the hot-wire anemometer is three orders of magnitude larger than the velocity associated with the sound wave. Such a large velocity fluctuation could only come from the "pumping" of fluid by the displacement of the loudspeaker cone. We believe this is the primary source of the vortical disturbance, not the acoustic field.

The azimuthal pressure distributions obtained with the slot positioned at -30^{o}, 30^{o}, 45^{o}, 75^{o} and 110^{o} from the forward stagnation line are shown in Figure 5, corresponding to a freestream speed of 5.27 m/s. The forcing conditions are the

same in all cases, frequency 240 Hz and r.m.s velocity 14 m/s. The most obvious feature is the large pressure spike associated with the forcing slot. The change in Cp from the undisturbed value is approximately $\Delta Cp = -2.5$ at the first pressure tap downstream of the slot. This is followed by a steep increase and overshoot in pressure at the next two pressure taps. We believe this is the time-averaged signature of a periodic vortex-like disturbance generated by the interaction of the unsteady forcing field with the flow around the cylinder. We suspect that the "vortex" forms during the suction phase of the forcing cycle, then is "released" during the ejection phase, although this is still being investigated. Provided the unsteady bleed slot is upstream of the separation point, the pressure spike has the same shape, irrespective of the slot location. The same behavior is likely to occur with unsteady bleed control applied to airfoils upstream of separation. If such strong localized pressure spikes can be formed by the forcing alone, then substantial changes in airfoil performance are possible.

Figure 5e shows that when the forcing slot is beyond the separation point, then the large pressure spike does not form. The flow across the slot in the separated region is too slow for the interaction with the forcing flow to produce a strong "vortex". However, the pressure distribution between $\Theta = 70^{o}$ and 125^{o} indicates that separation was delayed. In this situation we believe that the flow control mechanism is by enhanced Kelvin-Helmholtz instability (K-H effect) described by other investigators. The K-H effect can be seen in each case shown in Figure 5. It is quite interesting that the pressure modification appears to be the superposition of the pressure spike at the slot location and the K-H effect. This observation supports the notion that these control mechanisms are fundamentally different mechanisms.

Conclusions

The unsteady bleed technique and internal acoustic forcing are synonyms for the same localized flow control technique. Measurements of the sound pressure level and the r.m.s. velocity amplitude at the slot have shown that the dominant disturbance is associated with the "pumping" of fluid by the loudspeaker, not the acoustic wave.

Pressure distributions obtained around the cylinder show three independent mechanisms are present that modify the flow. The weakest is the "streaming" effect created by the rectification of the unsteady pressure field at the bleed slot. This is likely to be insignificant in most cases unless the forcing amplitude is very strong. The second mechanism is a strong "vortex-like" disturbance created by the interaction between the forcing flow and the flow around the body. This resulted in a very strong pressure spike immediately downstream of the slot. The third mechanism is the enhancement of the Kelvin-Helmholtz instability in the separating shear layer, which produced a change in the pressure field slightly weaker than the

pressure spike.

The latter two mechanisms will likely be present on all types of bodies in which the unsteady bleed technique is applied. The relative importance of the two will depend on the details of the forcing configuration, such as the location of the bleed slot and the forcing amplitude.

Acknowledgements

Special thanks go to Z. Grabavac and S. Mitus for their expert design and construction of the model and for their preliminary experiments. This experiment was conducted with the support of the Air Force Office of Scientific Research under contract F49620-86-C-0133, monitored by Capt. H Helin and Dr. J. McMichael.

References

Huang, L.S., Maestrello, L. and Bryant, T.D. 1987 "Separation Control Over an Airfoil at High Angles of Attack by Sound Emanating from the Surface", AIAA paper no. 87-1261, presented at 19th Fluid Dynamics, Plasma Dynamics and Lasers Conf. Honolulu, HA.

Huang, L.S., Bryant, T.D. and Maestrello, L. 1988 "The Effect of Acoustic Forcing on Trailing Edge Separation and Near Wake Development of an Airfoil", AIAA paper no. 88-3531-CP, presented at 1st National Fluid Dynamics Cong. Cincinnati, OH.

Hsiao, F.B. Liu, C.F. and Shyu,J.Y. 1989 "Control of Wall-Separated Flow by Internal Acoustic Excitation", AIAA paper 89-0974, presented at 2nd Shear Flow Control Conf., Tempe AZ.

Sigurdson, L.W., and Roshko, A. 1985 "Controlled Unsteady Excitation of a Reattaching Flow", AIAA paper no. 85-0552, presented at Shear Flow Control Conf., Boulder CO.

Williams, D.R. and Amato, C.W. 1988a "Unsteady Pulsing of Cylinder Wakes", AIAA paper 88-3532-CP, presented at 1st National Fluid Dynamics Cong. Cincinnati, OH.

Williams, D.R. and Amato, C.W. 1988b "Unsteady Pulsing of Cylinder Wakes", Frontiers in Experimental Fluid Mechanics (ed. M. Gad-el-Hak) Lecture Notes in Engineering, Vol. 46.

Springer.

Williams, D.R., El-Khabiry, S. and Papazian, H. 1989 "Control of Asymmetric Vortices around a Cone-Cylinder Geometry with Unsteady Base Bleed", AIAA paper 89-1004, presented at 2nd Shear Flow Conf. Tempe, AZ.

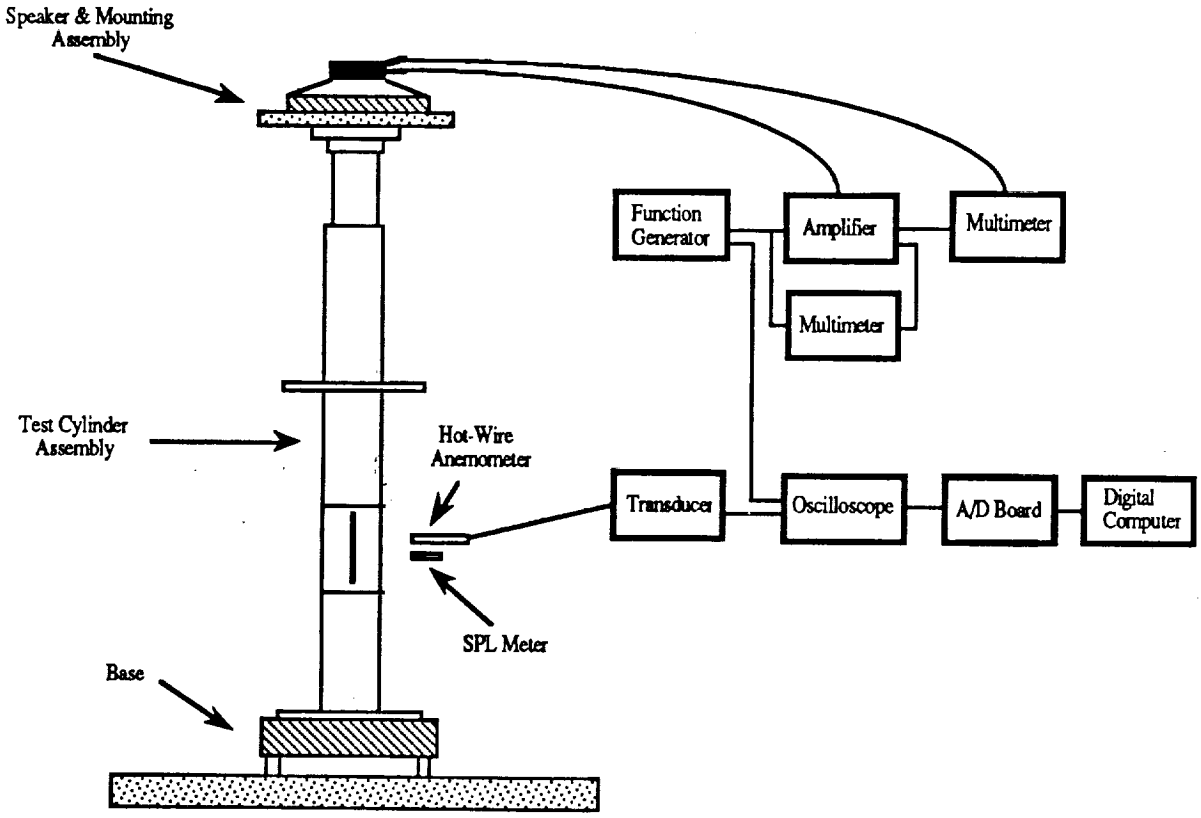

Figure 1 - Schematic of the cylinder and unsteady bleed apparatus.

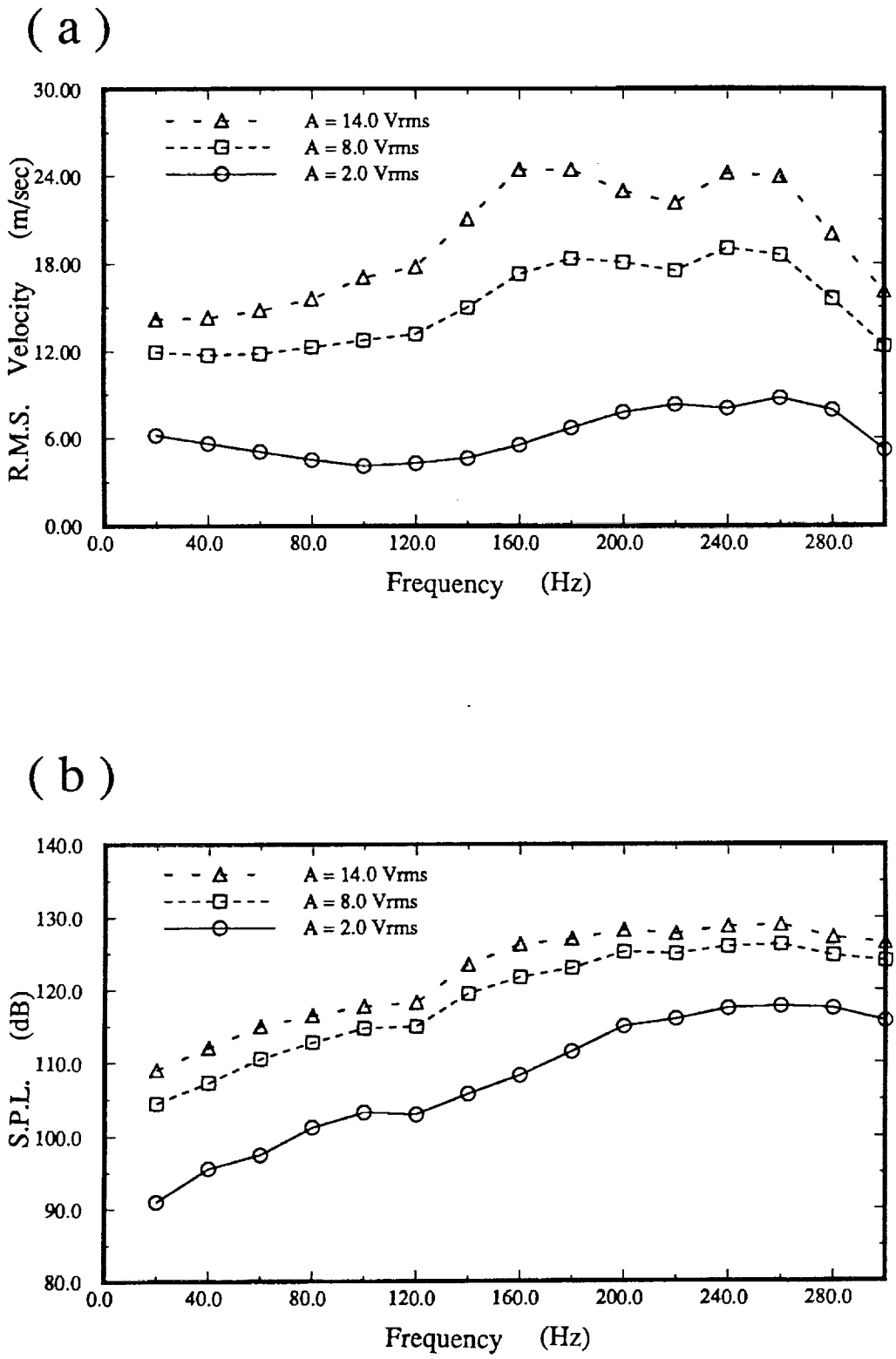

Figure 2 - (a) r.m.s. velocity at the exit of the slot with different forcing frequencies and voltages. (b) Sound pressure level at the exit of the slot for the same forcing conditions in (a).

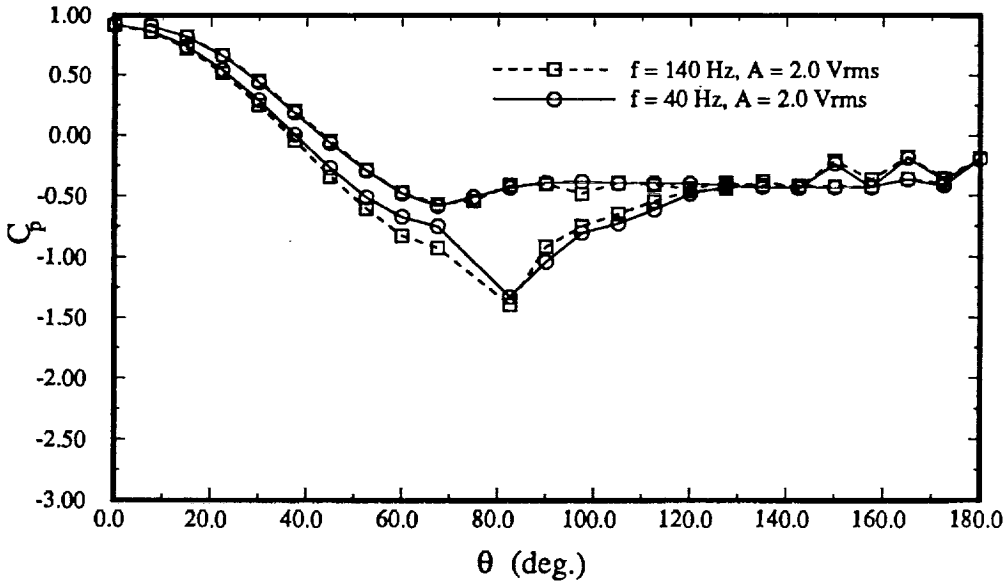

Figure 3 - Comparison of the azimuthal pressure distribution with two different forcing frequencies, 40 Hz and 140 Hz.

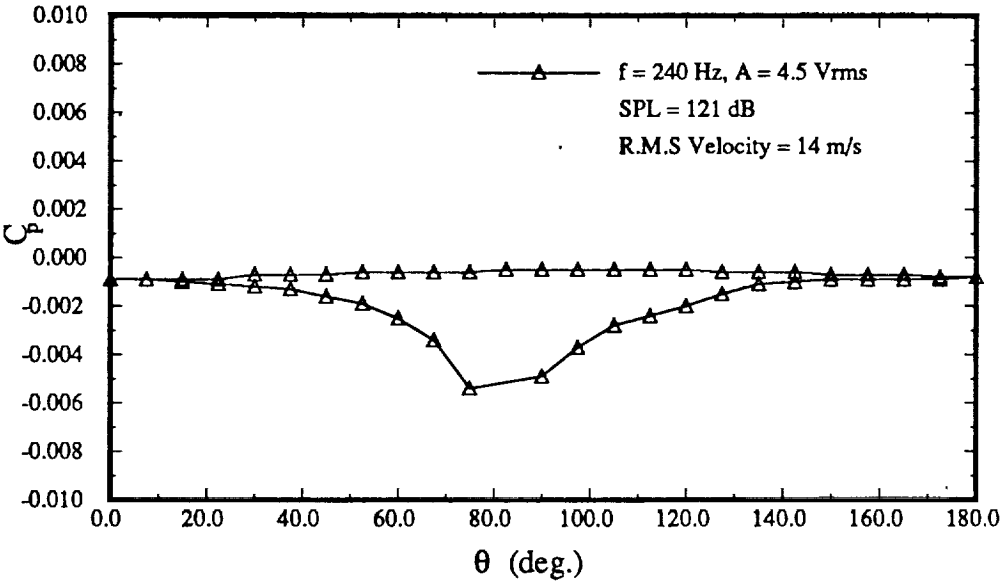

Figure 4 - Azimuthal pressure distribution obtained with no external flow in the wind tunnel. Forcing frequency 240 Hz, r.m.s. velocity 14 m/s.

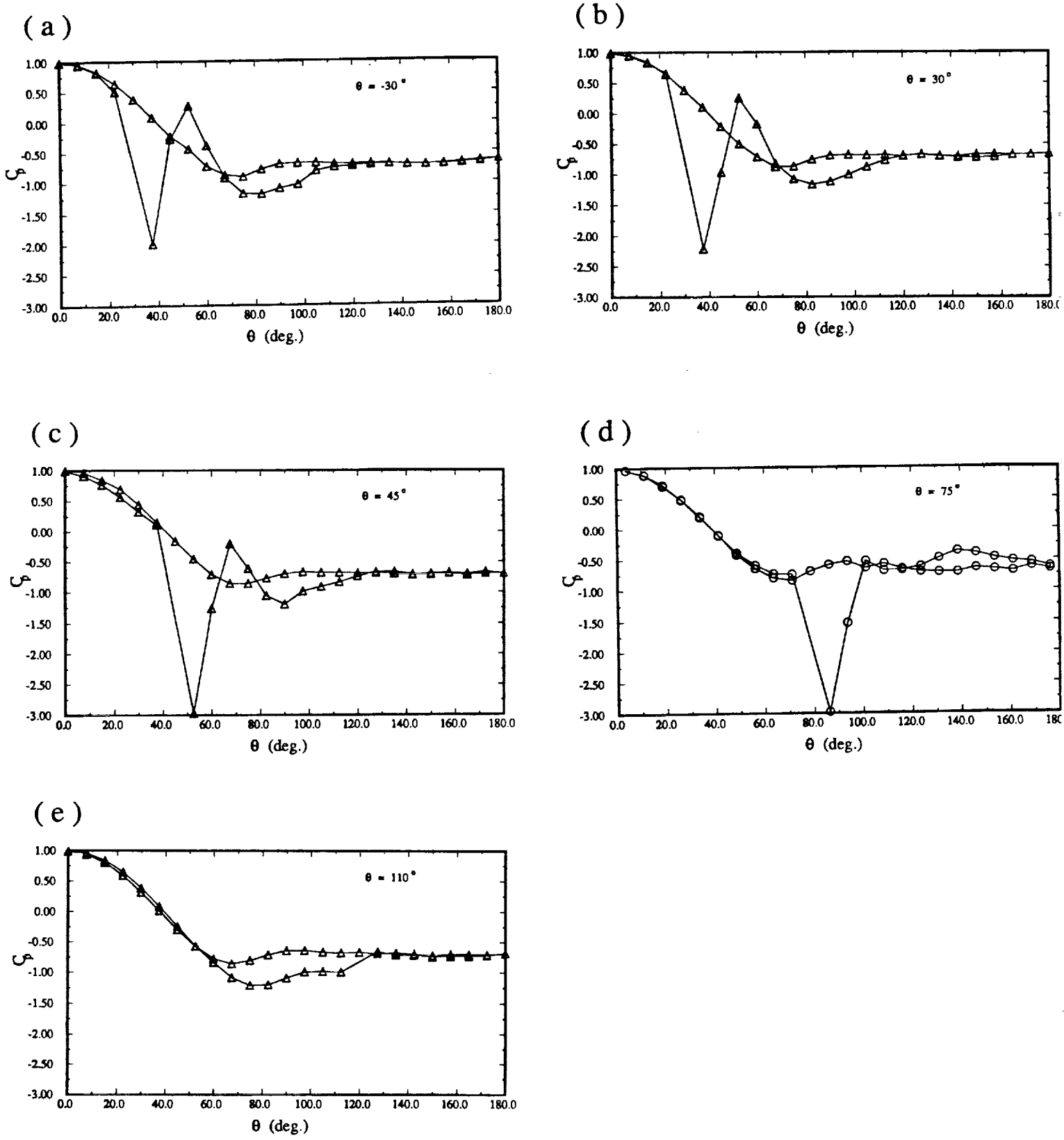

Figure 5 - Pressure distributions obtained with the unsteady bleed slot located at Θ = -30°, 30°, 45°, 75° and 110°. Forcing frequency 240 Hz, r.m.s. velocity 14 m/s.

Conclusions

Unsteady bleed and internal acoustic forcing are synonyms for the same phenomenon.

Acoustic effects are insignificant in this type of control.
The effects of forcing scale with the velocity fluctuation level, not the SPL.

The second-order "streaming" effect is present, but insignificant.

The forcing flow interacts with the external flow to produce a localized, large-amplitude pressure spike.

The effects of enhanced K-H instability appear to be present.
Measurements of the velocity spectrum are required.

Concepts and application of dynamic separation for agility and super-maneuverability of aircraft-an assessment.

Peter Freymuth, University of Colorado, Boulder, CO 80309-0429

1. Introduction

Aims for improvement of fighter aircraft pursued by the unsteady flow community are high agility[1] (the ability of the aircraft to make close turns in a low-speed regime) and super maneuverability[2] (the ability of the aircraft to operate at high angles of attack in a post stall regime during quick maneuvers in a more extended speed range). High agility requires high lift coefficients at low speeds in a dynamic situation and this requirement can be met by dynamically forced separation or by quasistatic stall control. The competing methods will be assessed based on the known physics. Maneuvering into the post stall regime also involves dynamic separation but because even fast maneuvers involving the entire aircraft are "aerodynamically slow" the resulting dynamic vortex structures should be considered "elicited" rather than "forced". More work seems to be needed in this area of elicited dynamic separation.

2. Dynamic separation as a vortex phenomenon

Everyone who visualizes flow around airfoils in rapid maneuvers quickly realizes that separation foremost means vorticity separation from various points of the lifting surface, i.e., from leading edge, trailing edge and other surface points. As a consequence physical understanding is mainly approached from the vorticity point of view[3] and is greatly aided by vortex visualization methods[4]. A large body of information on forced dynamic separation has been collected by many experimentalists as previous workshops

on unsteady flow attest to [5, 6]. Many flow configurations and their parameter spaces have been surveyed and are available for assessment.

3. Transient dynamic stall phenomenon (Kramer[7] effect).

The dynamic stall phenomenon of temporary lift augmentation during transient maneuvers of airfoils beyond static stall is interpreted as a diffusive-inertial delay of leading edge vortex development and subsequent convective shedding into the free stream. Unfortunately, the stall vortex gets useless for lift augmentation when shed and a low lift deep stall regime ensues. The time and strength of transient lift augmentation depend considerably on flow configuration and parameter space. Usually the stronger the lift augmentation is, the shorter is the lift augmentation time, which is an unfortunate correlation when applications to agility are considered. Lift augmentation time does not exceed a few times the convection time $t_c = c/U_0$ of the airfoil, where c is the chord length and U_0 is the free stream speed. Since this time is orders of magnitude smaller than the time needed for high lift maneuvers, no decisive advantage can be obtained from the Kramer effect nor is it likely that this will change in the future.

4. Repetitive dynamic stall phenomenon (Harper-Flanigan[8] effect).

If during maneuver time the dynamic stall phenomenon could be rapidly repeated a useful cumulative dynamic stall enhancement of lift could be achieved. This is indeed possible as was first demonstrated by Harper and Flanigan[8] and has since been demonstrated many times[1, 3]. In essence, the airfoil has to be rapidly cycled between stalled and unstalled conditions. For instance, a lift coefficient of 1.8 was achieved by Maresca, et al.[9] by dynamic periodic forcing. Jumper and Stephen[10] have proposed the study of an unsteady-flow airplane based on a dynamic lift augmentation by a factor 1.5.

An area of maneuverability where utilization of repetitive dynamic stall seems to have found its niche is far removed from aircraft application: the hovering flight of insects. According to Freymuth[11, 12] a single airfoil executing appropriate periodic pitch-plunge maneuvers in still air is capable of generating a hover-jet (Fig. 1) with a lift coefficient as high as 7. In these maneuvers stall vortices generate high lift and are discarded into the jet before deep stall sets in. Every half cycle generates a new stall vortex for generation of high lift. Insects seem to use these maneuvers during their hovering flight.

It thus seems that repetitive dynamic stall is a viable means for lift enhancement in principle. It must be judged, however, against competing methods of lift enhancement, which will be assessed in the next section.

5. Stall control-the equivalence of dynamic and static stall control.

An important strategy to circumvent the fleetingness of dynamic stall is to prevent dynamic stall vortex generation during high angle of attack maneuvers while trailing edge separation of starting vortices allows buildup of airfoil circulation to high values for lift generation. This task is essentially the same as the task of static stall control in conventional aircraft by means of flaps, suction, blowing, moving boundaries and turbulators[13, 14] (slats and 3-d vortex generators). The effectiveness of static stall control methods in a dynamic situation has recently been demonstrated by Freymuth[15]. An airfoil with a nose consisting of a rotating cylinder (stall control by a moving boundary) was rapidly pitched from 0° to 50° angle of attack and held (Fig. 2). During and after pitchup a trailing edge stall vortex separated from the airfoil while leading edge vortex generation was inhibited as long as the cylinder was kept rotating. Similar results were obtained for periodic pitching. Therefore, static stall control measures are applicable in a dynamic

Fig. 1
Hover-jet moving upward into a still air environment (from Ref. 11).

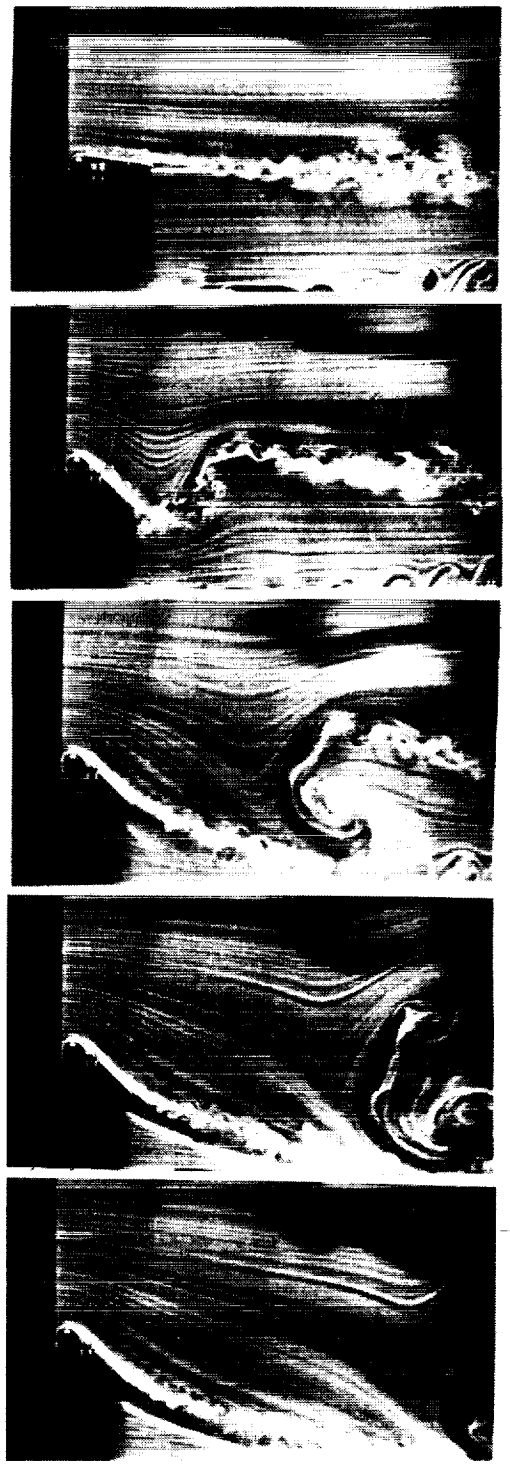

Fig. 2
Stall controlled pitch-down maneuver of an airfoil (from Ref. 15).

situation and represent a viable alternative for lift enhancement in fast maneuvers at low speed (compressibility effects decrease static and dynamic lift enhancement[1]).

Static stall control methods have produced lift coefficients in the range 2 to 6[13, 14]. Oversizing the wings would further increase the lift range capabilities if this need arises in special aircraft and thrust vectoring at near zero speed adds further lift control.

Comparing lift enhancement by dynamic stall methods and by dynamic stall control methods it seems unlikely that the former will outperform the latter in aircraft applications and currently hardly reaches into the same range. The dynamic stall method of lift enhancement therefore hardly represents a crucial development toward the achievement of high agility and even a minor niche for it has yet to be found.

6. Dynamic stall elicitation for super maneuverability

What benefits could post stall maneuvers add to a high agility aircraft? A quick turn of a high agility aircraft can only be realized at a speed low enough to not exceed the g-load limits suitable for pilots. In order to decelerate an aircraft to this low speed and for target pointing post stall maneuvers could still remain attractive. Since force coefficients are not enhanced in such maneuvers they can be initiated at considerably higher speed U_0 than high agility maneuvers without exceeding set g-limits. Since post stall maneuvers are aerodynamically slow, the resulting dynamic vortex structures are not forced but elicited.

From the workshop proceedings[5, 6] it seems that dynamic elicitation has not received detailed attention. This author recommends investigation of elicited vortex structures and their influence on maneuvering control. Such work should entail two-and three-dimensional lifting surfaces and possibly entire aircraft models as has been investigated by Ashworth, et al.[16] in the forced

range. This recommendation amounts to investigating the low dimensionless pitch rate range during entire maneuvers for whichever configuration and associated parameter space appeals to an investigator.

7. Conclusion

Methods of lift enhancement by means of dynamic stall and by means of dynamic stall control have been assessed for application to high agility aircraft. It appears that stall control methods outperform stall enhancement. Therefore dynamic stall cannot play a crucial role in design of high agility aircraft. This is in contrast to helicopter blade and vertical windmill blade design[1] and to insect hovering flight[12] where dynamic stall is of the essence.

The role of dynamic separation in supermaneuvers has also been assessed. Dynamic elicitation in contrast to dynamic forcing of separation seems to be the key and should be investigated.

References

1. Carr, L. W. Dynamic stall progress in analysis and prediction. Paper AIAA-85-1769-CP, 1985.
2. Herbst, W. B. Supermaneuverability.Workshop on Unsteady Separated Flow, U. S. Airforce Academy, August 10-11, 1983, pp. 1-9, 1984.
3. Reynolds, W. C., Carr, L. W. Review of unsteady, driven, separated flows, Paper AIAA-85-0527, 1985.
4. Freymuth, P. Progress in visualizing unsteady separation. Workshop II on Unsteady Separated Flow, U. S. Air Force Academy, CO, July 28-30, 1988, pp. 197-210, 1989.
5. Workshop on Unsteady Separated Flow. U. S. Airforce Academy, CO, August 10-11, 1983.
6. Workshop II on Unsteady Separated Flow, U. S. Airforce Academy, CO, July 28-30, 1988.

7. Kramer, M. Die Zunahme des Maximalauftriebes von Tragfluegeln bei ploetzlicher Anstellwinkelvergroesserung (Boeen Effekt). Zeitschift fuer Flugtecknik und Motorluftschiffahrt, Vol. 23, pp. 185-189, 1932.
8. Harper, P. W., Flanigan, R. E. The effect of change of angle of attack on the maximum lift of a small model. NACA TN-2061, 1950.
9. Maresca, C., Favier, D., Rebont, F. Experiments on an airfoil at high angle of incidence in longitudinal oscillations. J. Fluid Mech., Vol. 92, pp. 671-690, 1979.
10. Jumper, E. F., Stephen, E. F. Toward an unsteady-flow airplane. Paper AIAA-88-0752.
11. Freymuth, P. An unsteady model of animal hovering. Low Reynolds Number Aerodynamics. T. J. Mueller (Editor), Lecture Notes in Engineering, Vol. 54, Springer Verlag, pp. 231-245, 1989.
12. Freymuth P. Thrust generation by an airfoil in hover modes. Experiments in Fluids, Vol. 8, 1990 (in press).
13. Carr, F. E. An aerodynamic comparison of blown and mechanical high lift airfoils. Proceedings of the Circulation Control Workshop, Feb. 19-21, 1986, pp. 449-447, NASA Ames.
14. Nichols, F. H., Harris, M. J. Fixed wing CCW Aerodynamics with and without supplementary thrust deflection. Proceedings of the Circulation Control Workshop, Feb. 19-21, 1986, pp. 479-489, NASA Ames.
15. Freymuth P. Toward Dynamic separation without dynamic stall. Experiments in Fluids, Vol. 7, pp. 187-196, 1989.
16. Ashworth, F., Mouch, T. and Luttges, M. Application of forced unsteady aerodynamics to a forward swept wing X-29 model. Paper AIAA-88-0563, 1988.

DYNAMIC
STALL
CONTROL

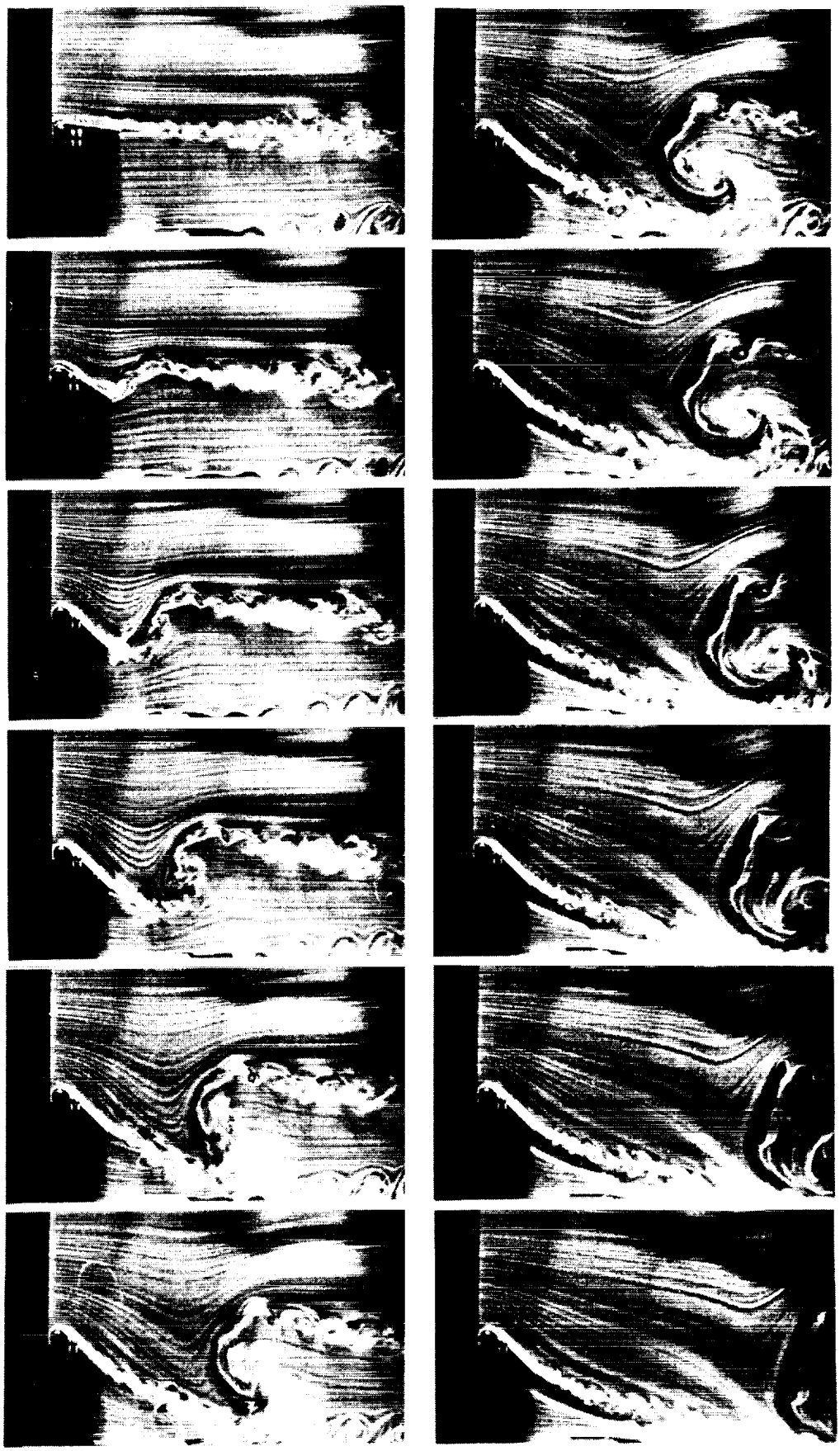

N94-34989

Effect of Initial Acceleration on the Development of the Flow Field of an Airfoil Pitching at Constant Rate

M. M. Koochesfahani, V. Smiljanovski, and T. A. Brown

Michigan State University

Introduction

We present results from a series of experiments where an airfoil is pitched at constant rate from 0 to 60 degrees angle of attack. It is well documented (e.g. references 1-4) that the dynamic stall behavior of such an airfoil strongly depends on the nondimensional pitch rate $K = \dot{\alpha}C/(2U_\infty)$, where C is the chord, $\dot{\alpha}$ the constant pitch rate, and U_∞ the free stream speed. In reality, the actual motion of the airfoil deviates from the ideal ramp due to the finite acceleration and deceleration periods imposed by the damping of drive system and response characteristics of the airfoil (see Figure 1). It is possible that the pitch rate alone may not suffice in describing the flow and that the details of the motion trajectory before achieving a desired constant pitch rate may also affect the processes involved in the dynamic stall phenomenon. We note that the flux of vorticity for attached flow at the airfoil surface, $(\partial\omega/\partial y)_s$, is given by [5]

$$\nu \left(\frac{\partial \omega}{\partial y}\right)_s = \frac{1}{\rho}\left(\frac{\partial p}{\partial x}\right)_s + \frac{\partial U_s}{\partial t}$$

The details of the acceleration phase may, therefore, modify the surface vorticity flux by altering the time-varying surface pressure gradient $(\partial p/\partial x)_s$, and also directly through the surface acceleration term $(\partial U_s/\partial t)$.

To our knowledge, a systematic investigation of the effects of acceleration/deceleration periods on dynamic stall characteristics of nominally constant pitch rate motions has not been reported. Studying these effects should give further insight into the processes of vorticity generation and accumulation on unsteady surfaces. The study is expected to also provide clues to how these processes may be modified/controlled by the deliberate shaping of the pitch motion trajectory. Practical applications of the study are to be noted since in real devices infinite (i.e. extremely large) acceleration/deceleration is neither possible nor

desirable.

In the present experiments, we investigate the effects of acceleration and deceleration periods by systematically varying the acceleration magnitude and its duration through the initial acceleration phase to constant pitch rate. The magnitude and duration of deceleration needed to bring the airfoil motion to rest are similarly controlled. Our preliminary results indicate that the elapsed time (from start of motion) until the first indication of leading edge separation is affected by the acceleration period; the airfoil angle of attack where leading edge separation occurs is, however, practically unchanged. Many of the details of the dynamic stall vortex formation and its interactions appear to be also insensitive to the details of the acceleration period for the range of parameters studied so far. We provide a scaling argument for the acceleration period which may explain the insensitivity of the angle of attack for leading edge separation observed here. This scaling further suggests the conditions under which acceleration effects may become important.

Experimental Setup and Results

The experiments were performed in a water tunnel with a NACA 0012 airfoil (chord length C = 8 cm) pivoted about the 1/4-chord point. For the results described here, the free stream speed was set to U_∞ = 10 cm/s resulting in a chord Reynolds number of 8000. A DC servo motor in conjunction with a digital servo controller were used to pitch the airfoil. A schematic of the type of motion considered is shown in Figure 1. The airfoil starts at zero angle of attack, reaches the desired constant pitch rate of $\dot{\alpha}$ during an acceleration period of T_a, and stops at the final angle of attack of 60 degrees through a deceleration period of T_d. We characterize the pitch trajectory by the usual nondimensional pitch rate, K, and the parameter $e = 0.5(T_a + T_d)/T_c$, where T_c is the "ideal" constant pitch rate time scale needed for the motion. The acceleration parameter e gives an indication of the fraction of the motion time used for acceleration/deceleration. The magnitudes of the acceleration and deceleration were the same for the present results so that $T_a = T_d$ and $e = T_d/T_c$.

We present flow visualization results for the case K = 0.4 and different values of e. The actual pitch trajectories recorded during the experiment for the two cases of e = 0.6 and 0.15 are shown for comparison in Figure 2. The evolution of the flow field for K = 0.4, e = 0.6 is illustrated in Figure 3. For each picture, the elapsed time from the start of the motion and the instantaneous angle of attack are indicated. This sequence of pictures was obtained using the Hydrogen-bubble technique and laser sheet illumination at the airfoil mid-span location. Images were

sensed by a CCD camera at a rate of 60 fields/sec with an exposure time of 2 msec/field and acquired by a digital image acquisition system into hard disk in real time.

Figure 3 shows that the first visual indication of separation and vortex formation near the leading edge occurs between (t = 0.73 s, α = 27 $deg.$) and (t = 0.83 s, α = 32 $deg.$). The actual elapsed time and angle of attack were determined to be (t = 0.80 s, α = 31 $deg.$) after close inspection of the image sequence versus time. There are many interesting features in the flow development shown in Figure 3. Note, for example, the number of vortices formed and their interaction and also the upstream (reversed) flow near the airfoil surface at (t = 2.17, 2.37 s).

Reducing the acceleration period by a factor of four to e = 0.15 resulted in the flow development shown in Figure 4. The first visual appearance of leading edge separation and vortex formation was determined to be at (t = 0.64 s, α = 32 $deg.$). In fact many of the details of flow development are nearly the same in Figures 3 and 4 except for a time shift between the occurrence of the events. Reducing the value of e by another factor of four to 0.037 confirmed the observation that while the elapsed time for leading edge separation and vortex formation is affected by e, the angle of attack where this occurs remains unchanged. Similar conclusion was reached when the two cases of e = 0.037, 0.15 at a reduced frequency of K = 0.2 were compared. We should note that our results and conclusions only address the timing of the various events in the flow field development. We do not know, at this time, how the vorticity flux into the separated zone, the circulation of the dynamic stall vortex, and forces on the airfoil are affected as we change the acceleration period.

We now present a scaling argument which suggests that our lowest acceleration corresponds to a time scale that may be too fast for the flow to respond to. For an airfoil reaching a constant pitch rate $\dot{\alpha}$ at a constant acceleration $\ddot{\alpha}$, the acceleration time scale T_a can be defined as

$$T_a = \frac{\dot{\alpha}}{\ddot{\alpha}}$$

The flow convection time scale T_{flow} corresponds to the time it takes for the flow to travel the length of the chord and can be written as

$$T_{flow} = \frac{C}{2U_\infty}$$

A nondimensional acceleration time scale K_{acc} can now be defined and simplified as follows

$$K_{acc} = \frac{T_{flow}}{T_a} = \frac{K}{\alpha_{max}\, e}$$

where K is the reduced frequency, α_{max} the maximum angle of attack, and e the acceleration parameter defined earlier.

Carta [6] has shown that unsteady inviscid effects lead to a reduction of the chordwise pressure gradient which he proposed as the mechanism responsible for dynamic stall delay. These ideas were later extended by McCroskey [7] who showed that unsteady attenuation of the inviscid pressure gradient near the leading edge could explain the dynamic delay in laminar boundary-layer separation. Carta's results, which were derived for oscillating airfoils, show that for high enough reduced frequencies, $2\pi fC/(2U_\infty) > 0.5$, the unsteady reduction of the inviscid pressure gradient reaches an asymptotic value. We interpret this to mean that if the motion time scale is short enough relative to the convection time scale, the inviscid pressure gradient over the airfoil reaches an asymptotic state. We, therefore, suggest that for our experiment the condition $K_{acc} > 0.5$ corresponds to a "frozen" inviscid pressure gradient. According to McCroskey's [7] results, we expect laminar separation to be mostly dictated by the inviscid pressure gradient with little influence from unsteady boundary-layer response.

In all the cases we have presented here, the value of K_{acc} exceeds 0.6. Based on the argument above, for all three cases of e = 0.6, 0.15, 0.037, the airfoil boundary layer is exposed to the same "frozen" inviscid pressure gradient. This may be the reason why all three cases show the first indication of leading edge separation at the same angle of attack. The scaling argument also suggests that at low values of K_{acc} the effects of acceleration period may become important. Since the maximum value of e is unity, low values of reduced frequency K would be required for this to happen.

References

1. Francis, M. S. and Keesee, J. E. [1985] "Airfoil dynamic stall performance with large-amplitude motions." *AIAA J.*, Vol. 23, No. 11, pp. 1653-1659.
2. Graham, G. M. and Strickland, J. H. [1986] "An experimental investigation of an airfoil pitching at moderate to high rates to large angles of attack." AIAA-86-0008.
3. Jumper, E. J., Shreck, S. J. and Dimmick, R. L. [1986] "Lift-curve characteristics for an airfoil pitching at constant rate." AIAA-86-0117.

4. Carr, L. W. [1988] "Progress in analysis and prediction of dynamic stall." *AIAA J.*, Vol. 25, No. 1, pp. 6-17.

5. Reynolds, W. C. and Carr, L. W. [1985] "Review of unsteady, driven, separated flows." AIAA-85-0527.

6. Carta, F. O. [1971] "Effect of unsteady pressure gradient reduction on dynamic stall delay." *J. Aircraft*, Vol. 8, No. 10, pp. 839-841.

7. McCroskey, W. J. [1973] "Inviscid flowfield of an unsteady airfoil." *AIAA J.*, Vol. 11, No. 8, pp. 1130-1137.

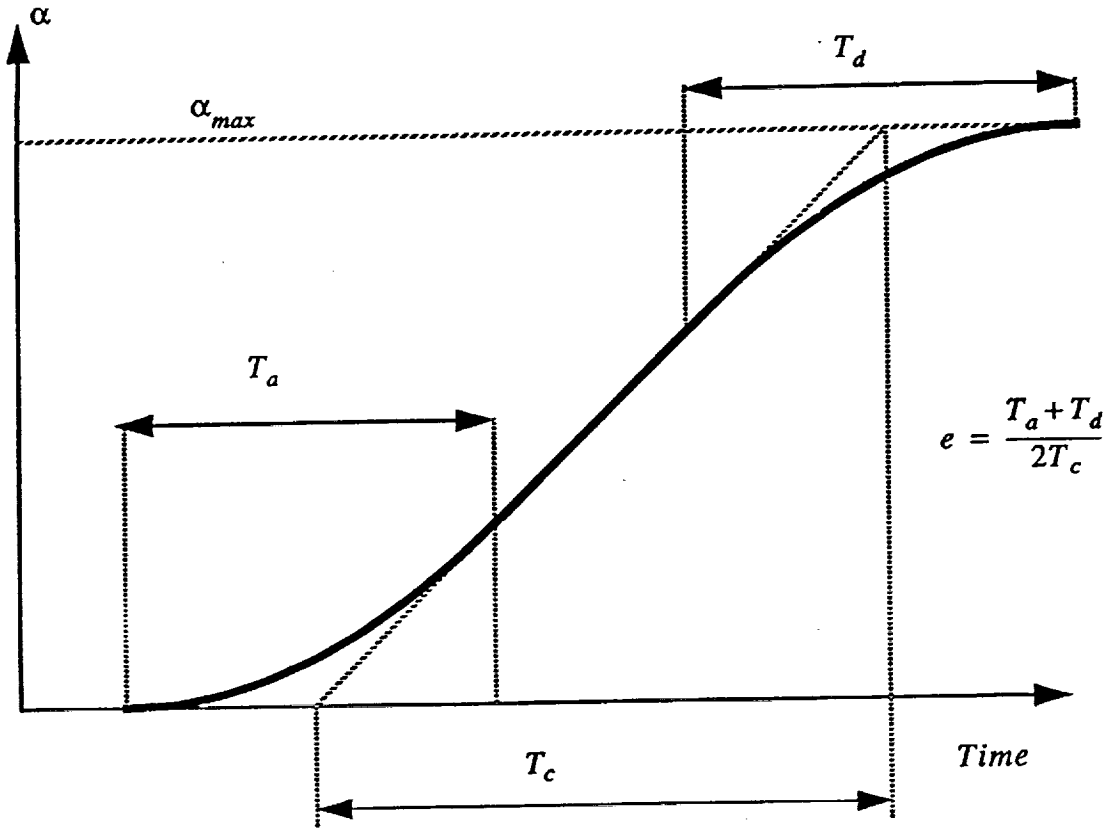

Figure 1. Constant pitch rate motion with finite acceleration and deceleration.

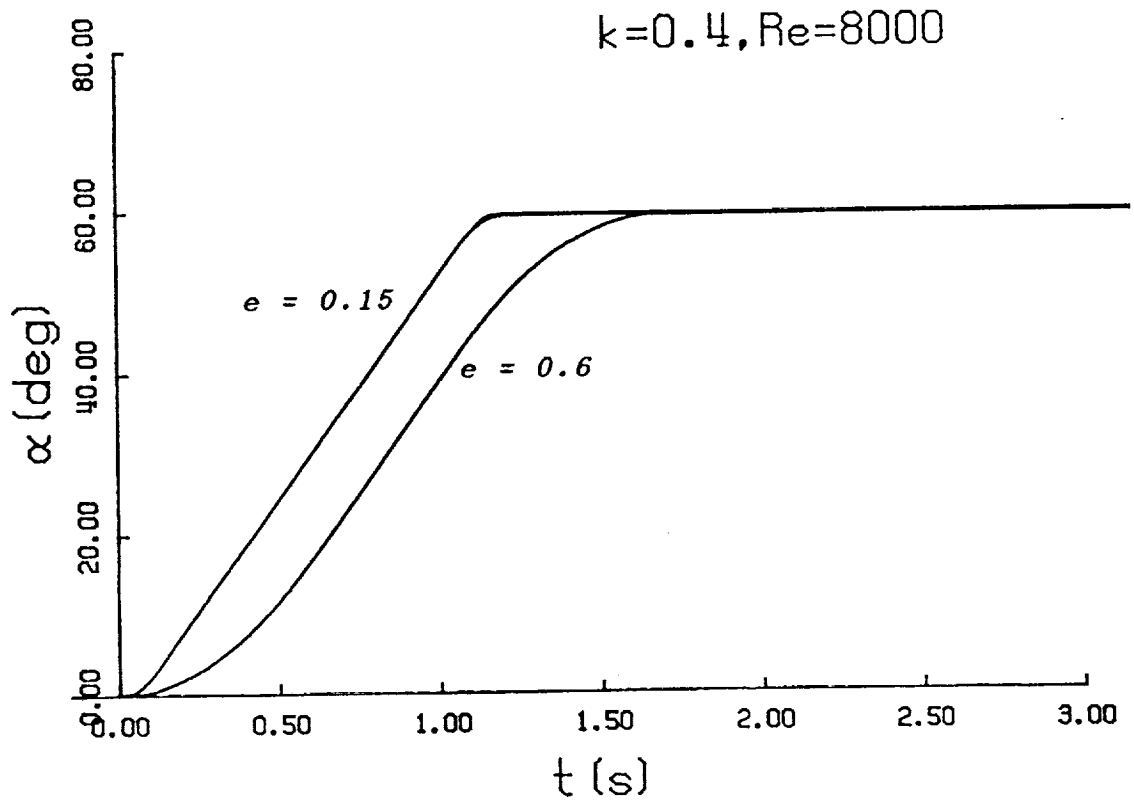

Figure 2. Time history of the airfoil pitch angle recorded during the experiment. Both trajectories reach the same constant pitch rate but with different constant accelerations.

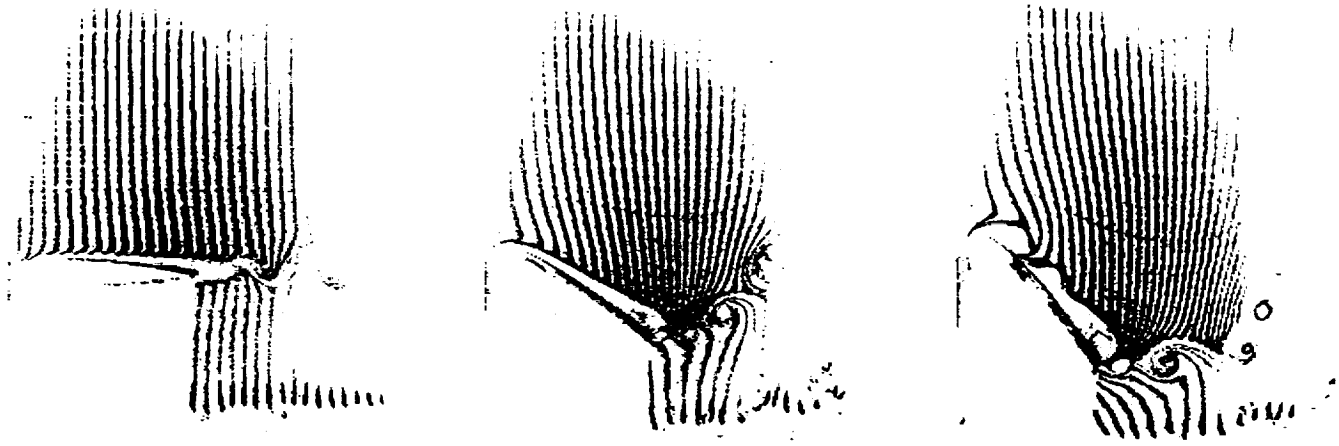

t = 0 s, α = 0° t = 0.73 s, α = 27° t = 1.03 s, α = 43°

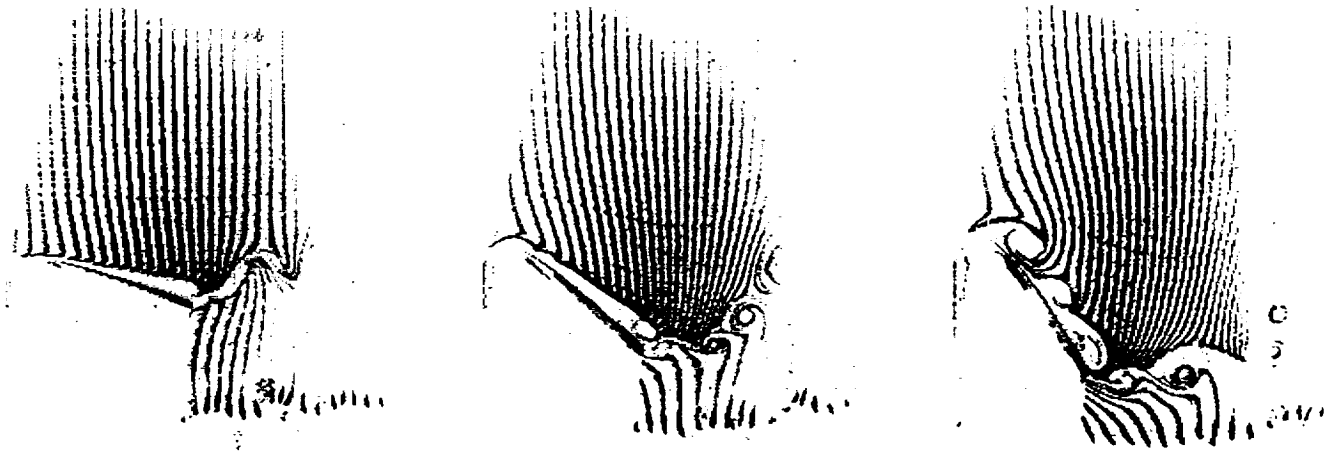

t = 0.43 s, α = 11° t = 0.83 s, α = 32° t = 1.13 s, α = 48°

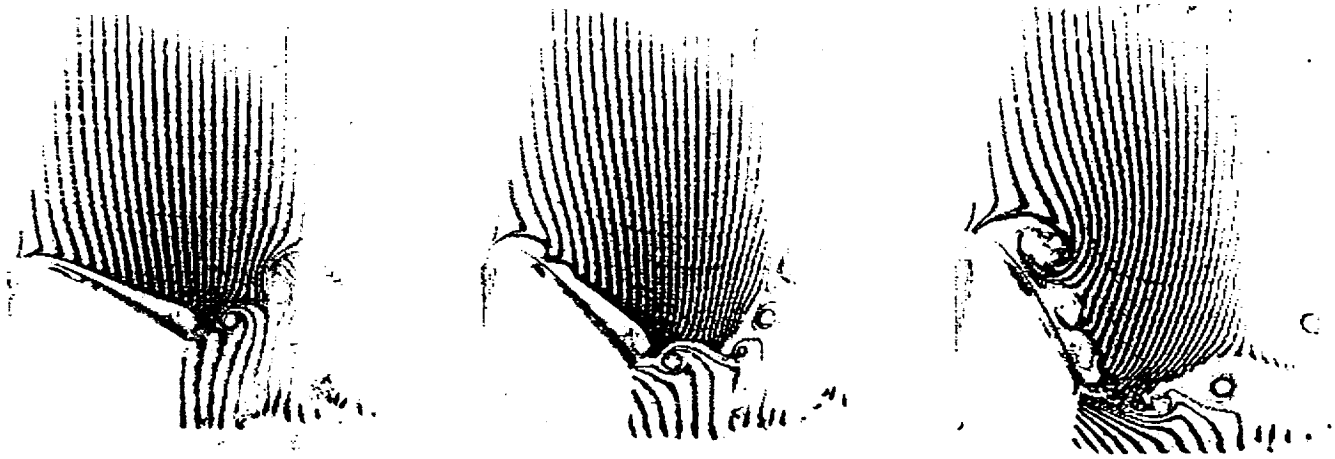

t = 0.63 s, α = 21° t = 0.93 s, α = 38° t = 1.30 s, α = 54°

Figure 3. Evolution of the flow field on the airfoil suction side. (K = 0.4, e = 0.6)

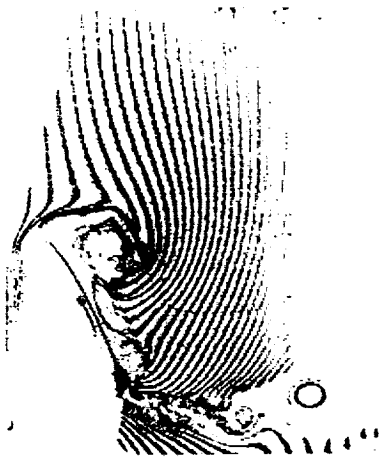

t = 1.47 s, α = 58°

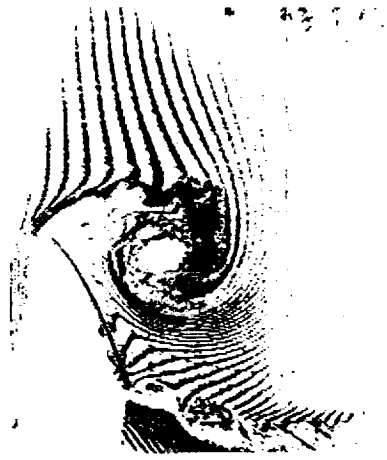

t = 1.97 s, α = 60°

t = 2.63 s, α = 60°

t = 1.63 s, α = 59°

t = 2.17 s, α = 60°

t = 3.06 s, α = 60°

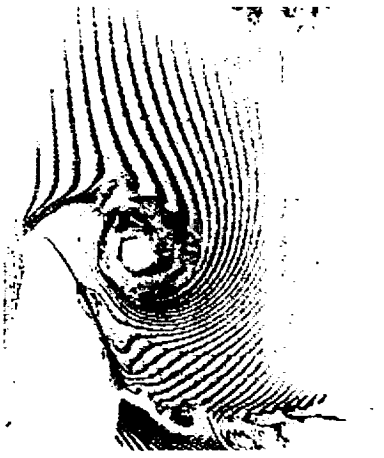

t = 1.80 s, α = 60°

t = 2.37 s, α = 60°

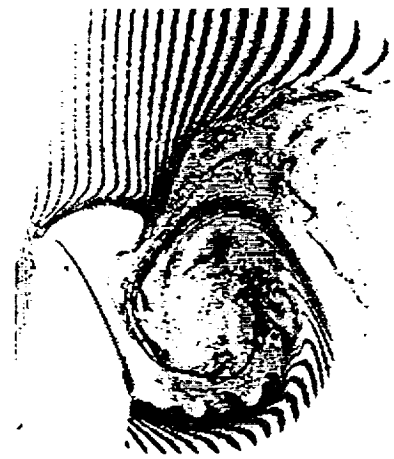

t = 3.57 s, α = 60°

Figure 3. Continued.

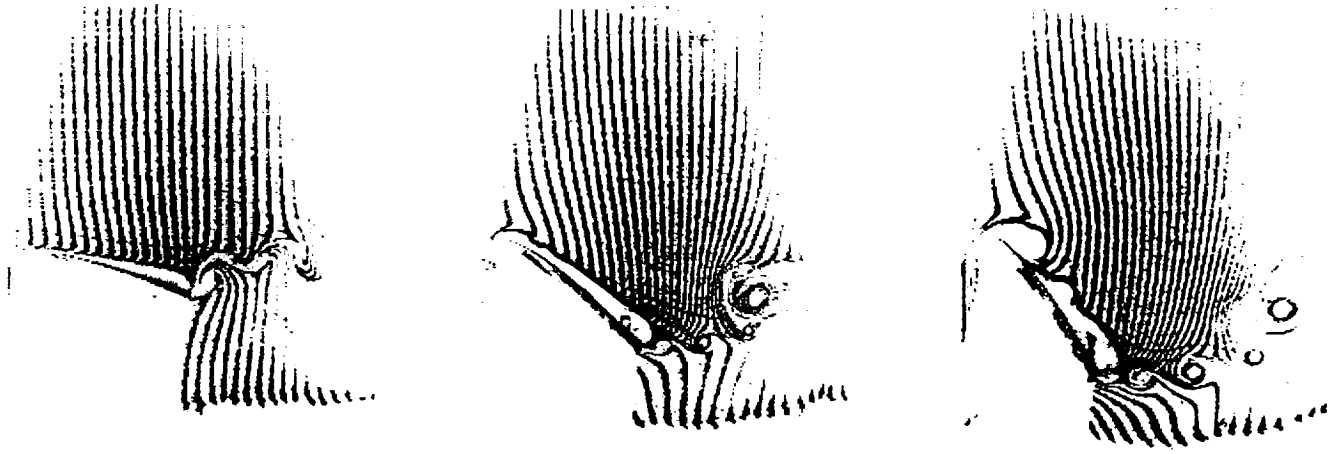

t = 0.24 s, α = 10° t = 0.67 s, α = 34° t = 0.94 s, α = 49°

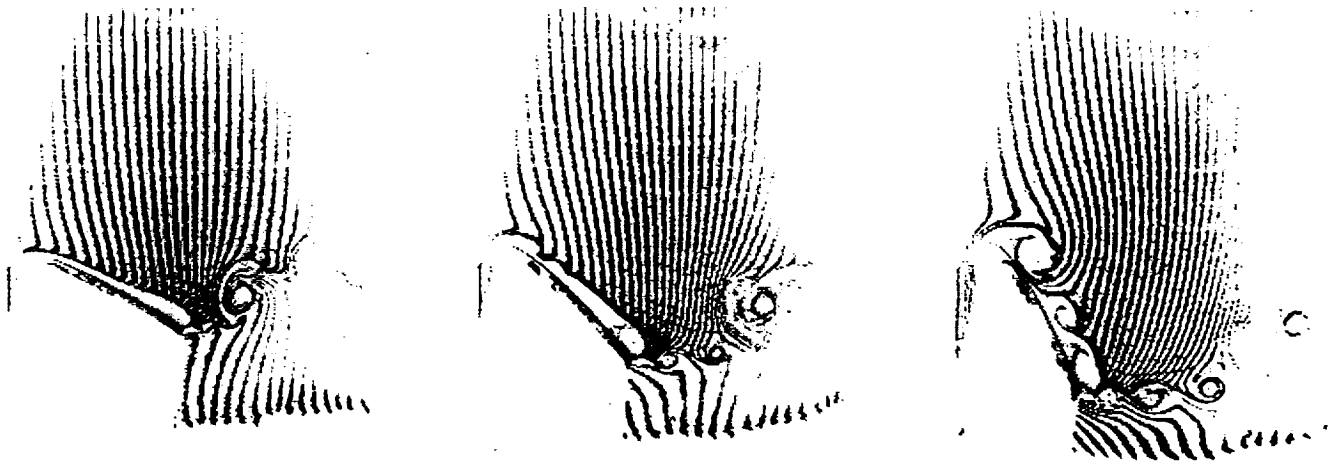

t = 0.44 s, α = 21° t = 0.74 s, α = 38° t = 1.04 s, α = 54°

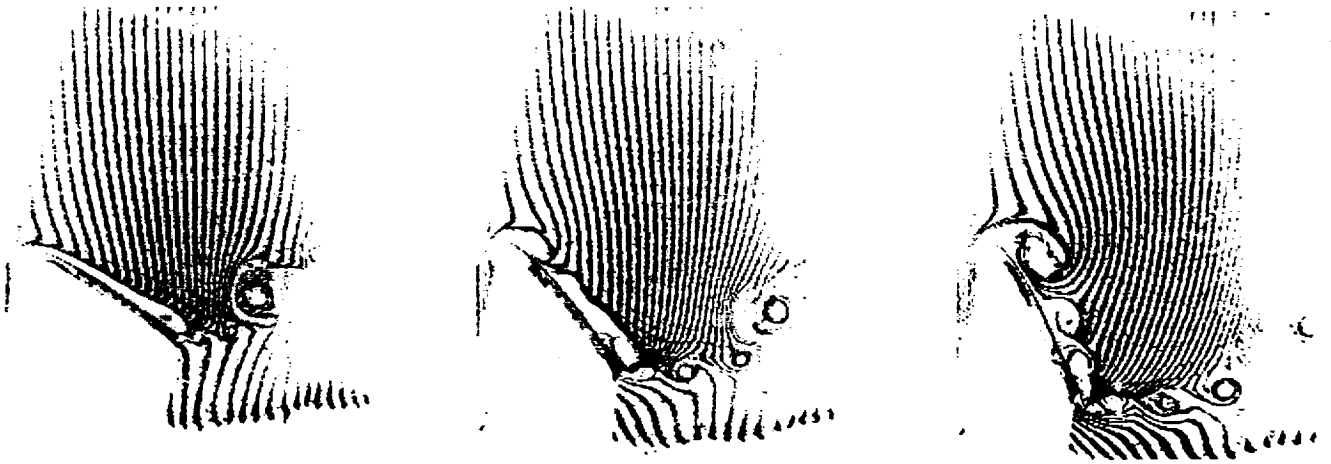

t = 0.54 s, α = 27° t = 0.84 s, α = 43° t = 1.11 s, α = 58°

Figure 4. Evolution of the flow field on the airfoil suction side. (K = 0.4, e = 0.15)

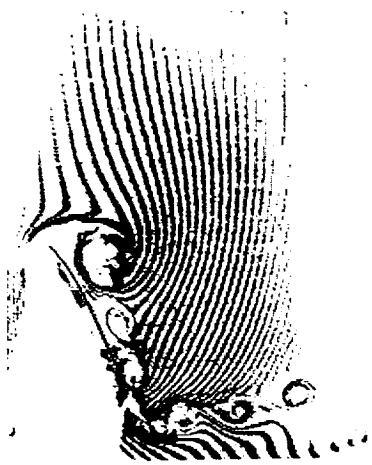

t = 1.21 s, α = 60°

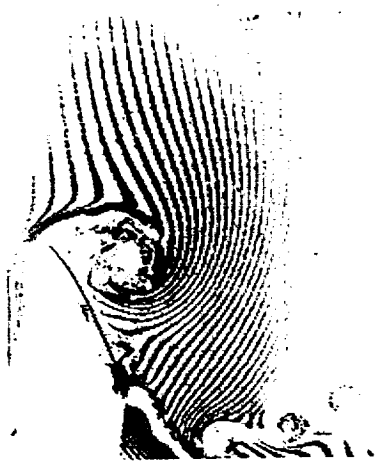

t = 1.44 s, α = 60°

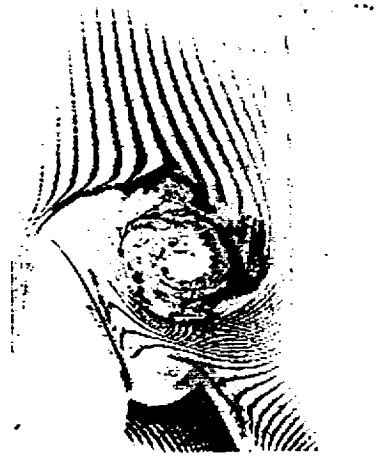

t = 1.97 s, α = 60°

t = 1.27 s, α = 60°

t = 1.57 s, α = 60°

t = 2.11 s, α = 60°

t = 1.34 s, α = 60°

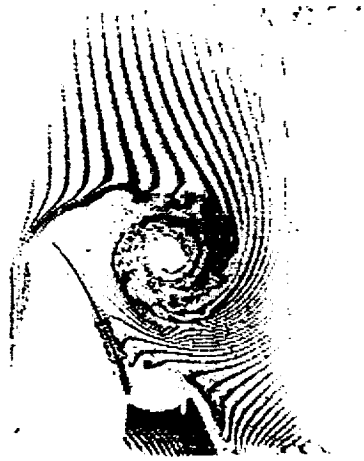

t = 1.84 s, α = 60°

t = 2.27 s, α = 60°

Figure 4. Continued.

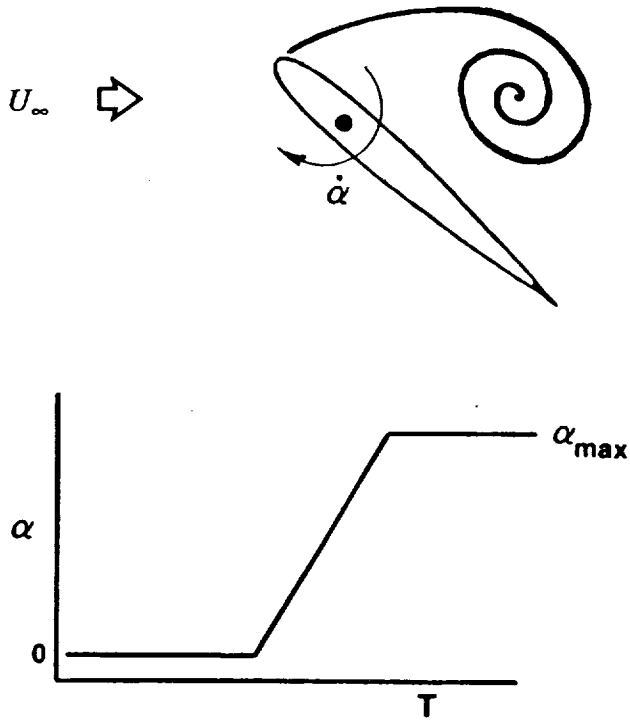

Schematic of constant pitch rate motion.

$$\text{Nondimensional pitch rate } K = \frac{\dot{\alpha}C}{2U_\infty}$$

In reality, the actual motion of the airfoil deviates from the ideal ramp due to the finite acceleration and deceleration periods imposed by the damping of drive system and response characteristics of the airfoil. The flux of vorticity for attached flow at the airfoil surface, $(\partial\omega/\partial y)_s$, is given by

$$\nu \left(\frac{\partial \omega}{\partial y}\right)_s = \frac{1}{\rho}\left(\frac{\partial p}{\partial x}\right)_s + \frac{\partial U_s}{\partial t}$$

The details of the acceleration phase may, therefore, modify the surface vorticity flux by altering the time-varying surface pressure gradient $(\partial p/\partial x)_s$, and also directly through the surface acceleration term $(\partial U_s/\partial t)$.

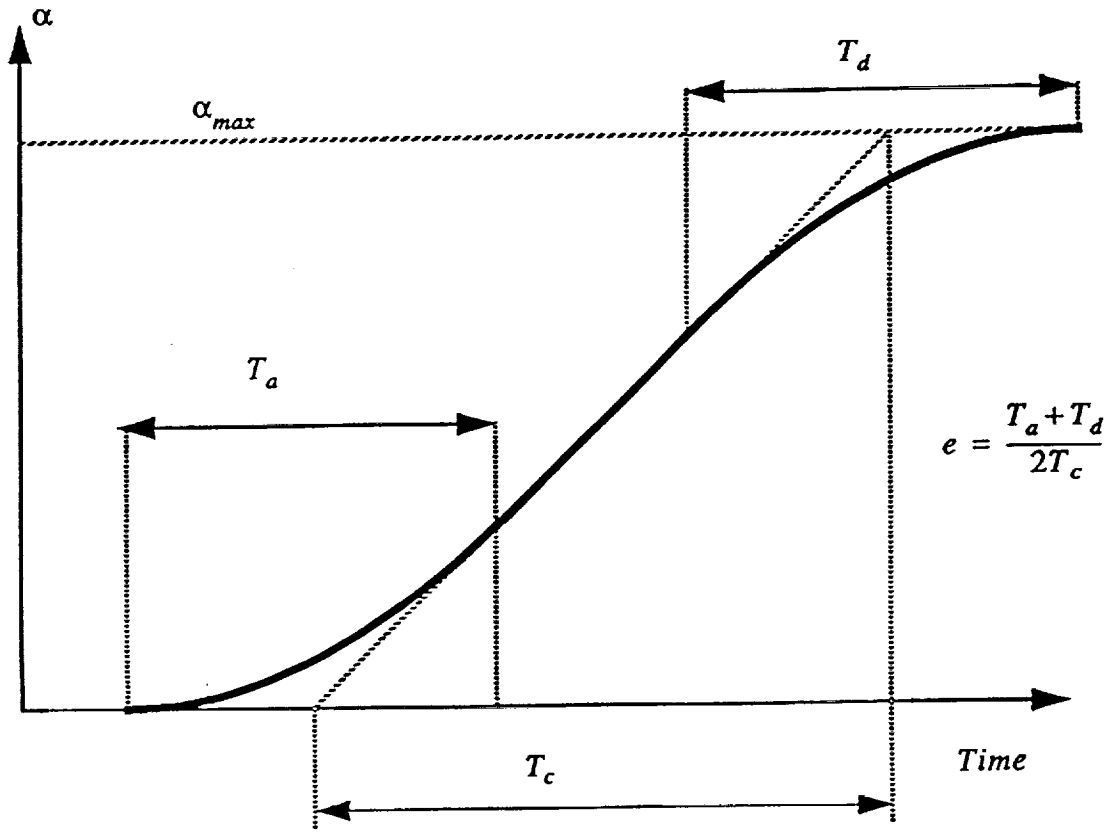

Constant pitch rate motion with finite acceleration and deceleration.

Experimental Setup

Airfoil	NACA 0012
Chord length	C = 8 cm
Pitch axis	1/4-chord
Free stream speed	U_∞ = 10 cm/s
Chord Reynolds number	8,000
Angle of attack variation	0 to 60 degrees
Nondimensional pitch rate	K = 0.2, e = 0.15, 0.037
	K = 0.4, e = 0.6, 0.15, 0.037

Flow visualization	Hydrogen-bubble technique
Illumination	Laser sheet at airfoil mid-span
Image sensing	CCD camera, 60 fields/s, 2 msec exp.
Image acquisition	Digitized in real-time into hard disk

Summary of Results

T_s = elapsed time for leading edge separation (sec).
α_s = angle of attack at leading edge separation (degrees).

	T_s	α_s
$K = 0.2, \quad e = 0.15$	0.97	24
$K = 0.2, \quad e = 0.037$	0.90	25
$K = 0.4, \quad e = 0.6$	0.80	31
$K = 0.4, \quad e = 0.15$	0.60	30
$K = 0.4, \quad e = 0.037$	0.57	31

Flow convection time scale $T_{flow} = \frac{C}{2U_\infty}$

"Constant" pitch rate time scale $T_c = \frac{1}{\dot{\alpha}}$

Acceleration time scale $T_a = \frac{\dot{\alpha}}{\ddot{\alpha}}$

$T_a = e\ T_c$

Nondimensional pitch rate $K = \frac{T_{flow}}{T_c} = \frac{\dot{\alpha}C}{2U_\infty}$

Nondimensional acceleration time $K_{acc} = \frac{T_{flow}}{T_a} = \frac{K}{e}$

It is suggested that for large enough value of K_{acc} (i.e. $K_{acc} > 0.5$), the inviscid pressure gradient remains "frozen".

Conclusions

For the range of parameters studied, the finite acceleration period does not affect the angle of attack where leading edge separation occurs. Many of the details of dynamic stall vortex formation and its interactions appear to be also unaffected.

It is suggested that the value of $K_{acc} = K/e$ must be low enough before the finite acceleration period affects the flow development.

What Next ?

Test the proposed hypothesis by performing experiments at low values of K_{acc}.

Current results are qualitative and only address the timing of various events in the flow field development. Quantify the study by measuring the velocity field and determining the evolution of the circulation of the dynamic stall vortex.

REPORT ON THE WORKSHOP ON ANALYTICAL METHODS IN UNSTEADY SEPARATION

by

A. T. Conlisk
Department of Mechanical Engineering
The Ohio State University
Columbus, OH 43210

A workshop centered around the use of analytical techniques in the computation of unsteady separated flow was held at the Ramada university Hotel and Conference Center on January 25 and 26, 1990. The meeting was sponsored by the U.S. Army Research Office in Research Triangle Park, North Carolina and was hosted by the Departments of Aeronautical and Astronautical Engineering and Mechanical Engineering of The Ohio State University. Meeting Co-Chairmen were R. J. Bodonyi and A. T. Conlisk. During this presentation the Workshop will be summarized and the main conclusions of the Workshop participants will be discussed.

The organization of such a workshop focused on the use of analytical methods in computing unsteady separated flows was motivated by the fact that until the last several years, little was known about the structure of large-scale unsteady separation. Indeed, in problems where the precise details of the unsteady separation boundary layer have been required, such as in the high Reynolds number flow past a bluff body where vortex shedding occurs, ad hoc procedures have generally been used to determine the separation point and the magnitude of the shed vorticity. Furthermore, the computation of accurate solutions to the full time-dependent Navier-Stokes equations at high Reynolds numbers, especially in three-dimensions, remains a difficult, if not impossible, task because of the many different scales of motion which can occur in such a large-scale separated flow. Given these difficulties, a natural question to ask is whether analytical techniques could profitably be used to reduce the amount of numerical computation required or to render untractable numerical problems tractable.

The first day of the workshop consisted of presentations by the invited speakers who were: Professor F. T. Smith, The Ohio State university and University College London, Professor O. R. Burggraf, The Ohio State University, Professor S.F. Shen, Cornell University, Professor J.D.A. Walker, Lehigh University, Dr. P. W. Duck, University of Manchester, Professor N. Riley, University of East Anglia, Professor S. J. Cowley, Imperial College of Science and Technology, and Professor L. Van Dommelen, Florida State University.. The second day consisted of a session wherein the other participants presented short discussions of their particular research in the area., This rather informal session was followed by a panel discussion led by the invited speakers and involving all participants ® unsteady separated flow problems involving

eruptions of boundary layer fluid from the wall layer into the main flow. F. T. Smith discussed a possible structure for such a eruptive behavior in general terms within an interactive framework and he defined a sequence of stages of the flow leading to formation of a vortex structure all involving quite distinct length and time scales (all scaling with an inverse power of the Reynolds number); the numerical problems associated with computing such a flow are obvious. The other speakers addressed the above question through discussion of a particular problem. J.D.A. Walker focused on the emergence of a singularity in the boundary layer flow induced by a potential vortex; he discussed computations of the flow up to the singular time using a Lagrangian scheme. Professors Shen and Riley addressed the problem of high Reynolds number unsteady flow past a cylinder while Professor Burggraf addressed the problem of propagating stall in compressors. Professor Duck considered the problem of unsteady separation in a local region near a line of symmetry and Professors Cowley and Van Dommelen discussed the unsteady separation process in three-dimensions.

The main conclusions of the Workshop were that although we know much more about unsteady separation than we did say ten years ago, the numerical methods which must be employed to bridge the gap between small and large scale separation have not been developed. Indeed, while there seems little doubt that there does exist a singularity in the boundary layer equations at finite time in these unsteady separated flow problems, the concensus of the workshop was that considerable effort should be directed to developing methods by which computation of the flow may be effected beyond the singularity.

REPORT DOCUMENTATION PAGE

Form Approved
OMB No. 0704-0188

1. AGENCY USE ONLY *(Leave blank)*	2. REPORT DATE	3. REPORT TYPE AND DATES COVERED
	March 1992	Conference Publication

4. TITLE AND SUBTITLE
Physics of Forced Unsteady Separation

5. FUNDING NUMBERS
505-59-53

6. EDITOR(S)
L. W. Carr

7. PERFORMING ORGANIZATION NAME(S) AND ADDRESS(ES)
Ames Research Center
Moffett Field, CA 94035-1000

8. PERFORMING ORGANIZATION REPORT NUMBER
A-91055

9. SPONSORING/MONITORING AGENCY NAME(S) AND ADDRESS(ES)
National Aeronautics and Space Administration
Washington, DC 20546-0001

10. SPONSORING/MONITORING AGENCY REPORT NUMBER
NASA CP-3144

11. SUPPLEMENTARY NOTES
Point of Contact: L. W. Carr, Ames Research Center, MS 260-1, Moffett Field, CA 94035-1000
(415) 604-4143 or FTS 464-4143

12a. DISTRIBUTION/AVAILABILITY STATEMENT
Unclassified-Unlimited
Subject Category – 34

12b. DISTRIBUTION CODE

13. ABSTRACT *(Maximum 200 words)*

This report contains the proceedings of a workshop held at NASA Ames Research Center in April 1990. This workshop was jointly organized by NASA, the Air Force Office of Scientific Research (AFOSR), and the Army Research Office (ARO), and was directed toward improved understanding of the physical processes that cause unsteady separation to occur. The proceedings contain the written contributions for the workshop, and include selected viewgraphs used in the various presentations.

14. SUBJECT TERMS
Aerodynamic stalling, Airfoil oscillations, Airfoils, Boundary layer separation, Computational fluid dynamics, Separated flow, Unsteady flow, Viscous flow, Vortices, Vorticity, Rotary wings

15. NUMBER OF PAGES
340

16. PRICE CODE
A15

17. SECURITY CLASSIFICATION OF REPORT	18. SECURITY CLASSIFICATION OF THIS PAGE	19. SECURITY CLASSIFICATION OF ABSTRACT	20. LIMITATION OF ABSTRACT
Unclassified	Unclassified		